



Norwegian University of
Science and Technology

Modeling and Analysis of a Submerged Floating Tunnel

Hans Jakob Vik

Marine Technology

Submission date: February 2017

Supervisor: Bernt Johan Leira, IMT

Co-supervisor: Senthuran Ravinthrakumar, IMT

Norwegian University of Science and Technology
Department of Marine Technology

Preface

This is a Master's thesis in marine structures at the Department of Marine Technology, NTNU. It is written during the fall semester 2016 and beginning of the spring semester 2017. The thesis has been carried out in cooperation with the Department of Marine Technology, represented by Prof. Bernt Johan Leira and Ph.D. Candidate Senthuran Ravinthrakumar.

The thesis topic is floating bridges and contains modeling and analysis of a previously developed concept. The concept is developed by Dr. Techn. Olav Olsen and Reinertsen under the name Reinertsen Olav Olsen Group. It was developed during 2012/2013. The topic concerning floating bridges is very relevant due to the planning of a ferry-free European route E39 in Norway. Some of the ferry crossings are planned to be replaced by floating bridges, still allowing some of the world's biggest cruise ships to cross over or under the bridge. This has resulted in many never before built, floating bridge concepts.

The reader of the thesis is assumed to have a background in finite element method and hydrodynamics. Knowledge of the computer software ANSYS, which has been used in the modeling and analysis, is preferable, but not necessary.

Trondheim, February 24, 2017



Hans Jakob Vik

Acknowledgment

I would like to thank my friends and fellow students at the Department of Marine Technology, NTNU. You have made my time at the Norwegian University of Science and Technology some of the best times of my life, from hard and long periods of tough work to many fantastic trips, events and parties. You made it all worthwhile.

My supervisor Professor Bernt Johan Leira deserves special appreciation for both guidance and help during the work with my Master's thesis. Thank you for your good advice during the unraveling of the Thesis and good luck in the future.

Lastly, I would like to thank my co-supervisor, PhD Candidate Senthuran Ravinthrakumar. His help, advice, guidance and support has meant a lot for the final results of the Thesis. He has guided in both theory, software usage, thesis layout and linguistic matters. He has also ensured high morale and optimism during challenging times, which has resulted in many extra hours of effort and work.

H.J.V.

Summary

This master thesis is a study of a submerged floating tunnel and its responses exposed to hydrodynamic loading. Static, modal and dynamic analyses have been performed in ANSYS Mechanical 16.2 for the a global bridge model.

First, a literature study of existing and planed marine bridges was included. It focuses on the differences and similarities for marine bridge concepts, emphasizing bridges planed for a ferry-free E39. A submerged floating tunnel, like the bridge modeled in this thesis, has never been built before.

A study of pontoon configurations focuses on the differences between two pontoon geometries. The restoring and damping coefficients from the analysis results are implemented in the global submerged floating bridge model. A comparison of pontoon behavior is also used to verify the hydrodynamic modeling in ANSYS. The comparison is carried out by modeling the same pontoon in two different softwares, Wadam and ANSYS, and comparing motion and behavior. The results are good, but uncertainties connected to added mass and boundary condition modeling, effects the results. The challenges with correct boundary conditions are not present in the global model, and the results are therefore deemed good for further analyses.

The static analysis results, focusing on a neutrally buoyant structure, has a maximum displacement of 0.24 meters and a minimum displacement of -0.17 meters. These results are considered good and the structure is concluded neutrally buoyant.

The eigenfrequencies from the eigenfrequency analysis coincide with the frequencies from a compared study conducted by the Reinertsen Olav Olsen Group, for the same submerged floating tunnel. The mean deviation for the 25 first eigenfrequencies is 6.4 %, with a maximum of 19 % and a minimum of 1.3 %. The eigenperiods from mode 25 to 1 range from 5.1 - 45.1 seconds and the mode shapes of the first 10 modes coincide with the ones from the compared study.

The thesis includes multiple dynamic analyses with different wave loading. The maximum harmonic wave loading is estimated from the the irregular significant wave height and period of 2.14 meters and 4.8 seconds. The final harmonic wave, causing maximum harmonic bridge re-

sponse, has a height of 4.85 meters and a period of 6.75 seconds.

A 300 seconds long irregular wave analysis is carried out in order to estimate the maximum irregular bridge response. The analysis was supposed to be 3 hours long, but due to memory limitations, the maximum length was 300 seconds. The most probable and maximum expected irregular responses for a 3-hour sea state are estimated from the 300 seconds long irregular analysis, in order to compare the results with the maximum harmonic wave responses. While maximum bending moments about global Y- and Z-axis and minimum bending moment about Z-axis occur for the harmonic maximum wave loading, the rest occur for the estimated 3-hour irregular wave response.

The maximum and minimum bending moments about global Y-axis are 939 and -1028 MNm. The location for the extremes are in the main tunnels of the bridge at the biggest spans between supports. The biggest spans are at the center or at the ends of the bridge. The maximum and minimum torsional moments about global X-axis occur in the main tunnels at the supports closest to the largest spans. It has an absolute value of 931.4 MNm. For the bending moments about global Z-axis, the values are 301 and -356 MNm. These moments are situated at the main tunnels where shafts connect the pontoons to the tunnels.

The maximum displacement for the harmonic analysis is 1.11 meters, while the estimated expected maximum for the irregular analysis is 1.85 meters. This is reflected in the maximum von Mises stress, which is 44 MPa for the harmonic analysis and 164 MPa for the estimated irregular expected maximum.

The maximum responses from the regular and irregular analysis are good compared to each other. The fact that the characteristics of the regular wave is estimated from the irregular spectrum parameters, implies that similar magnitudes, directions and locations for the responses are to be expected. The differences in the response values have its origin from the harmonic and irregular wave loading. The wave loading causes different bridge motions, which eventually results in different response magnitudes.

The overall results for the analyses carried out are considered reasonable and accurate. Further modeling and analyses can be performed in order to verify the results in more detail.

Sammendrag

Denne masteroppgaven omfatter en studie av en neddykket flytebro med tilhørende hydrodynamiske last- og responsanalyser. ANSYS Mechanical 16.2 har blitt brukt for å gjennomføre statisk og dynamisk analyse for konstruksjonen. I tillegg er det gjennomført en modal analyse og en studie av to forskjellige pongtong geometrier.

Den første delen av arbeidet med oppgaven er en litteraturstudie av eksisterende og planlagte flytende broer. Studien legger spesielt vekt på utviklede konsepter for ferjefri E39. En neddykket rørbro, som er modellert og analysert i oppgaven, har aldri før blitt bygget.

Pongtongstudien fokuserer på forskjellen mellom to geometrier. Den endelige pongtong konfigurasjonens stivhet og demping er implementert i den globale bromodellen. En sammenligning av pongtongrespons og bevegelse er også blitt gjort for å verifisere den hydrodynamiske modellen i ANSYS. Den samme pongtongen er modellert og testet i to forskjellige programmer, ANSYS og Wadam, hvor resultatene er sammenlignet. Resultatene av sammenligningen er ganske gode, men usikkerhet forbundet med hydrodynamisk tilleggs masse og grensebetingelser, påvirker resultatene slik at det oppstår forskjeller. utfordringene forbundet med pongtongens grensebetingelser er imidlertid ikke er problem i forbindelse med global modellanalyse, som gjør at resultatene anses som gode.

Resultatene av den statiske analysen, hvor målet er en bromodell med nøytral oppdrift, har en maksimum og minimum vertikal utbøying på 0.24 og -0.17 meter cm. Utbøyingens verdi gjør at modellen regnes å ha tilnærmet nøytral oppdrift.

Eigenfrekvensene fra egenfrekvensanalysen er samsvarende med frekvensene fra en studie utarbeidet av Reinertsen Olav Olsen Gruppen for tilsvarende bromodell. Gjennomsnittlig avvik ligger på 6.4 %, hvor maksimum er 19 % og minimum er 1.3 %. Egenperiodene for de 25 første svingemodene, i rekkefølge fra 25 til 1, ligger mellom 5.1-45.1 sekunder. Formen til de 10 første svingemodene samsvarer også med de 10 første svingemodene fra sammenligningsstudien.

Oppgaven inkluderer flere dynamiske analyser med forskjellige bølgelaster. Den høyeste harmoniske bølgen som er brukt i analysene, er estimert fra et irregulært bølgespekter. Den es-

timerte bølgehøyden for den høyeste harmoniske bølgen er 4.85 meter, med en tilhørende maksresponsperiode på 6.75 sekunder.

En 300 sekunder lang irregulær bølgeanalyse er gjennomført for å estimere maksimal konstruksjonsrespons i irregulær sjø. Den mest sannsynlige og den høyest forventede irregulære responsen for en tre timers sjøtilstand er estimert ut i fra den 300 sekunder lange irregulære analysen. Dette er gjort for å kunne sammenligne responsen fra den regulære analysen med den estimerte irregulære maksresponsen.

Maksimum og minimum bøyemoment om global Y-akse forekommer i den harmoniske analysen. Dette gjelder også for maks bøyemoment om global Z-akse. Alle andre ekstremverdier for respons forekommer for den estimerte tre timers sjøtilstanden. Maksimum og minimum bøyemoment om global Y-akse er 939 og -1028 MNm. Momentene forekommer i broens hovedspenn, enten i midten eller ved endene. Det er her de lengste spennene i konstruksjonen er. Maksimum torsjonsmoment om global X-akse forekommer også ved hovedspennene, men ved pongtongene eller ved landfeste. Forskjellen er at det ikke er i midten av selve spennene, men ved støttene på hver side. Maksimum torsjonsmoment har en absoluttverdi på 931.4 MNm. Maksimum og minimum bøyemoment for global Z-akse opptrer i hovedrørene rett under pongtongene. Verdien er 301 og -356 MNm.

Maksimum utbøying for den harmoniske analysen er 1.11 meter, mens den forventede maksimale utbøyingen, estimert for en 3 timers sjøtilstand, er 1.85 meter. Dette gjenspeiles i von Mises spenningene, som er 44 MPa for harmoniske analyse og 164 MPa for den høyeste forventede irregulære responsen.

Maksimal harmonisk og irregulær respons synes å sammenfalle godt. Verdiene er like og i samme størrelsesorden. Det faktum at den maksimale harmoniske bølgen er estimert ut fra det irregulære spekterets parametere, gjør at sammenfallende resultater er å forvente. Forskjellene har mest sannsynlig sitt utspring i det faktum at bølgelastene er forskjellige, nemlig regulære og irregulære. Dette gjør at broens beveger seg ulikt, som igjen fører til forskjell i respons. De sammenfattede resultatene for gjennomførte analyser betraktes som fornuftige og presise. Fremtidig arbeid, som videre modellering og analysering av konstruksjonen, kan fortsatt gjennomføres for å ytterligere verifisere resultatet.

Contents

Preface	i
Acknowledgment	iii
Summary	v
Sammendrag	vii
1 Introduction	1
1.1 Thesis Objectives	2
1.2 Background	3
1.3 Limitations	3
1.3.1 Modeling Limitations	3
1.3.2 ANSYS Ocean Data Input	4
1.3.3 Computer and Software Limitations	4
1.3.4 Concrete Structure Knowledge	4
1.4 Structure of the Report	4
2 Review - Floating Bridges	7
2.1 Submerged Floating Tunnel	7
2.1.1 Submerged Tunnel with Excess Buoyancy	8
2.1.2 Pontoon Supported Submerged Floating Tunnel	8
2.1.3 Feasibility Study for Crossing of Sognefjorden by Reinertsen Olav Olsen Group.	9
2.2 Suspension Bridge on Floating Foundations	12
2.2.1 Feasibility Study of Sognefjorden with Suspension Bridge on Floating Foun- dations	12
2.2.2 Floating Bridge with TLP Technology	13

2.3	Conventional Floating Bridges	15
2.4	Ship Channel at Shore	16
2.5	Combination Bridges	17
2.6	SFTs with Conventional Floating Bridge	17
3	Structural Loads and Load Theory	19
3.1	Specific Gravity	19
3.2	Hydrostatic Loads - Buoyancy	20
3.3	Traffic Loads	20
3.4	Snow and Ice	21
3.5	Tide	22
3.6	Currents	22
3.6.1	Viscous Forces	22
3.6.2	Vortex Induced Vibrations - ViV	24
3.7	Wave Loads	24
3.7.1	Avalanche Induced Waves	25
3.7.2	Effects of Stratified Flows - Internal Waves	25
3.8	Wind	25
3.9	Ship Collision	26
4	Response and Wave Theory	27
4.1	Static Response Analysis	27
4.2	Dynamic Response Analysis	29
4.3	Modal Analysis	30
4.3.1	Eigenvalue Analysis	30
4.3.2	Rayleigh Damping Coefficient Procedure	31
4.4	Harmonic Wave Height Estimation	34
4.5	Estimating Maximum Irregular Response	38
5	Global Modeling of an SFT	41
5.1	Modeling and Calculation Software	41

5.1.1	Computer Software	42
5.1.2	Main Program Description	42
5.1.3	Pontoon Program Description	44
5.1.4	MATLAB and ANSYS APDL scripts	44
5.2	ANSYS Elements	45
5.2.1	BEAM189 - A Beam Element	45
5.2.2	COMBIN14 - A Combination Spring Element	46
5.2.3	MASS21 - A Concentrated Mass Element	47
5.2.4	PIPE289 - A Pipe Element	47
5.3	Submerged Floating Tunnel - Global Dimensions	48
5.4	Cross Sections	49
5.4.1	Cross Section Geometries	49
5.4.2	Cross Section Modeling	50
5.5	Global Model Line Arrangement	51
5.5.1	Element Representation	51
5.5.2	Line Arrangement - Cross Section Offset	52
5.6	Pontoon Modeling	53
5.6.1	Pontoon Arrangement	53
5.6.2	Pontoon Geometry and Properties	54
5.6.3	Pontoon Buoyancy Modeling	56
5.6.4	Pontoon Mass and Added Mass	57
5.7	Boundary Conditions	57
5.8	ANSYS Ocean Loading	58
5.8.1	Basic Ocean Loading	59
5.8.2	Current Ocean Loading	60
5.8.3	Wave Ocean Loading	60
5.9	Modeling Ballast and Flooded Pipes	61
5.9.1	Ballast in Main Tunnel Pipe	61
5.9.2	Lower and Upper Bridge Weight and Buoyancy Considerations	62
5.9.3	Flooded Pipes	63

5.10	Buoyancy	64
5.10.1	Buoyancy Modeling	64
5.10.2	Neutral Buoyancy	65
5.11	Added Mass - Hydrodynamic Added Mass with OCDATA	65
5.12	Material Properties	66
5.12.1	Concrete Properties	66
5.12.2	Steel Properties	67
5.12.3	Pontoon Material Properties	67
6	Analyses	69
6.1	ANSYS Analysis Solving Limitations	70
6.1.1	Remote Desktops at the Department of Marine Technology, NTNU	70
6.2	Mesh Analysis	72
6.2.1	Decreasing Mesh Size Analysis	73
6.2.2	Mesh Optimization Analysis using Particle Swarm Optimization	73
6.3	Pontoon Analysis	75
6.3.1	GeniE Modeling - Mass and Panel Model	75
6.3.1.1	HydroD - Pontoon Analysis	76
6.3.2	ANSYS Pontoon Analysis	77
6.3.2.1	Heave Motion Analysis	79
6.3.2.2	Roll Motion Analysis	79
6.3.2.3	Pitch Motion Analysis	80
6.3.3	ANSYS Pontoon RAOs	80
6.4	Static Analysis	82
6.5	Modal Analysis	83
6.5.1	Eigenfrequency and Mode Shape Analysis	83
6.5.2	Effective Mass Participation Analysis	84
6.5.3	Rayleigh Damping Coefficient Calculations	84
6.6	Global Harmonic Wave Response Analysis	85
6.6.1	ANSYS Harmonic Wave Parameters	85

6.6.2	Harmonic Wave Analysis	86
6.7	Global Irregular Wave Response Analysis	88
6.7.1	Remote Desktop Simultaneous Analyses and Time Consumption	88
6.7.2	Expected Maximum Response	89
7	Results and Description	91
7.1	Mesh Convergence Results	92
7.1.1	Decreasing Mesh Size Results	92
7.1.2	PSO Results	94
7.2	Pontoon Analysis Results	96
7.2.1	WADAM Pontoon Results	96
7.2.1.1	Restoring Coefficients	96
7.2.1.2	WADAM RAOs - Peak Frequencies and Response	97
7.2.1.3	WADAM Potential Damping and Curve Fitting	102
7.2.2	ANSYS Simplified Pontoon Results and Wadam Comparison	103
7.2.2.1	ANSYS RAOs - Comparison to WADAM Results	103
7.3	Static Analysis	108
7.3.1	Static Results with Tidal Change	108
7.3.1.1	Mean Sea Level	109
7.3.1.2	High Tide: 1.85 Meters	110
7.3.1.3	Low Tide: -1.58 Meters	111
7.4	Modal Analysis Results	112
7.4.1	Eigenfrequency Analysis Results	112
7.4.1.1	Horizontal Mode Shapes	114
7.4.1.2	Vertical Mode Shapes	114
7.4.2	Participating Masses	116
7.4.3	Estimating Rayleigh Damping Coefficients	118
7.5	Global Harmonic Wave Analysis Results	120
7.5.1	Maximum Response for Different Wave Periods	120
7.5.1.1	Rotational Response	121

7.5.1.2	Harmonic Wave Loading Displacement	125
7.5.1.3	Von Mises Stress due to Harmonic Wave Loading	128
7.5.2	Bending and Torsional Moments due to Harmonic Loading	130
7.5.2.1	Bending Moment about Global Y-axis	130
7.5.2.2	Bending Moment about Global Z-axis	132
7.5.2.3	Rotational Moment about Global X-Axis	134
7.5.2.4	Worst Harmonic Wave Period	136
7.6	Global Irregular Wave Analysis Results	138
7.6.1	Maximum Global Response for a 300 Second Irregular Wave Loading Anal- ysis	138
7.6.2	Irregular 3-hour Sea State Results and Comparison	142
8	Discussion	145
9	Concluding Remarks	151
9.1	Conclusion	151
9.2	Recommendations for Further Work	154
	Bibliography	156
	Appendix	I
A	Program Descriptions and Flowcharts	I
A.1	Main Program	I
A.1.1	Main Program - Complimentary Program Description	I
A.1.2	How to Run the Program	II
A.2	Pontoon Program	III
A.2.1	Program Description	III
A.2.2	How to Run the Program	IV
B	Scripts and Input Files	V
B.1	Matlab	V
B.2	TextPad Ansys Input File	IX

C	Wadam Results	XV
C.1	Pontoon Analysis	XV
C.1.1	Potential Damping - Curve Fitting Results	XV
D	ANSYS Results	XIX
D.1	Pontoon Analysis	XIX
D.1.1	Roll RAO	XIX
D.2	Static Analysis Results	XX
D.2.1	Displacement	XX
D.2.1.1	Mean Sea Level	XX
D.2.1.2	High Tide: +1.85m	XXI
D.2.1.3	Min Tide: -1.58m	XXII
D.3	Modal Analysis Results	XXIII
D.3.1	Participating Masses	XXIII
D.3.2	Rayleigh Damping Ratio Calculation	XXIII
D.3.3	Harmonic Wave Results	XXV
D.3.4	Worst Harmonic Wave Period, $T = 6.75s$	XXV
D.3.5	Harmonic Wave Results	XXIX
D.3.6	Irregular Wave Results	XXIX
D.3.6.1	Maximum and Minimum Nodal and Elemental Reponses	XXIX
E	Digital Appendix	XLI

List of Figures

2.1	Tethered submerged tunnel, illustration Vegvesen (2011)	8
2.2	Submerged tunnel with pontoon supports, illustration Vegvesen (2011, p. 12) . . .	9
2.3	The main dimensions of the submerged tunnel, illustration (Group, 2013, p. 6) . .	10
2.4	Complete cross section of the structure, illustration Group (2013, p. 7)	11
2.5	Main dimensions of main section, picture from Group (2013, p. 8)	11
2.6	Sognefjorden floating bridge, illustration Vegvesen et al. (2013, p. 6)	12
2.7	Main dimensions of the bridge, illustration Vegvesen et al. (2013, Appendix) . . .	13
2.8	The TLP suspension bridge concept over Bjørnafjorden, illustration Holtberget (2015)	14
2.9	Tension leg platform, illustration Offshore-Technology	14
2.10	Floating bridges on pontoon supports	15
2.11	Mid-fjord ship channel, illustration Vegvesen (2011, p. 6)	16
2.12	Floating bridges with suspension close to shore	16
2.13	SFTs combined with conventional floating bridges	17
3.1	Traffic loaded bridge, Illustration Vegvesenet	21
4.1	Probability density for a gaussian response process	39
5.1	Flowchart for the main program	43
5.2	Illustration a of BEAM189 element, illustration (ANS, 2016, Element Library) . . .	46
5.3	Illustration of a COMBIN14 element, illustration (ANS, 2016, Element Library) . .	46
5.4	Illustration of a MASS21 element, illustration (ANS, 2016, Element Library)	47
5.5	Illustration of a pipe289 element, illustration (ANS, 2016, Element Library)	48

5.6	Comparison of main cross section from Reinertsen Olav Olsen Group study and ANSYS model	50
5.7	Line arrangement and cross section offset - Main tunnel and bracing	51
5.8	Line arrangement and cross section offset - Connection shaft and pontoon	52
5.9	Line arrangement and cross section offset - Tunnel and bracing vertical offset	52
5.10	Comparison of general pontoon arrangement from Reinertsen Olav Olsen Group study and ANSYS model	53
5.11	Simplified and final pontoon geometries	54
5.12	The springs representing the pontoon characteristics, explanation in Table 5.5	56
5.13	Pontoon Layer Modeling	57
5.14	Submerged floating tunnel boundary conditions	58
5.15	Main cross section from Reinertsen Olav Olsen Group study, illustration (Group, 2013, p. 8)	62
5.16	The ballast nodes of the main tunnel pipes	64
6.1	Flow chart describing how an analysis can be split into subanalyses on several computers	71
6.2	Mesh attributes for the pipe cross sections	72
6.3	Simplified GeniE pontoon modeling	76
6.4	Final GeniE pontoon modeling	76
6.5	Simplified HydroD pontoon modeling	77
6.6	ANSYS elemental pontoon lines	77
6.7	Broad side view of ANSYS pontoon	78
6.8	Short side view of ANSYS pontoon	78
6.9	Pontoon with boundary conditions and springs assimilating heave motion	79
6.10	Pontoon with boundary conditions and springs assimilating roll motion	79
6.11	Pontoon with boundary conditions and springs assimilating pitch motion	80
7.1	Maximum and minimum vertical displacement for decreasing mesh size	92
7.2	Static analysis completion time vs mesh size for global model	93
7.3	PSO results	95

7.4	Wadam heave RAO for simplified and final pontoon, head sea	98
7.5	Wadam Heave RAO for simplified and final pontoon, Beam Sea	99
7.6	Wadam roll RAO for simplified and final pontoon, beam sea	100
7.7	Wadam pitch RAO for simplified and final pontoon, head sea	101
7.8	Wadam potential heave damping for harmonic wave frequency	102
7.9	Potential damping in roll and pitch for the two pontoon designs	103
7.10	Pure heave global vertical pontoon displacement	104
7.11	Heave motion, frequency = 1.85 rad/s, period = 3.4 s	105
7.12	Heave RAO comparison for ANSYS and Wadam	105
7.13	Pitch RAO comparison for ANSYS and Wadam	106
7.14	Global Z-component displacement [m], mean water level	109
7.15	Global Z-component displacement [m], tidal change = 1.85 meters	110
7.16	Global Z-component displacement [m], tidal change = -1.58 meters	111
7.17	Mode 1: First mode shape, horizontal	114
7.18	Mode 2: Second mode shape, horizontal	114
7.19	Mode 10: Tenth mode shape, horizontal	114
7.20	Mode 3: Third mode shape, vertical	115
7.21	Mode 4: Fourth mode shape, vertical	115
7.22	Mode 5: Fifth mode shape, vertical	115
7.23	Mode 6; Sixth mode shape, vertical	115
7.24	Mode 7: Seventh mode shape, vertical	115
7.25	Mode 8: Eighth mode shape, vertical	115
7.26	Mode 9: Ninth mode shape, vertical	115
7.27	Summation of effective mass for the modes of the global model	116
7.28	Rayleigh damping ratio for the different approximations	119
7.29	Sampled harmonic displacement maximums for wave period, T=6.25s	121
7.30	Global harmonic maximum and minimum rotations about Y- and Z-axis	122
7.31	Maximum rotation about Y-axis [rad], T = 6.25s	122
7.32	Global harmonic maximum and minimum rotation about X-axis	123
7.33	Minimum rotation about X-axis [rad], T = 6.25s	123

7.34	Maximum rotation about X-axis [rad], T = 6.25s	124
7.35	Rotational sum of all global directions	124
7.36	Vertical maximum and minimum displacement for wave periods	125
7.37	Maximum displacement [m], T = 6.25s	126
7.38	Maximum displacement [m], T = 6.75s	127
7.39	Difference in vertical displacement for pontoon ends and the main tunnels di- rectly below [m]	127
7.40	Maximum and minimum von Mises stress for wave periods	128
7.41	Maximum mid bridge stress with connection shafts [Pa], T = 6.75s	129
7.42	Maximum mid bridge stress without connection shafts [Pa], T = 6.75s	129
7.43	Maximum stress with connection shafts for [Pa], T = 6.50s	130
7.44	Maximum and minimum bending moment about Y-axis	131
7.45	Maximum bending moment about Y-axis [Nm], T=6.75s	132
7.46	Maximum and minimum bending moment about Z-axis	132
7.47	Maximum bending moment about global Z-axis in inner main tunnel [Nm], T=6.75s	133
7.48	Minimum bending moment about global Z-axis in outer main tunnel [Nm], T=6.75s	133
7.49	Maximum and minimum torsional moment about X-axis	134
7.50	Maximum and minimum torsional moment about X-axis for inner main tunnel [Nm], T = 6.25s	135
7.51	Maximum and minimum bending moment about the Y-axis for bracing [Nm], T = 6.75s	136
7.52	Maximum and minimum rotation about the global axes for irregular wave loading	139
7.53	Maximum and minimum displacement for irregular wave loading	140
7.54	Maximum and minimum bending moment about Y-axis for irregular wave loading	141
7.55	Maximum and minimum moments for the lower part of the structure	141
7.56	Bending moment about global Z-axis for the elements where maximum and min- imum moment occurs	142
A.1	Flowchart for the main program	I
A.2	Flowchart for APDL inputfiles	II

A.3	Flowchart for pontoon testing program	III
C.1	Polyfitting of pontoon potential damping in heave	XVI
C.2	Polyfitting of pontoon potential damping in roll	XVII
C.3	Polyfitting of pontoon potential damping in pitch	XVIII
D.1	Roll RAO comparison for Ansys and Wadam	XIX
D.2	Z-component of displacement with evenly distributed ballast	XX
D.3	X-component of global displacement, mean water level	XXI
D.4	Y-component of global displacement, mean water level	XXI
D.5	X-component of global displacement, tidal change of 1.85 m	XXI
D.6	Y-component of global displacement, tidal change of 1.85 m	XXII
D.7	X-component of global displacement, tidal change of -1.58 m	XXII
D.8	Y-component of global displacement, tidal change of 1.58 m	XXII
D.9	Directional mass summation for 200 modes	XXIII
D.10	Rotations for wave period of 6.75s	XXV
D.11	The global maximum and minimum vertical displacement, T=6.75s	XXVI
D.12	Maximum and minimum von Mises stress, T=6.75s	XXVI
D.13	Maximum and minimum bending moment about Y-axis, T=6.75s	XXVII
D.14	Maximum and minimum bending moment about Z-axis, T=6.75s	XXVII
D.15	Rotational maximum and minimum moment, T=6.75s	XXVIII
D.16	Maximum bending moment about Y-axis for harmonic wave loading	XXIX
D.17	Minimum bending moment about Y-axis for harmonic wave loading	XXIX
D.18	Vertical displacement for the nodes with maximum and minimum response for the whole structure, irregular wave loading	XXX
D.19	Rotation for the nodes with maximum and minimum response about all global axes, irregular wave loading	XXXI
D.20	Von Mises stress for the nodes where maximum and minimum stress occurs, ir- regular wave loading	XXXII
D.21	Bending moment about global Y-axis for the elements where maximum and min- imum moment occurs	XXXIII

D.22 Bending moment about global Y-axis in the bracingXXXIV

D.23 Bending moment about global Y-axis in the outer main tunnelXXXIV

D.24 Bending moment about global Y-axis in the inner main tunnelXXXV

D.25 Bending moment about global Z-axis for the elements where maximum and minimum moment occursXXXVI

D.26 Bending moment about global Z-axis in bracingXXXVII

D.27 Bending moment about global Z-axis in the outer main tunnelXXXVII

D.28 Bending moment about global Z-axis in the inner main tunnelXXXVIII

D.29 Torsional moment about global Z-axis for the elements where maximum and minimum moment occursXXXIX

D.30 Torsional moment in the whole lower structureXL

List of Tables

3.1	Traffic Loads	20
3.2	Snow and ice loading	21
4.1	50 year return period spectrum parameters for wind generated waves	34
4.2	JONSWAP parameters and calculated parameters from spectrum considerations .	37
4.3	Wave amplitude calculation parameters	38
5.1	Number of files for the SFT and pontoon programs	44
5.2	Main geometries of the ANSYS bridge model	49
5.3	Cross section data	49
5.4	Element representation	51
5.5	Conventional and torsional spring stiffnesses	55
5.6	Basic Ocean Data	59
5.7	Current Velocity	60
5.8	Mass contributions to main MASS21	61
5.9	Mass per meter for the flooded pipe ballast	64
5.10	Material Properties	66
5.11	Examples of exposure classes for durability class M40	67
6.1	Feasible mesh size sets for PSO	74
6.2	PSO inputs	74
6.3	Wave characteristics	75
6.4	Wave direction sets for ANSYS pontoon analyses	80
6.5	Water levels expressed in tidal change	82
6.6	Wave parameter and time input for harmonic wave response analysis	85

6.7	50 year return period spectrum parameters for wind generated waves	88
6.8	ANSYSinput parameters for JONSWAP spectrum response analysis	89
7.1	Converged maximum and minimum displacement	93
7.2	Mesh size results	94
7.3	Pontoon restoring coefficients	96
7.4	Peak response frequencies for head sea	97
7.5	Peak response frequencies for beam sea	97
7.6	Heave head sea peak period/frequency and amplitude for unit wave height	98
7.7	Heave beam sea peak period/frequency and amplitude for unit wave height	99
7.8	Roll beam sea peak period/frequency and amplitude for unit wave height	100
7.9	Pitch head sea peak period/frequency and amplitude for unit wave height	101
7.10	Max and min global component displacement due to tidal change	108
7.11	Absolute maximum vertical displacement for different tidal inputs	108
7.12	Direction of mode motion	112
7.13	Comparion of eigenfrequencies	113
7.14	Modal analysis results for ANSYS global SFT model	117
7.15	α and β coefficients for the different approximations	118
7.16	Final Rayleigh damping ratios	119
7.17	Rotation about global axes for the wave periods with the highest response	125
7.18	Maximum von Mises stress	130
7.19	Bending moment about global Y-axis	131
7.20	Bending moment about global Z-axis	133
7.21	Rotational moment about global X-axis	135
7.22	Summarized grading of harmonic responses	137
7.23	Maximum responses for 50 year return period wave	137
7.24	Comparison of dynamic responses for different wave loading	143
9.1	Restoring Coefficients	151
9.2	Comparison of maximum dynamic responses	152
D.1	The data for the Rayleigh damping ratio plot in Section 7.4.3	XXIV

Nomenclature

Acronyms

APDL ANSYS Parametric Design Language

DOF Degree of freedom

JONSWAP Joint North Sea Wave Project

PSO Particle Swarm Optimization

RAO Response Amplitude Operator

SFT Submerged Floating Tunnel

TLP Tension Leg Platform

ViV Vortex Induced Vibrations

VM Von Mises Stress

Zmsl Vertical distance from mean sea level

Greek Symbols

α Angle between wind direction and axis of wind effected area for wind forces

α Form parameter for Jonswap spectrum in the high frequency part of the spectrum

α Mass damping matrix coefficient for Rayleigh damping

α Wave exceedence probability

β Stiffnes damping matrix coefficient for Rayleigh damping

η_{slurry}	Water ballast filling factor
η_{water}	Concrete slurry ballast filling factor
γ	Peak enhancement factor for Jonswap spectrum
λ	Wave length
ν	Poisson's ratio
ω_p	Peak wave frequency
ω_i	Natural frequency for the i^{th} eigenmode in Rayleigh damping procedure
ω_m	Natural frequency for the m^{th} eigenmode in Rayleigh damping procedure
ρ	Density
ρ_{sf}	Surface water density, mixture of salt and fresh water
ρ_{slurry}	Density of ballast concrete slurry
$\rho_{structure}$	Density of the internal structure of the main tunnel pipe
ρ_w	Water density
σ	Jonswap spectral width period
σ^2	Variance
σ_a	Jonswap spectral width period when $\omega \leq \omega_p$
σ_b	Jonswap spectral width period when $\omega > \omega_p$
ξ	Wave amplitude
ζ_a	Wave amplitude
ζ_i	Damping ratio for the i^{th} eigenmode in Rayleigh damping procedure
ζ_m	Damping ratio for the m^{th} significant eigenmode in Rayleigh damping procedure
$S(\omega)$	Spectrum

Matrices and vectors

$\ddot{\mathbf{r}}$	Nodal acceleration vector
$\dot{\mathbf{r}}$	Nodal velocity vector
\mathbf{C}	Damping matrix
\mathbf{K}	Global stiffness matrix
\mathbf{K}	Stiffness matrix
\mathbf{k}	Element stiffness matrix
\mathbf{M}	Mass matrix
\mathbf{R}	Global load vector
\mathbf{r}	Displacement vector
\mathbf{r}	Nodal displacement vector
\mathbf{S}	End-force vector
\mathbf{v}	end-point displacement vector

Roman Symbols

St	Strouhals number
T_{Sp}	Vortex shedding period
Tc	Tidal change
kN	Kilonewton, force
kN/m	Pressure per unit meter

Superscripts

A	Projected area for drag force calculation
A_{ij}	Added mass in i-th direction due to motion in the j-th direction
A_{slurry}	Area of the concrete slurry ballast tank in main tunnel
$A_{structure}$	Area of the internal structure of the main tunnel

A_{water}	Area of the water ballast tank in main tunnel
A_w	Waterplane area
B_{ij}	Damping in i-th direction due to motion in the j-th direction
C_D	Drag coefficient
C_f	Frequency dependent hydrostatic damping coefficient
C_s	Structural damping coefficient
C_{ay}	Added mass ratio in y-direction
C_{az}	Added mass ratio in z-direction
C_{ij}	restoring coefficient in i-th direction due to motion in j-th direction
D	Pipe diameter for drag force calculation
F_W	Wind force on exposed structure
F_{Btot}	Total buoyancy force
F_D	Drag force
$F_{X_{lm}}$	Distribution function for the largest maximum
H_s	Significant wave height
H_{m0}	Estimat for H_s when significant wave height is calculated from the spectrum
H_{max}	Estimated maximum waveheight from Jonswap spectrum H_s and T_p
K_{MX}	Torsional spring force in roll
K_{MY}	Torsional spring force in pitch
N	Number of zero-up-crossing periods during a sea state
R^k	Nodal load vector
R^o	Distributed load vector acting on element fixed end forces
T_p	Spectral peak period

T_z	Zero-up-crossing period
U_∞	Incident current velocity
V_{tot}	Total displaced volume
X_{lm}	Wave amplitude, largest maximum
B	Beam
C	Shape coefficient for wind loading
K	Structural stiffness coefficient
L	Length
M	Structural mass-inertia
N	Newton, force
Pa	Pascal
Q(t)	Dynamic force
Q(t)	Wave excitation force
S	Projected Wind Area

Subscripts

\ddot{u}	Acceleration
\dot{u}	Velocity
l	Length between pipe center when calculating incident wake cylinder velocity
m^3	Cubic meter
m_n	Spectral moments for $n = 0,1,2,\dots$
t_p	Initial pontoon wall thickness
$t_{adjusted}$	Adjusted pontoon wall thickness
u	Incident velocity on wake cylinder

c	Damping
g	Gravitational Acceleration
k	Stiffness
kg	Kilogram
m	Mass
m	Meter
q	Wind pressure/suction
rad	Radians
u	Displacement
x	Coordinate symbol, 1. global direction
y	Coordinate symbol, 2. global direction

Greek matrices and vectors

$\ddot{\xi}$	Acceleration vector in transformed coordinate
$\dot{\xi}$	Velocity vector in transformed coordinate
Φ	Normalized eigen vector
Φ^T	Transposed normalized eigen vector
ξ	Displacement vector in transformed coordinate

Chapter 1

Introduction

This chapter contains the thesis objectives, a background study, limitations for the master thesis and a description of the structure of the report.

1.1 Thesis Objectives

Floating bridges are relevant for crossing of very deep and wide fjords along the Norwegian Coast. In order to compute the static and dynamic response of these bridges, the joint properties of the whole hydro-elastic system needs to be accounted for.

Main objectives of the master thesis:

- A review is to be made of existing marine bridges and future plans for such bridges. Similarities and differences between the different bridge types are to be highlighted.
- Loads acting on submerged floating bridges are described together with associated structural models. Methods for both static and dynamic response analysis are elaborated and relevant numerical algorithms are described.
- A global model of a particular bridge is to be established in relation to a proper computer program selected in cooperation with the supervisor. The hydrodynamic and structural properties are to be determined.
- A static and eigenvalue problem is to be analyzed for the global model with a belonging result analysis.
- A dynamic response analysis for both regular and irregular wave loading is going to be carried out. The global responses for an estimated maximum harmonic wave is to be compared to the responses from an irregular wave loading.

Trondheim, August 20, 2016

20/8-2016



Bernt J. Leira



Hans Jakob Vik

1.2 Background

As a background for the thesis, a literature and concept study of existing floating bridge concepts has been carried out. Due to the number of concepts, many of them developed for a ferry-free E39 in Norway, the study is given in its own chapter, Chapter 2. It describes both existing and future plans for floating bridges.

In short, the marine bridges can be divided into three main groups. One group are the submerged floating tunnels, where ships can pass over the main spans. These bridges are supported either by pontoons or has excess buoyancy and is tethered to the seabed. The other group of floating bridges is the one where the ships pass underneath the structures. Examples can be suspension bridges on floating supports or a pontoons supported structure with a cable supported bridge and ship channel at shore. Combinations of these two groups form the third types of marine bridges.

1.3 Limitations

1.3.1 Modeling Limitations

The modeling of the structure analyzed in the thesis is carried out based on a study done by the Reinertsen Olav Olsen Group for crossing Sognefjorden in a submerged floating tunnel. Modeling a frequency dependent added mass for surface piercing structures and viscous damping for the global model has not been done due to the complexity of these operations. In addition to these limitations, some model features from the Reinertsen Olav Olsen study has been left out. There is no vertical curvature for the model, there is no internal structure for the main tunnel pipes and the evacuation pipes described in Chapter 5 concerning the modeling, has been left out.

Additional limitations and modeling simplifications are given in Chapter 5, along with the modeling description.

1.3.2 ANSYS Ocean Data Input

The software input commands used for modeling the ocean and wave environment is called the ocean data input. Solving the global model with the ocean data input as loads has proven to be the most challenging part the thesis analyses. This is mostly due to the fact that there are no examples of ANSYS ocean data analyses with time dependent loading, which has resulted in a lot of time consumption figuring out exactly how the analyses are to be solved.

1.3.3 Computer and Software Limitations

The different kinds of modeling and analyses are carried out on the remote desktops made available by NTNU, at the Department of Marine Technology. This opens for opportunities, but also limitations. The opportunities are the possibility of running multiple analyses simultaneously, being helpful when for example testing different loading for the same model.

Some limitations are computer system access and shared usage of both memory and CPU. As many people are using the computers at the same time, memory and CPU limitations become present. In addition to this, it has not been possible to allocate more memory and cores when running analysis in the software ANSYS. This is most likely because of limited user privileges in the software license

1.3.4 Concrete Structure Knowledge

Limited knowledge about concrete structures means that the modeling of the concrete is a bit uncertain. Further knowledge about concrete could improve the final verification of the results.

1.4 Structure of the Report

The structure of the report follows a standard layout with preface, acknowledgment, English summary and Norwegian summary before the main part begins. The main parts consist of 9

chapters, before the thesis report ends with a reference list and appendix.

The first chapter is an introduction to the thesis. The chapter contains the thesis objectives, a short background study, limitations and a description of the structure of the report.

Chapter two is a detailed review of existing marine bridges and future plans. The future plans are all different versions of marine bridges developed to make a ferry-free E39 in Norway.

The third chapter is about structural loads and theory for the floating submerged bridge investigated in the thesis. The main part of the information for this section is gathered from the Reinsertsen Olav Olsen Study.

Methods for both static and dynamic response analysis are elaborated with relevant numerical algorithms in Chapter 4. The chapter also contains wave theory description to explain choices and parameters implemented for the hydrodynamic loading.

Chapter 5 describes the modeling of the main global model. It also includes specific pontoon modeling, a description of the self written code for analysis and software descriptions. The description of the main structure modeling is detailed in order for the reader to understand every step of the way, and also to substantiate the results in the end of the thesis.

The sixth chapter concerns the different analyses carried out. It describes the analysis inputs, how they are carried out and the results which are going to be post processed. Each subsection in chapter 6 refers to the results section for the described analysis in the next chapter

Chapter 7 contains the results for all the analyses described in Chapter 6. The most important results are given with a belonging description, supported by result plots generated in MATLAB or taken from ANSYS.

Chapter 8 contains a discussion for all the results in the thesis. The whole analysis procedure is discussed, from start to finish. The results are compared to each other and to external information.

The ninth chapter is the concluding remarks. The thesis conclusion is presented, based upon the results from Chapter 7 and the discussion in Chapter 8. In addition to this, the chapter lists multiple suggestions for further work to verify the model additionally.

The last parts of the thesis are the list of references and the appendix. The appendix includes additional information, especially for the result chapter. Additional results describing the global responses of the model for different analyses are added and described to some detail. The chapter also includes a description for the electronic appendix and some information about the self written code.

Chapter 2

Review - Floating Bridges

In this chapter a review of existing marine bridges and future plans for such bridges is carried out. The similarities and differences of the different bridge types are highlighted. For future plans, the concepts for a ferry-free E39 will be closely reviewed.

2.1 Submerged Floating Tunnel

There has never been constructed a submerged floating tunnel, but several ideas and plans have been created. The first proposals were made in 1987 with the goal of crossing Høgsfjorden. Four companies developed their own solution, where both the concepts of excess buoyancy and pontoon supported tunnels was created (Vegvesen, 1994). The general idea of a submerged tunnel is to fully submerge a circular pipe and support it with surface pontoons, bottom or land anchoring or a combination of these supports. There has been made sketches and plans for both singular and double-piped submerged tunnels, single for seabed anchored excess buoyancy concepts and double for neutral buoyancy, pontoon supported submerged floating tunnels.

In this section different proposals for submerged tunnels connected to the project concerning a ferry-free E39 will be described, highlighting the similarities and the differences. In general submerged bridges can be divided into two groups: Excess buoyancy tunnels connected to the seabed and submerged floating tunnels supported by pontoons.

2.1.1 Submerged Tunnel with Excess Buoyancy

The submerged tunnel with excess buoyancy is a tethered version with tension in all tethers at all time. According to a feasibility study done by the Norwegian Public Roads Administration, (Vegvesen, 2011) considering the crossing of Sognefjorden, the length of the crossing is not of importance to the feasibility, while the depth is. A sketch of a submerged tethered tunnel can be seen in Figure 2.1.

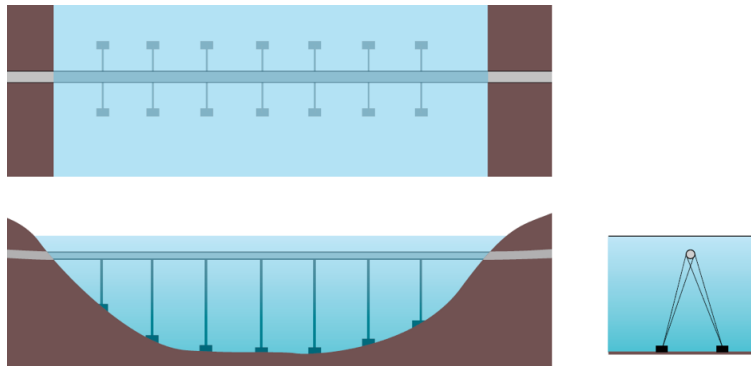


Figure 2.1: Tethered submerged tunnel, illustration Vegvesen (2011)

This bridge has the advantage of being out of harms way concerning ship collision. In addition to this, wave loads will be of less significance when no surface piercing pontoons are attached to the tunnel, interacting with the waves. Vacuum anchors has been considered as one of the best ways to connect the tethers to the seabed.

2.1.2 Pontoon Supported Submerged Floating Tunnel

The main difference between submerged excess buoyancy and pontoon tunnels are the supports, equipped with tethers connected to the seabed or pontoons in the water surface, respectively. A submerged tunnel with pontoons will need to be horizontally curved in order to have enough horizontal stiffness. It can also be connected with horizontal tethers to the sea shore.

The red dots along the structure in Figure 2.2 are the supporting pontoons. The larger gap in the middle is the ship channel where the tunnel has its lowest point. There are proposals with single and double tunnels. A single tunnel has lower horizontal stiffness and is considered realistic for

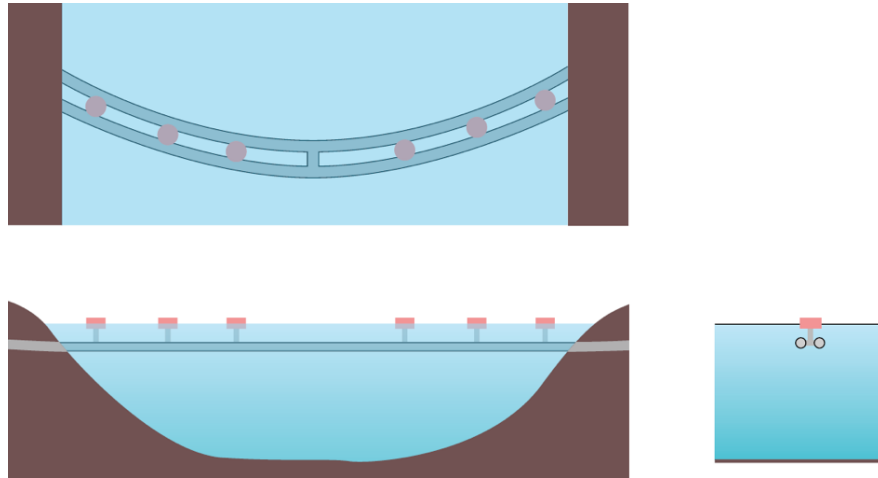


Figure 2.2: Submerged tunnel with pontoon supports, illustration Vegvesen (2011, p. 12)

crossings up to 2000 meters (Vegvesen, 2011, p. 14). The concept in Figure 2.2 has been looked upon as a promising solution for Sognefjorden, being both deep and wide. For other crossings, such as Bjørnefjorden, it is also a possible solution.

There are several similarities between a submerged tunnel with excess buoyancy and one with pontoon supports. The effect of the current on the cylindrical tunnels can be considered similar. The difference will be the stiffness of the supports and if there are one or two tunnels. The waves will be of greater importance for the pontoons and ship collision will be one of the main dimensioning factors for a final concept. This rises the question of why pontoons are necessary, making it more complex with wave and ship collision interactions. The answer is the fjord depths. The main challenge with excess buoyancy SFTs will be the tether lengths.

In order to obtain a closer knowledge of submerged tunnels and future plans, a feasibility study carried out by Reinertsen Olav Olsen Group (Group, 2013) has been studied. The main outlines of the final results are shortly described in the next part of the thesis.

2.1.3 Feasibility Study for Crossing of Sognefjorden by Reinertsen Olav Olsen Group.

A feasibility study for submerged tunnel technology has been carried out for Sognefjorden by Reinertsen Olav Olsen Group on behalf of the Norwegian Public Roads Administration. This

is, as mentioned, because of the extreme span and depth of the fjord. If a submerged tunnel can be constructed in Sognefjorden, the concept is easily transferable to other crossings with less extreme geometry requirements. This concept is shortly described in order to get a clear understanding of how a submerged tunnel could be built.

The main dimensions of the final concept, which was concluded feasible, is shown in Figure 2.3. The total span of 3700 meters and a radius of 2682 meters results in a 4083 meters long bridge. The ship channel is 400 meters, while the span length between the pontoons varies from 150-500 meters. The most common distance between the pontoons is 205 meters.

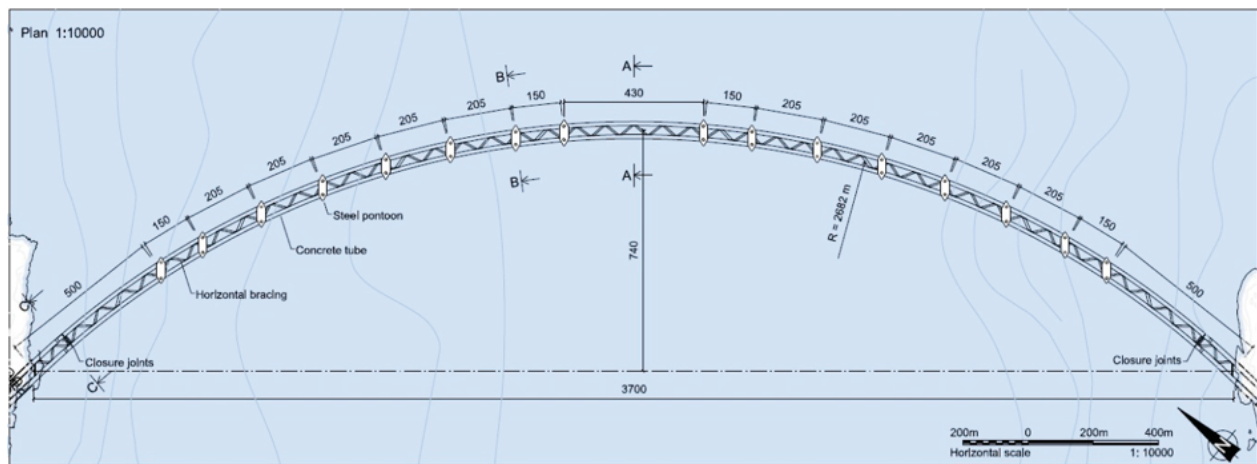


Figure 2.3: The main dimensions of the submerged tunnel, illustration (Group, 2013, p. 6)

The cross section of the structure is shown in Figure 2.4. A concept with two tunnels for higher horizontal stiffness was chosen, with traffic in both tubes. It also creates a smaller drag force on the second tube. The connecting pipe between the two main tunnels works both as a stiffener and an emergency tunnel from one tunnel to the other. There is one emergency tunnel approximately every 500 meter.

At the middle of the pipe connecting the pontoon with the submerged tunnel, there is a highlighted line. This is where the pipe is planned to disconnect if a ship collision with enough force would occur. This is to prevent harm to the submerged tunnel. The structure has pontoon redundancy, meaning it will be fully operative when missing one pontoon.

The main dimensions of the tunnel are shown in Figure 2.5. The lower left and right chambers will be filled with solid ballast, while the middle will be filled with water. The pipe will have

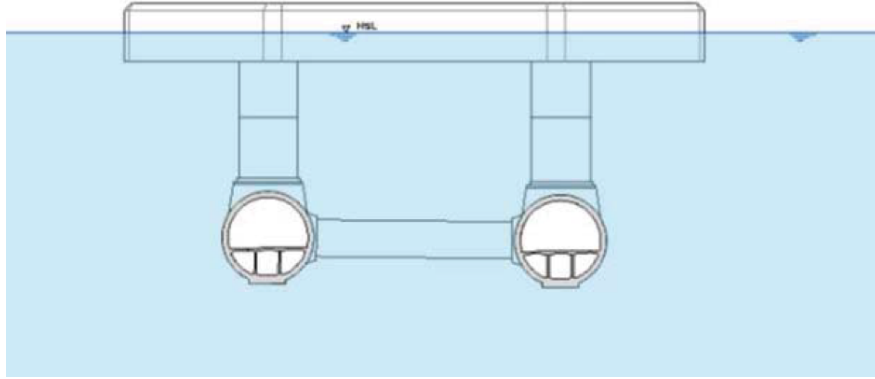


Figure 2.4: Complete cross section of the structure, illustration Group (2013, p. 7)

traffic in one lane while the other will be closed for maintenance or if accidents occur. This solution is very similar to the first concepts ever made, in 1987 when working with a submerged tunnel for Høgsfjorden. The difference is the double pipe.

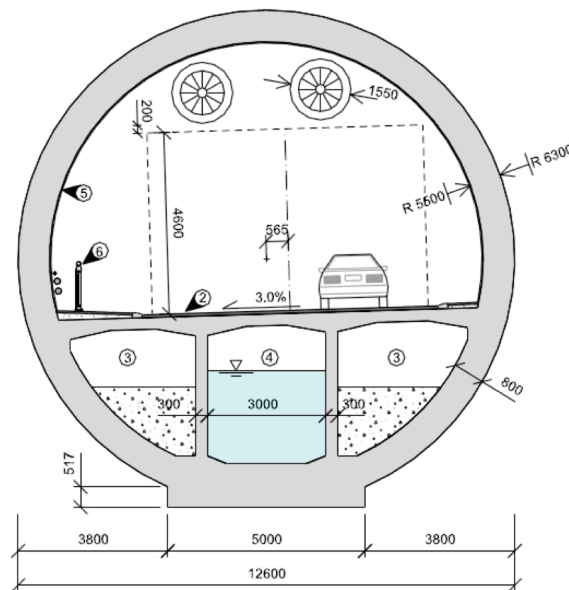


Figure 2.5: Main dimensions of main section, picture from Group (2013, p. 8)

The main difference for the submerged tunnels and the other floating bridges is the importance of the currents and vortex induced vibrations (ViV). This will be discussed in Chapter 3, concerning bridge loading.

2.2 Suspension Bridge on Floating Foundations

Another planned, but never built concept, is a suspension bridge on floating foundations anchored to the seabed. The concept uses either tension leg platform (TLP) technology or other anchoring technology known from the Norwegian offshore industry in combination with classical suspension bridge technology. There has been developed several concepts related to a ferry-free E39 in the last couple of years.

2.2.1 Feasibility Study of Sognefjorden with Suspension Bridge on Floating Foundations

In 2013 the Norwegian Public Roads Administration published a report on a suspension bridge on floating foundations over Sognefjorden (Vegvesen et al., 2013). The feasibility study was made by a joint group of Aas-Jakobsen, John. Holt As, Cowi, NGI and Skanska. The study was deemed feasible.

The main span is 3700 meters with two floating foundations. The suspension span between foundations and between the foundations and the towers at shore is 1234 meters. In Figure 2.6 a concept illustration shows the finished concept.

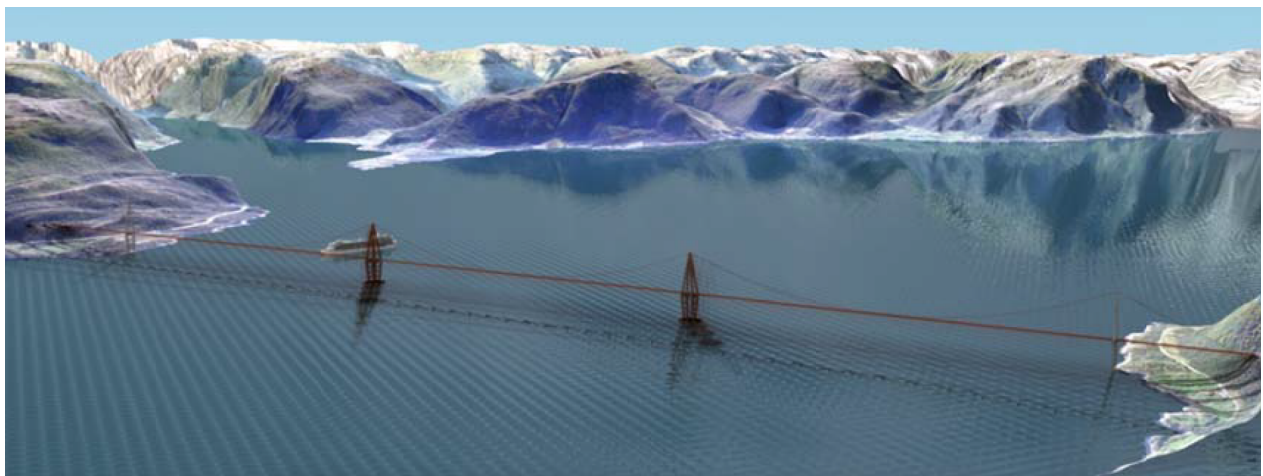


Figure 2.6: Sognefjorden floating bridge, illustration Vegvesen et al. (2013, p. 6)

The main difference between this concept and a SFT is the suspension bridges, the ship channel

being underneath the bridge and off course, the main structure being above water. With only two supports at water level probability for ship collisions to occur decreases. The wind and the suspension bridge wind response is of great importance, unlike for the SFT, concerning the eigenfrequencies. This can be related to ViV for the SFTs.

The anchoring for this concept will be suction anchors at seabed with anchor lines from the anchors to the floating supports. The anchor lines in this study are made of steel, but synthetic lines used in the North Sea could also be a solution. A tension leg concept like the TLPs offshore is another solution, especially fit for shallower fjords. The floating supports will also be anchored to the shore. The supports, in concrete, and the towers, in steel, will be constructed based on known offshore technology. The main dimensions of the concept can be seen in Figure 2.7.

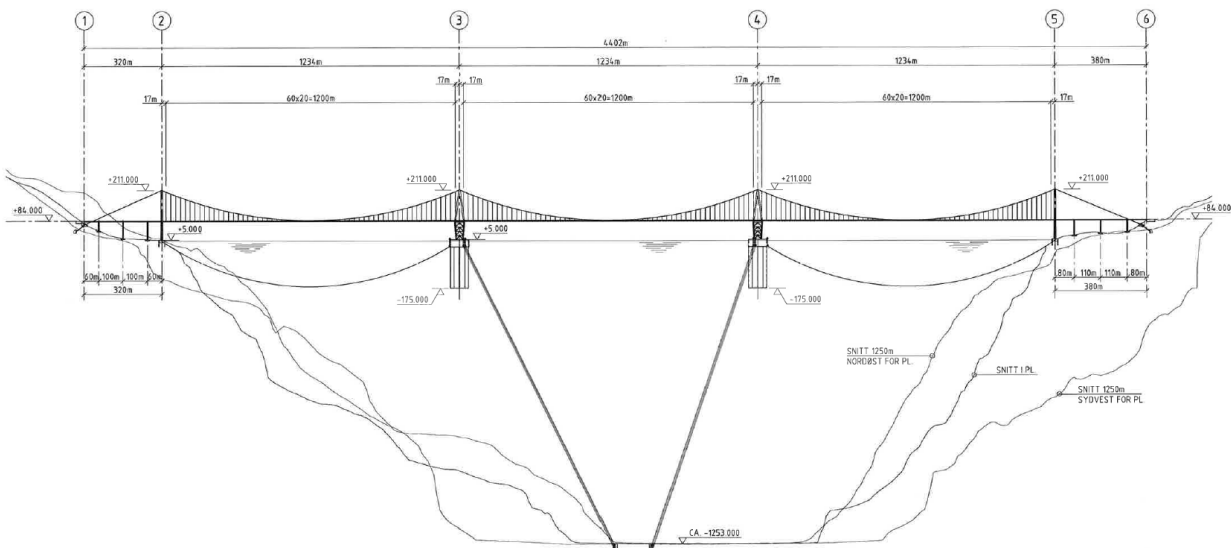


Figure 2.7: Main dimensions of the bridge, illustration Vegvesen et al. (2013, Appendix)

2.2.2 Floating Bridge with TLP Technology

This concept is very similar to the one described in Section 2.2.1. It uses the same idea of suspension bridge technology on floating foundations to minimize the main spans. The difference is the tension leg anchoring, which is used in the offshore industry for anchoring platforms. These platforms are known as TLPs or tension leg platforms. An illustration of a TLP can be seen in Figure 2.9.

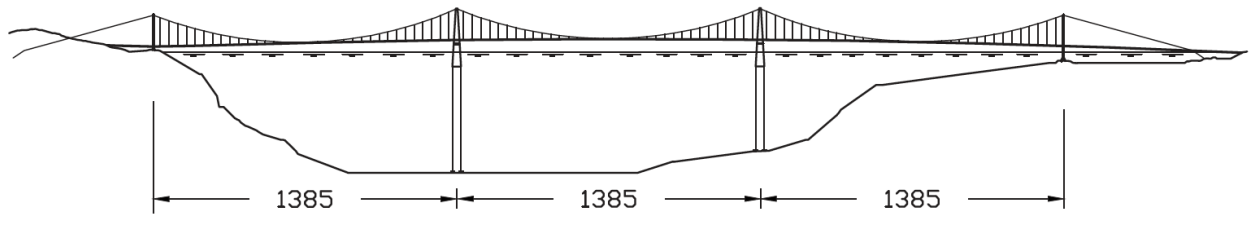


Figure 2.8: The TLP suspension bridge concept over Bjørnafjorden, illustration Holtberget (2015)

A TLP bridge is one of the studied concepts for crossing Bjørnafjorden and Sulafjorden for a ferry-free E39. Figure 2.8 shows the bridge with tension legs and a suspension bridge span of 1385 meters. The floating foundations for the suspension bridge are excess buoyancy elements which is pulled down by the force in the tension legs, creating a vertically stable structure. The floating supports, will as a tension leg platform, have a movement in horizontal direction. This will be stabilized by the stiffness of the bridge spans.

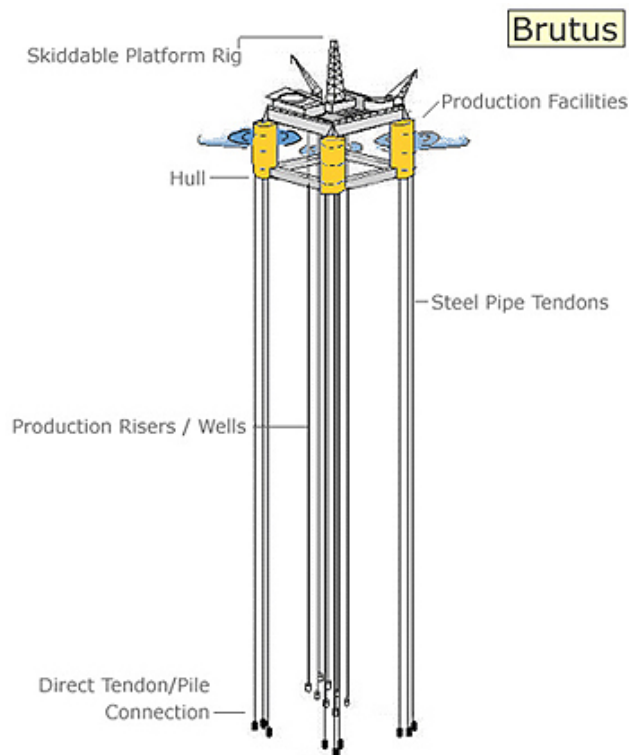


Figure 2.9: Tension leg platform, illustration Offshore-Technology

2.3 Conventional Floating Bridges

Unlike the floating bridge concepts the previous sections, there are several floating bridges which already have been built. These structures are most commonly pontoon supported bridges like the one in Figure 2.10a. The figure shows Bergsøysund bridge. It has a length of 931 meters, with main spans of 106 meters and a ship channel height of 6 meters.



(a) Bergsøysund Bridge, illustration broer.no (a)



(b) Homer Hadley and Lacey V. Murrow Memorial bridge, illustration Wikipedia (2016)

Figure 2.10: Floating bridges on pontoon supports

Figure 2.10b shows the Homer M. Hadley and Lacey V. Murrow Memorial bridge. The Lacey V. Murrow is the second longest floating bridge in the world, with a total length of 2020 meters. The Homer M. Hadley is 1772 meters. Both are pontoon supported bridges.

The bridge shown in Figure 2.11 is a proposed concept crossing Sognefjorden. It has a mid-fjord ship channel and was one of the earliest alternatives for crossing. It is a so-called "bucket handle alternative" and has never been built before. It is assumed to be horizontally stiff enough, but separate bridge lane decks could be a way of increasing the stiffness, (Vegvesen, 2011, p. 6-7)



Figure 2.11: Mid-fjord ship channel, illustration Vegvesen (2011, p. 6)

2.4 Ship Channel at Shore

The Nordhordland Bridge uses the same principle as the bridges in Figure 2.10b only in a larger scale. Nordhordland Bridge allows bigger ships to cross under a cable or suspension bridge close to shore. For the rest of the bridge, an easier and more standard floating bridge concept is used. The bridge, which was built in 1994, can be seen in Figure 2.12a. It has a total length of 1614 meters, a total height of 99 meters, a bridge clearance of 32 meters and a main span of 172 meters (broer.no, b). Nordhordland bridge is not anchored to the seabed.



(a) Nordhordland bridge, illustration broer.no



(b) Nordhordland concept, Sognefjorden, illustration Vegvesen (2011, p. 8)

Figure 2.12: Floating bridges with suspension close to shore

This kind of concept has also been worked with trying to find the best solution for crossing Sognefjorden. An illustration of the idea can be seen in Figure 2.12b.

2.5 Combination Bridges

When discussing combination bridges, the concepts in Section 2.1, 2.2 and 2.3 are combined to better solve the ship channel issue. For conventional floating bridges the challenge is to construct a ship channel high enough in relation to a low connection to shore. For suspension bridges on pontoon supports, the whole bridge has to be in the same height, where minimum height is clearance for the biggest cruise ships entering the Norwegian Fjords.

When combining the previous concepts, some of these aspects can be solved in new ways.

2.6 SFTs with Conventional Floating Bridge

When combining a conventional floating bridge with a submerged tunnel, the ship channel will be above the submerged tunnel. This leads to an easier bridge construction for the rest of the span. An example can be seen in Figure 2.13a and 2.13b where the submerged tunnel is at the shore and in the middle of the fjord.



(a) Submerged tunnels at shore, illustration Vegvesen (2011, p. 10)



(b) Submerge tunnel at mid-fjord, illustration Vegvesen (2011, p. 9)

Figure 2.13: SFTs combined with conventional floating bridges

In Figure 2.13a there is one tunnel for each traffic direction. This creates a y-shaped geometry, increasing the horizontal stiffness of the structure.

Chapter 3

Structural Loads and Load Theory

In this chapter loads acting on a floating submerged bridge supported by pontoons are described with its associated structural model. As far as possible, the loads are described by Norwegian fjord conditions. Insufficient load data for the exact environment is substituted by loads from standards concerning conditions and loads at the Norwegian Continental Shelf or other collected data.

The loads described in this chapter are gathered from the study by Reinertsen Olav Olsen Group for a pontoon supported SFT crossing the Sognefjorden, (Group, 2013, p. 15-41). The loads are described in general, with a concluded effect on the global model in the thesis.

3.1 Specific Gravity

Specific gravity of an SFT is built up of two main groups, the permanent weight of the structure and a variable weight. The permanent weight consists of the tunnel pipe, structural elements inside, ballast, asphalt and equipment weight. The variable weight consists of marine growth and water absorbed either by the concrete or solid ballast.

3.2 Hydrostatic Loads - Buoyancy

The total hydrostatic buoyancy loading on the global SFT model is equal to the force of the total displaced fluid by the model. This is shown in Equation 3.1.

$$F_{Btot} = V_{tot} \cdot g \cdot \rho_w \quad (3.1)$$

where:

F_{Btot} = total buoyancy force, in N

V_{tot} = total displaced volume, in m^3

g = acceleration of gravity, in m/s^2

ρ_w = water density, in kg/m^3

This volume includes the displaced volume of the main tunnels, the bracing elements between the tunnels, the shafts connecting the pontoons to the rest of the structure and the submerged part of the pontoons.

3.3 Traffic Loads

The traffic loads are the weight of vehicles and pedestrians in main tunnel pipes. The most interesting scenario is full traffic load for a lane multiplied with the number of operational lanes in the SFT. For the structural model in the thesis there are two lanes per main tunnel. One of the lanes is free of traffic, being available for maintenance work and handling of possible accidents. The traffic loads are gathered from *Håndbok 185 - Prosjekteringsregler for bruer* (Administration, 2009, Section 3.3) by Statens Vegvesen. It is a handbook concerning design rules for bridges. The load for one main pipe is listed in Table 3.1:

Table 3.1: Traffic Loads

Load	Magnitude	Units	Reference
Lane with full traffic	9	[kN/m]	B185 - Section 3.3.1
Road shoulder with pedestrians	1	[kN/m]	HB - Section 3.4.1
Axel loads	1260	[kN]	HB - section 3.3.1

An illustration of vehicle loading presented in Table 3.1 is shown in Figure 3.1 gathered from (Administration, 2009, 3.3.1).

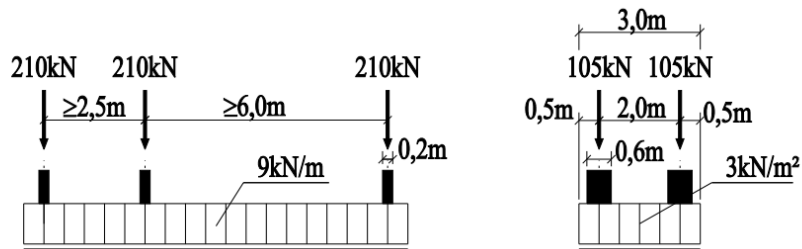


Figure 3.1: Traffic loaded bridge, Illustration Vegvesenet

3.4 Snow and Ice

The loading of snow and ice is given in Table 3.2. The pressure magnitudes, given in kN/m^2 are from (Norge, 2007)

Table 3.2: Snow and ice loading

Load	Magnitude [kN/m^2]
Snow	2.5
Ice	0.9

Simultaneous ice and snow loading is not possible, meaning that the snow load is the interesting load concerning a global maximum load. For a pontoon supported SFT, the area and number of pontoons will determine the global snow loading.

$$\Delta Z = \frac{2500 \text{ N}/\text{m}^2}{\rho_w \cdot g} = 0.25 \text{ m} \quad (3.2)$$

where:

ΔZ = draft change, in m

For the pontoon of the SFT modeled in the thesis, a snow load of $2.5 \text{ kN}/\text{m}^2$ will result in 0.25 meter change in draft. The density of water is set to $1015 \text{ kg}/\text{m}^3$ due to high concentrations of fresh water in the summer.

3.5 Tide

The general tide effect on the SFT is that buoyant forces will increase or decrease, changing the forces at the boundaries of the bridge due to the change in water levels at the pontoons.

Tide registration done in Ålesund from 1961 (Ålesund Havnevesen, 2016) shows a maximum tide of +3.06 meters and a minimum tide of -0.36 meters where lowest astronomical tide is 0. With an average tide of 1.20 meters the high and low tide is equal to +1.86 and -1.56 meters.

3.6 Currents

The current loading is mainly viscous forces. One example of a viscous force is vortex induced vibrations (ViV), which is connected to drag forces on the submerged pipes of the SFT.

3.6.1 Viscous Forces

The viscous forces, in this case drag forces, for a pontoon supported SFT will have contributions from both the pontoons and the pipes. The pipes include the main tunnel pipes, the bracing pipes and the connection shaft between the pontoon and the main tunnel.

For the pontoons the viscous force is modelled as a point load, described by Equation (3.3).

$$F_D = \frac{1}{2} \cdot \rho_w \cdot C_D \cdot A \cdot U_\infty^2 \quad (3.3)$$

where:

F_D = drag force, in newton

C_D = drag coefficient

A = projected area, in m^2

U_∞ = incident current velocity in m/s

For the first tunnel pipes, meaning the connection shafts and the main tunnel pipe which first meet the current, the uniformly distributed force is calculated with Equation (3.4)

$$F_D = \frac{1}{2} \cdot \rho_w \cdot C_D \cdot D \cdot U_\infty^2 \quad (3.4)$$

where:

D = pipe diameter, in meters

For pontoon supported SFTs, a double main tunnel pipe is used. This causes a shadow effect, leading to a different drag force on the second pipe. This is because the second pipe is in the wake of the first pipe. The uniform drag force is described by Equation (3.5),

$$F_D = \frac{1}{2} \cdot \rho_w \cdot C_D \cdot D \cdot u^2 \quad (3.5)$$

where:

u^2 = Incoming velocity, in m/s, given by Schlichting's formula. See Equation (3.6) (Faltinsen, 1990, p. 204).

$$u^2 = U_\infty^2 \cdot \left(1 - 2 \cdot 0.95 \left[\frac{C_D D}{l} \right]^{\frac{1}{2}} \right) \quad (3.6)$$

where:

u = incident velocity acting on a cylinder in the wake of another, m/s

l = length from first pipe center to the next in current direction, in m

An additional Blevins correction can be added to the length, being a number of diameters behind the pipe. Different current scenarios will occur in the wide fjord, causing different drag loading. Examples are uniform constant current over the whole width, half the width and asymmetrical current over the fjord.

3.6.2 Vortex Induced Vibrations - ViV

Due to flow separation along the outer pipe layer, a change in pressure at top and bottom separation point causes the pipes of the tunnels to vibrate. The period of the vortex shedding is given by Equation 3.7.

$$T_{Sp} = \frac{D}{St \cdot U_{\infty}} \quad (3.7)$$

where:

T_{Sp} = vortex shedding period, in s

St = Strouhals number

This period is compared to the modes of the structure, both vertical and horizontal. If the vortex shedding frequency is close to the natural frequency of the structure, a lock-in effect between the motion of the structure and the shedding might occur. This could result in a resonance effect which could cause vortex induced cross-flow and in-line motion. These motions causes a moment on the pipes of the SFT.

3.7 Wave Loads

The wave loads for a floating bridge in the Norwegian Fjords will be much smaller than for a structure operating in the North Sea. Each fjord will of course have individual sea states.

For the concept studied and modeled, the sea state is described by a JONSWAP spectrum with a maximum significant wave height of 2.14 m and a wave period of 4.8 second with a return period of 50 years. The data is provided by SINTEF. The ocean swell will have a significant wave height of 0.1 meters due to the topography of Sognefjorden. Maximum wave height under storm conditions can be set to 0.2 meters (Group, 2013). A direction function must be added to the sea state in order to have a two dimensional description of the sea state. Resulting forces are expressed with the wave acceleration. Froude second order load effects will have to be calculated for the tunnel pipes and the pontoons for a final model. Second order wave effects has to be addressed for the pipe and pontoons.

3.7.1 Avalanche Induced Waves

The outcome of a possible avalanche in Flåm, 140 km from the SFT location, is according to SINTEF a wave amplitude of approximately 0.2 meters and a period of 85 seconds. This is outside the natural periods of the structure.

3.7.2 Effects of Stratified Flows - Internal Waves

Internal waves created by passing ships is assumed having a period outside the response of the structure, and not being important for the loading of the submerged floating tunnel

3.8 Wind

The wind loads for a pontoon can be calculated with Equation (3.8), from DNV-RP-C205 , Environmental conditions and environmental loads, (Veritas, 2007).

$$F_W = C \cdot q \cdot S \cdot \sin(\alpha) \quad (3.8)$$

where:

F_W = wind force, in N

C = shape Coefficient

q = basic wind pressure or suction, in N/m^2

S = projected area normal to wind direction, in m^2

α = Angle between wind direction and the projected area exposed to wind

For the associated model structure of the pontoon in the Reinertsen Olav Olsen Group concept, the dimensions are L x B x H = 80 x 26 x 8m. The shape coefficient for sides is found in Table 5.5 in DNV-RP-C205, being 0.7 for the short side and 1.1 for the long side with a perpendicular wind.

With an air density of 1.226 kg/m^3 and a wind speed of 28 m/s the wind pressure for the pontoon sides become 482 N/m^2 , as shown in Equation 3.9.

$$q = 0.5 \cdot 1.226 \cdot 28^2 = 482 \text{ N/m}^2 \quad (3.9)$$

The minimum pressure for a structure in the North Sea, according to DNV-OS-C101, Design of offshore steel structures, general (Veritas, 2011), is 2500 N/m^2 . As a conservative estimate the wind force is, using Equation (3.8), 182 kN for the pontoon short side and 880 kN for the pontoon long side. For this floating bridge, the magnitude of the wind forces are considered negligible in comparison to the other forces.

3.9 Ship Collision

Ship collision is an advanced and important problem for floating bridges. The main criteria is that the structural integrity of the bridge is intact after a collision. In the study carried out by the Reinertsen Olav Olsen Group a weak link solution will detach the pontoon at a collision magnitude of a certain level. This magnitude is estimated by a probability analysis with a collision energy of 2 MNm with a 100 year return period. The dimensioning collision energy from this study is 52 MNm . The weak link solution is dimensioned for collisions with energies exceeding the dimensioning collision force. The pontoons can be considered either stiff or deformable.

Chapter 4

Response and Wave Theory

In this chapter methods for both static, modal and dynamic response analysis are elaborated and relevant numerical algorithms are described. Material used to produce this chapter is gathered from Rahman (2014), Langen and Sigbjörnsson (1979) and Moan (2003). The chapter also contains wave theory, describing underlying theory for the harmonic and spectrum wave loading in Ansys.

No non-linear solving of the global problem has been used in the thesis. Consequently, no solving of non-linear theory has been described.

4.1 Static Response Analysis

Information about static response is gathered from Moan (2003). The equation for the global static problem is described by Equation 4.1. The goal is to solve this equation for the global nodal displacement vector, \mathbf{r} .

$$\mathbf{R} = \mathbf{K}\mathbf{r} \quad (4.1)$$

where:

\mathbf{R} = global load vector

\mathbf{K} = global stiffness matrix

\mathbf{r} = global nodal displacement vector

The global load vector is shown in Equation 4.2.

$$\mathbf{R} = \mathbf{R}^k - \mathbf{R}^o \quad (4.2)$$

where:

\mathbf{R}^k = matrix of loads acting on nodes

\mathbf{R}^o = matrix of distributed loads acting on element fixed ends.

Solving Equation 4.1 for the nodal displacement vector \mathbf{r} , results in a solution of a set of linear equations equal to the number of degrees of freedom for the global system.

$$\mathbf{r} = \mathbf{K}^{-1} \mathbf{R} \quad (4.3)$$

where:

\mathbf{K}^{-1} = the inverse global stiffness matrix

System displacement element forces can now be found from Equation 4.4.

$$\mathbf{S} = \mathbf{k} \mathbf{v} \quad (4.4)$$

where:

\mathbf{S} = end-force vector

\mathbf{k} = element stiffness matrix

\mathbf{v} = end-point displacement vector

Solving the problem in the description above will give good results, if the model is built up of elements describing the reality of the problem.

4.2 Dynamic Response Analysis

The global response of a structure can be found by solving the dynamic equilibrium equation of the system. This is given by Equation 4.5. The difference from a static response is that dynamic loads has a time dependent solution and introduce inertia loads throughout the structure.

$$m\ddot{u} + c\dot{u} + ku = Q(t) \quad (4.5)$$

where:

\ddot{u} = acceleration

\dot{u} = velocity

u = displacement

k = stiffness

m = mass

c = damping

$Q(t)$ = wave excitation force

For any given structure a discretization is performed by defining a finite number of degrees-of-freedom (DOFs). In dynamic analysis, the motion of mass must be accounted for. For a floating structure a single degree of freedom system is expressed with Equation 4.6.

$$(M + A)\ddot{u} + (C_s + C_f)\dot{u} + (K + k)u = Q(t) \quad (4.6)$$

where:

M = structural mass-inertia

A = added Mass

C_s = structural damping coefficient

C_f = frequency dependent hydrodynamic damping coefficient

K = structural Stiffness coefficient

k = hydrostatic stiffness coefficient

By representing the whole system in a discretized system with mass, damping and stiffness matrices, the global dynamic response for a structure can be solved. Solving the equation of motion

can be solved in deterministic time-domain og probabilistic frequency-domain. The probabilistic frequency-domain is the simplest to solve, but is only applicable for linear systems.

4.3 Modal Analysis

4.3.1 Eigenvalue Analysis

Theory in this section is gathered from Langen and Sigbjörnsson (1979, Chapter 4). The dynamic equilibrium equation given by Equation 4.7 is used to establish the general eigenvalue problem.

$$M\ddot{\mathbf{r}} + C\dot{\mathbf{r}} + K\mathbf{r} = \mathbf{Q}(t) \quad (4.7)$$

where:

\mathbf{r} = Nodal displacement vector

$\dot{\mathbf{r}}$ = Nodal velocity vector

$\ddot{\mathbf{r}}$ = Nodal acceleration vector

M = Mass Matrix

C = Damping Matrix

K = Stiffness Matrix

$\mathbf{Q}(t)$ = Time dependent force vector

This equation can be modified by assuming a free undamped vibration. This means that there is no damping and no time dependent loading. The time dependent force vector and the damping matrix is set to zero. When these assumptions are set, the dynamic equilibrium equation is transformed to the general eigenvalue problem, given by Equation 4.8.

$$M\ddot{\mathbf{r}} + K\mathbf{r} = 0 \quad (4.8)$$

By introducing the following for harmonic vibration,

$$\mathbf{r} = \boldsymbol{\phi} \cdot \sin(\omega t)$$

$$\dot{\mathbf{r}} = \omega \cdot \boldsymbol{\phi} \cdot \cos(\omega t)$$

$$\ddot{\mathbf{r}} = -\omega^2 \cdot \boldsymbol{\phi} \cdot \sin(\omega t)$$

where

$\boldsymbol{\phi}$ = eigenvector

ω = frequency, in rad/s

in Equation 4.8, the final general eigenvalue problem can be solved by Equation 4.9.

$$(\mathbf{K} - \omega^2 \mathbf{M}) = 0 \quad (4.9)$$

\mathbf{K} and \mathbf{M} are symmetric and positive definite matrices. \mathbf{K} , while applying element method, is a banded matrix. \mathbf{M} is banded for consistent mass and diagonal for concentrated mass.

4.3.2 Rayleigh Damping Coefficient Procedure

This section describes a procedure to estimate Rayleigh damping coefficients. The procedure is gathered from the article *Computation of Rayleigh Damping Coefficients for Large System* (Chowdhury and Dasgupta, 2003).

In the dynamic equilibrium equation, Equation 4.7, the damping C , is treated as Rayleigh damping in the Ansys transient dynamic solver. The Rayleigh damping, shown in Equation 4.10, is governed by the mass and stiffness matrices along with two damping coefficients, α and β . These are the two coefficients which are to be determined by the procedure described in this section.

$$\mathbf{C} = \alpha \mathbf{M} + \beta \mathbf{K} \quad (4.10)$$

where:

α = mass matrix damping coefficient

β = stiffness matrix damping coefficient

By performing an orthogonal transformation for Equation 4.7, the dynamic equilibrium equation is reduced to Equation 4.11.

$$\Phi^T M \Phi \ddot{\xi} + \Phi^T C \Phi \dot{\xi} + \Phi^T K \Phi \xi = \Phi^T Q(t) \quad (4.11)$$

where:

Φ = normalized eigenvector

Φ^T = transposed normalized eigenvector

ξ = displacement vector in transformed coordinate

$\dot{\xi}$ = velocity vector in transformed coordinate

$\ddot{\xi}$ = acceleration vector in transformed coordinate

This is then written as finite number of uncoupled equations, shown in Equation 4.12.

$$\ddot{\xi} + 2\zeta_j \omega_j \dot{\xi} + \omega_j^2 \xi = Q_j(t) \quad (4.12)$$

where:

ζ_j = damping ratio for mode j

ω_j = natural frequency for mode j

The orthogonal transformation is only valid if the damping matrix is a function of both the mass and stiffness matrix. This leads to the orthogonal transformation of the damping matrix, which can be rearranged to an expression for the uncoupled damping ratio for mode i, see Equation 4.13

$$2\zeta_i \omega_i = \alpha + \beta \omega_i^2 \quad \zeta_i = \frac{\alpha}{2\omega_i} + \frac{\beta \omega_i}{2} \quad (4.13)$$

where:

test

The expression for the modal damping ratio is often divided into a linear and a non-linear part. Because many civil engineering structures has a higher fundamental frequency, explained in

(Chowdhury and Dasgupta, 2003), it is realistic to assumed that the natural frequency and the damping ratio for a mode is linearly proportional. Based on this assumption, the damping ratio for the i^{th} mode can be obtained from Equation 4.14 or Equation 4.15.

$$\zeta_i = \frac{\zeta_m - \zeta_1}{\omega_m - \omega_1}(\omega_i - \omega_1) + \zeta_1, \quad \text{where } 1 < i < m \quad (4.14)$$

$$\zeta_i = \frac{\zeta_m - \zeta_1}{\omega_m - \omega_1}(\omega_{m+i} - \omega_m) + \zeta_1, \quad \text{where } m < i < 2.5m \quad (4.15)$$

where:

ζ_1 = Damping ratio for the first mode

ζ_i = Damping ratio for the i^{th} mode

ζ_m = Damping ratio for the m^{th} mode

ω_1 = Natural frequency for the first mode

ω_i = Natural frequency for the i^{th} mode

ω_m = Natural frequency for the m^{th} mode

By first completing an eigenvalue analysis for the system of interest with n-analyses equal to $2.5m$, where m is the number of modes needed to have a modal mass participation of approximately 95 %, the following procedure can be used to estimate the Rayleigh damping coefficients:

1. Select a damping ratio for the first and m^{th} mode, ζ_1 and ζ_m .
2. Calculate the damping ratios for all modes with Equation 4.14 or 4.15. This makes out the linearized damping curve for the system.
3. Calculate β and α from the expressions in Equation 4.16.

$$\beta = \frac{2\zeta_1\omega_1 - 2\zeta_m\omega_m}{\omega_1^2 - \omega_m^2} \quad \alpha = 2\zeta_1\omega_1 - \beta\omega_1^2 \quad (4.16)$$

4. Calculate a second β and α with a new set of values, called the full set, consisting of the damping ratio and eigen frequencies of the first and the $2.5m$ mode.
5. The third set of coefficients is the average between the first and second.
6. The last step is to multiply the linear damping ratios for the system with the three different coefficients sets. Plot all three sets along with the linear damping ratios and see which set

is closest to the linear result. The coefficients for this set can be used as the Rayleigh damping coefficients for the system damping.

This procedure is used to estimate the damping for the SFT model in this thesis. The results of the analysis are given in Section 7.4 about the results of the modal analysis.

4.4 Harmonic Wave Height Estimation

The procedure about to be described is based upon the 50 year return period significant wave height, H_s , for a JONSWAP spectrum in Sognefjorden. JONSWAP is short for the "Joint North Sea Wave Project", and is a joint multinational project from the south eastern parts of the North Sea from 1968-1969 (Myrhaug, 2004). The waves are wind generated waves. The JONSWAP spectrum parameters are given in Table 4.1.

Table 4.1: 50 year return period spectrum parameters for wind generated waves

Parameter	Magnitude
H_s [m]	2.14
T_p [s]	4.8

The procedure on how to estimate the maximum 50 year wave height is gathered from a number of compendiums used for lecturing different courses at NTNU. The references are Haver (2016), Myrhaug (2005) and Myrhaug (2004).

With a known significant wave height, the maximum wave amplitude can be estimated with a probability of exceedence in a given sea state. Equation 4.17, gathered from Myrhaug (2004, p. 12), is the general equation for the spectral moments, where the first spectral moment, Equation 4.18, is the variance, σ^2 .

$$m_n = \int_0^{\infty} \omega^n S(\omega) d\omega; n = 0, 1, 2 \quad (4.17)$$

$$m_0 = \int_0^{\infty} S(\omega) d\omega = \sigma^2 \quad (4.18)$$

where:

m_n = spectral moment for moment n

m_0 = spectral moment for moment n

$S(\omega)$ = spectrum

σ^2 = variance

The variance can also be calculated from the connection between the significant wave height and m_0 . This connection is given by Equation 4.19, and valid when assuming narrow banded, stationary, Gaussian distributed waves.

$$H_s = H_{m0} = 4\sqrt{m_0} \quad (4.19)$$

where:

H_s = significant wave height

H_{m0} = estimated H_s if significant wave height is estimated from the spectrum

When combining Equation 4.18 and 4.19, one end up with an expression, showing the relation between the significant wave height and the root of the variance, given in Equation 4.20

$$\sigma = \frac{H_s}{4} \quad (4.20)$$

where:

σ = standard deviation

The second spectral moment, m^2 , is given by Equation 4.21.

$$m_2 = \int_0^{\infty} \omega^2 S(\omega) d\omega \quad (4.21)$$

The JONSWAP spectrum form, $S(\omega)$ is given in Equation 4.22. This is the expression which is integrated in order to obtain the spectral moments. It is based on the Pierson-Moskowitz spectrum, but is multiplied for a peaknessfactor, γ .

$$S(\omega) = \alpha \frac{g^2}{\omega^5} \exp\left[-\frac{5}{4}\left(\frac{\omega_p}{\omega}\right)^4\right] \gamma \exp\left[-\frac{1}{2}\left(\frac{\omega - \omega_p}{\sigma \omega_p}\right)^2\right] \quad (4.22)$$

where:

α = form parameter in the high frequency part of the spectrum

ω_p = peak wave frequency, in rad/s

γ = peak enhancement factor [-]

σ = spectral width period

– $\sigma = \sigma_a$, when $\omega \leq \omega_p$

– $\sigma = \sigma_b$, when $\omega > \omega_p$

The expression for α is shown in Equation 4.23, and is gathered from the DNV GL standard for design of offshore wind turbine structures (win, 2014, p. 48).

$$\alpha = 5 \frac{H_s^2}{g^2 T_p^4} (1 - 0.287 \ln(\gamma)) \cdot \pi^4 \quad (4.23)$$

The zero-up-crossing period, T_z , can be calculated from the spectral moments. This can be used to calculate the wave amplitude. The zero-up-crossing period is given by Equation 4.24.

$$T_z = 2\pi \sqrt{\frac{m_0}{m_2}} \quad (4.24)$$

The parameters connected to the JONSWAP spectrum, both calculated from and used as spectrum parameters, are given in Table 4.2.

With a known variance and zero-up-crossing period, an expression for the largest maximum wave amplitude for a return period of 50 years can be derived. Equation 4.25, being the expression for the probability of a wave being higher than the max estimated wave height for a chosen return period, is gathered from Myrhaug (2005, p. 20). It is assumed that the sea state is stationary for 3 hours.

$$P(X_{lm} > \xi_a) = 1 - F_{X_{lm}}(\xi_a) = \alpha \quad (4.25)$$

Table 4.2: JONSWAP parameters and calculated parameters from spectrum considerations

JONSWAP parameters	Magnitude
ω [rad/s]	0 - $20T_p$
ω_p [rad/s]	1.31
γ [-]	3.3
σ_a [-]	0.07
σ_b [-]	0.09
α [-]	0.029
Calculated Parameters	Magnitude
m_0 [-]	0.287
m_2 [-]	0.810
T_z [s]	3.739
σ_X [-]	0.535

where:

X_{lm} = wave amplitude largest maximum

$F_{X_{lm}}$ = distribution function for the largest maximum

ξ_α = wave amplitude

α = probability that a wave in a given sea state will be bigger than the estimated maximum wave amplitude.

By introducing Equation 4.25 for the distribution function for the largest maximum the expression becomes,

$$\left[1 - \exp\left(-\frac{\xi_\alpha^2}{2\sigma_X^2}\right)\right]^N = 1 - \alpha \quad (4.26)$$

where:

N = number of zero-up-crossing waves

When solving this for ξ_α , the final expression for the wave amplitude is given by Equation 4.28

$$1 - \exp\left(-\frac{\xi_\alpha^2}{2\sigma_X^2}\right) = (1 - \alpha)^{1/N} \quad (4.27)$$

$$\xi_\alpha = \sigma_X \sqrt{2 \ln \frac{N}{\alpha}} \quad (4.28)$$

The parameters N is the number of zero-up-crossing waves during a three hour sea state, given by Equation 4.29.

$$N = \frac{3 \cdot 3600}{T_z} \quad (4.29)$$

All parameters for calculating the 50 year return period maximum wave amplitude, with a probability exceedence for a given sea state, are now known. The last parameters are given Table 4.3, with the final results for the procedure.

Table 4.3: Wave amplitude calculation parameters

Parameter	Magnitude
α	0.1
N	2888
σ_X	0.535
ξ_α [m]	2.42
H_{max} [m]	4.85

4.5 Estimating Maximum Irregular Response

The procedure for estimating the largest expected maximum with a Gumbel distribution is collected from (Langen and Sigbjörnsson, 1979, ch. 10.5.4). This is used later in the thesis to estimate the expected maximum and most probable maximum responses for an irregular wave loading analysis of the global model.

When using the Gumbel distribution to estimate the extremes, a Gaussian narrow banded process is assumed.

Figure 4.1 shows the probability density for a Gaussian response process. When the number of maximums increase, a Gumbel distribution can be used to estimate the expected and most probable maximum. The function for estimating these numbers is given in Equation 4.30.

$$E[z_{max}] = \sigma_r \left[\sqrt{2 \ln(E[n_+(0,1)] \Delta T)} + \frac{0.5772}{\sqrt{2 \ln(E[n_+(0,1)] \Delta T)}} \right] \quad (4.30)$$

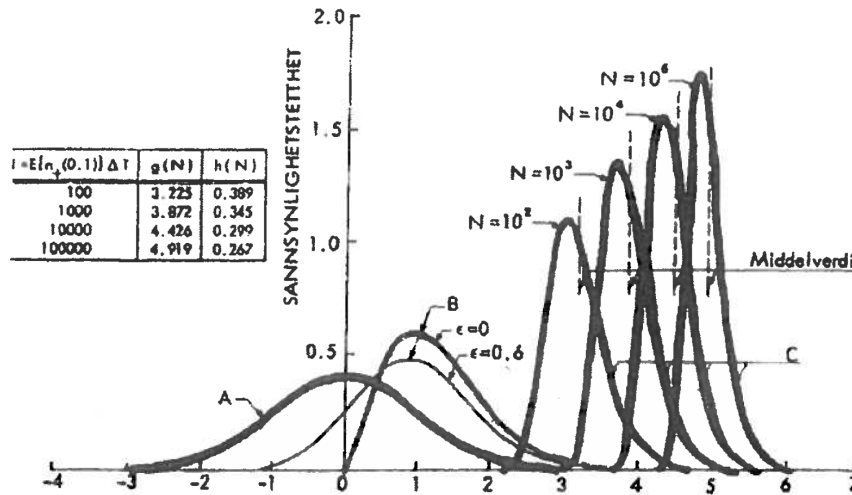


Figure 4.1: Probability density for a gaussian response process

where:

- σ_r = standard deviation for the response
- $E[n_+(0,1)]\Delta T$ = the number N of registered mean-up-crossings for maximum responses

The standard deviation is found from the variance of the response, given by Equation 4.31.

$$\sigma^2 = \frac{1}{n-1} \sum_{i=1}^n (r_i - \bar{r})^2 \quad (4.31)$$

where:

n = number of sampled responses for the time series

r_i = response for current time step

\bar{r} = response mean value

If the mean of the response in consideration is different from zero, it needs to be added to the expression for the expected maximum, see Equation 4.32.

$$E[z_{max}] = \sigma_r \left[(\sqrt{2 \ln(N)} + \frac{0.5772}{\sqrt{2 \ln(N)}}) \right] + \mu \quad (4.32)$$

where:

μ = mean response value

N = number of registered mean-up-crossings for maximum responses

Chapter 5

Global Modeling of an SFT

In this chapter the description of how the submerged floating tunnel has been modeled is included. It contains information about the utilized software in the different steps of the modeling for both the complete model and individual pontoons. A description of how the final code works is also included. This includes different flowcharts describing sub steps in the final code. How the code/program can be used is described in Appendix A.

The model is a combined beam and pipe element model where the objective is to run static, modal and dynamic response analyses for hydrodynamic loading. Dynamic response analysis includes harmonic and irregular wave loading. The concept used is developed by Reinertsen Olav Olsen Group for crossing Sognefjorden in a submerged floating tunnel, see (Group, 2013). It is modeled as similar as possible, but includes simplifications making the modeling easier to carry out. The simplifications made during the modeling is described in each section.

5.1 Modeling and Calculation Software

When modeling, a number of different softwares are utilized. These softwares are again combined in a main program carrying out the modeling, analyses and post processing of the final results. The softwares are listed in Section 5.1.1 and the main code description with belonging flowcharts is described in Section 5.1.2. A short description of a self written pontoon testing

program is also given in Section 5.1.3.

5.1.1 Computer Software

The softwares utilized in the thesis are listed below. Sesam is used for confirmation of pontoon modeling and ANSYS comparison. MATLAB and ANSYS are used in combination to carry out parametric modeling and analyses of both the global SFT model and pontoon testing.

Utilized software:

- Sesam
- ANSYS Mechanical 16.2
- MATLAB
 - Genie
 - HydroD

The software used to create the global model is ANSYS Mechanical APDL version 16.2. APDL is an acronym for ANSYS Parametric Design Language which uses either C or FORTRAN programming syntax, creating input files for ANSYS. APDL uses built in ANSYS commands in combination with C or FORTRAN syntax, allowing for example do-loops, if-sentences and while-loops in order to effectively create a global model. By using parametric modeling language the geometry and analysis input files can be written in either MATLAB or TextPad and then used to run ANSYS.

5.1.2 Main Program Description

The overall flowchart of the main program is given in Figure 5.1. It consists of three different colored boxes. The yellow, blue and orange colored boxes are MATLAB scripts, TextPad input files and ANSYS operations, respectively. The general idea of the program is to run ANSYS from MATLAB with TextPad generated input files. The results are saved in text files in ANSYS and post processed in MATLAB. The whole program runs in a loop until a requested number of analyses are completed or until a certain result is obtained. The main steps are described below.

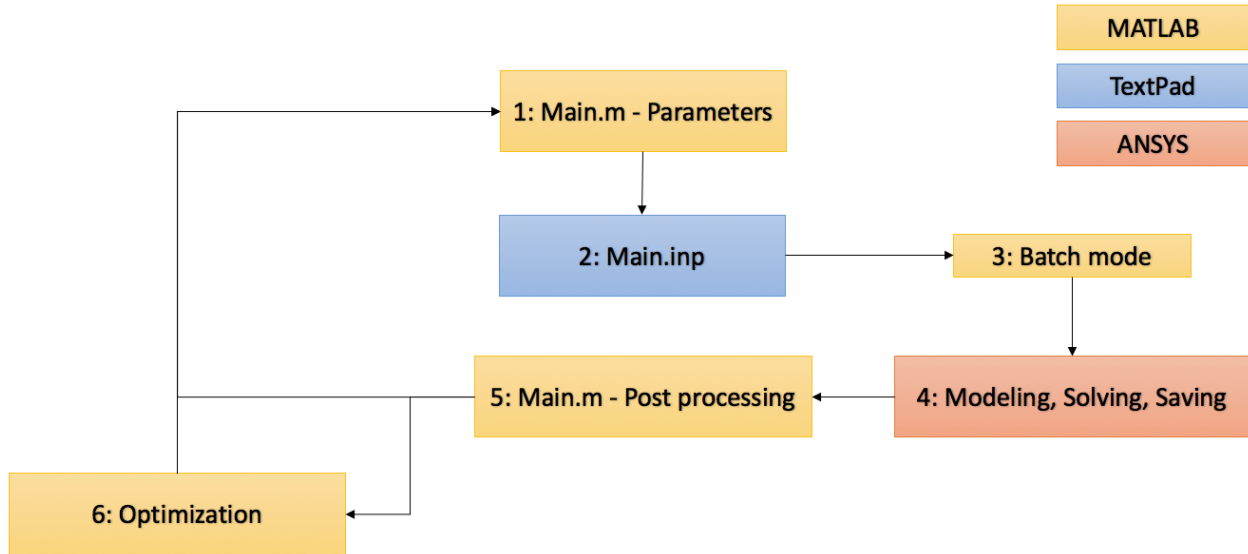


Figure 5.1: Flowchart for the main program

- 1 - **MATLAB parameters:** All parameters needed for modeling, solving and saving are given. These parameters are then written into parameter input files.
- 2 - **TextPad main input:** The main.inp file is built up of a number of input files. These files are parametric modeling input files written in APDL, using the parameters from the MATLAB text files. The idea is that they are the same in every loop, only changing due to the parameter values given in step 1. The flowchart for main.inp is given in Appendix A.1 with belonging explanation and figure, Figure A.2.
- 3 - **Batch mode:** MATLAB executes a batch file, starting ANSYS and running the file main.inp. The batch file is executed from the MATLAB main file, main.m.
- 4 - **ANSYS modeling, solving, saving:** ANSYS carries out all necessary steps in batch mode. When ANSYS is running in batch mode, there are no graphical or optional maneuvering possibilities. The steps carried out, is decided by the main.inp file.
- 5 - **MATLAB Post Processing:** After the requested information is saved in text files, post processing is carried out in MATLAB.
- 6 - **MATLAB Optimization:** If an optimization is requested, a MATLAB particle swarm optimization script can be utilized. This is when for example an optimal mesh size for the

different model elements is necessary. This can be a troublesome process when done manually, testing a lot of different mesh sizes.

After all six steps have been completed, an analysis with new parameters can be carried out.

A guide explaining how the program can be executed is added in Appendix A. The guide explains how a user can run the `main.m` script with correct input parameters in order to solve an analysis for the submerged floating tunnel. The codes is added in a zipped file in the digital appendix.

5.1.3 Pontoon Program Description

In order to verify ANSYS assumptions, a pontoon analysis program has been made. The goal is to compare the results from this program with the analysis done i Sesam for the simplified pontoon geometry. The description of the program is added in Appendix A.2 with belonging flowchart, Figure A.3.

5.1.4 MATLAB and ANSYS APDL scripts

Table 5.1 shows the number of MATLAB files and input files written for the main SFT and pontoon program. As examples, the following files have been added in Appendix B:

- *main.m* - Appendix B.1 - Main script for the SFT program
- *main_geometry.inp* - Appendix B.2 - Input file for creating the main geometry of the model.

In addition to the files listed in 5.1, a number of approximately 20 additional MATLAB scripts has been written for post processing and plotting of results from ANSYS.

Table 5.1: Number of files for the SFT and pontoon programs

Type	SFT program	Pontoon program
file.m	4	1
file.inp	28	10

5.2 ANSYS Elements

In order to create a realistic global model a number of different element types have been utilized. The objective has been to describe the different parts of the model with the correct elements. The parts in particular are the concrete pipes, the steel shafts connecting the pipes with the pontoons, the pontoon beams and it's spring stiffnesses. The elements used in the model are:

- BEAM189 - A three-noded beam element
- COMBIN14 - A combination spring element
- MASS21 - A concentrated mass element
- PIPE289 - A three-noded pipe element

The element information has been gathered from ANSYS documentation which is available along with ANSYS or on various websites (ANS, 2016, Element Library).

5.2.1 BEAM189 - A Beam Element

The element used to model the pontoons is BEAM189, a 3-D three-node beam element. It is based on Timoshenko beam theory and is suitable for analyzing slender to moderately thick beam structures (ANS, 2016, Element Library).

The element is a quadratic three-noded beam element and has six degrees of freedom at each node, three translations and three rotations. There is an optional seventh degree of freedom, a warping magnitude, available. It is suitable for both linear and/or large strain nonlinear applications. A schematic illustration of the element is shown in Figure 5.2.

The element is available with an ocean environment input which can be modeled when using BEAM189, among other elements. A description of the ocean data environment is given in Section 5.8.

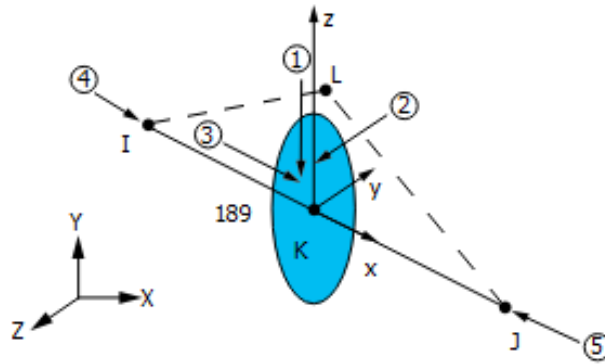


Figure 5.2: Illustration of a BEAM189 element, illustration (ANS, 2016, Element Library)

5.2.2 COMBIN14 - A Combination Spring Element

The COMBIN14 element is a combination spring element with a longitudinal and a torsional option. Both of these two options have been used when modelling the spring stiffnesses of the pontoon. The torsional option has been used for the roll and pitch stiffness and the longitudinal option for the restoring in heave. No bending is considered for any of the two capabilities. A schematic figure from the ANSYS element library is shown in Figure 5.3, with the following symbols:

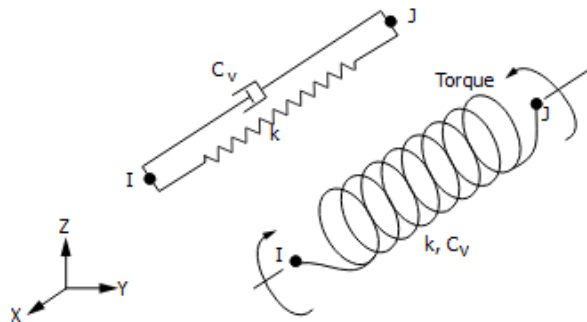


Figure 5.3: Illustration of a COMBIN14 element, illustration (ANS, 2016, Element Library)

I = Node I

J = Node J

k = Rotational or longitudinal spring stiffness

C_v = Rotational or longitudinal spring damping

The damping capability of the spring is not used in the modal analysis. It is used for the static and dynamic analysis, where its magnitude is equal to the potential damping for the free pontoon.

5.2.3 MASS21 - A Concentrated Mass Element

The MASS21 element is a mass element with six degrees of freedom, three translations and three rotations. The main idea of the element is adding mass to a node, making it possible to represent for example a constant force or ballast. A schematic figure of the element is shown in Figure 5.4. The element coordinate system may be initially parallel to either the global Cartesian coordinate system or the nodal coordinate system.

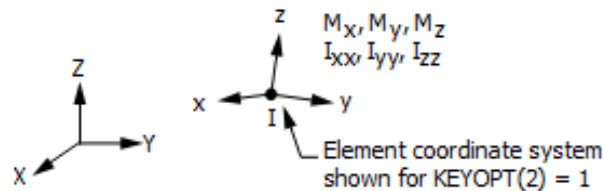


Figure 5.4: Illustration of a MASS21 element, illustration (ANS, 2016, Element Library)

One of the options for MASS21 is an individual mass in x-, y- and z-direction, respectively MASSX, MASSY and MASSZ. This can be used for directional added mass representation. The MASS21 element also has an option with only three translations, having only one mass input. This is an appropriate option when representing ballast for the model.

The element mass has an effect on static analyses, even when no dynamic forces are acting on the element. This means it is unsuitable for representing hydrodynamical added mass.

5.2.4 PIPE289 - A Pipe Element

The pipe element is used for modeling the main pipes, the bracing and the connection shafts between the pontoons and the main tunnel. It is based on Timoshenko beam theory and is

suitable for analyzing slender to moderately thick pipe structures (ANS, 2016, Element Library). A schematic geometrical figure of the element is shown in Figure 5.5.

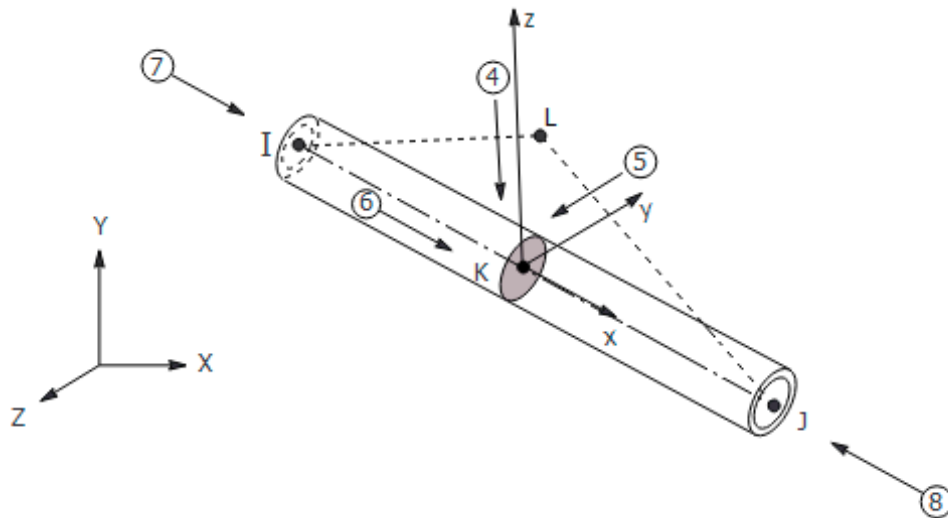


Figure 5.5: Illustration of a pipe289 element, illustration (ANS, 2016, Element Library)

The element is a quadratic three-node pipe element in 3-D. It has six degrees of freedom at each node, three translational and three rotational. It is suited for linear analysis, large rotation and/or large strain. The element has an added mass option like BEAM189. It also works with the ocean data input values.

The important difference for PIPE289 and BEAM189 is that it is not possible to model air inside a submerged circular BEAM189 element. This means that the added mass is based solely on the displaced water by the material cross section of the beam element. This will eventually result in a bad added mass representation.

5.3 Submerged Floating Tunnel - Global Dimensions

The main geometries of the bridge taken from the Reinertsen Olav Olsen Group study are used in order to create the model. The final model values are slightly different than the ones given in the study, because the modeling becomes a little easier to carry out. The final ANSYS model geometries are given in Table 5.2.

Table 5.2: Main geometries of the ANSYS bridge model

Geometry	Value	Unit
Main span	3672	[m]
Bridge length	≈ 4000	[m]
Horizontal bridge radius	2682	[m]
Vertical radius	∞	[m]
Clearance above tunnel	20	[m]
Spans between pontoons	150-500	[m]
Center distance between main pipes	40	[m]
Number of tunnels	2	[-]

There are a total of 94 bracing elements in the structure. They have an angle of approximately 45 degrees to the center line between the two tunnel pipes. The 16 pontoons in the structure are connected with two steel shafts to the main submerged tunnels. There are several different cross sections in the model, all discussed in Section 5.4

There are numerous simplifications carried out, both considering the real problem and the model specifications given in the Reinertsen Olav Olsen study. The model in ANSYS has no vertical radius, meaning a constant clearance above the submerged tunnel of 20 meters. The bracing angle is also set to 45 instead of 40 degrees.

5.4 Cross Sections

5.4.1 Cross Section Geometries

All cross section geometries are taken from Group (2013) and can be seen in Table 5.3. The inner walls are an estimation done from the Reinertsen Olav Olsen Group concept.

Table 5.3: Cross section data

Section	Outer radius [m]	Thickness [m]	Inner walls [m]	Material	Condition
Main pipe	6.3	0.8	0.3	Concrete	Dry/ballast
Bracing pipe	2.5	0.5	-	Concrete	Wet
Evacuation pipe	4.0	0.5	0.3	Concrete	Dry
Connection shaft	4.0	0.5	-	Steel	Wet

The evacuation pipe occurs approximately every 500 meter of the bridge length. Considering

that there are only a few of them, they are not included in the ANSYS model. Instead, standard bracing pipes are used. This means that the bridge loses some of its excess buoyancy. The mass of the dry evacuation pipe and the wet bracing pipe is approximately equal, but the buoyancy of the evacuation pipe is a lot bigger.

5.4.2 Cross Section Modeling

Figure 5.6 shows the ANSYS modeled main cross section and the main cross section from the Reinertsen Olav Olsen Group study. There are two ANSYS models, one simplified and one accurate. The differences are small between the accurate ANSYS cross section and the one proposed by Reinertsen Olav Olsen Group. The one used in the global model is the cross section in Figure 5.6c. This is because the main tunnel is modeled by a pipe element, only allowing for circular cross sections. The missing weight due to inner cross section arrangements, are accounted for when modeling ballast, while the stiffness due to the inner structure is ignored.

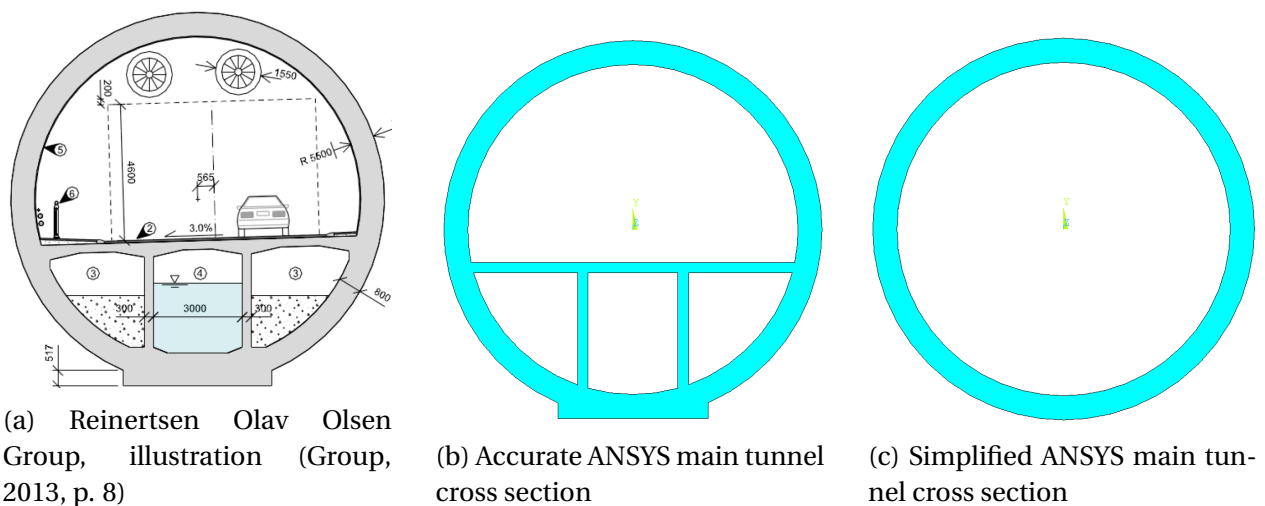


Figure 5.6: Comparison of main cross section from Reinertsen Olav Olsen Group study and ANSYS model

The bracing elements and the shafts between the main tunnels and the pontoons are modeled as pipes with the geometries given in Table 5.3.

5.5 Global Model Line Arrangement

5.5.1 Element Representation

The general line arrangement is shown in Figure 5.7a . The display of the elements is shown Figure 5.7b. The bracing, main tunnel and connection shaft lines are all modeled with PIPE289 elements. The pontoons are modeled with BEAM189 elements and the springs with the COMBIN14 element.

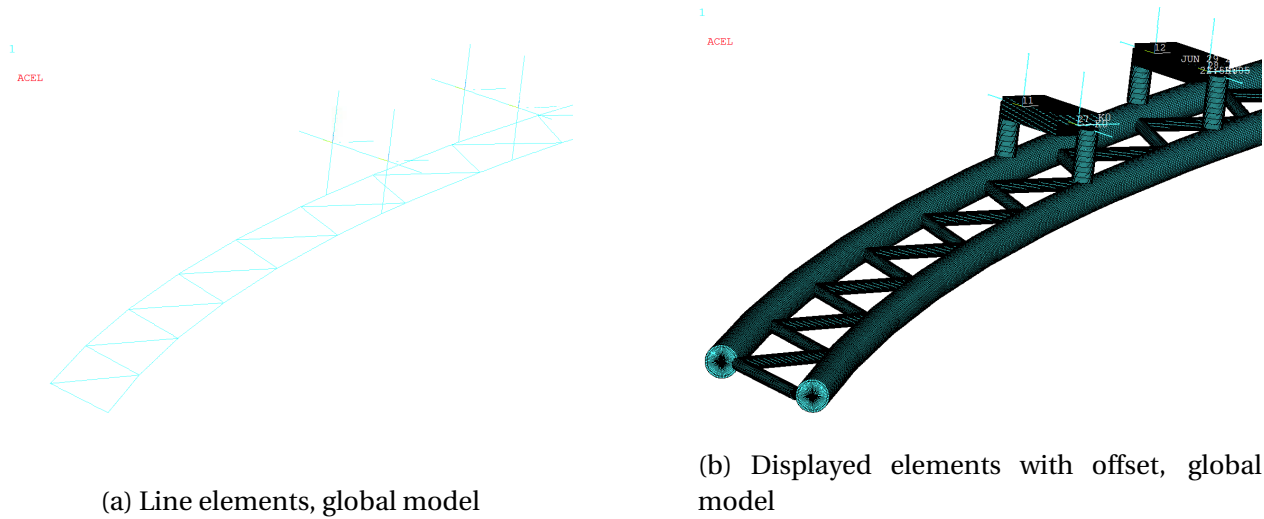


Figure 5.7: Line arrangement and cross section offset - Main tunnel and bracing

An overview of the element representation in the model is given in Table 5.4.

Table 5.4: Element representation

Section	Element
Main section	PIPE289
Bracing	PIPE289
Shaft	PIPE289
Pontoon	BEAM189
Springs	COMBIN14

5.5.2 Line Arrangement - Cross Section Offset

In order to avoid pipe or beam element cross sections entering each other, a cross section offset is used for all sections. By comparing the pictures in Figure 5.8, it is clear that the main pipe cross sections have a horizontal offset equal to their radius, outwards from the bridge center. The center line distance between the main tunnel pipes is 40 meters.

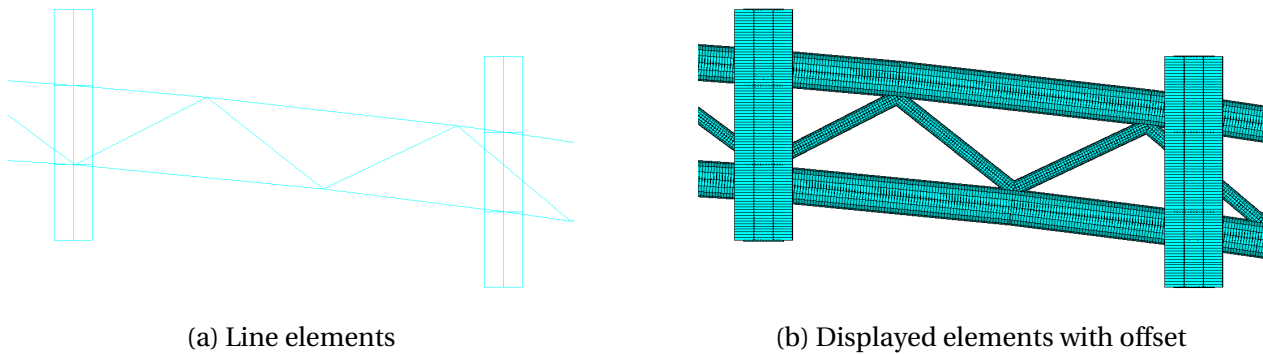


Figure 5.8: Line arrangement and cross section offset - Connection shaft and pontoon

The main pipes and the bracing elements also have an offset equal to the main radius in negative z-direction. This is to prevent the connection shaft from going into the main tunnel. This offset is clear by comparing the aligned view of the figures in Figure 5.9.

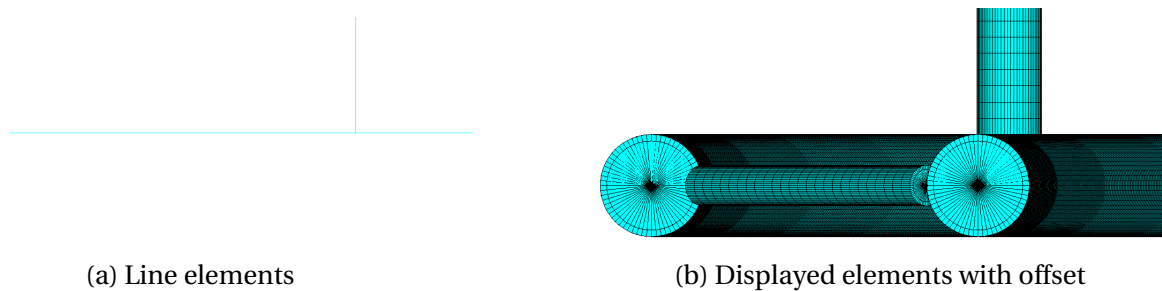
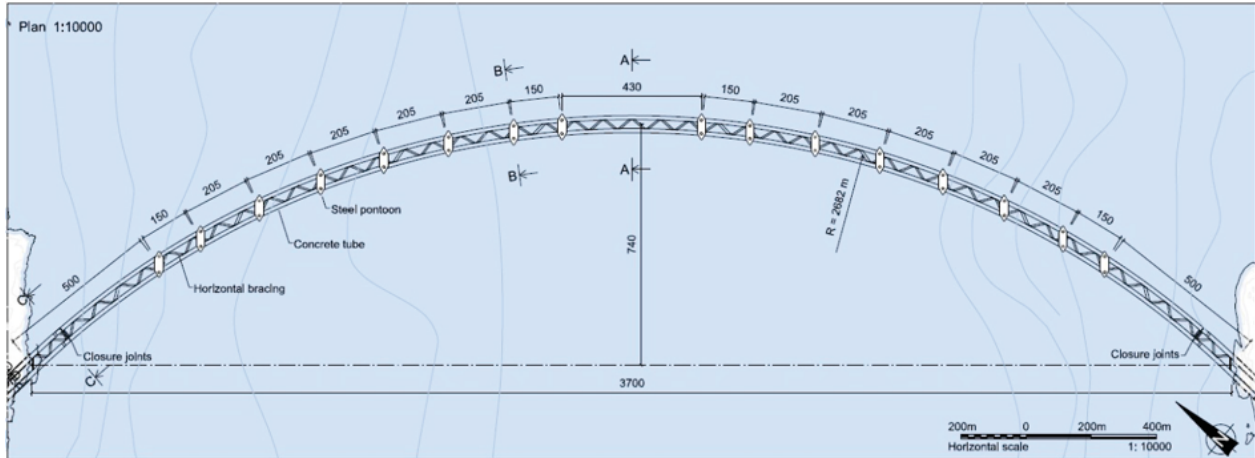


Figure 5.9: Line arrangement and cross section offset - Tunnel and bracing vertical offset

5.6 Pontoon Modeling

5.6.1 Pontoon Arrangement

In the bridge model there are 16 pontoons supporting the submerged floating tunnel. The most common distance between neighbouring pontoons is 205 meters, but closest to the longest spans the distances are 150 meters. This is in order to have more support and relieve the stress at the individual pontoon (Group, 2013). The general pontoon arrangement can be seen in Figure 5.10. Figure 5.10a shows the arrangement as proposed in the Reinertsen Olav Olsen Group study while Figure 5.10b shows the pontoon arrangement in ANSYS.



(a) Reinertsen Olav Olsen Group, illustration (Group, 2013, p. 6)



(b) ANSYS model without bracing elements

Figure 5.10: Comparison of general pontoon arrangement from Reinertsen Olav Olsen Group study and ANSYS model

Measurement tools in ANSYS show that the pontoon distance in the ANSYS model is equal to what is proposed in Figure 5.10a. If required, the pontoon distance can easily be altered in the

MATLAB program.

5.6.2 Pontoon Geometry and Properties

A picture of both a simplified and final pontoon for the SFT can be seen in Figure 5.11. For the rest of the thesis, these two configurations will be re-

ferred to as the simplified and final pontoon geometries. For the global model in ANSYS the geometry to the left is used, with the properties of the final pontoon. The final pontoon is modeled in GenIE and HydroD in order to obtain the restoring coefficients which are used as torsional and longitudinal spring stiffnesses in ANSYS. The geometrical parameters are:

Simplified Pontoon Geometry

- Length = 80 m
- Beam = 20 m
- Height = 8 m
- Draught = 4 m
- Waterplane area = 1600 m^2

Final pontoon Geometry

- Length = 80 m
- Beam = 26 m
- Height = 8 m
- Draught = 4 m
- Waterplane area = 1560 m^2
- Shaft center distance = 40 m

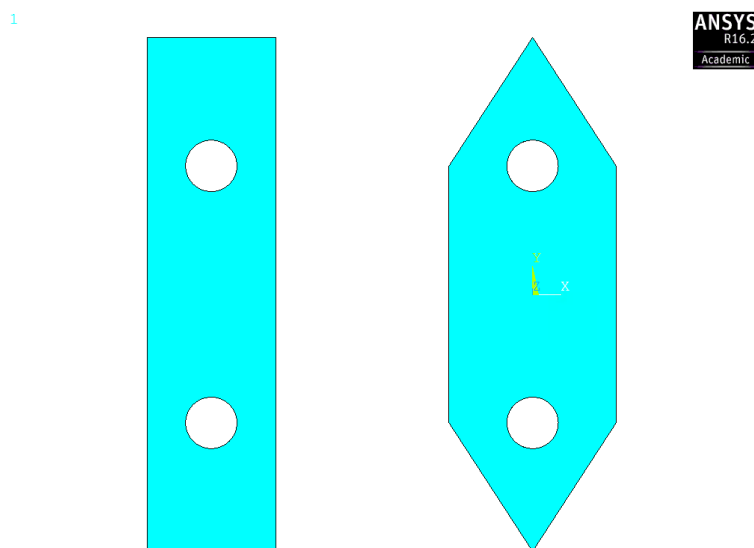


Figure 5.11: Simplified and final pontoon geometries

During the summer there can be a 4 meter deep column of fresh water in the fjords water surface (Group, 2013, p. 29). Due to this high concentration of fresh water, the water density used for the pontoon calculations is 1015 kg/m^3 .

For the mounted pontoon, the most interesting restoring coefficients are the ones in heave, roll and pitch. These are calculated for both pontoon geometries, hand calculations for the simplified geometry and with Wadam analysis for the actual pontoon. The spring stiffnesses are given in Table 5.5.

Table 5.5: Conventional and torsional spring stiffnesses

Motion	Simplified	Actual	Spring capability	Numbering, Figure 5.12	Unit
Heave	$1.59 \cdot 10^7$	$1.55 \cdot 10^7$	Longitudinal	1	$[N/m]$
Pitch	$8.50 \cdot 10^9$	$5.05 \cdot 10^9$	Torsional	2	$[N/rad]$
Roll	$5.31 \cdot 10^8$	$6.05 \cdot 10^8$	Torsional	3	$[N/rad]$

Restoring in heave for the simplified pontoon is given by Equation 5.1.

$$C_{33} = \rho_{sf} \cdot g \cdot A_w \quad (5.1)$$

where:

C_{33} = restoring coefficient in heave, in N/m

A_w = Water plane area, in m^2

ρ_{sf} = Surface water density, in kg/m^3

The torsional stiffnesses for roll and pitch for the simplified pontoon are given by Equation 5.2 and 5.3 (Group, 2013, p.44).

$$C_{44} = \int_{-\frac{L}{2}}^{\frac{L}{2}} y^2 \rho_w g dx B \quad (5.2)$$

$$C_{55} = \int_{-\frac{B}{2}}^{\frac{B}{2}} x^2 \rho_w g dx L \quad (5.3)$$

In Figure 5.12 the representation of the springs is shown with red lines. Each spring magnitude in Table 5.5 is divided between two springs. The numbering for the springs are given in Table 5.5.

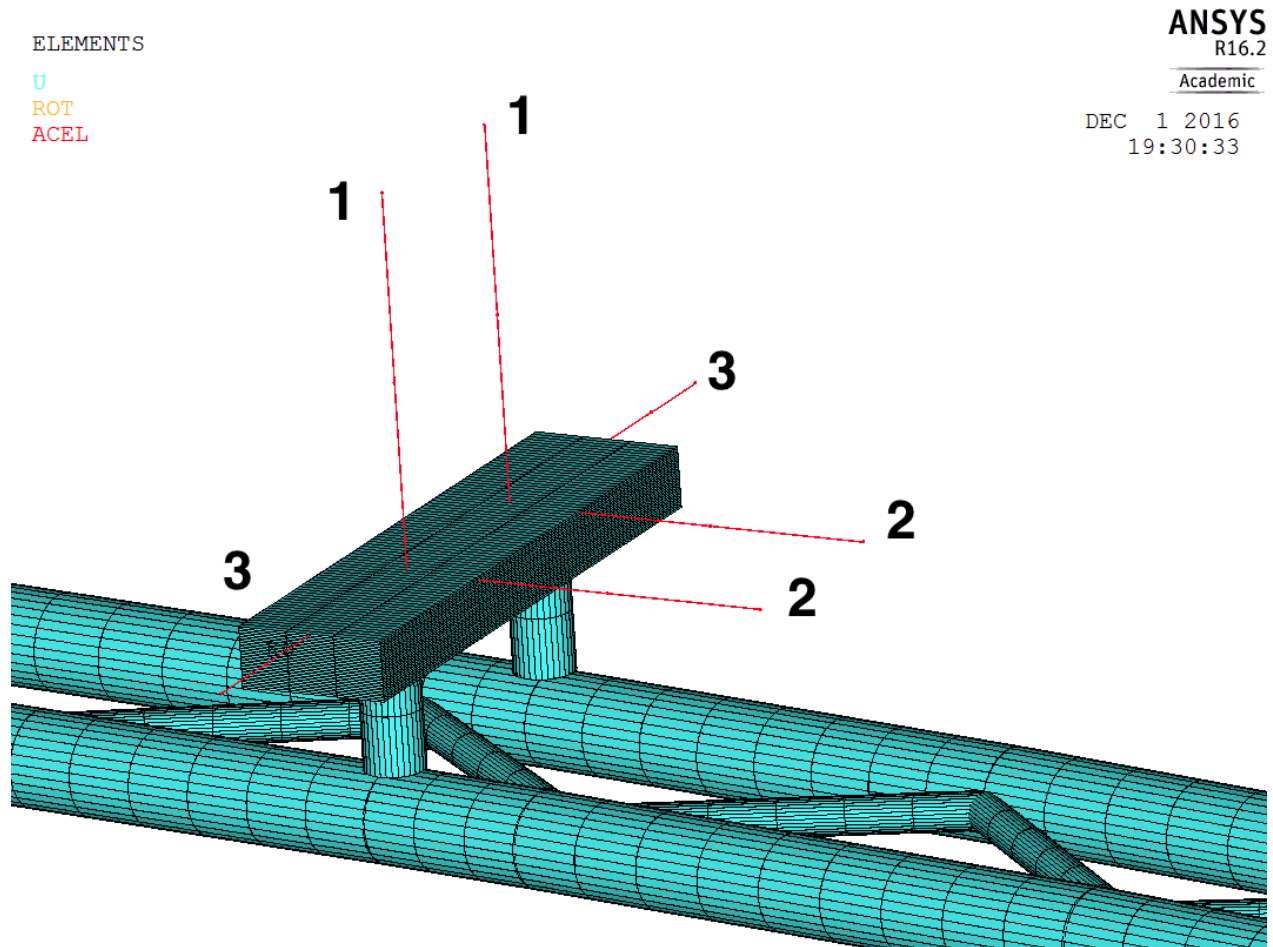


Figure 5.12: The springs representing the pontoon characteristics, explanation in Table 5.5

5.6.3 Pontoon Buoyancy Modeling

The pontoon is modeled in several layers, both in horizontal and vertical direction. This is done in order to obtain the right buoyancy for different mean water surface levels. If an element line, such as the ones shown in Figure 5.13a, is submerged, the buoyancy force will be equal to the volume of the whole element meshed on this line. If the whole pontoon was modeled with only one beam element, being 20 meters wide and 8 meters tall, this element would contribute with a buoyancy force equal to the full volume of the pontoon as long as the line is submerged. Changing the mean water surface level would not change the total buoyancy of the model. This is handled with the horizontal and vertical beam element layering.

The pontoon beam elements are not connected to each other along the length of the pontoon. Considering the height of each individual element being small, the Young's Modulus is set to a

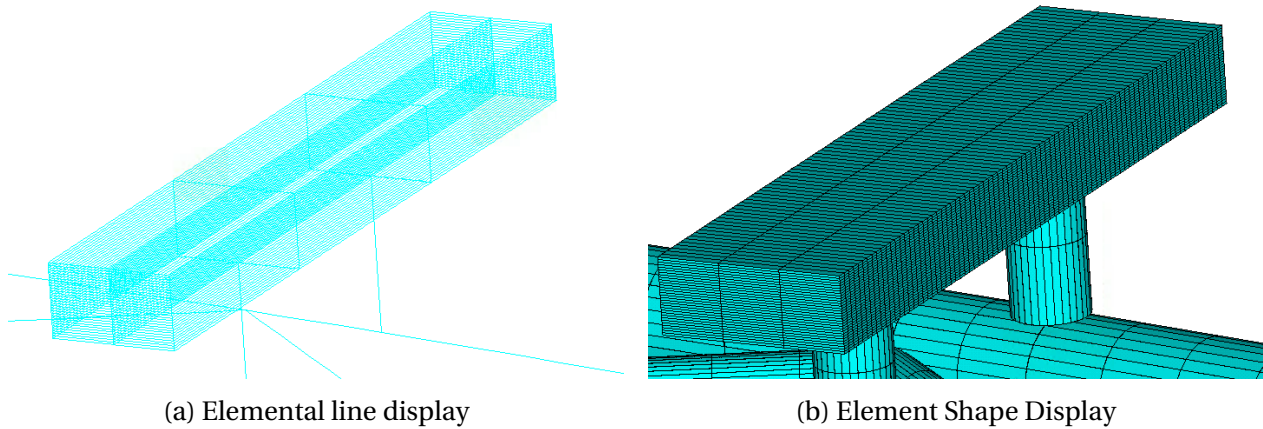


Figure 5.13: Pontoon Layer Modeling

high value in order to secure a stiff pontoon. This is not considered to have a great impact on the bridge in a whole, but secures a well modeled buoyancy.

5.6.4 Pontoon Mass and Added Mass

Other geometrical parameters for the pontoon than the overall geometries was not found. The weight of the pontoon was therefore estimated by assuming a wall thickness for the pontoon. This wall thickness includes an addition connected to internal structure of the pontoon. The wall thickness is called $t_{adjusted}$ in the MATLAB program. The weight of the pontoon is highly uncertain, being based on nothing but simple wall thickness assumptions.

The added mass of the pontoon is accounted for in the ocean data input, which is described in Section 5.8.1 about the basic ocean loading.

5.7 Boundary Conditions

The bridge model is constrained at the ends and at the springs representing the restoring and damping of the pontoons. The ends of the bridge are fixed in all translations and rotations. This is illustrated in Figure 5.14a. This is assumed to be the most realistic boundary condition considering that the submerged tunnels go into the mountain before they emerge into free air.

This constrains the tunnels from rotating at the boundary. In the figure the crossing diagonal lines are the bracing elements and the others are the submerged tunnels for traffic. This means that the end elements for the bracings are fully constrained.

The spring ends are also fixed in all translations and rotations. When the springs represent either longitudinal or rotational stiffness and damping, the ends have to be held for the forces to be absorbed by the springs. As seen in picture 5.14b there are three springs representing the pontoon characteristics for stiffness and damping in heave, roll and sway.

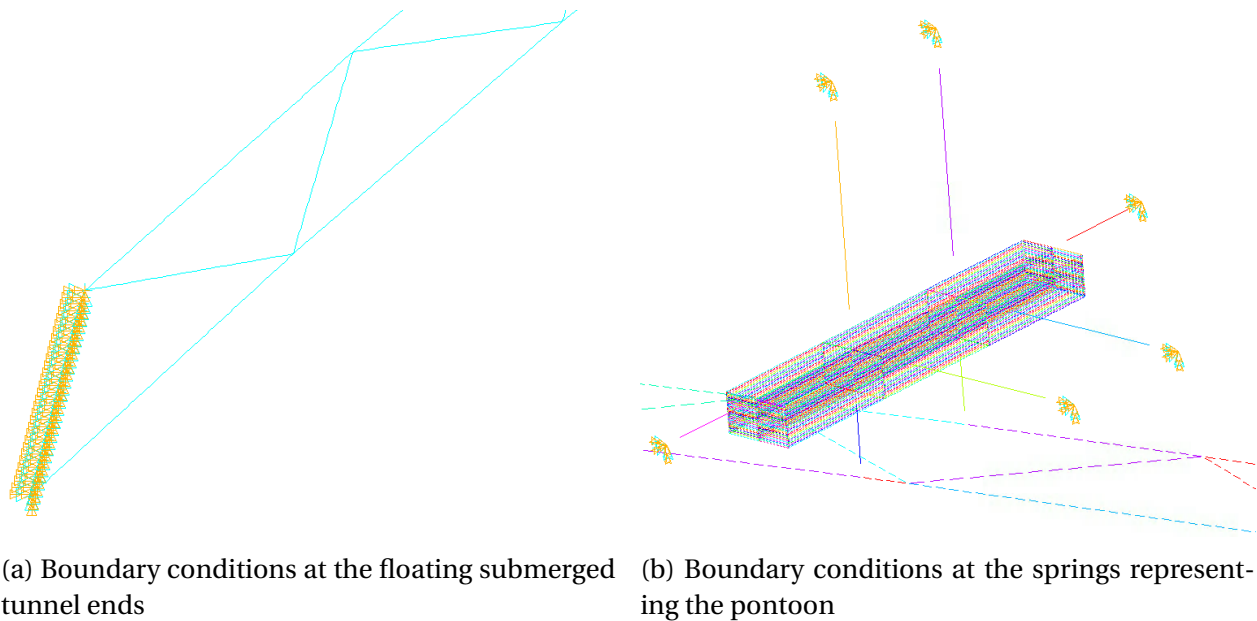


Figure 5.14: Submerged floating tunnel boundary conditions

5.8 ANSYS Ocean Loading

Having established the model geometry, the next step is to model ballast, buoyancy and added mass. In ANSYS there is a built in ocean loading available when modeling with ANSYS pipe and beam elements. The ocean loading includes the following types of loading:

- Basic - Defining a basic environment
- Current - Defining an optional drift current
- Wave - Defining an optional ocean wave state

5.8.1 Basic Ocean Loading

With a basic ocean loading important features for both dynamical and statical analysis is defined. It is necessary to apply the basic loading in order to define a wave state. The loading includes buoyancy, depth, an ocean density, a model global offset from mean water level, a flooding factor and directional added mass. All these inputs are defined as the ocean data input for the model environment. The assigned values for the basic ocean loading is listed in Table 5.6 with a description of each value in a list below. The depth, with a fjord depth ranging from 0 to 1290 meters, is set to 750 meters. The variable Zmsl is a mean sea water level offset in vertical direction. It is the length from the global Cartesian Z-coordinate equal to zero, to the mean water level. The directional added mass coefficient is set to 1.0, being the value for a circle in both directions.

Table 5.6: Basic Ocean Data

Parameter	Magnitude	Unit
Depth	750	[m]
Ocean density	1025	[kg/m^3]
Buoyancy coefficient	1.0	[-]
Added mass coefficient	1.0	[-]
Zmsl	19.95	[m]
Kflood	0	[-]

The parameters in Table 5.6:

- Depth - depth from mud line to mean water level
- Ocean density - The density of the ocean surrounding the structure
- Buoyancy coefficient - Buoyancy used over actual buoyancy force
- Added mass coefficient - Added mass coefficient for fully submerged body
- Zmsl - Vertical offset from global coordinate system origin to mean water level
- Kflood - Flooding of the pipe289 elements, 1=yes, 0=no

The bracing pipes and connection shafts are flooded with water. This is not done by flooding the pipes with the basic ocean loading input, Kflood. If this parameters had been activated, all pipes would be flooded. Instead, a mass element is added to each nodes of the flooded pipes.

5.8.2 Current Ocean Loading

The values for current ocean loading is listed in Table 5.7. Both current velocity, drift angle and water temperature can vary in depth direction. The depth current value is defined from mean water surface level and increases as the Cartesian Z coordinate value decrease (Group, 2013). The current velocity decreases or increases linearly between two input depths. The current input does not allow for different directions at the same water depth, which implies the the drift angle can only be modeled as uniform along the fjord width.

Table 5.7: Current Velocity

Depth	depth \leq 10m	10m < depth \leq 32.6m	32.6m < depth \leq 750m	Unit
Velocity	1.27	0.55	0	[m/s]
Drift Angle	90	90	90	[°]
Temperatur		10	10	10[°C]

The lowest point of the model is at a water depth of 32.6 meters. The current velocity below this point is not of importance, but the last input value for the current must be set at seabed (maximum water depth). The drift angle can of course be set to different values in order to check how the bridge responds. It is measured in angles from the global Cartesian X-axis towards the Y-axis. The current input data has not been implemented in this thesis, but should be implemented for further analyses of the SFT for verification.

5.8.3 Wave Ocean Loading

The wave ocean loading has a variety of inputs, depending on the incident wave type. The different incident wave types will be described shortly here. In Chapter 6 about the different analyses which have been carried out, the input values for the parameters of the used incident wave types will be listed along with the analysis description. The wave types used in this thesis are:

- Airy - A small amplitude Airy wave without modifications. It follows linear wave theory with potential flow.
- JONSWAP Spectrum - A Pierson-Moskowitz wind generated spectrum with a peak frequency and a peak enhancement factor.

Some of the general wave ocean load inputs are listed below. Specific values for different incident wave types with their input value will be given for each analysis in Chapter 6.

1. KWAVE - Incident Wave Type
2. WAVE THETA - Angle of wave direction
3. WAVELOC/SPECTRUM - The wave location on the elements / Spectrum type
4. KCR - Wave-current Interaction
5. KMF - MacCamy-Fuchs adjustment key
6. PRKEY - Wavelength wave-print out key

Wave location input data is set in accordance with chosen incident wave type. This will also be listed together with belonging analysis.

5.9 Modeling Ballast and Flooded Pipes

5.9.1 Ballast in Main Tunnel Pipe

In order to have a close to neutrally buoyant global model, ballast has to be added to the main tunnel pipes. This ballast is concrete slurry and water, shown in chamber 3 and 4 in Figure 5.15. The ballast is represented with the MASS21 element. A version with only tree translations and one input mass is used. A filling fraction for the slurry and water chambers is introduced in order to obtain a close to neutrally buoyant bridge. The weight of the internal structure of the main tunnel is also added in the MASS21 element. The input value of the element is mass per node.

Table 5.8: Mass contributions to main MASS21

Mass	Symbol	Dens. [kg/m^3]	Area symbol	Unit Area [m^2/m]	Fraction
Slurry ballast	ρ_{slurry}	2400	A_{slurry}	17.2	η_{slurry}
Water ballast	ρ_{water}	1025	A_{water}	11.9	η_{water}
Internal structure	$\rho_{structure}$	2400	$A_{structure}$	-	-

The material properties of the ballast and internal structure is given in Table 5.8. It is assumed that the internal structure and the slurry have the same density as ordinary concrete. The available area in Table 5.8 is an estimation of the two slurry chambers and the water ballast chamber

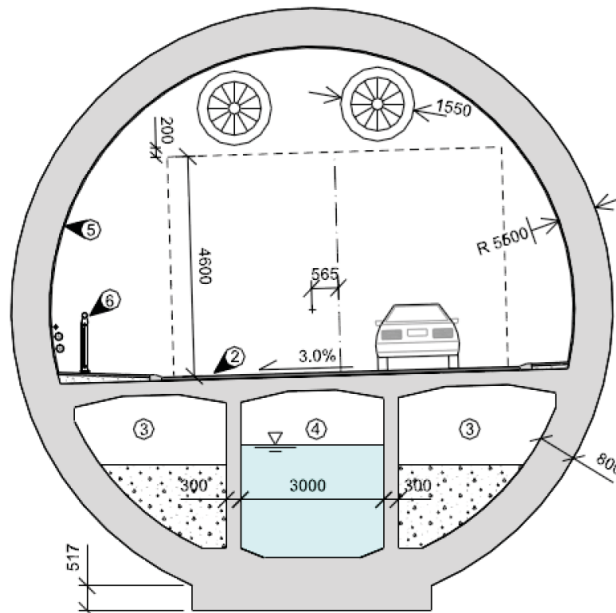


Figure 5.15: Main cross section from Reinertsen Olav Olsen Group study, illustration (Group, 2013, p. 8)

using measurement tools on the accurate main cross section in ANSYS, Figure 5.6b. This is only a value used for calculating the final ballast and input value for the MASS21 elements.

The unit mass along the main pipes is given by Equation 5.4. The final value for the MASS21 element is obtained by multiplying the unit mass per meter with the relevant length of the individual main cross sections and dividing them by the number of chosen nodes. How the necessary ballast is distributed among the different parts of the bridge span is described in Section 5.9.2.

$$mass = \rho_{slurry} A_{slurry} \eta_{slurry} + \rho_{water} A_{water} \eta_{water} + \rho_{structure} A_{structure} \quad (5.4)$$

5.9.2 Lower and Upper Bridge Weight and Buoyancy Considerations

The pontoon draft at vertical neutral position is assumed to be 4 meters. The assumption is made in agreement with co-supervisor. It seems reasonable considering that 4 meters is equal to half the pontoon height. The pontoons draft contributes with buoyancy, but still has excess draft for heavier load conditions with for example high traffic and other environmental loading.

The buoyancy force on the main tunnel caused by the pontoons is counteracted with ballast.

In order to minimize the vertical bridge displacement along the span, the ballast needs to be distributed in accordance with the location of the pontoons. This is done in several steps

The first step is to calculate the net requirement of ballast in the main tunnels in order to have a global net buoyancy equal to zero. This means that the total bridge weight is equal to the total buoyancy. If this ballast is evenly distributed over the nodes of the main tunnels, there will be a local excess buoyancy under the pontoons, and the opposite at non-supported spans and the middle and sides.

In order to solve this, the required ballast for a neutrally buoyant lower bridge is calculated. The main tunnels and bracing are the lower parts, while the connection shafts and the pontoons are the upper part of the bridge. The lower required ballast is divided by all the nodes of the main tunnels, while the excess buoyancy from the upper bridge part is added to the nodes beneath the pontoons. They are shown in Figure 5.16. Figure 5.16a shows the nodes with ballast for lower and upper buoyancy and Figure 5.16b shows the nodes where only the lower required ballast is added.

The choosing of nodes for the two ballast groups is done based on the line arrangement of the main tunnels and an approximation of the bridge parts from the Reinertsen Olav Olsen Group concept. It is assumed that the different parts making out the bridge span can be ballasted differently.

5.9.3 Flooded Pipes

As explained in Section 5.4 the bracing and connection shaft pipes are filled with water. The built in "flooded pipes" option in basic ocean data is not used to flood the pipes. This would flood all the pipes, including the main pipe. In stead, the flooding is modeled in the same manner as the ballast in the main pipes, with MASS21 elements. The element buoyancy is equal to the displaced fluid of the outside radius of the pipe, while the water ballast is added to flood the pipes.

The final unit mass is obtained by dividing the mass per meter by the number of nodes per meter.

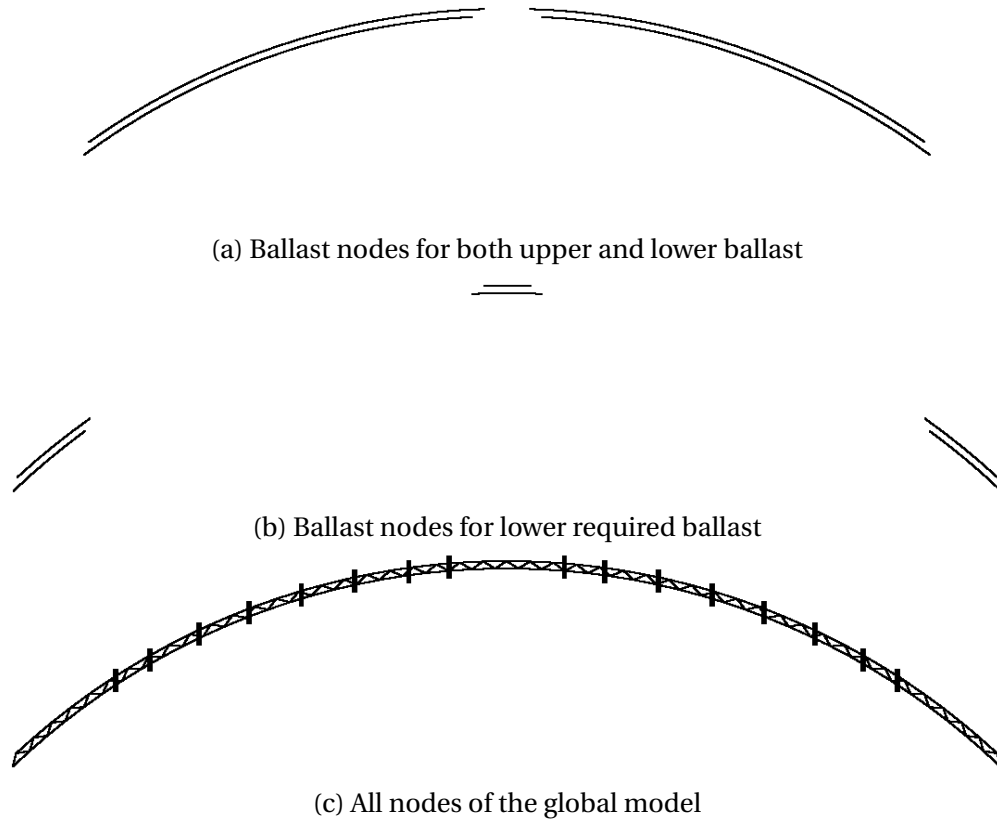


Figure 5.16: The ballast nodes of the main tunnel pipes

Table 5.9: Mass per meter for the flooded pipe ballast

Section	Flooding Area [m^2]	Water Density [kg/m^3]	Unit mass [tonnes/m]
Bracing	12.57	1025	≈ 12.9
Connection Shaft	38.5	1025	≈ 39.4

5.10 Buoyancy

5.10.1 Buoyancy Modeling

The buoyancy modeling is automatic with ocean loading. When setting the buoyancy factor to 1.0, the pipe and beam element buoyancy is automatically included in the model. The buoyancy is calculated from the displaced fluid of the elements, not the outer boundaries. When using a beam element which is hollow in the middle, the buoyancy will be smaller than for a pipe with the same radius. This is because the automatic `kflood` input value is 1 for hollow BEAM189 and BEAM289 elements. They are always flooded in ANSYS.

This is not an issue for the beam elements in the pontoon. They are not hollow, and has the right buoyancy.

5.10.2 Neutral Buoyancy

In order to obtain neutral buoyancy, the bridge is evaluated in two parts. The first part concerns the lower part, meaning the main tunnel pipes and the bracing pipes. By adding water and concrete slurry ballast, as explained in Section 5.9.1, the buoyancy of the main tunnels and the bracing pipes becomes equal to the gravitational force of the pipe structure and the ballast of both the main tunnels and the bracing pipes.

The neutral buoyancy draft for the pontoon is then calculated and used together with the other geometrical and material information to establish the value of the mean water level. This secures a neutrally buoyant bridge.

5.11 Added Mass - Hydrodynamic Added Mass with OCDA

The added mass for the model is a part of the OCDA-command explained in Section 5.8. It contains two values concerning added mass, Cay and Caz. Both values represent the ratio of added mass of the external fluid over the mass of the fluid displaced by the element cross section in y- and z-direction. This can be explained as the mass coefficient of the element cross section, given by (5.5). The added mass coefficient is found in Pettersen (2007, Appendix 1 - Added Mass Coefficients) for the right cross sections. For a circle the value is 1.0 in infinite fluid and non-oscillatory flow conditions.

$$C = \frac{A'}{A'_{circle}} \quad (5.5)$$

where:

test

The added mass represents the mass of the external fluid that moves with the beam in a dynamic analysis. It will have no effect on a static analysis of the model. This is the difference from the

added mass element, MASS21, which has an effect on statical analysis when an acceleration is present, such as the acceleration of gravity. The added mass input coefficient is different for the rectangular BEAM289 elements representing the pontoon and the circular PIPE289 elements representing the other parts of the SFT.

5.12 Material Properties

At this stage modeling of the geometrical and hydrodynamical aspects (ballast, buoyancy and added mass) have been addressed. The final stage is to create the material models and properties for the model. The materials used in the model are listed in Table 5.10 along with their properties. The material model used for both materials is linear elastic material with isotropic behavior.

Table 5.10: Material Properties

Material	Type	ρ [kg/m^3]	E [10^9 Pa]	ν [-]
Concrete	B55 M40	2400	38	0.2
Steel	Structural	7800	210	0.3
Pontoon Material	Undefined	-	3000	0.3

5.12.1 Concrete Properties

The concrete suggested by Reinertsen Olav Olsen Group in their study is B55 M40. From table 3.1 in *Eurocode 2: Design of concrete structures - Part 1-1: General rules and rules for buildings* the elasticity module for concrete strength class B55 is 38 GPa (Eur, 2004, Table 3.1).

The durability class of the concrete is M40. The durability class is a measurement of concrete deterioration concerning the steel reinforcement or the prestressing steel of the concrete. There are different exposure classes where the durability class M40 is a minimum. The exposure classes for durability class M40 are given in Table 5.11. They are found in the *Eurocode 2* in table NA.4.4N and NA.4.5N (Eur, 2004, Table NA.4.4N & NA.4.5N). Table 4.1 in the *Eurocode 2* gives a description of the environment and examples for each exposure class. An excerpt of relevant classes are listed in Table 5.11.

Table 5.11: Examples of exposure classes for durability class M40

Class	Description of environment:	Example of environment:
XD2	Wet, seldom dry	Exposure to industrial water with chlorides
XD3	Alternating between wet and dry	Part of bridge exposed to chloride water
XS2	Permanently submerged	Parts of marine structures
XS3	Tidal, splash and spray zones	Parts of marine structures

From the exposure classes in the table it is clear that the exposure class XD2 is the most suitable class.

5.12.2 Steel Properties

The steel used in the material model is conventional structural steel with a Young's modulus of 210 GPa, a density of 7800 kg/m^3 and a Poisson's ratio of 0.3. This steel is used for the shafts. The properties represent linear steel behavior.

The steel properties are different for the pontoons. The Young's modulus is a lot higher due to the layering of the pontoons. With a high modulus rigid body motions are secured. With a lower Young's modulus, the pontoon might bend due to the small thickness of the elements representing it.

5.12.3 Pontoon Material Properties

Because the pontoon is represented with a beam model, not a shell model with beam elemental stiffeners and girders, some extra considerations have to be made. The full weight of the pontoon has to be divided on the total volume to get the density of the material. In addition to this, the material Young's modulus has to be a lot higher than conventional structural steel. This is because the slenderness of the beam elements is really small. When this is combined with the length directional beam elements not being connected with each other, the Young's modulus needs to be higher so the pontoon will as undeformed as possible.

Chapter 6

Analyses

In this chapter, a description of the analyses performed are included. The sections labeled global analysis are analyses carried out for the global SFT model. The analyses concerning the pontoon are carried out in both Sesam and ANSYS Mechanical in order to verify the ocean modeling in ANSYS. The sections in this chapter are:

- Ansys Solving Limitations
- Mesh Analysis
- Pontoon Analysis
- Global Static Analysis
- Global Modal Analysis
- Global Harmonic Wave Response Analysis
- Global Irregular Wave Response Analysis

Discussions concerning the results are given in Chapter 7.

6.1 ANSYS Analysis Solving Limitations

This section describes how the ANSYS analyses are solved, concerning both the simultaneous use of multiple remote desktops to optimize time consumption and the issue of allocating memory for solving larger analyses.

6.1.1 Remote Desktops at the Department of Marine Technology, NTNU

The analysis done in ANSYS are carried out on different remote desktops managed by the Department of Marine Technology at NTNU. The remotes are available for all students and PhDs at the department. They are accessible through personal computers and allows for multiple analyses running simultaneously.

It can be time consuming to find out exactly how and if an analysis works. This means that a lot of the time spent working with the different analyses of the thesis, ends up with no results due to errors during solving etc. When such problems and challenges are solved a number of analyses might be ready for solving.

At such moments, all the remotes can be used to solve different aspects of the same problem, saving a lot of time. An example can be different pontoon configurations, where the pontoon can be solved for pure heave, pitch and roll motion, for different wave inputs. Each analysis is an independent analysis, and therefore needs its own run in ANSYS. By running all these analyses on different remotes, a lot of time is spared. At most, 8 remotes have been used simultaneously to carry out ANSYS analyses.

Another example can be a wave analysis of the global SFT model over a longer period of time. If memory limitations occur due to the size of the analysis and the analysis is terminated, a solution can be to only save certain time steps and not all. The issue is that an analysis with a time series often needs to run for a given amount of time in order to stabilize. By saving only certain steps, analysis can be run for a longer time span, extracting only certain steps on the way.

A problem with only extracting certain time steps, is the possibility of missing peaks in the re-

sponse. This is solved by doing the same analysis at different remote computers, sampling different time steps. Figure 6.1 shows a flow chart of how a spectrum analysis with an end time of 300 seconds is divided between 7 remote desktops.

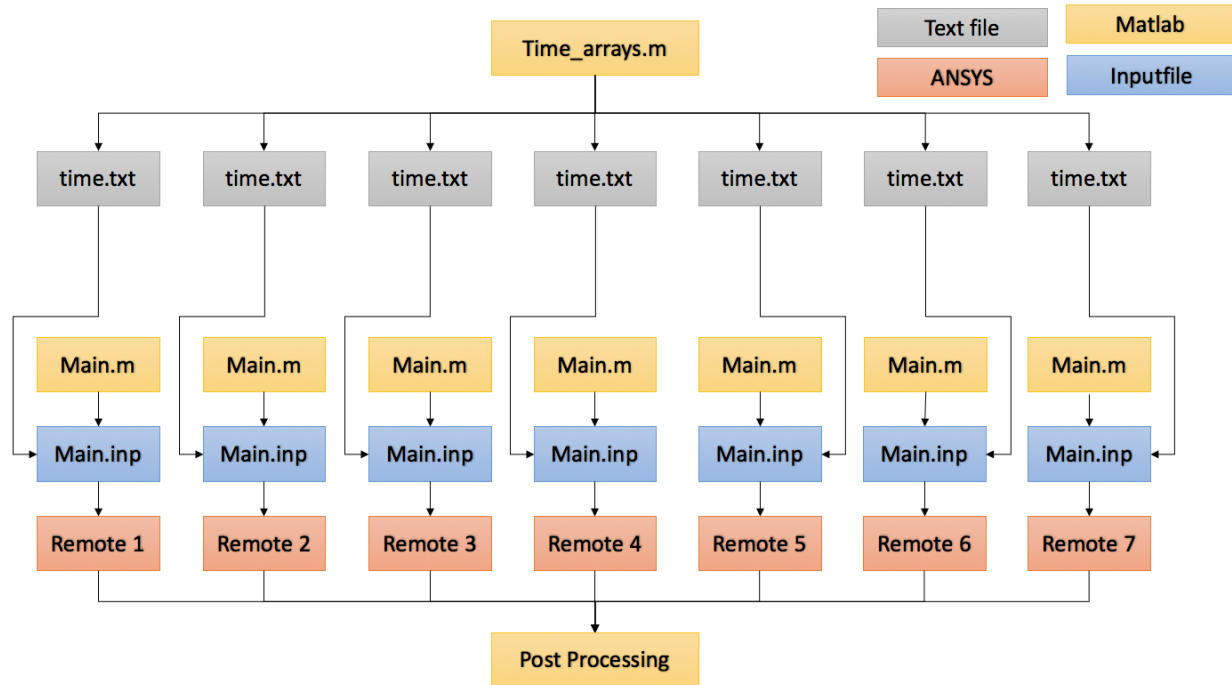


Figure 6.1: Flow chart describing how an analysis can be split into subanalyses on several computers

Each analysis is run separately, but uses an individual time array, *time.txt*, which decides the sample time for storing results. After each analysis is completed, all the information is gathered in a post processing MATLAB script where the complete analysis with all sampled time steps is available.

6.2 Mesh Analysis

The mesh convergence analysis is performed in order to establish whether the model converges and the to obtain the required mesh size for a sufficient result. The global model has seven different mesh size inputs, all listed below:

- Main element mesh size - The main tunnel pipes
- Bracing element mesh size - The bracing elements between the main pipes
- Connection shaft element mesh size - The pipes between the main pipes and pontoons
- Pontoon support element mesh size - The pontoon support element mesh size
- Main pontoon element mesh size - The main beam elements of the pontoons
- Transverse mesh size - Number of transverse sections
- Radial mesh size - Number of sections in radial direction

The two last points in the list can be seen in Figure 6.2b. There are three transverse and 16 radially meshed sections in this specific pipe mesh. The middle transverse section is wide compared to the outer and inner sections.

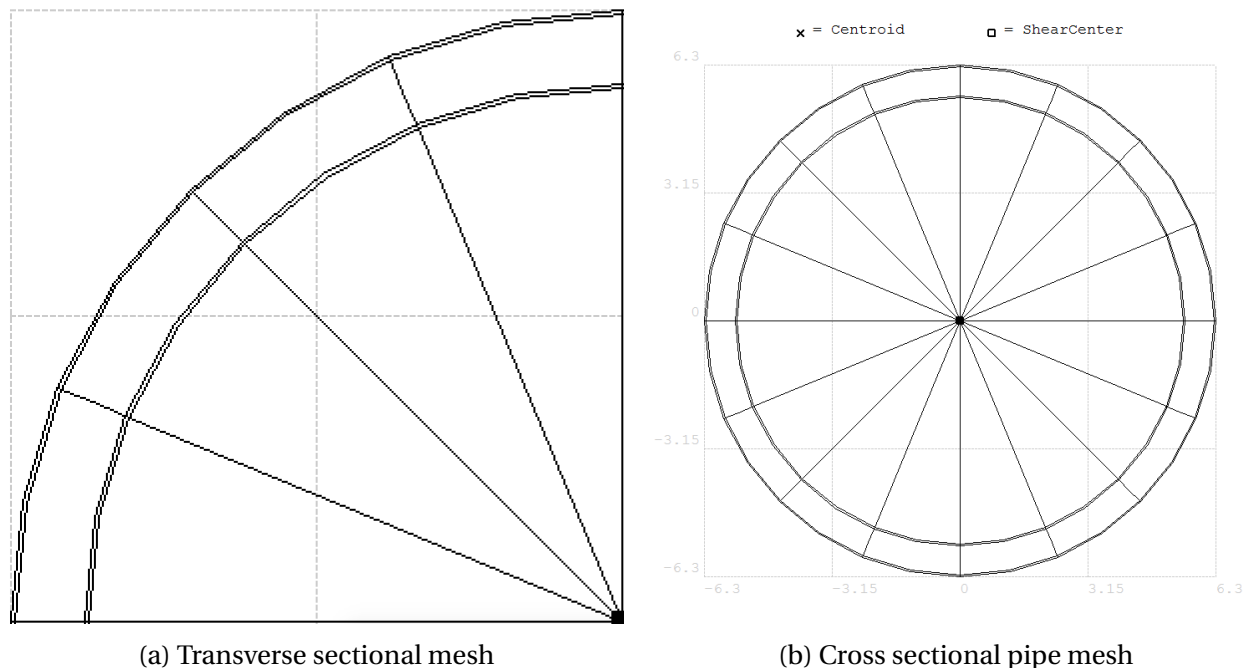


Figure 6.2: Mesh attributes for the pipe cross sections

When talking about global mesh sizes in the thesis, these are the ones being discussed. The mesh results of the mesh analysis is mainly used in early analyses to save time making controls

of the results. When the final analyses are completed, the mesh refinement will be smaller in order to obtain as correct results as possible.

6.2.1 Decreasing Mesh Size Analysis

In the first part of the analysis, the mesh size is set to decrease while sampling the global maximum and minimum vertical displacement. All mesh sizes will have the same magnitude in order to establish a basic understanding of when the global analysis starts to converge. The unit of the mesh size is elemental length, in meter per element. The size first decreases from 30 to 0.2 meters per element with a step of 0.1. From 0.2 it decreases with a step size of 0.01 to 0.12 meters per element.

The goal of the analysis is to establish the value of global maximum and minimum vertical displacement and compare this to computational time. After having established a the value for the converging displacement, an optimization process can be carried out. This process will give different mesh sizes for the various parts of the bridge, within a required error rate of the original displacement value.

6.2.2 Mesh Optimization Analysis using Particle Swarm Optimization

The mesh convergence analysis is carried out with a particle swarm optimization (PSO), see Kennedy and Eberhart (1995). The PSO used for finding the optimal mesh sizes in this thesis is a modified version of a previously written MATLAB implementation (Ehlers, 2012). The implementation uses an object and constraint, set by the user in order to find feasible solutions. The object, which is what the process is optimizing for, is the time used for completing a static analysis. The constraint, is a 10 % vertical displacement deviation of what is considered the final displacement. Final displacement is the displacement for the structure when the mesh size is very small, meaning that the results are correct in consideration to the modeling of the structure.

The goal of the optimization process is to find the optimal global mesh sizes for the different parts of the bridge. The sets of different mesh sizes used in the optimization process are pre-

sented in Table 6.1. The mesh size sets for the model has approximately $1.98 \cdot 10^{12}$ possible global mesh size combinations.

Table 6.1: Feasible mesh size sets for PSO

Model Part	Feasible mesh size sets [meter/element]
Main Pipes	[0.1:0.05:2.0 , 2.1:0.1:10.0 , 11:1.0:15 , 20:5.0:30]
Bracing Pipe	[0.1:0.05:2.0 , 2.1:0.1:10.0 , 11:1.0:15 , 20:5.0:30]
Connection Shaft	[0.1:0.05:2.0 , 2.1:0.1:10.0 , 11:1.0:15 , 20:5.0:30]
Pontoon support lines	[0.1:0.05:2.0 , 2.1:0.1:10.0 , 11:1.0:15 , 20:5.0:30]
Pontoon lines	[0.1:0.05:2.0 , 2.1:0.1:10.0 , 11:1.0:15 , 20:5.0:30]
Transverse circular mesh	[3:2:9]
Radial circular mesh	[8:8:120]

The other PSO input values are listed in Table 6.2. The swarm size is the number of particles in each generation. The number of feasible solutions for each generation is saved while the PSO find the best results. Best known results are used in order to find even better results as the PSO develops.

Table 6.2: PSO inputs

Swarm Size	40
Generations/iterations	10
Number of Analyses	400

For further information about the PSO, see Kennedy and Eberhart (1995) and Ehlers (2012).

6.3 Pontoon Analysis

A pontoon analysis is carried out in both ANSYS and Wadam. The Wadam analysis is done in order to compare the characteristics of the simplified and final pontoon geometry. The results for the final pontoon geometry are implemented in the global SFT model in ANSYS. The simplified Wadam pontoon results are used as a comparison for the pontoon modeling in ANSYS.

A harmonic analysis is run in both Wadam and ANSYS. The roll motion are tested for beam waves and the pitch motion for head waves. Heave is analysed in both directions. The periods and frequencies for Wadam and ANSYS analysis are listed in Table 6.3.

Table 6.3: Wave characteristics

Software	T [s]	f [1/s]	w [$2\pi/s$]
ANSYS	$\pi - 628$	$1.59 \cdot 10^{-3} - 1/\pi$	
Wadam	$\pi - 628$		0.01 - 2.0

6.3.1 GeniE Modeling - Mass and Panel Model

In order to run an analysis in HydroD, the mass and panel model is created in GeniE. The mass of the mass model is equal to the pontoon mean draught times the water plane area. The draught for both pontoon geometries is 4 meters, which is the assumed mean draught of the pontoons when mounted on the SFT.

The panel model is created for the wet areas of the pontoon. Both the simplified and final pontoon mass and panel models are shown in Figures 6.3 and 6.4. The panel model is saved with filename T1.FEM and the mass model is saved with filename T3.FEM. This is the correct format for the panel and mass model files in order to upload them in a HydroD workspace, where the analysis of the pontoons are performed.

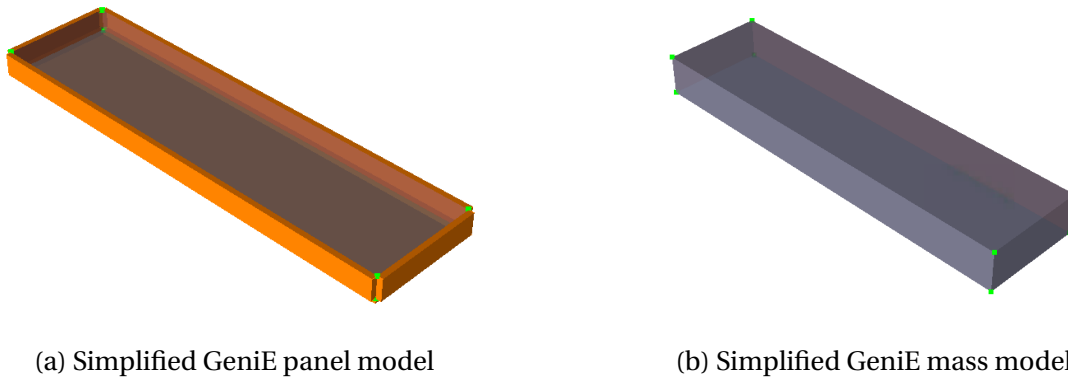


Figure 6.3: Simplified GeniE pontoon modeling

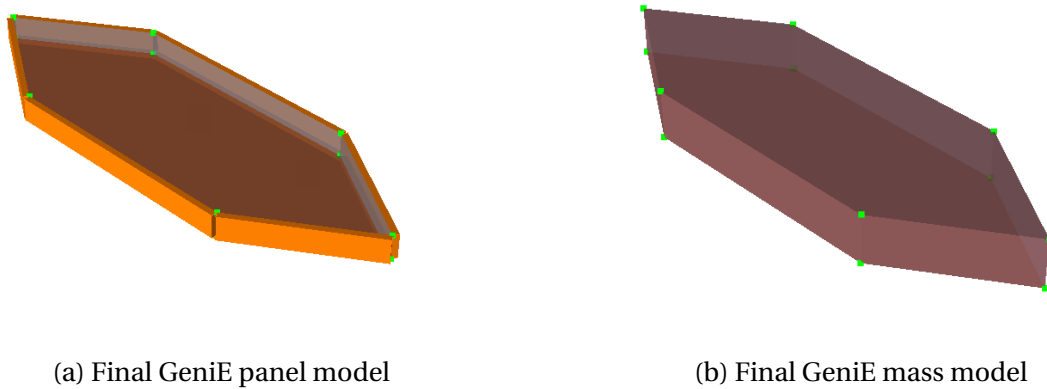


Figure 6.4: Final GeniE pontoon modeling

6.3.1.1 HydroD - Pontoon Analysis

The analyses of the pontoons are done in HydroD for harmonic wave inputs. A wizard is used in order to run the analysis, with an element panel model. The analyses are done for beam and head waves, with a frequency span from 0.01 - 2.0 rad/s. The span covers the most interesting periods and frequencies. The analysis is done with a mean water level at 4 meters, equal to the draught, a water depth of 700 meters and a water density of 1015 kg/m^3 . The simplified panel model is shown in Figure 6.5a. The part of the mass model not being submerged is shown in Figure 6.5b.

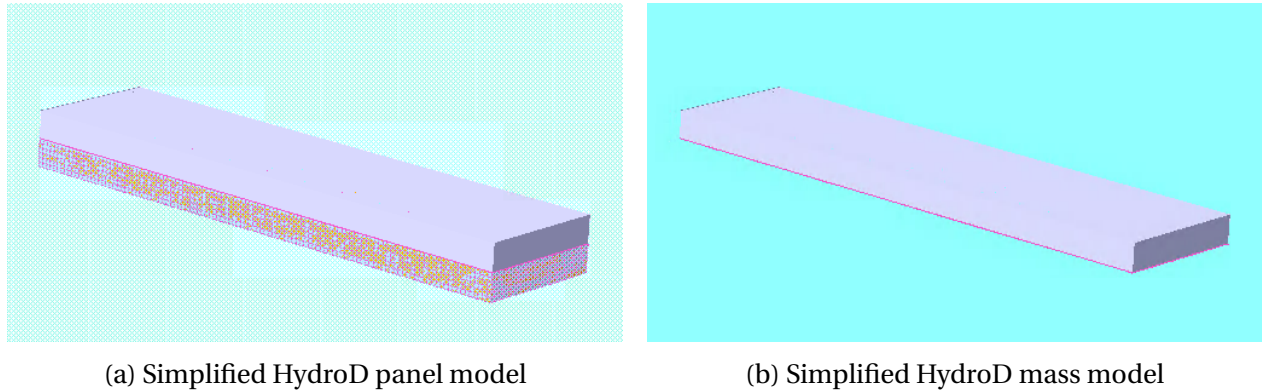


Figure 6.5: Simplified HydroD pontoon modeling

6.3.2 ANSYS Pontoon Analysis

The pontoon in this analysis is modeled in the same way as the pontoon in the global model. It is divided into horizontal and vertical layers with BEAM289 elements meshed on these lines. The support lines on the sides are also BEAM289 elements. Figure 6.6 shows the short and long sides of the pontoon together with internal elemental beam lines. All eight corner nodes of the pontoon are examined when analyzing the pontoon. This gives the maximum and minimum displacement for the pontoon when the harmonic wave loading is acting on the body. The numbering for the nodes used in the post process analysis is shown in Figure 6.6.

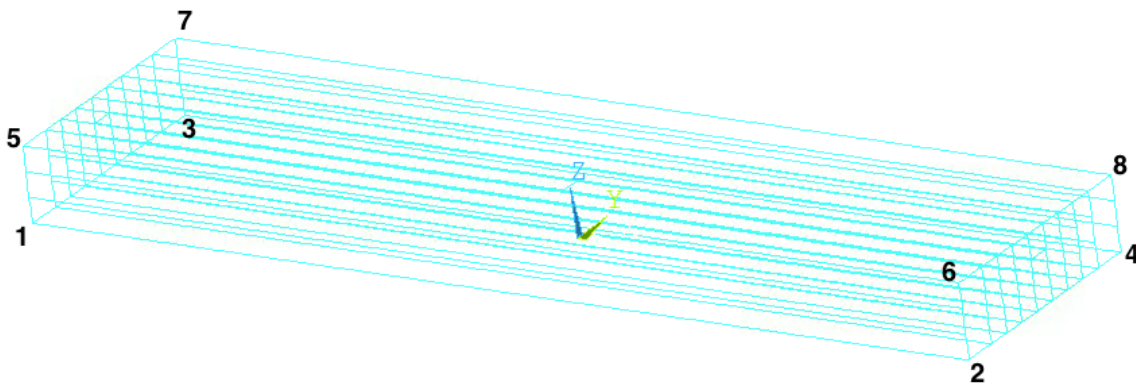
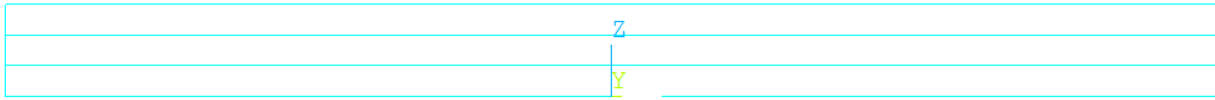
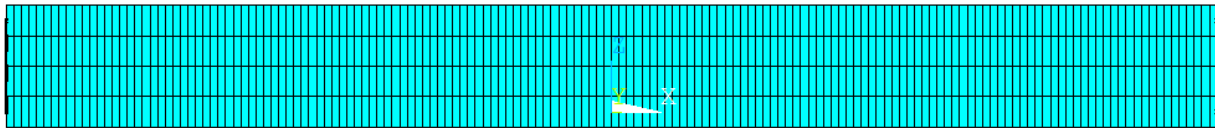


Figure 6.6: ANSYS elemental pontoon lines

The Young's Modulus for the support lines on the sides is very high in order to maintain small deformations in the pontoon geometry. This is done since the rigid body motions of the pontoon are of interest. The elemental line model and elemental display model is shown in Figure 6.7 and Figure 6.8. The pontoon floats with a draught of 4 meters.

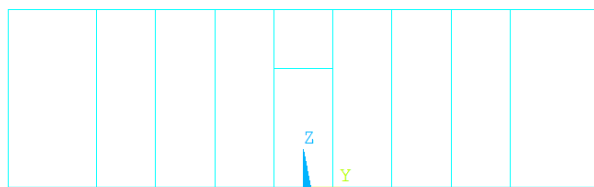


(a) Element lines

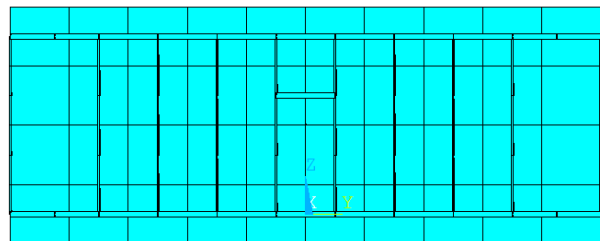


(b) Elemental display

Figure 6.7: Broad side view of ANSYS pontoon



(a) Element lines



(b) Elemental display

Figure 6.8: Short side view of ANSYS pontoon

6.3.2.1 Heave Motion Analysis

In order to analyze the pontoon in pure heave motion, the pontoon ends are held for translation in global Y- and X-direction. These are marked with red coloring and can be seen in Figure 6.9. The heave springs, in green, are connected to each corner of the pontoon and held in all translations and rotations at the ends.

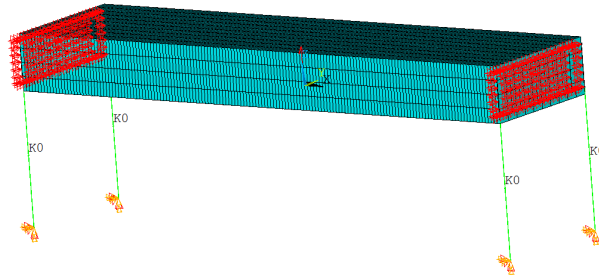


Figure 6.9: Pontoon with boundary conditions and springs assimilating heave motion

Due to the material Young's modulus and the boundary conditions, all pontoon nodes have approximately the same displacement in Z-direction when running harmonic wave analysis.

6.3.2.2 Roll Motion Analysis

The roll pontoon configuration is held against translation in X- and Y-direction at the end node of the longitudinal center line of the pontoon. The body rolls about this line. The roll springs are connected at this node and held against all translations and rotations. This can be seen in Figure 6.10

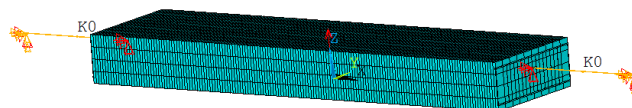


Figure 6.10: Pontoon with boundary conditions and springs assimilating roll motion

6.3.2.3 Pitch Motion Analysis

The pitch pontoon configuration is shown in Figure 6.11. The nodes where the springs are connected, marked in red, are held against all translations. They are free to rotate in all directions. This way, the pontoon will only be able to rotate around these points, assimilating pure pitch motion.

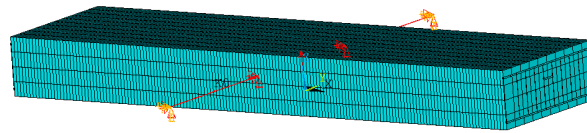


Figure 6.11: Pontoon with boundary conditions and springs assimilating pitch motion

6.3.3 ANSYS Pontoon RAOs

The ANSYS response amplitude operators (RAOs) for the pontoon are created by running an analysis with a harmonic Airy wave. The analysis is carried out for all the configurations described in Section 6.3.2.1, 6.3.2.2 and 6.3.2.3. The wave has an amplitude of 1 meter for all the configurations. The wave analyses are carried out with a wave frequency from 0.05 to 2.0 rad/s with a stepsize of 0.025 rad/s.

The direction set for the pontoons are given in Table 6.4

Table 6.4: Wave direction sets for ANSYS pontoon analyses

Motion	Heave	Roll	Pitch
Direction set 1	90 deg	90 deg	-
Direction set 2	0 deg	-	0 deg

Direction set 1, 90 degrees, means beam waves (wave hitting the long side of the pontoon) and 0 degrees means head wave (short side of the pontoon).

The results from the analyses are presented in RAO plots, where the displacement at corner number 2 in Figure 6.6 is post processed. The heave response amplitude operator has the unit

meters, while it is given in radians for the rotations, roll and pitch. The results from this section is presented in 7.2.2

6.4 Static Analysis

The static analyses are carried out for three different water levels. The water levels are given in Table 6.5, in form of tidal change from neutral position. The static analysis are carried out in order to check the criteria of neutral buoyancy. Measurements for criteria is displacement. Global X-, Y- and Z-displacement is also checked for maximum and minimum tidal change.

Table 6.5: Water levels expressed in tidal change

Water level	Max	Mean	Min
Amplitude [m]	1.85	0	-1.58

When running the static analyses, ocean loads such as waves are not taken into account. Only hydrostatic forces are included.

6.5 Modal Analysis

The modal analysis is carried out in order to obtain the mode shapes, the eigenfrequencies and directional mode mass participation. The mode mass participation is used to calculate the Rayleigh damping coefficients for the global model. The underlying theory for solving modal analysis is described in Chapter 4.

6.5.1 Eigenfrequency and Mode Shape Analysis

As explained in Section 4.3.1 about the general eigenvalue problem, the system is assumed undamped and under no loading. This leads to Equation 6.1, which is solved for the natural frequencies of the system.

$$(\mathbf{K} - \omega^2 \mathbf{M}) = 0 \quad (6.1)$$

The natural frequencies are of interest in relation to external loading and the global response this causes. The magnitude of the global response might be too high if the external loading frequency is in the range of the mode natural frequencies. This is especially important for the modes with high effective mass participation.

Load amplitude and frequency, for loads such as wave loading and ViV, should be checked towards the eigenfrequencies of the system in order to confirm whether the design is feasible or not.

Block Lanczos mode-extraction method is used for the modal analysis. It uses the sparse matrix solver. No start or end frequency for the solver is applied, meaning that the n-number of eigenmodes from the analysis, are the first n-modes (Chowdhury and Dasgupta, 2003).

6.5.2 Effective Mass Participation Analysis

The effective mass participation analysis is performed in order to estimate how many significant modes are needed in order to calculate the Rayleigh damping coefficients. As explained in Section 4.3.2 from the reference Chowdhury and Dasgupta (2003), the number of significant modes required for the coefficient estimation is 2.5 multiplied by m modes. The m number of modes needs to include approximately 95% of the mass participation.

For each mode the directional mass participation is written to a file and post processed in MATLAB. The mass is summarized continuously. When the summarized requested participating mass for all directions is satisfied, the number of significant modes, m is known. The process becomes an iteration process in order to include enough significant modes in the analysis. A final analysis needs to be carried out with the required number of $2.5m$ in order to estimate the Rayleigh damping coefficients.

6.5.3 Rayleigh Damping Coefficient Calculations

When the number of significant modes has been established, the Rayleigh damping coefficients can be estimated. A selected linear damping ratio for the first and m^{th} mode is used to calculate a linear damping ratio curve for the system. This is compared to three different damping ratio curves calculated from the α and β coefficients which have been estimated from three chosen datasets. The damping ratio curves are calculated from Equation 6.2.

$$\zeta_i = \frac{\alpha}{2\omega_i} + \frac{\beta\omega_i}{2} \quad (6.2)$$

The procedure has been described to detail in Section 4.3.2

6.6 Global Harmonic Wave Response Analysis

This section contains a description of the analysis scheme for the harmonic wave response analysis. The input wave height of 4.85 meters, is estimated from the JONSWAP spectrum significant wave height. The procedure is described in Section 4.4.

6.6.1 ANSYS Harmonic Wave Parameters

The global harmonic wave analysis will be carried out for the bridge with one estimated wave height and a number of different wave periods. The wave height of 4.85 meters, is estimated from a known significant wave height, made available through the Reinertsen Olav Olsen Group study, (Group, 2013, p. 26). The procedure for estimating the wave height is given in Section 4.4.

The periods for the harmonic wave response analyses are given in Table 6.6, showing the different time dependent solving parameters. The general idea is that the periods vary around the JONSWAP peak period of 4.8 seconds, which also is gathered from the Reinertsen Olav Olsen Group study.

Table 6.6: Wave parameter and time input for harmonic wave response analysis

Period [s]	Sample start time [s]	Analysis end Time [s]	Sampled points [no.]	Periods
4.50	45.0	94.0	99	11
4.75	45.0	98.0	107	11
5.00	50.0	99.0	99	10
5.25	50.0	99.0	99	9
5.50	49.5	98.0	98	9
5.75	49.5	98.0	98	8
6.00	52.5	97.0	90	7
6.25	48.0	101.0	107	8
6.50	49.5	94.5	91	7
6.75	45.5	96.0	102	7

The number of sampled points for each wave period is the number of steps between the start and end time, with a chosen step size. The step size for these analyses are 0.5 seconds. The start sample time is the first time step when results are saved for post processing. In order for the analysis results to stabilize, the analyses need to run for a certain time. This time is typically

equal to the length of a couple of wave periods. This part of the analysis is therefore not of interest and not stored due to memory restrictions for saving results. Whether the start sample time is too early or not, can be observed from the cyclic behavior of the results compared to the wave period in the result section, Section 7.5. If the results seem to not have stabilized yet, a new analysis with a later start sampling time has to be carried out.

From Table 6.6, one can see that the lowest period for the harmonic wave is 4.5 seconds, even though the period is supposed to be varied around the peak period of 4.8 seconds. The reason for the wave period not being smaller, is the wave breaking criteria for waves at deep water, shown in Equation 6.3.

$$\frac{2\zeta_a}{\lambda} \leq \frac{1}{7} \quad (6.3)$$

where:

ζ_a = Wave amplitude in m

λ = Wave length in m

The minimum wave period for the breaking wave criteria is 4.65s, but a wave period of 4.5 second is included in the analysis. It is not far from the minimum wave period, and it also secures values on both sides of the spectral peak period.

The longest wave period for the maximum wave height is 6.75 seconds. This is, together with the first wave period, considered enough coverage around the spectral peak period.

6.6.2 Harmonic Wave Analysis

The goal of the harmonic wave analysis is to first find the worst period of the set shown in Table 6.6. This is done by considering the maximum global rotations, displacements, stresses and moments for each period over the analysis time. The period with the highest response is investigated over its whole timespan to find the maximum responses along the bridge. The items of interest will be the global maximum moment along the main span of the bridge, especially focusing on the main tunnels and the bracing elements in between.

When the results from the harmonic wave analysis with the highest responses have been obtained, a comparison with the results from the irregular analysis can be carried out.

6.7 Global Irregular Wave Response Analysis

The main objectives when carrying out the global irregular analysis is to find the maximum responses for the bridge during the whole time span. Considering the fact that the maximum harmonic wave parameters are estimated based on the irregular JONSWAP spectrum parameters, the responses from the irregular and harmonic analysis should be compared. In order to compare the two results, the spectrum analysis needs to run for 3 hours, or 10800 seconds. This is because the harmonic maximum wave height is estimated based on the 50 year return period wave for a 3-hour sea state. An analysis of this length has proven to be impossible to complete due to memory limitations, and therefore other measures has to be taken in order to secure an irregular result for comparison.

The parameters for the JONSWAP spectrum used for the irregular analysis, are given in Table 6.7.

Table 6.7: 50 year return period spectrum parameters for wind generated waves

Parameter	Magnitude
H_s [m]	2.14
T_p [s]	4.8
γ [-]	3.3

The sampled responses are the same as for the harmonic analysis, in order to be able to compare results.

6.7.1 Remote Desktop Simultaneous Analyses and Time Consumption

As explained in Section 6.1.1, concerning running multiple analysis on different remote desktops simultaneously, the JONSWAP spectrum analysis needs to be split into multiple analyses. This is due to memory insufficiency when solving for a longer simulated time with a small time step. The spectrum analysis was run for a total of 300 seconds of simulated time. The analysis was split between 5 remotes, where each remote desktop sampled 1/5 of the time steps. The total number of sampled time steps from all sub-analyses are 520. The rest of the time input is shown in Table 6.8.

Table 6.8: ANSYSinput parameters for JONSWAP spectrum response analysis

Start time [s]	End time [s]	Time step [s]	Time Steps [no.]	Remotes [no.]
40	300	0.5	520	7

6.7.2 Expected Maximum Response

The maximum responses sampled from the 300 second long irregular analysis can not be compared directly to the results from the harmonic analysis. They are used to estimate the expected maximum value for the responses by using a Gumbel maximum distribution. The procedure of the estimation is given in Section 4.5. The standard deviation and mean for the responses are estimated for the 300 second irregular analysis. These parameters are assumed to also describe the standard deviation and mean responses for a three hour long irregular process. By also using the number of zero-mean-crossings for the responses and multiplying it by the number of 300 second analysis within three hours, the expected maximum can be calculated with Equation 6.4.

$$E[z_{max}] = \sigma_r \left[\left(\sqrt{2 \ln(N_{3h})} + \frac{0.5772}{\sqrt{2 \ln(N_{3h})}} \right) \right] + \mu \quad (6.4)$$

where:

N_{3h} = The number of mean-zero-crossings for a three hour process, based on $N_{3h} = N_{300s} \cdot \frac{10800}{260}$
 N_{300s} = The number of mean-zero-crossings for the 300 second analysis.

The number of mean-zero-crossings for the 300 second analysis is multiplied with 10800/260 because there are 10800 seconds in three hours, and the sampled time for the harmonic analysis is the start sample time (40) subtracted from the end time (300).

These expected maximum responses are the ones which can be used as a comparison for the maximum harmonic responses.

Chapter 7

Results and Description

This chapter contains the results of the analyses described in Chapter 6. The results are described in order to have a final discussion in Chapter 8. The parts of the analysis results which are of less importance, but still a part of the final conclusion or discussion, are all given in its belonging appendices. The sections concerning global results are, as for Chapter 6, results for the submerged floating tunnel. This includes the mesh analysis results. The result sections are:

- Mesh Results
- Pontoon Analysis Results
- Global Static Results
- Global Modal Analysis Results
- Global Harmonic Wave Analysis Results
- Global Irregular Wave Analysis Results

7.1 Mesh Convergence Results

7.1.1 Decreasing Mesh Size Results

Figure 7.1 shows the results of the mesh convergence analysis. The maximum and minimum displacement is shown by the blue and red line, respectively. When reaching a global mesh size of approximately 2.0 meters per element, meaning an element mesh size of 2.0 meters for all elements, the displacement starts to stabilize and converge.

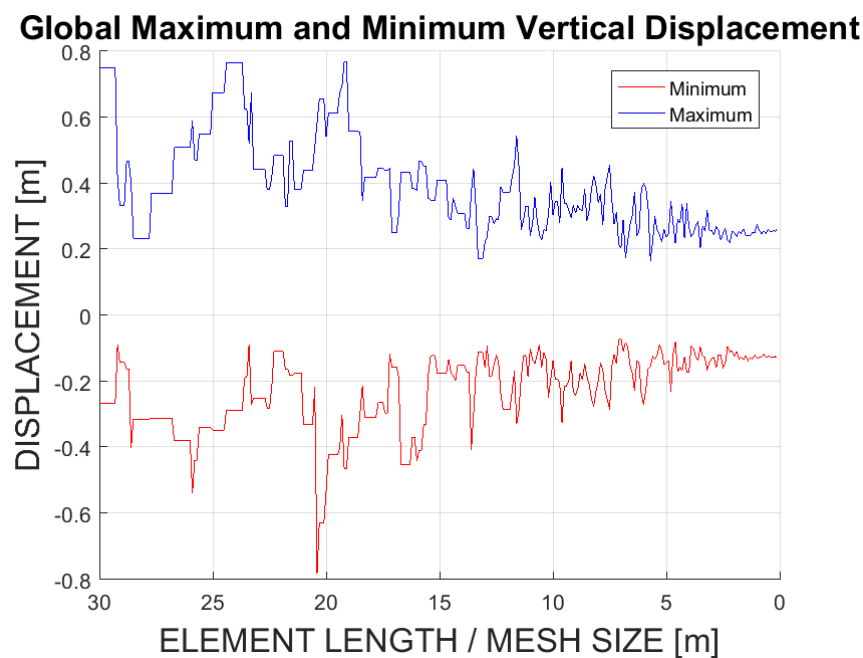


Figure 7.1: Maximum and minimum vertical displacement for decreasing mesh size

When comparing Figure 7.1 and 7.2 with each other, it is clear that around convergence (mesh size $\approx 2.0\text{m}$) the computational time increases rapidly. When looking at computational time, it is important to have in mind that all analysis are carried out on NTNUs remote desktop computers. This means that different computers have different specifications and the time can vary. The computer is also used by other people at different times, affecting the results, due to uneven CPU and memory usage. The real importance of Figure 7.2 is the relationship between time and mesh size, not necessarily the amount of time spent completing each analysis.

The converging max and minimum results for the analysis is listed in Table 7.1.

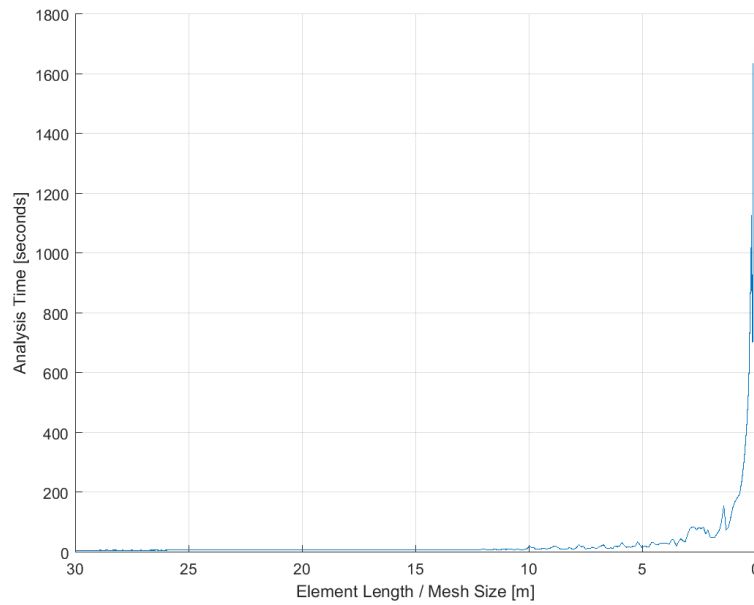


Figure 7.2: Static analysis completion time vs mesh size for global model

Table 7.1: Converged maximum and minimum displacement

Displacement	Magnitude
Max [m]	≈ 0.23
Min [m]	≈ -0.17

When comparing the graphs for time consumption with the converging global mesh size, it is clear that it is unreasonable running analyses with the smallest mesh size. What is important to have in mind, is that the time consumption shown in Figure 7.2 is the time used to complete a static analysis. In practice, this means one load step. When solving time dependent analyses with for example harmonic or irregular wave loading, the time consumption for the static analysis would have to be multiplied by the number of time steps in an analysis. The time consumption for each step would of course vary, but it gives a good indication of how long the total computational time for one analysis would become.

After these considerations, a global element mesh size of 2 meters per element is chosen for the global SFT ANSYS analyses. The size of 2 meters is used as long as the wave parameters of the analyses are in compliance with the mesh size, according to ANSYS. ANSYS has one restriction concerning the relationship between harmonic wave length and horizontal element mesh size

length for the elements in the water surface. The mesh size length can not be longer than the wavelength/20, described by Equation 7.1.

$$\delta < \frac{\lambda}{20} = \frac{gT^2}{2\pi} \frac{1}{20} \quad (7.1)$$

where:

δ = Maximum mesh length for horizontal elements in the water surface in meters

λ = Harmonic wave length in meters

T = Harmonic wave period in seconds

If the maximum mesh length for the elements in the water surface is smaller than the global mesh size, 2.0 meters per element, the required mesh size will be calculated for each new harmonic mesh size.

7.1.2 PSO Results

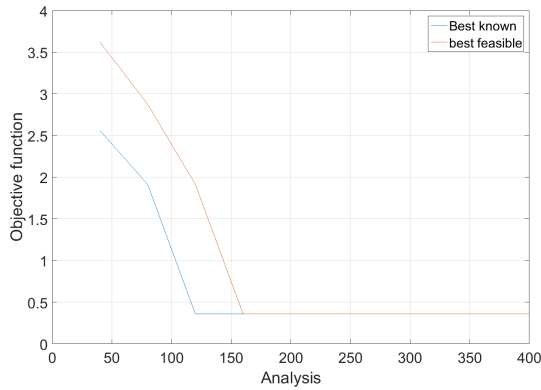
The results from the PSO process are given in Table 7.2. This is an individual mesh given in meters per element for all the parts of the bridge.

Table 7.2: Mesh size results

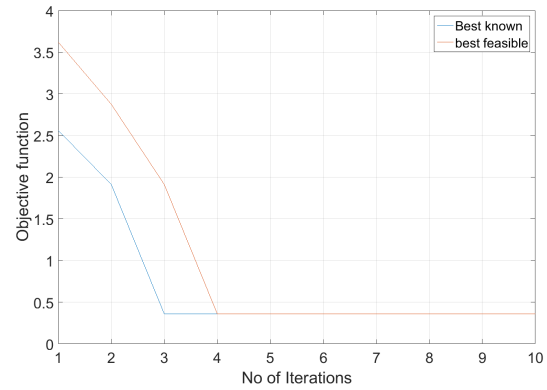
Model Part	Mesh Size [m]
Main Pipes	2.7
Bracing Pipe	3.6
Connection Shaft	18.5
Pontoon support lines	10.5
Pontoon lines	11.0
Transverse circular mesh	3
Radial circular mesh	8

The graphs in Figure 7.3 shows the objective development, as explained in Section 6.2.2. The x-axis shows the number of analysis or the number of iterations. The fastest time with a feasible solution is shown in the lines. The *best known* shows the fastest time the problem has been solved, but not within the requirements of an approved solution. The *best feasible* shows the fastest solution time with a feasible solution. The best known solution is found after 160 analy-

sis, or at the end of the fourth iteration. As explained in Section 6.2.2, one iteration has a number of analysis equal to the swarm size set by the user of the PSO.



(a) Analysis vs the PSO objective, time



(b) Number of iterations vs PSO objective, time

Figure 7.3: PSO results

With the optimized mesh size, analysis can be completed within a small time window. This allows for model analysis testing with different ANSYS inputs in order to see whether an analysis is successful or not. When it is clear that an analysis is running the right way, finer mesh can be used to obtain the final results.

7.2 Pontoon Analysis Results

The results of the pontoon analyses are included in this section. The pontoon is analyzed in heave, pitch and roll. The roll analysis is performed in beam sea (90 degrees wave direction), while the pitch analysis is carried out in head sea (0 degrees wave direction). The heave analysis is completed for both directions. Analyses are done in both WADAM and ANSYS in order to compare results and verify the ANSYS representation of the pontoon for further use in the global SFT model.

7.2.1 WADAM Pontoon Results

The WADAM results for both the simplified and final pontoon geometry are presented below. This is in order to compare the two geometries to each other, to use the final model results in the complete SFT model and to compare the simplified results with the simplified ANSYS pontoon representation. The plots are made in MATLAB, with values from WADAM.

7.2.1.1 Restoring Coefficients

The restoring coefficients from Wadam for both the final and simplified geometry are given in Table 7.3. The results for restoring in heave are a bit different due to the water plane area being a bit smaller for the final pontoon geometry. Roll restoring is higher for the final pontoon due to a width of 26 compared to 20 meters for the simplified pontoon. The lack in fullness at the end does not change the outcome of which pontoon has the most roll restoring. This does on the other hand influence the pitch restoring coefficient, which is higher for the square water plane area of the simplified pontoon.

Table 7.3: Pontoon restoring coefficients

Coefficients	Heave [N/m]	Roll [N/rad]	Pitch [N/rad]
Simplified Geometry	$1.59 \cdot 10^7$	$5.31 \cdot 10^8$	$8.50 \cdot 10^9$
Final Geometry	$1.55 \cdot 10^7$	$6.05 \cdot 10^8$	$5.05 \cdot 10^9$

Despite the fact that the pointy end of the final pontoon gives less restoring in pitch, its advantage of less drag and resistance, makes it the better choice for the submerged floating tunnel.

7.2.1.2 WADAM RAOs - Peak Frequencies and Response

This subsection contains the RAO plots for the simplified and final pontoon geometries. The final geometry is represented by a blue line, while the simplified geometry is represented by a red line in the plots. The peak frequencies for the different RAOs are given in Table 7.4 and 7.5. Amplitude is given with each RAO plot.

Table 7.4: Peak response frequencies for head sea

Motion	Heave [rad/s]	Pitch [rad/s]
Simplified	0.99	0.77
Final	NaN	0.84

Table 7.5: Peak response frequencies for beam sea

Motion	Heave [rad/s]	Roll [rad/s]
Simplified pontoon	0.93	0.82
Final pontoon	0.84	0.84

Heave RAO - Head Sea:

Figure 7.4 shows heave motion for head waves with a wave amplitude of 1 meter. The simplified pontoon has a peak at approximately 1 rad/s or a period of 2π . The final pontoon experience no such peaks. The peak at ≈ 1.5 rad/s is due to a numerical error in Wadam. In relationship to the heave restoring coefficient and potential damping, the motion for the simplified geometry is smaller than for the final geometry, with increasing frequency. The pontoon has an amplitude of 1 for small frequency waves/high period waves. This is correct for free floating structures, which motion follows the waves with long periods compared to geometrical length in the wave direction.

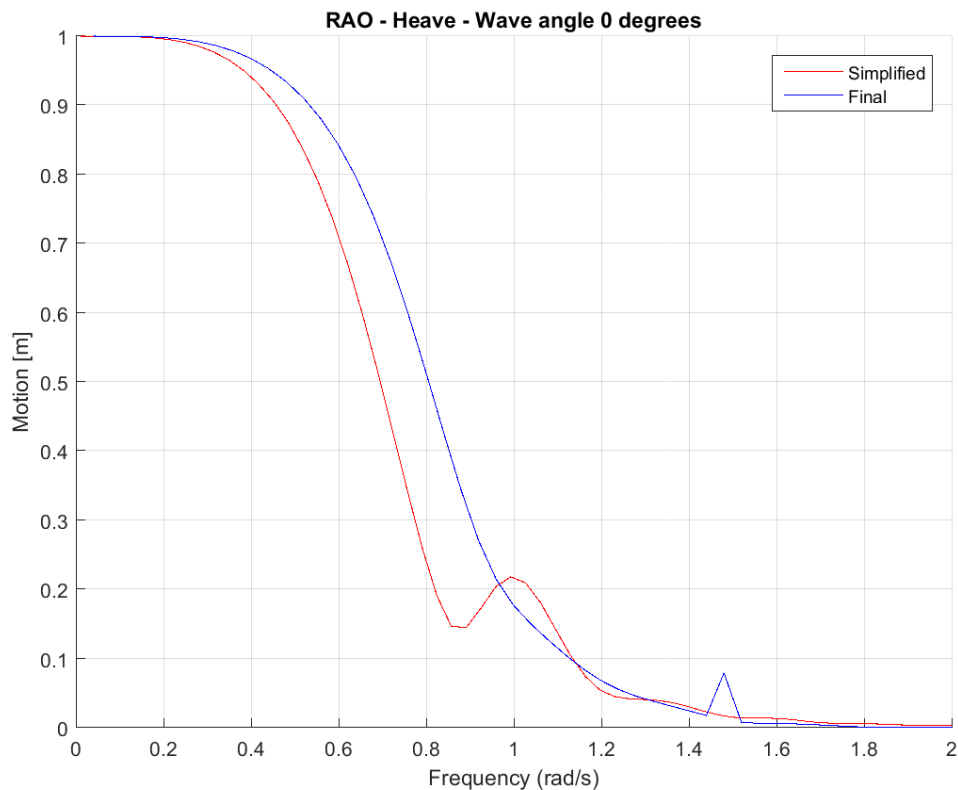


Figure 7.4: Wadam heave RAO for simplified and final pontoon, head sea

Table 7.6: Heave head sea peak period/frequency and amplitude for unit wave height

Pontoon geometry	Freq [rad/s]	Period [s]	Amplitude [m]
Simplified	0.99	6.35	0.218
Final	-	-	-

Heave RAO - Beam Sea:

The heave RAO for beam sea (90 degrees wave angle) is given in Figure 7.5. The peak period/frequency and amplitude is given in Table 7.7. The final pontoon has less motion than the simplified, due to a bigger width. The peak at ≈ 1.5 rad/s is also due to a numeric mistake in the Wadam software. The amplitude starts at 1, as to be expected for both pontoons. It increases around a wave frequency of 0.7-1.1, hitting their natural frequencies.

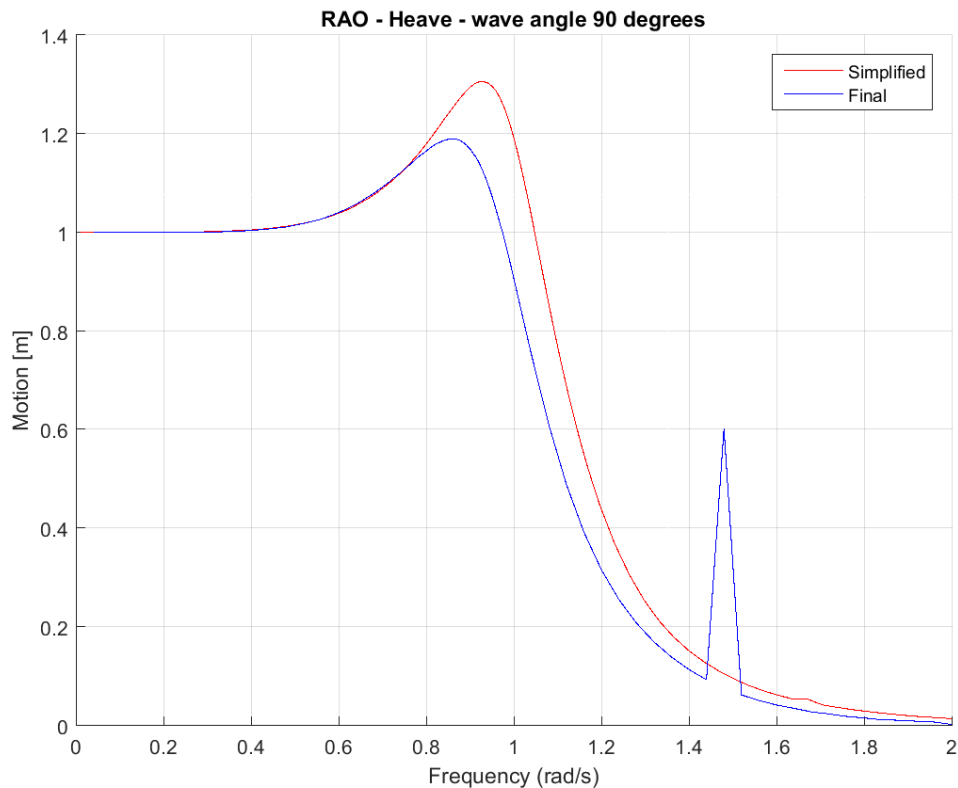


Figure 7.5: Wadam Heave RAO for simplified and final pontoon, Beam Sea

Table 7.7: Heave beam sea peak period/frequency and amplitude for unit wave height

Pontoon geometry	Freq [rad/s]	Period [s]	Amplitude [m]
Simplified	0.925	6.79	1.3
Final	0.84	7.48	1.186

Roll RAO - Beam Sea:

The response amplitude operator for roll in beam sea is presented in Figure 7.6. The motion amplitude is highest for the simplified pontoon. This is due to the width being smaller than for the final pontoon geometry. The peak period/frequency for both pontoons are given in Table 7.8.

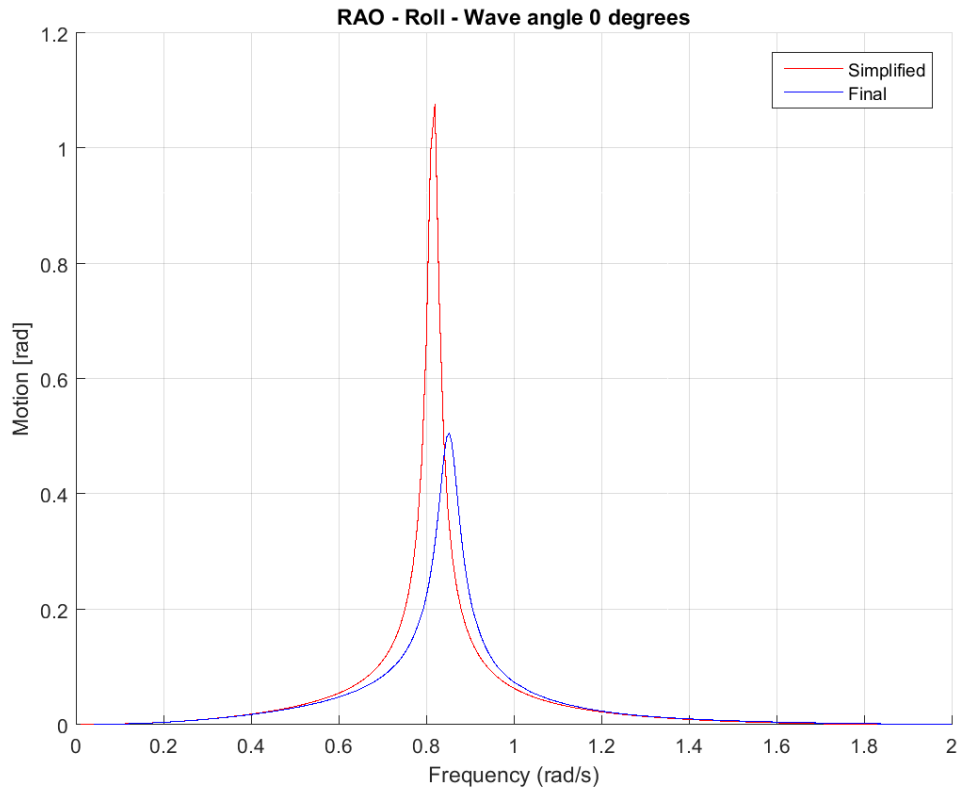


Figure 7.6: Wadam roll RAO for simplified and final pontoon, beam sea

Table 7.8: Roll beam sea peak period/frequency and amplitude for unit wave height

Pontoon geometry	Freq [rad/s]	Period [s]	Amplitude [m]
Simplified	0.77	8.16	0.43
Final	0.84	7.48	0.655

Pitch RAO - Head Sea:

The response amplitude operator for pitch shown in Figure 7.7 shows that the final pontoon has motions bigger than the simplified pontoon. This is as expected when comparing pitch potential damping and restoring coefficient for the pontoon designs. This simplified design has higher restoring coefficient and potential damping, resulting in smaller pitch motion amplitudes. The pitch motion is amplified at smaller wave frequencies compared to roll motion. This is because the length is larger than the width, resulting in bigger angular motion. The peak period/motions for the designs are presented in Table 7.9

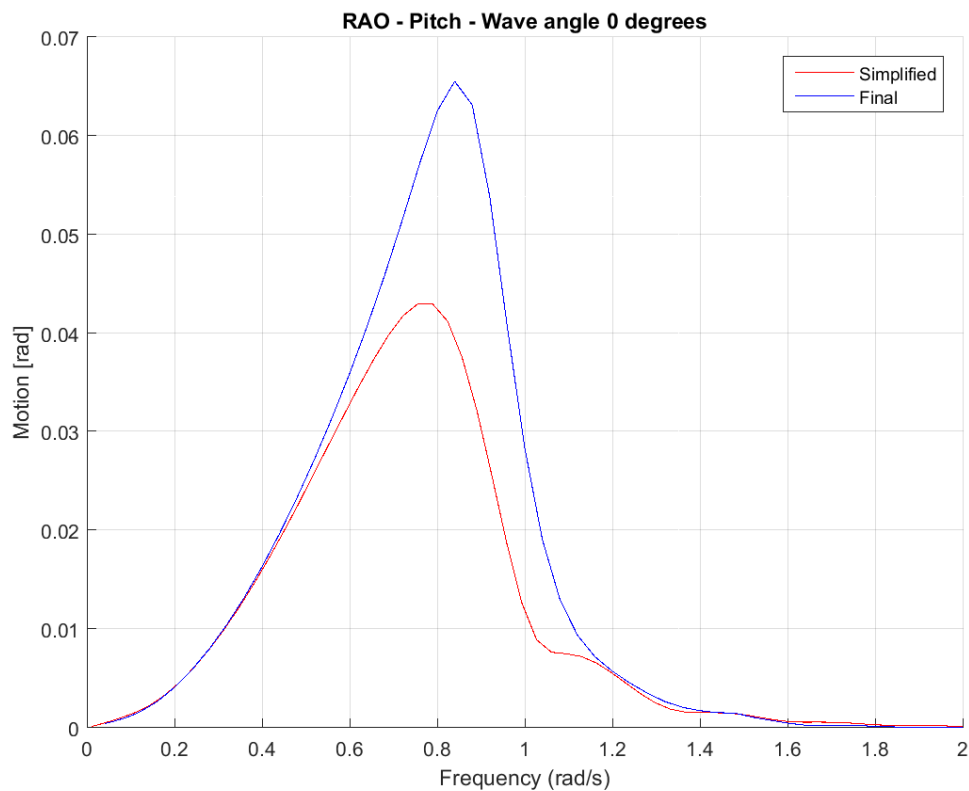


Figure 7.7: Wadam pitch RAO for simplified and final pontoon, head sea

Table 7.9: Pitch head sea peak period/frequency and amplitude for unit wave height

Pontoon geometry	Freq [rad/s]	Period [s]	Amplitude [m]
Simplified	0.77	8.16	0.43
Final	0.84	7.48	0.655

7.2.1.3 WADAM Potential Damping and Curve Fitting

In order to compare the results from Wadam with the simplified ANSYS pontoon configuration, the potential damping from Wadam needs to be implemented in ANSYS. In addition to this, the potential damping from the final configuration needs to be implemented in the global model. The potential damping is frequency dependent. The damping can be represented by establishing a function fitted to the potential damping plot. Figure 7.8 shows the potential damping for the two pontoon designs in heave. Due to numerical errors in the results, the curves need to be adjusted before a damping function can be obtained. This is done manually in the potential damping result files.

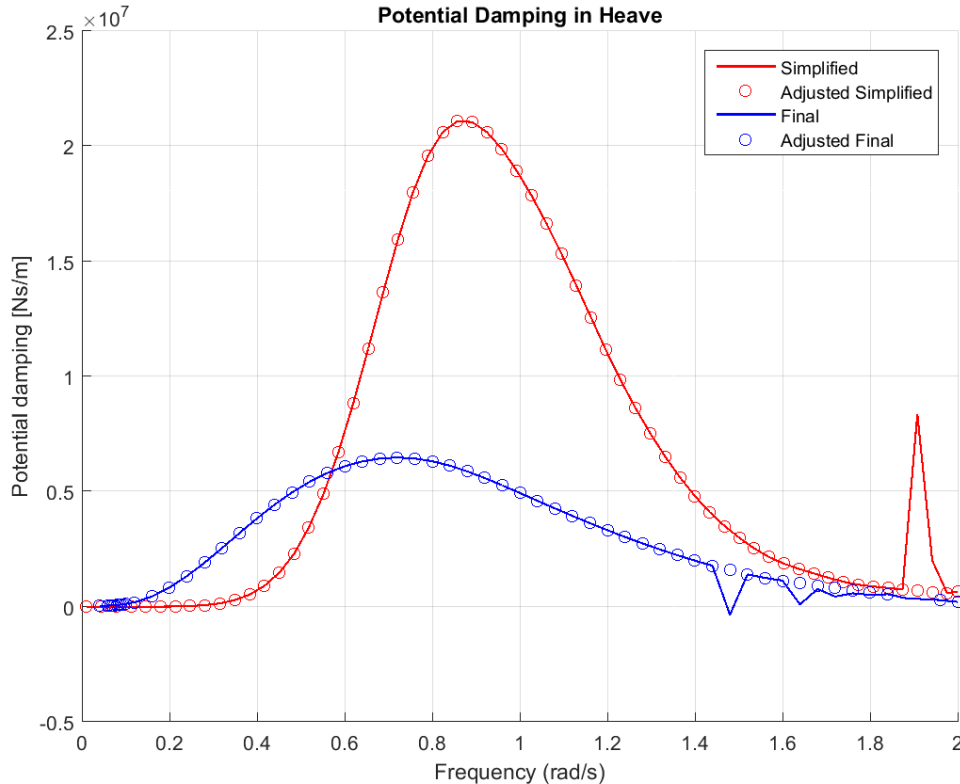


Figure 7.8: Wadam potential heave damping for harmonic wave frequency

The numerical mistakes are also present for the potential damping in pitch and roll. The same manual adjustments are made in order to be able to fit a curve to plots. The potential damping in roll and pitch are shown in Figures 7.9a and 7.9b. In accordance with the pontoon designs, the final design has higher potential damping in roll for most frequencies. This corresponds to

the smaller pitch motion in Figure 7.6. The opposite is true for potential pitch damping, where the simplified configuration has higher damping and thereby smaller pitch motion. This is a consequence a wider design.

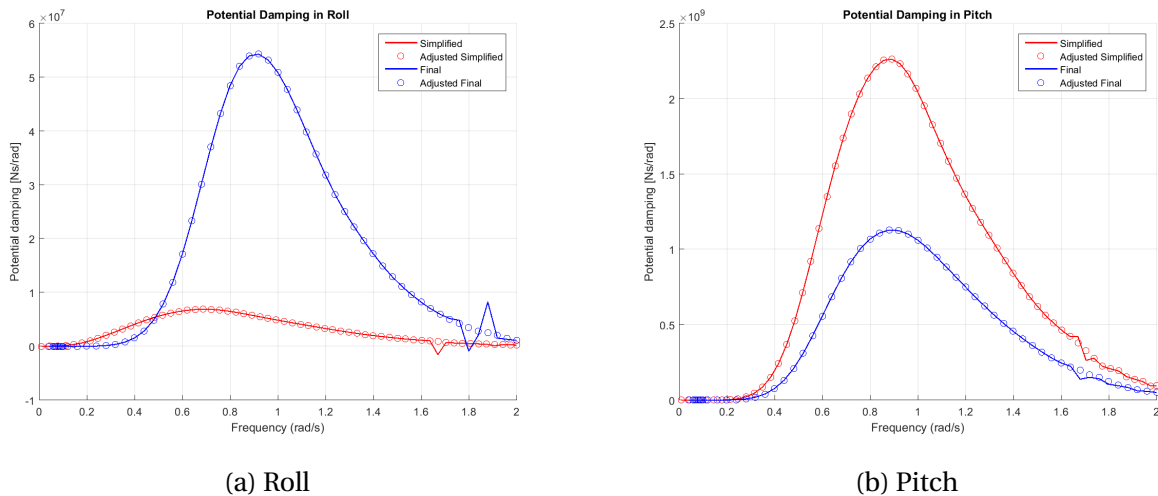


Figure 7.9: Potential damping in roll and pitch for the two pontoon designs

The curve fitting for the potential damping can be found in Appendix C.1.1. The curve fitting results in polynomial expressions which are implemented in ANSYS. The simplified damping into the pontoon analysis and the final into the global submerged floating tunnel.

7.2.2 ANSYS Simplified Pontoon Results and Wadam Comparison

This section contains the results from the ANSYS pontoon analysis described in Section 6.3.3. The RAOs for heave, pitch and roll motions are presented in MATLAB plots with post processed results from ANSYS. All the plots are compared with the Wadam results in Section 7.2.1.2.

7.2.2.1 ANSYS RAOs - Comparison to WADAM Results

As explained in the analyses description in Section 6.3.3, multiple harmonic waves with an amplitude of 1 meter and frequencies ranging from 0.05 to 2.0 rad/s are applied in the system. The vertical displacement for each harmonic wave analysis is stored and used to create the RAOs for the ANSYS pontoon. Figure 7.10a, 7.10b and 7.11 are examples of global heave displacements for

three harmonic waves with different frequencies. The analyses for these plots are done in pure heave motion. The x-axis shows the time duration of the analysis, while the y-axis shows the global vertical displacement.

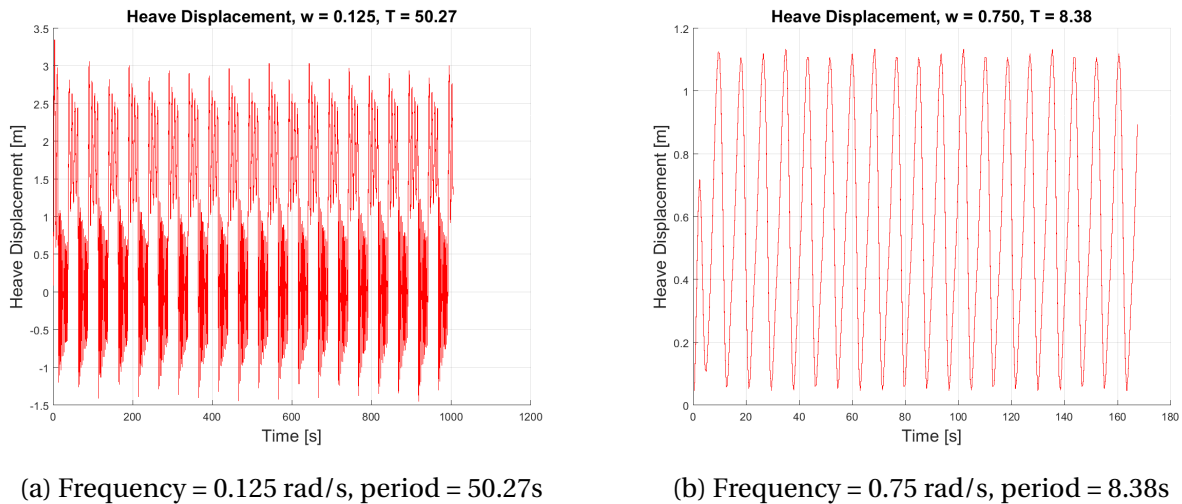


Figure 7.10: Pure heave global vertical pontoon displacement

By looking at Figure 7.10b, it is clear that the mean displacement for the pontoon is around 0.6 meters. This is most likely because the modeling of equilibrium between buoyancy and weight is a bit off, causing the pontoon to stabilize around a new equilibrium. This is probably because of the layer modeling of the pontoon and the way mass has been distributed to the pontoon elements.

Looking at Figure 7.11, it is clear that the wave needs to be applied for a number of periods in order for the results to stabilize. The duration of this analysis is approximately 136 seconds. With a wave period of 3.4 second, the analysis is running for approximately 40 wave periods. Only the last 20% of the analysis results are used. This secures that the sampled results used for the RAO representation are stabilized motions. The sampled results for each wave frequency is half the absolute difference between the maximum and minimum displacement. The unit is radians for roll and pitch motion and meters for heave motion. The response for each frequency is presented in a response amplitude operator plot. This is shown in Figure 7.12a

The procedure for producing the RAOs in roll and pitch are the same. The difference is that the sampled vertical displacement is presented as rotation.

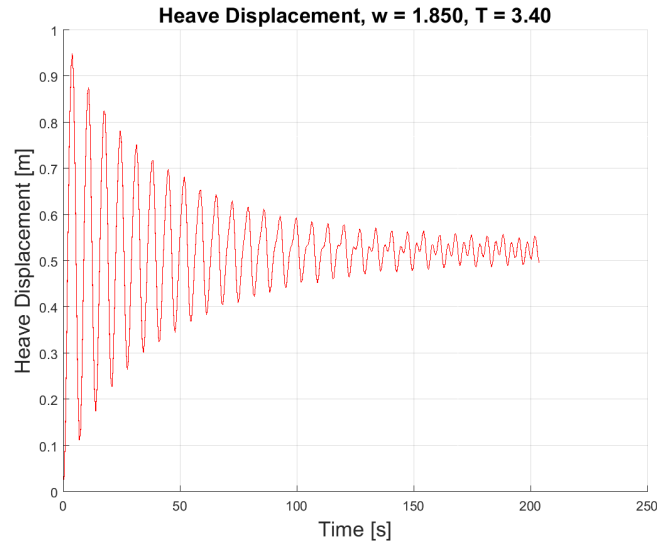
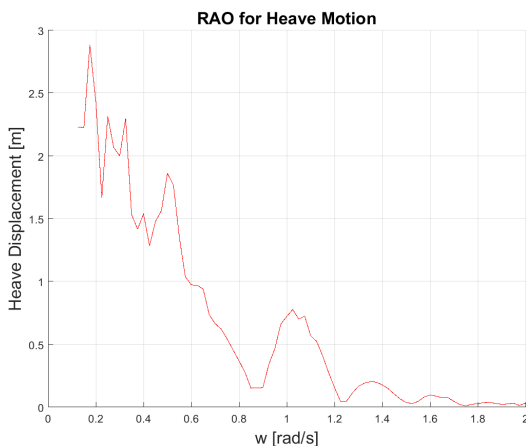


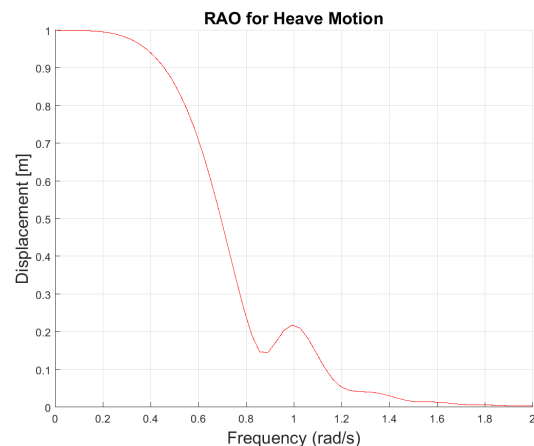
Figure 7.11: Heave motion, frequency = 1.85 rad/s, period = 3.4 s

Heave RAO - Head Sea:

The heave RAO for head waves is shown in Figure 7.12a, while Figure 7.12b shows the RAO from Wadam. The main features of the ANSYS RAO is similar to Wadam. It starts with the highest displacement for low frequencies/high periods and has a peak around 1 rad/s, as the Wadam pontoon has. After this, the displacements goes towards zero, which is correct considering heave movement for a floating object in small frequency waves.



(a) Ansys heave RAO



(b) Wadam heave RAO

Figure 7.12: Heave RAO comparison for ANSYS and Wadam

It is difficult to say why the magnitude of the displacement is different, considering that the wave

amplitude is 1 meter for both softwares. It is most likely due to the added mass representation, the boundary conditions and the fact that the pontoon displacement often stabilizes at a vertical magnitude unequal to zero. The shape of the RAO is considered good if the local peaks were to be smoothed out.

Roll RAO - Beam Sea:

The figure for the roll motion ANSYS RAO is added in appendix D.1.1. The result was not accurate, due to very high roll response towards the end of the tested frequency range. This is probably because of boundary conditions and the added mass representation. The potential damping in this frequency range is very small, causing huge response even though the pontoon response should have a small amplitude.

Pitch RAO - Head Sea:

The pontoon response for both ANSYS and Wadam is shown in Figure 7.13. The response in the pontoons eigenfrequency range around 1 rad/s is so high that ANSYS is unable to complete the analysis. From approximately 0.8 - 1.2 rad/s, there are no response results. This is in coherence with the Wadam results, where the pontoon has its maximum response at approximately 0.8 rad/s. This is also the pitch eigenfrequency of the Wadam pontoon.

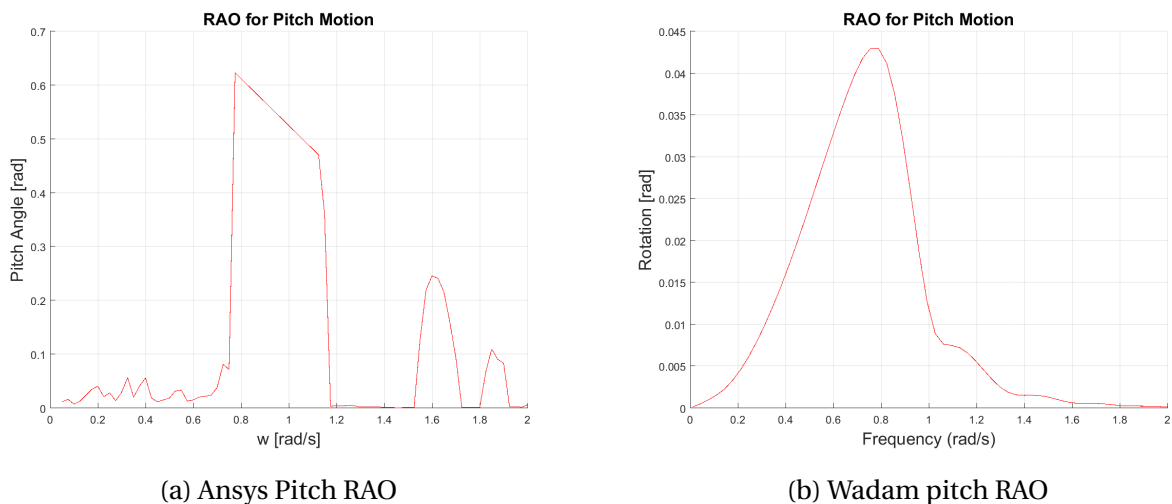


Figure 7.13: Pitch RAO comparison for ANSYS and Wadam

For the low frequency/high period incoming waves, the response is low, as it should be. The ANSYS RAO has some unexpected response in the top of the frequency range.

Concluding pontoon RAO remarks:

It is clear that the pontoon representation in ANSYS is far from perfect. It still gives some answers in confirming the modeling of the pontoon geometry. The heave RAO has correct main outlines, even though local peaks and troughs in the response plot shows deviations. This also concerns the pitch ANSYS RAO. The response is small in the upper and lower ranges, except for the two peaks at the end, and has its highest response in the expected frequency range.

The added mass representation along with the boundary conditions, trying to imitate pure motions, is the most probable reason for the deviations. It is hard to create a pontoon, accounting for all motions, coupled and uncoupled, and still sample information which can be used to describe uncoupled motions.

The sampling method of each individual wave frequency response into the RAO, can also be a reason for the sometimes deviant results. It is still not assumed to affect the results as much as the uncertainties with the added mass and boundary conditions

It is important to have in mind that the boundary conditions affecting the results, are not present in the global bridge model. The pontoons are connected with shafts to the main tunnels, and moves with the global bridge movements. The most important results, in terms of actual pontoon characteristics, are the restoring coefficients and the potential damping which can be transferred to the springs representing the characteristics of the pontoon, in the global SFT model.

7.3 Static Analysis

A static analysis is performed in order to check the criteria of global neutral buoyancy. It is measured in maximum and minimum displacement of the model in global Z-direction. The global X- and Y-component displacement is also considered. All these considerations are done for maximum and minimum tide and mean water level.

7.3.1 Static Results with Tidal Change

As explained in Section 3.5 about different tidal levels, the maximum and minimum tidal level measured in Ålesund since 1961 is +1.85m and -1.58m (Ålesund Havnevesen, 2016). These levels are used in static analyses in order to calculate the maximum and minimum displacements for the floating submerged tunnel. The main results of the analyses are presented in Table 7.10 for each tidal change. The absolute displacement is shown in Table 7.11

Table 7.10: Max and min global component displacement due to tidal change

	X-max [m]	X-min [m]	Y-max [m]	Y-min [m]	Z-max [m]	Z-min [m]
Tc = - 1.58	0.08	-0.08	0.02	-0.08	0.00	-1.80
Tc = 0	0.05	-0.05	0.01	-0.09	0.24	-0.17
Tc = 1.85	0.08	-0.08	0.00	-0.13	2.14	0.00

The figures showing the X- and Y-component of the displacement can be found in Appendix D.2.1. The main reasons for the small changes in displacement in the xy-plane is due to a slightly uneven distribution of ballast. This uneven distribution is present both in the bridge span and the outer and inner tunnel, compared to each other. It leads to different buoyancy forces causing the displacements.

Table 7.11: Absolute maximum vertical displacement for different tidal inputs

Tc	Absolute displacement [m]
- 1.58	1.80
0	0.41
1.85	2.14

7.3.1.1 Mean Sea Level

The mean sea level displacements for the Z-component are shown in Figure 7.14. It is clear that the ballast distribution along the bridge span is not perfect. Still, the results are pretty good. One can see that more ballast should have been distributed under the pontoons with a smaller pontoon distance (150 meters). An absolute displacement, from maximum to minimum, of 0.40 meters is deemed small enough in order to carry on with analyses.

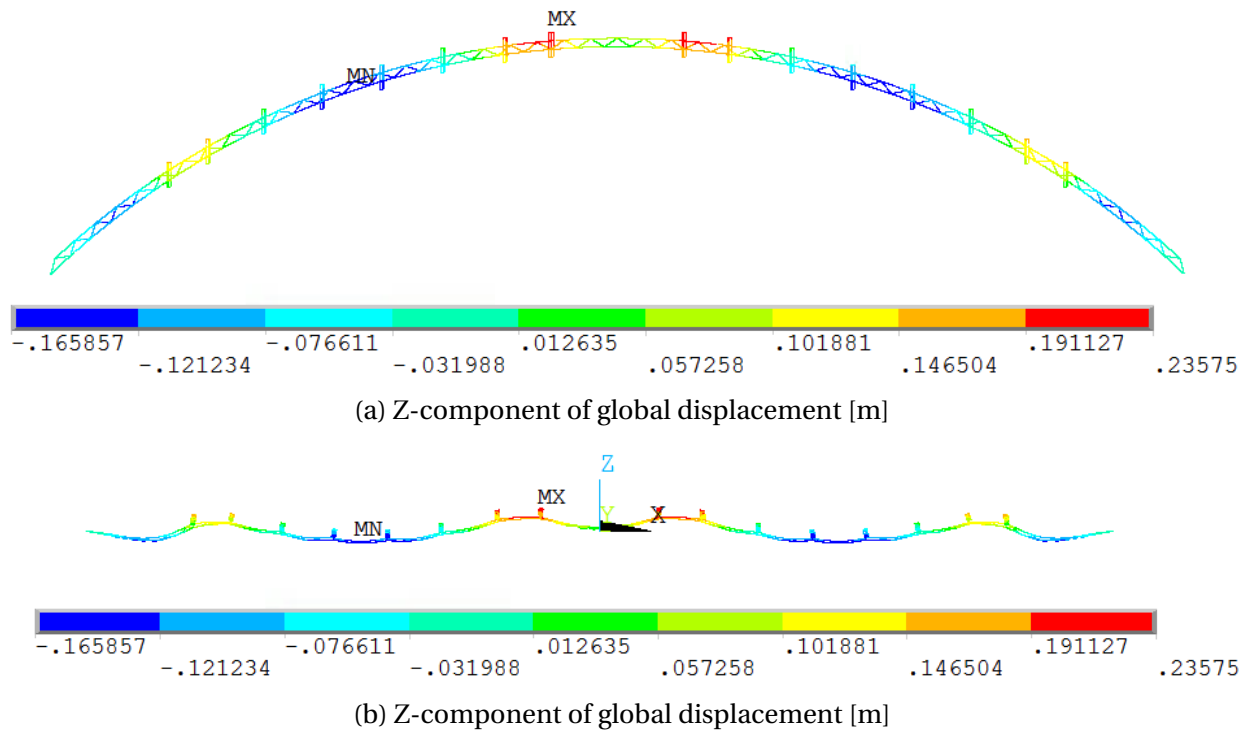


Figure 7.14: Global Z-component displacement [m], mean water level

The results of an evenly distributed ballast along the whole span is included in Appendix D.2.1.1. The absolute global vertical displacement is 0.90 meters with evenly distributed ballast.

7.3.1.2 High Tide: 1.85 Meters

For the high tide, with a tidal change of 1.85 meters from mean sea level, the vertical displacements are much higher. This is of course due to the pontoons extra buoyancy force, as a result of a bigger draft. The absolute displacement is 2.14 meters with the distribution shown in Figure 7.15a. As with the mean sea level static analysis, the maximum displacement is at the pontoons which are closest to each other.

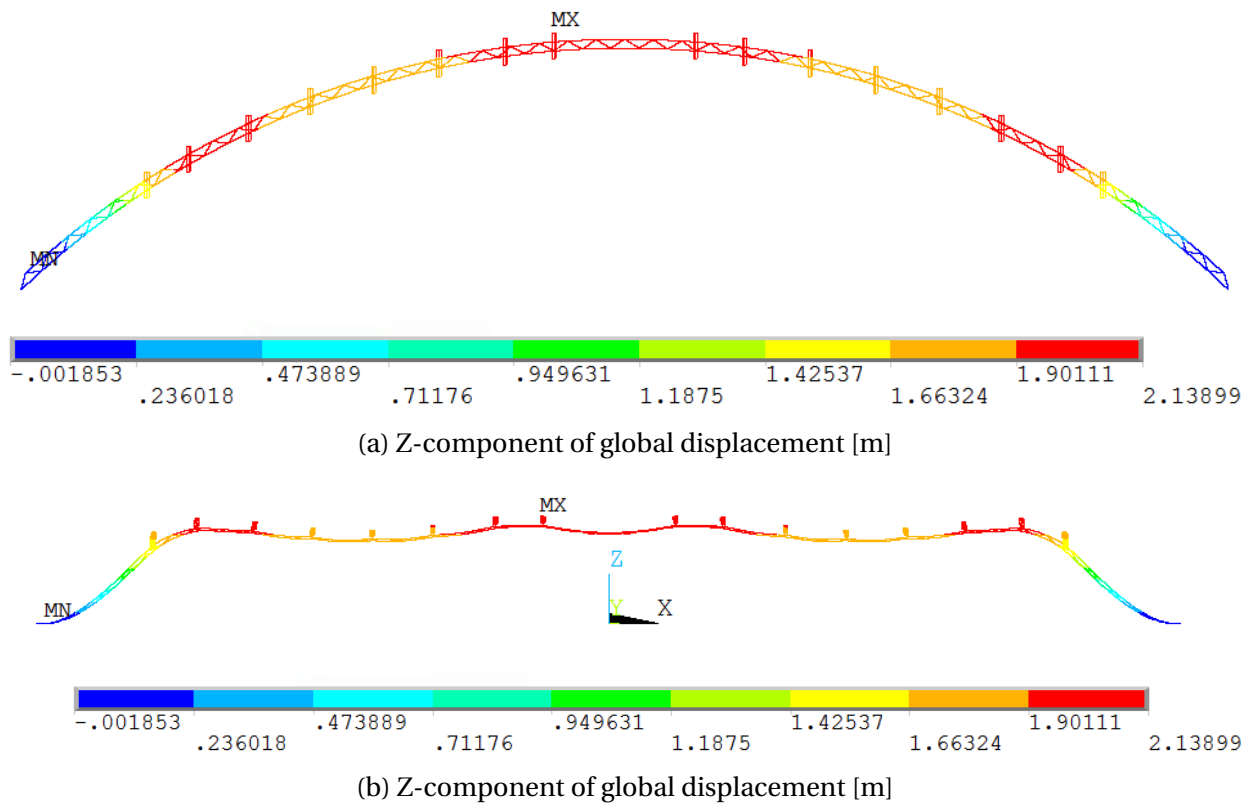


Figure 7.15: Global Z-component displacement [m], tidal change = 1.85 meters

The bridge stabilizes at +2.14 meters above the mean sea level, when the buoyancy forces of the pontoons is neutralized by the weight and the bridge stiffness.

7.3.1.3 Low Tide: -1.58 Meters

For the low tide at -1.58 m from mean water sea level, the absolute displacement is 1.80 meters. This is shown in Figure 7.16, where the same tendencies as with the other sea level inputs can be observed. The maximum local vertical displacement happens at the two pontoons on each side of the ship channel.

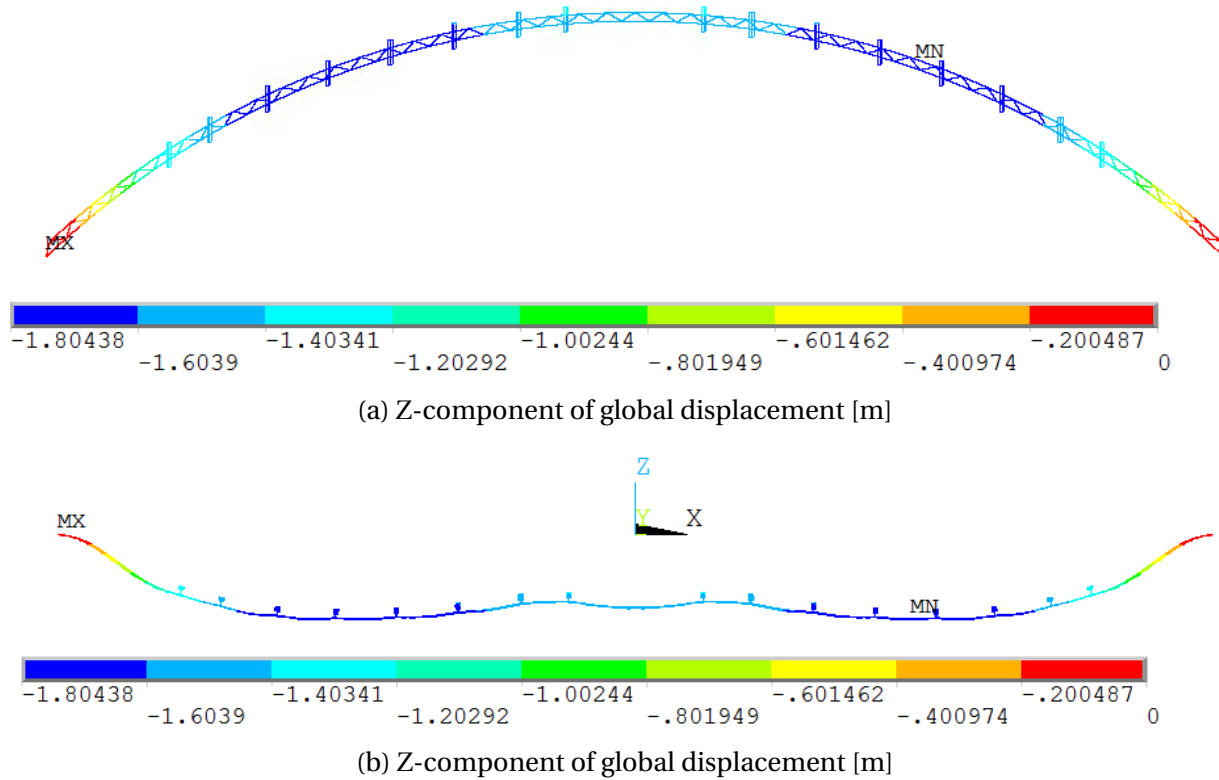


Figure 7.16: Global Z-component displacement [m], tidal change = -1.58 meters

7.4 Modal Analysis Results

This section presents the modal analysis results described in Section 6.5. This includes the eigenfrequency, mode shape and participating masses. The estimated results of the Rayleigh damping coefficients are also included.

7.4.1 Eigenfrequency Analysis Results

The theory behind the eigenvalue problem is described in Section 4.3.1 and a brief description of the importance and the ANSYS solver is given in Section 6.5.1. The direction of the mode motions are listed in Table 7.12. The *H* and *V* stands for horizontal and vertical mode shape, respectively. The only difference for the first 10 modes is that the third horizontal eigenmode in the Reinertsen Olav Olsen Group study is mode number eight. This is mode number 10 for the ANSYS model. The other mode numbers are shifted in coherence with this difference.

Table 7.12: Direction of mode motion

Mode	1	2	3	4	5	6	7	8	9	10
Reinertsen Olav Olsen Group	H	H	V	V	V	V	V	H	V	V
Global ANSYS Model	H	H	V	V	V	V	V	V	V	H

In Table 7.13 the frequencies of the Reinertsen Olav Olsen Group study is compared with the eigenfrequencies from the global ANSYS model. The modes coincide with small differences, which are given in the far right column. The mean deviation for the 25 first modes are 6.5 %.

The 10 first mode shapes are shown in Section 7.4.1.1 and 7.4.1.2.

Table 7.13: Comparison of eigenfrequencies

Mode	Reinsertsen Olav Olsen Group		Global ANSYS model		Difference [%]
	w [1/s]	T [s]	w [1/s]	T [s]	
1	0.018	55.6	0.022	45.1	19.2
2	0.034	29.4	0.041	24.7	14.5
3	0.044	22.7	0.046	21.8	4.7
4	0.055	18.2	0.056	17.7	1.3
5	0.055	18.2	0.056	17.7	1.3
6	0.057	17.5	0.058	17.2	3.2
7	0.057	17.5	0.059	17.0	3.2
8	0.060	16.7	0.064	15.7	5.8
9	0.061	16.4	0.067	14.9	8.7
10	0.062	16.1	0.072	13.9	13.4
11	0.073	13.7	0.078	12.9	6.4
12	0.079	12.7	0.087	11.5	8.1
13	0.081	12.3	0.091	11.0	10.7
14	0.091	11.0	0.098	1.,2	7.8
15	0.103	9.7	0.102	9.8	1.1
16	0.104	9.6	0.117	8.6	10.5
17	0.118	8.5	0.122	8.2	3.7
18	0.124	8.1	0.128	7.8	2.6
19	0.134	7.5	0.134	7.4	0.2
20	0.151	6.6	0.145	6.9	4.1
21	0.167	6.0	0.154	6.5	7.6
22	0.170	5.9	0.169	5.9	0.8
23	0.191	5.2	0.174	5.7	8.3
24	0.201	5.0	0.192	5.2	4.2
25	0.214	4.7	0.197	5.1	7.8

7.4.1.1 Horizontal Mode Shapes

The horizontal mode shapes are displaced in the horizontal XY-plane. The first, second and 10th. mode shapes are horizontal, and given in Figure 7.17, 7.18 and 7.19.

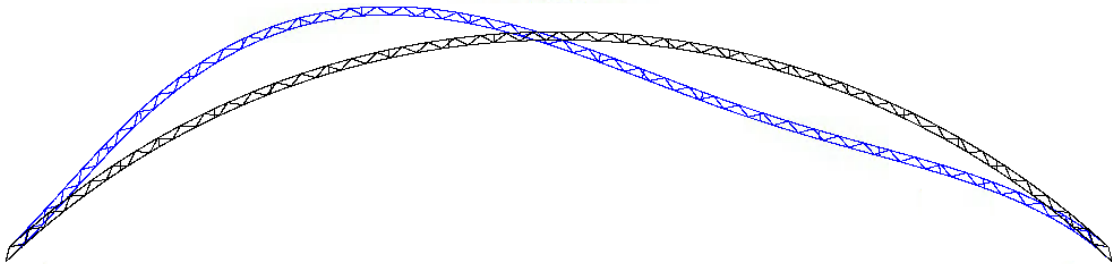


Figure 7.17: Mode 1: First mode shape, horizontal

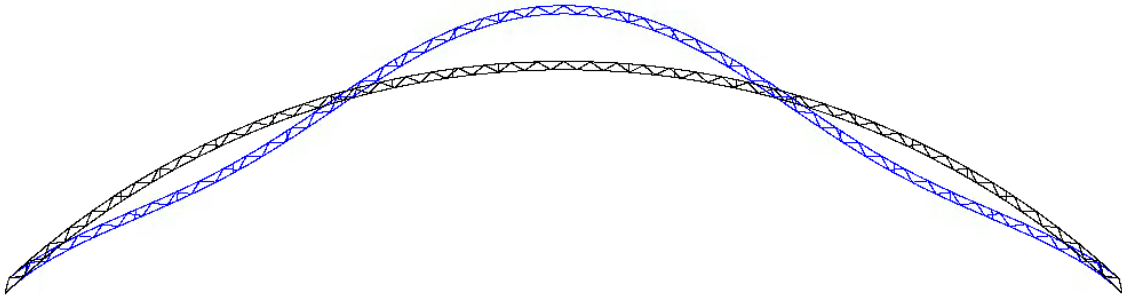


Figure 7.18: Mode 2: Second mode shape, horizontal

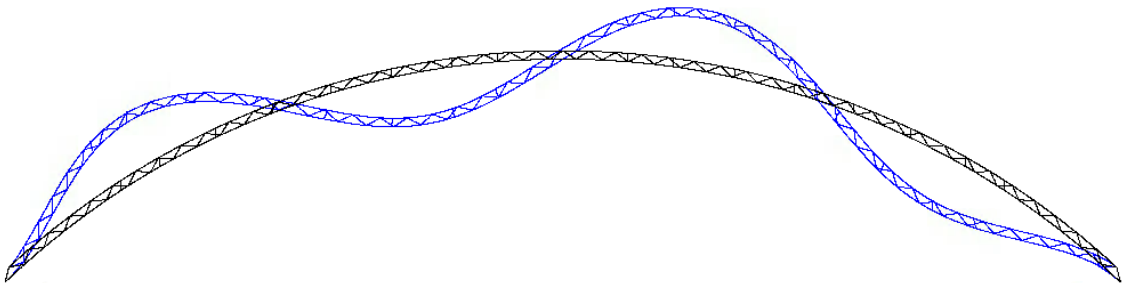


Figure 7.19: Mode 10: Tenth mode shape, horizontal

7.4.1.2 Vertical Mode Shapes

The vertical mode shapes are shown in the XZ-plane. The first seven modes are included in this section.

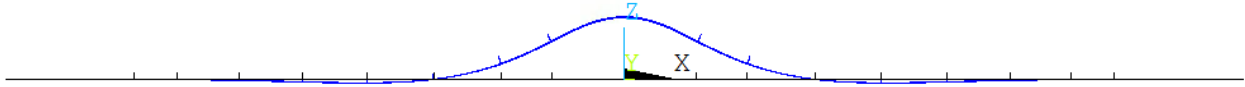


Figure 7.20: Mode 3: Third mode shape, vertical

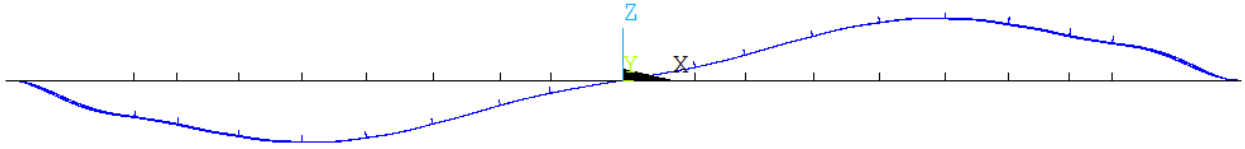


Figure 7.21: Mode 4: Fourth mode shape, vertical

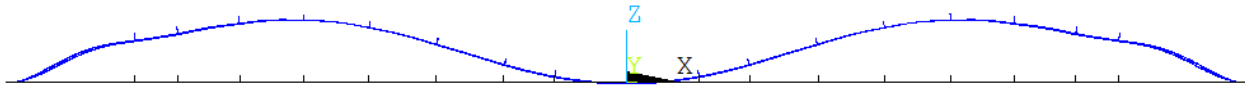


Figure 7.22: Mode 5: Fifth mode shape, vertical

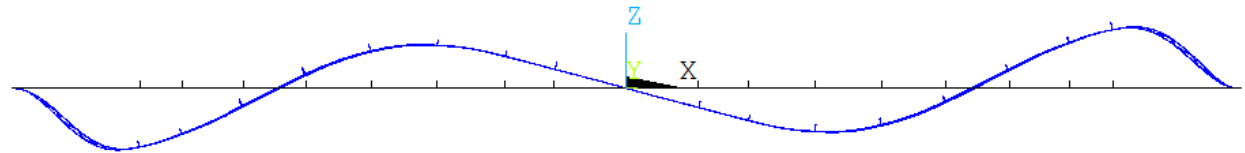


Figure 7.23: Mode 6; Sixth mode shape, vertical

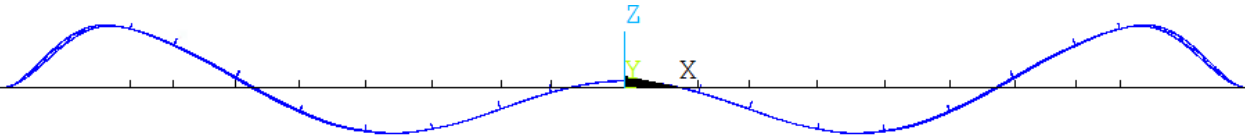


Figure 7.24: Mode 7: Seventh mode shape, vertical

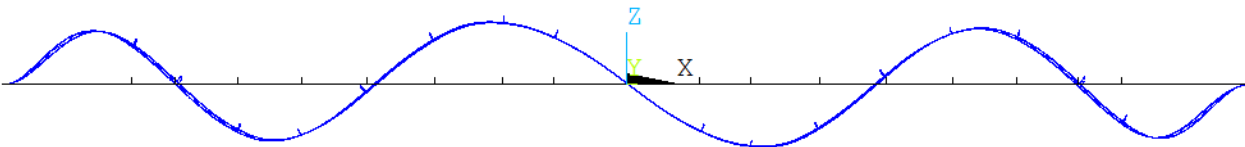


Figure 7.25: Mode 8: Eighth mode shape, vertical

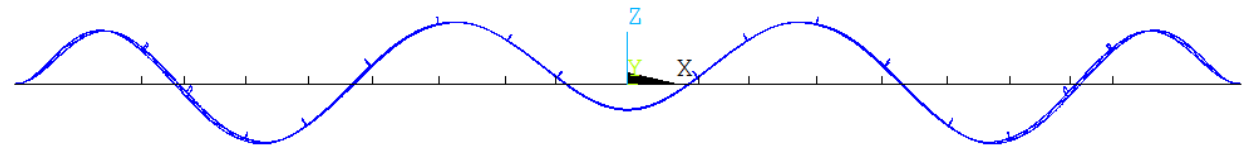


Figure 7.26: Mode 9: Ninth mode shape, vertical

7.4.2 Participating Masses

In order to estimate Rayleigh Damping coefficients for the harmonic and spectrum wave analysis, it is necessary to consider the modal mass participation. The directional modal mass participation for the 40 first modes is given in Table 7.14 with belonging mode number and eigenfrequency.

The summation process for the modal masses is shown in Figure 7.27. It shows the summation of the effective directional modal masses. The modes with significant mass contribution for the different directions are shown with a small circle in the plot. These modes and belonging eigenfrequencies are the most important when it comes to dynamic analyses and model response, due to their mass participation when the modes are displaced. This gives the most energy to the SFT, which again is most critical when it comes to the feasibility of the design.

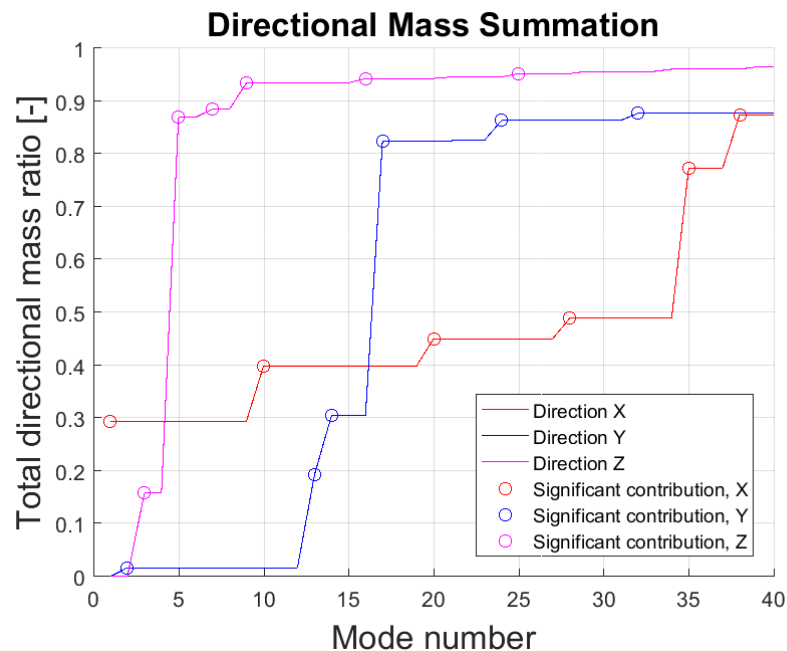


Figure 7.27: Summation of effective mass for the modes of the global model

By including 40 modes, approximately 90% of the mass is participating for all directions. According to Chowdhury and Dasgupta (2003), approximately 95% should be included to perform a Rayleigh damping coefficient procedure, in order to estimate a Rayleigh damping for the model. The results of this process is given in Section 7.4.3.

All mass participations are given in a percentage of the total directional mass.

Table 7.14: Modal analysis results for ANSYS global SFT model

Mode	w [rad/s]	T [s]	m_x	m_y	m_z	Σm_x	Σm_y	Σm_z
1	0.14	45.15	29.40	0.00	0.00	29.40	0.00	0.00
2	0.25	24.66	0.00	1.66	0.00	29.40	1.66	0.00
3	0.29	21.82	0.00	0.00	15.81	29.40	1.66	15.81
4	0.35	17.75	0.00	0.00	0.00	29.40	1.66	15.81
5	0.35	17.71	0.00	0.00	71.09	29.40	1.66	86.91
6	0.37	17.16	0.00	0.00	0.00	29.41	1.66	86.91
7	0.37	17.03	0.00	0.00	1.59	29.41	1.66	88.50
8	0.40	15.67	0.00	0.00	0.00	29.41	1.66	88.50
9	0.42	14.95	0.00	0.00	4.95	29.41	1.66	93.45
10	0.45	13.86	10.43	0.00	0.00	39.84	1.66	93.45
11	0.49	12.88	0.00	0.00	0.00	39.84	1.66	93.45
12	0.54	11.53	0.00	0.02	0.00	39.84	1.68	93.45
13	0.57	11.00	0.00	17.54	0.00	39.84	19.23	93.45
14	0.62	10.17	0.00	11.24	0.00	39.84	30.47	93.45
15	0.64	9.85	0.00	0.00	0.00	39.84	30.47	93.45
16	0.73	8.57	0.00	0.00	0.84	39.84	30.47	94.29
17	0.77	8.18	0.00	52.04	0.00	39.84	82.50	94.29
18	0.80	7.82	0.00	0.00	0.00	39.84	82.50	94.29
19	0.84	7.44	0.00	0.00	0.00	39.84	82.50	94.29
20	0.91	6.88	5.16	0.00	0.00	45.00	82.50	94.29
21	0.97	6.51	0.00	0.00	0.27	45.00	82.51	94.56
22	1.06	5.92	0.00	0.11	0.00	45.00	82.62	94.56
23	1.10	5.74	0.00	0.00	0.00	45.00	82.62	94.56
24	1.21	5.20	0.00	3.71	0.00	45.00	86.33	94.56
25	1.24	5.08	0.00	0.00	0.64	45.00	86.33	95.21
26	1.33	4.71	0.02	0.00	0.00	45.02	86.33	95.21
27	1.39	4.51	0.00	0.00	0.00	45.02	86.33	95.21
28	1.49	4.22	3.88	0.00	0.00	48.89	86.33	95.21
29	1.55	4.05	0.00	0.00	0.42	48.89	86.33	95.63
30	1.62	3.88	0.00	0.02	0.00	48.89	86.35	95.63
31	1.71	3.67	0.01	0.00	0.00	48.90	86.35	95.63
32	1.82	3.44	0.00	1.33	0.00	48.90	87.67	95.63
33	1.88	3.34	0.06	0.00	0.00	48.96	87.67	95.63
34	1.90	3.30	0.00	0.00	0.41	48.96	87.68	96.04
35	2.09	3.00	28.29	0.00	0.00	77.25	87.68	96.04
36	2.13	2.95	0.09	0.00	0.00	77.34	87.68	96.04
37	2.13	2.95	0.00	0.00	0.01	77.34	87.68	96.05
38	2.19	2.87	10.08	0.00	0.00	87.42	87.68	96.05
39	2.29	2.74	0.00	0.00	0.42	87.42	87.68	96.47
40	2.37	2.65	0.00	0.00	0.00	87.42	87.68	96.47

In order to have 95% mass participation for all directions for the SFT system, a number of 158 significant modes are required. In order to carry out the Rayleigh damping procedure, a total of 2.5 times significant modes are required. This results in a total of 395 required eigenmodes. The summarized mass participation plot for 200 modes is added in Appendix D.3.1 with a short description.

For approximately 90% mass participation, the number of significant modes are approximately 40. Due to the uncertainty of the procedure, it is not assumed necessary to include more than 40 significant modes with a mass participation of approximately 90% for all directions., as done in Section 7.4.3.

7.4.3 Estimating Rayleigh Damping Coefficients

As explained in Section 4.3.2, the goal of the Rayleigh damping procedure, is to estimate the α and β damping ratios for the damping of the system, given by Equation 7.2.

$$C = \alpha M + \beta K \quad (7.2)$$

As a results of the participating mass summation in Section 7.4.2, the number of significant modes in the coefficient calculation procedure is 40 modes. This requires a total of 100 extracted modes for the procedure. The α and β values for the three different approximations are given in Table 7.15.

Table 7.15: α and β coefficients for the different approximations

Coefficients	$m^{th} mode$	Full mode	Average
α	0.0020	0.0020	0.0020
β	0.5171	0.3587	0.4379

After calculating the coefficients, the damping ratio values for each approximation is calculated and plotted together with the linearized damping ratios. The final plot is shown in Figure 7.28. The approximation most equal to the linearized damping ratios is the damping ratios for the average data, between the m^{th} and full approximation.

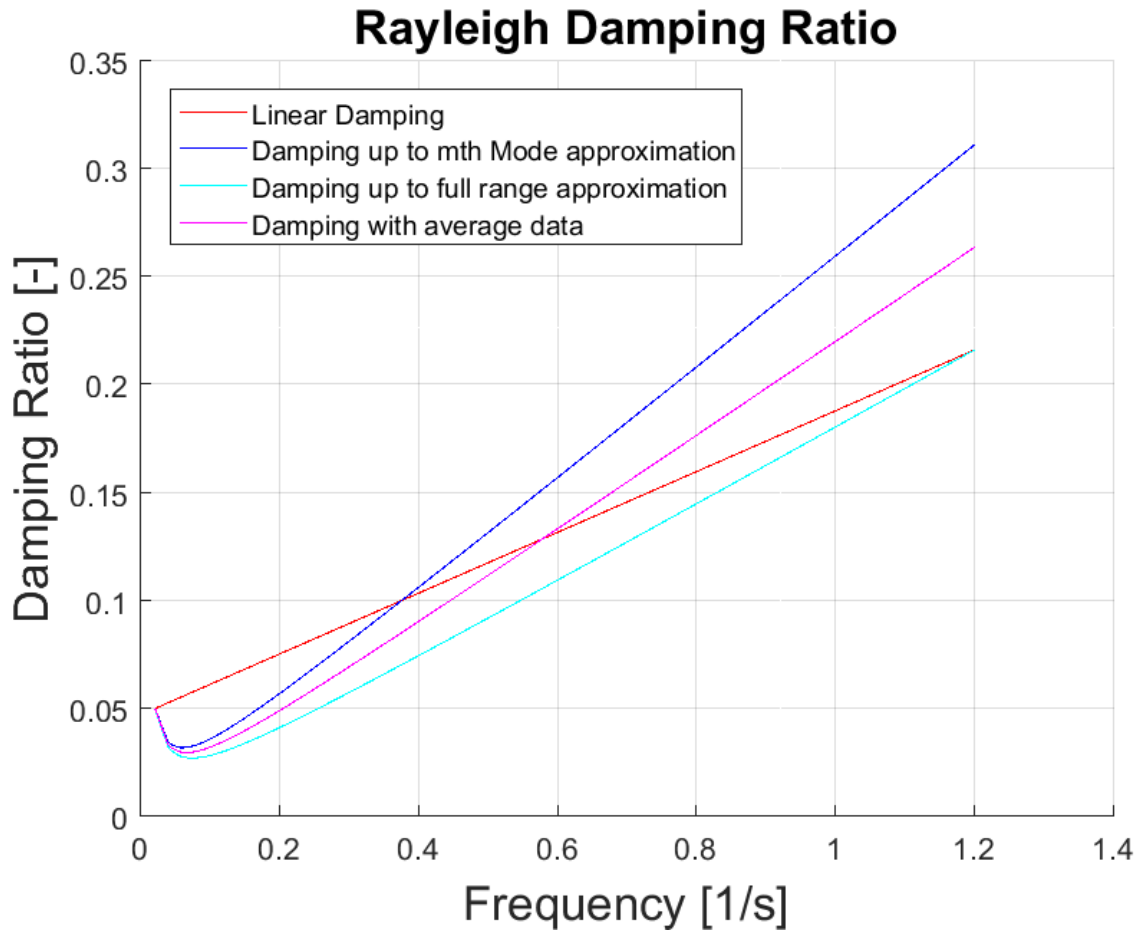


Figure 7.28: Rayleigh damping ratio for the different approximations

This results in a final damping ratios given in Table 7.16. These values are used in the harmonic and spectrum wave loading analyses for the global SFT model in ANSYS.

Table 7.16: Final Rayleigh damping ratios

Coefficient	Average approximation [-]
α	0.0020
β	0.4379

The values for the plot in Figure 7.28 is given in Appendix D.3.2. Only the values for the 40 first significant modes are listed.

7.5 Global Harmonic Wave Analysis Results

In this section the results from the harmonic wave analysis described in Section 6.6 are included. The first part, Section 7.5.1, describes the maximum response of the submerged floating tunnel for different wave periods. This is in order to describe which period gives the largest response in terms of rotations, displacement, stresses and moments.

When the maximum response wave period is known, further processing of the results for this specific period is carried out. Time increment for maximum response, where it occurs and also if for example maximum rotation occurs at the same time as maximum rotational moment is of interest. This part of the result analysis is described in Section 7.5.2.4.

7.5.1 Maximum Response for Different Wave Periods

As described in Chapter 6.6, the 50 year return period wave height is 4.85 meters. From the spectral peak period of 4.8 seconds, a span of wave periods is chosen along with the wave height to check the SFT response. By doing this, one can describe the most realistic maximum response for the 50 year return period wave. The wave periods range from 4.5 seconds to 6.75 seconds, with a step size of 0.25 seconds.

In order to describe each wave period response, the following parameters have been checked:

- Rotation - Rotation about the global X-, Y- and Z-axis and the rotational sum
- Displacement - Global maximum and minimum displacement
- Stress - Global maximum and minimum von Mises stress
- Moment - Elemental maximum and minimum bending and torsional moments

The global maximum and minimum wave period response for the parameters given in the previous list is collected by running a global model analysis for each period. By running the analysis for a given time the extremes for each period is sampled. The maximum and minimum vertical bridge displacement with a wave period of 6.25 seconds, seen in Figure 7.29, can be used as an example. The maximum and minimum displacements, marked with red and blue circles, are sampled and used in comparison to the other wave period extremes.

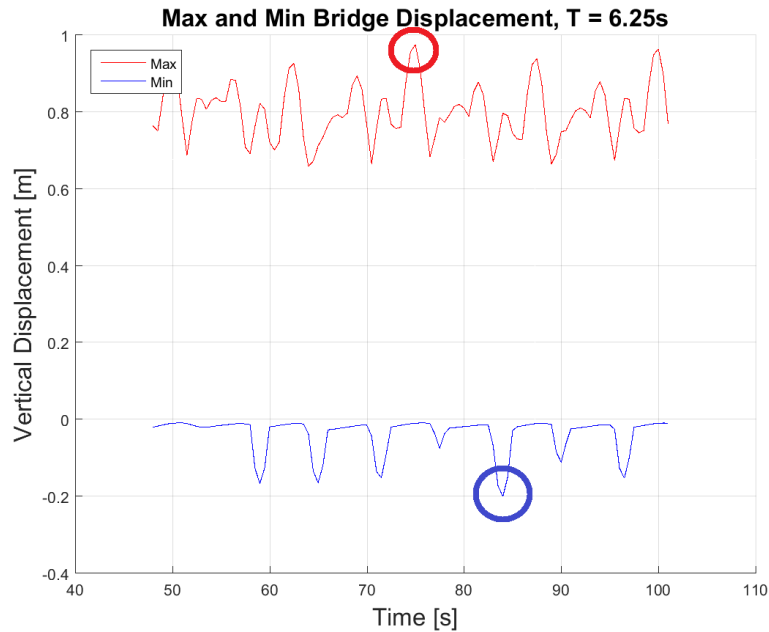


Figure 7.29: Sampled harmonic displacement maximas for wave period, $T=6.25s$

The same procedure is done for all wave periods, for all response parameters. By doing this, one misses the time steps where a maximum parameters might occur simultaneously. Investigating this would be too time consuming if done for each period, and will only be done for the period deemed the most critical in terms of response.

7.5.1.1 Rotational Response

The maximum and minimum rotational response for the tunnel about the Y- and Z-axis is given in Figure 7.30. What is important to have in mind, is that negative rotation is rotation about the negative direction of the global axes. The orientation would normally be given in absolute value, but is plotted with direction in order to discuss response symmetry.

The rotation about global Y- and Z-axis is symmetric. This implies a symmetrical response for the bridge during harmonic wave loading. This is of course true, considering that the loading is heading directly towards the orthogonal of the tunnels and that the SFT geometry is symmetrically modeled around the Y- and Z-axis.

Figure 7.31 shows the time increment where max rotation about Y-axis occurs for the 50 year

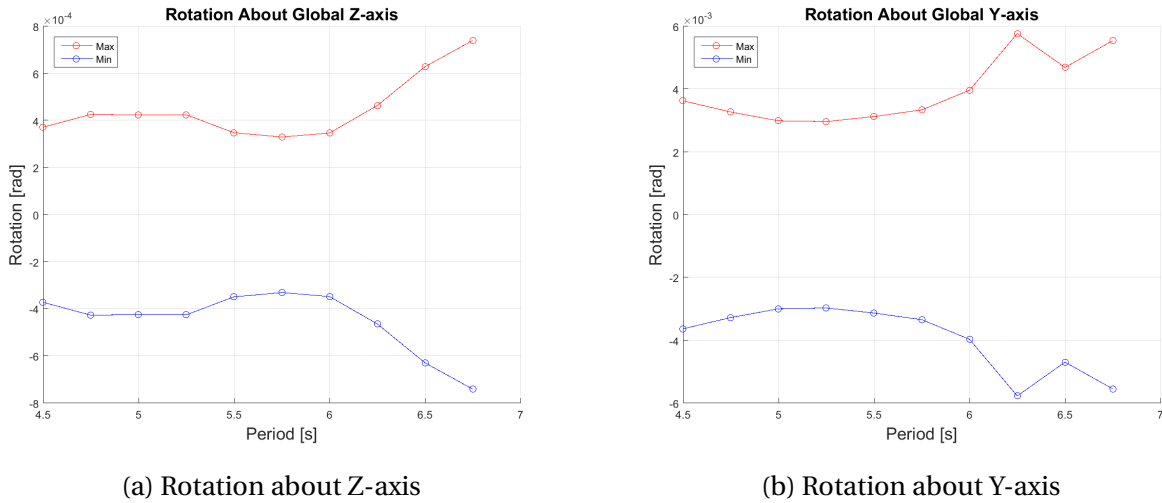


Figure 7.30: Global harmonic maximum and minimum rotations about Y- and Z-axis

return period wave with a wave period of 6.25 seconds. This is the maximum in Figure 7.30b.

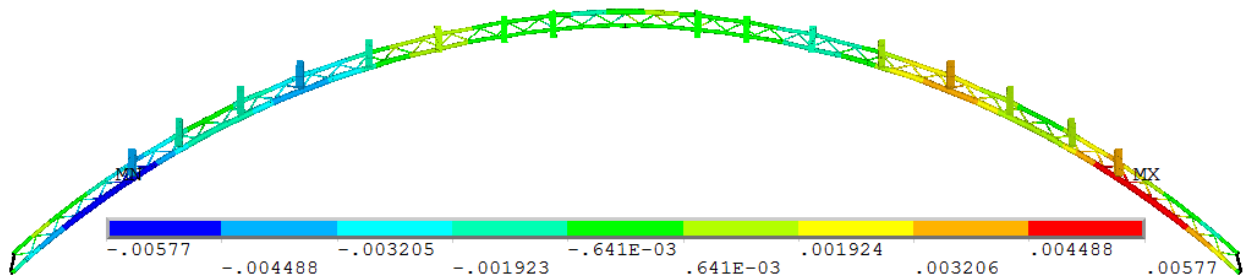


Figure 7.31: Maximum rotation about Y-axis [rad], T = 6.25s

From Figure 7.31 it is clear that the negative and positive maximas have the same absolute value, but the rotations in relation to the global coordinate system is opposite. The minimum value for the rotation is when the rotation is zero. By looking at the magnitude bar in Figure 7.31, is clear that the elements given in dark green and yellow are the ones closes to 0 radians rotation.

Figure 7.32 shows the rotation about the global X-axis. Unlike the plots for rotation about the global Y- and Z-axis, it is not symmetric for maximum and minimum rotations. While both max and min rotation about Y- and Z-axis occurs in the same time increment, this is not the case for the rotation about the X-axis.

In order to best describe the rotation shape about the global X-axis, the period T=6.25 at time increments for maximum and minimum rotation is shown. These two time increments are shown

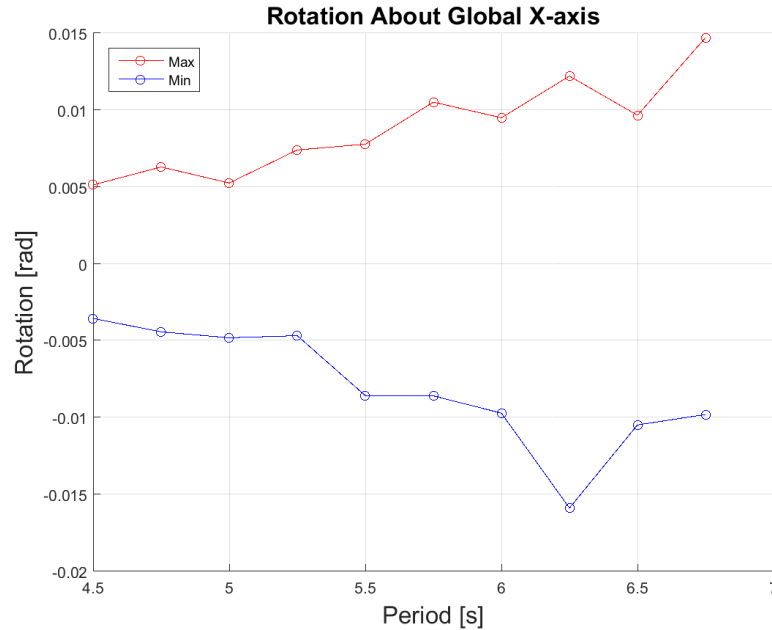


Figure 7.32: Global harmonic maximum and minimum rotation about X-axis

in Figures 7.33 and 7.34 and they are not the same. By looking at the two rotation shapes, one can observe that the shapes are opposite of each other.

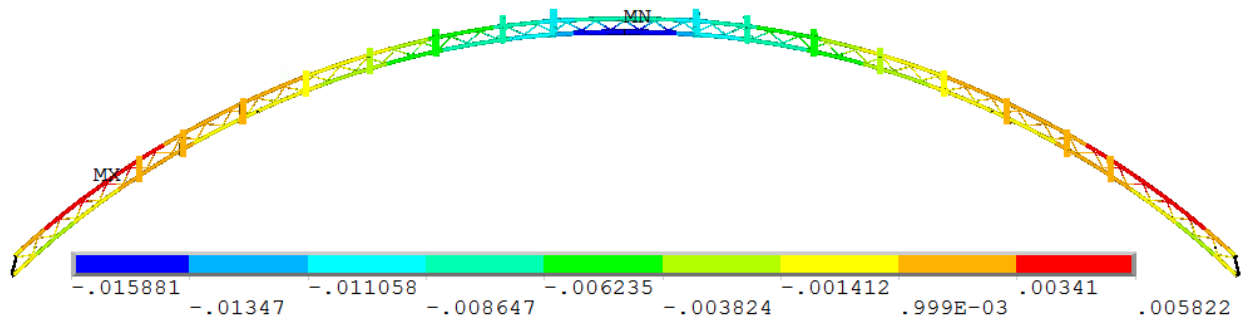


Figure 7.33: Minimum rotation about X-axis [rad], $T = 6.25s$

From Figure 7.33 it is observed that the inner main tunnel has maximum negative rotation at the middle of the span, while the outer main tunnel at the span ends has maximum positive rotation. For Figure 7.33 the shape is opposite, but not of the same magnitude. This results in different sampled maximum and minimum rotation for $T=6.25s$ in Figure 7.32.

It is the rotation about the global X-axis which has the largest magnitude, with a negative rotation of ≈ -0.016 rad. The rotation magnitude, being a lot higher for rotation about global X-axis

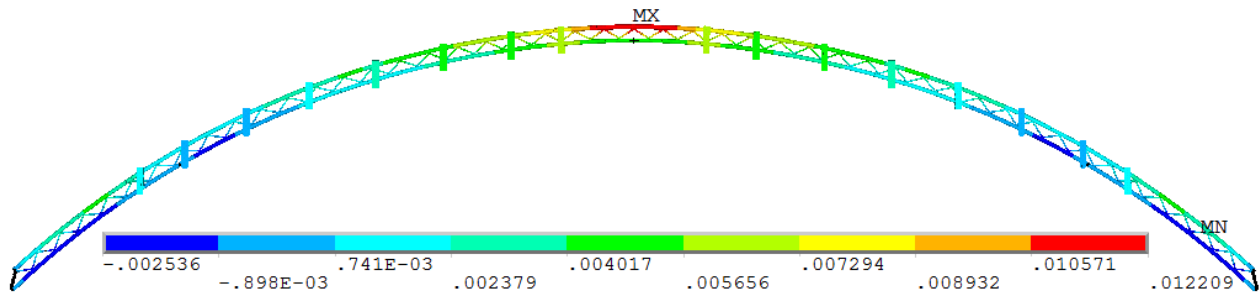


Figure 7.34: Maximum rotation about X-axis [rad], $T = 6.25\text{s}$

compared to the other axes, is because of the displacement of the two main tunnels compared to each other. The incoming wave displaces the tunnels differently, causing the rotation about the X-axis. This is also discovered when looking at the displaced shapes of the SFT.

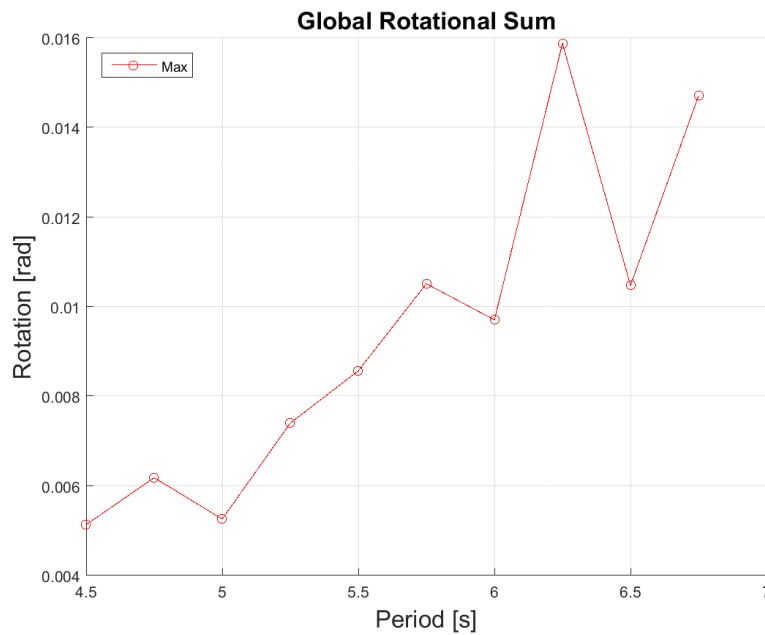


Figure 7.35: Rotational sum of all global directions

By looking at the sum of the three rotations, shown in Figure 7.35, it is clear that the wave periods of $T=6.26$ and $T=6.75\text{s}$ have the highest rotational response. The rotations for these wave periods are listed in Table 7.17

Table 7.17: Rotation about global axes for the wave periods with the highest response

Wave period [s]	Amplitude	X-axis [rad]	Y-axis [rad]	Z-axis [rad]	Sum [rad]
6.25	max	0.0122	0.0058	0.0005	0.0159
6.25	min	-0.0159	-0.0058	-0.0005	-
6.75	max	0.0147	0.0055	0.0007	0.0147
6.75	min	-0.0098	-0.0055	-0.0007	-

7.5.1.2 Harmonic Wave Loading Displacement

For the displacement due to the harmonic wave loading, only the vertical displacement is considered. This is the displacement which is the most dominating, and therefore also the most important when it comes to the structure response. Figure 7.36 shows the maximum and minimum displacement for each wave period. The lines denoted *upper*, show the displacement for the pontoons and the shafts between the pontoons and the main tunnels. The lines denoted *lower* show the displacement for the main tunnels and the bracing in between.

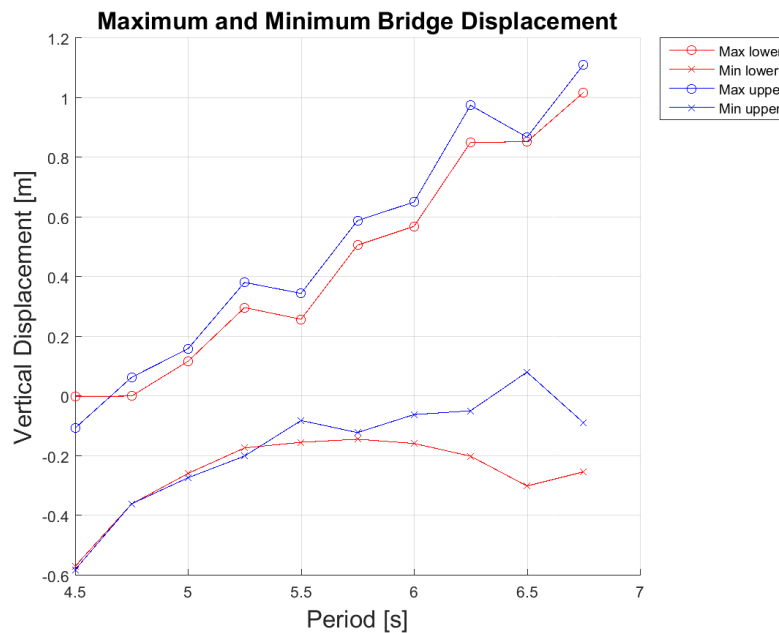


Figure 7.36: Vertical maximum and minimum displacement for wave periods

Since the maximum displacement of the main span, the connection shafts and the pontoons are of interest, all are included in the result study. What is important to have in mind, is that the maximum and minimum displacements for each wave period in Figure 7.36 can be from both

the same and different time increment.

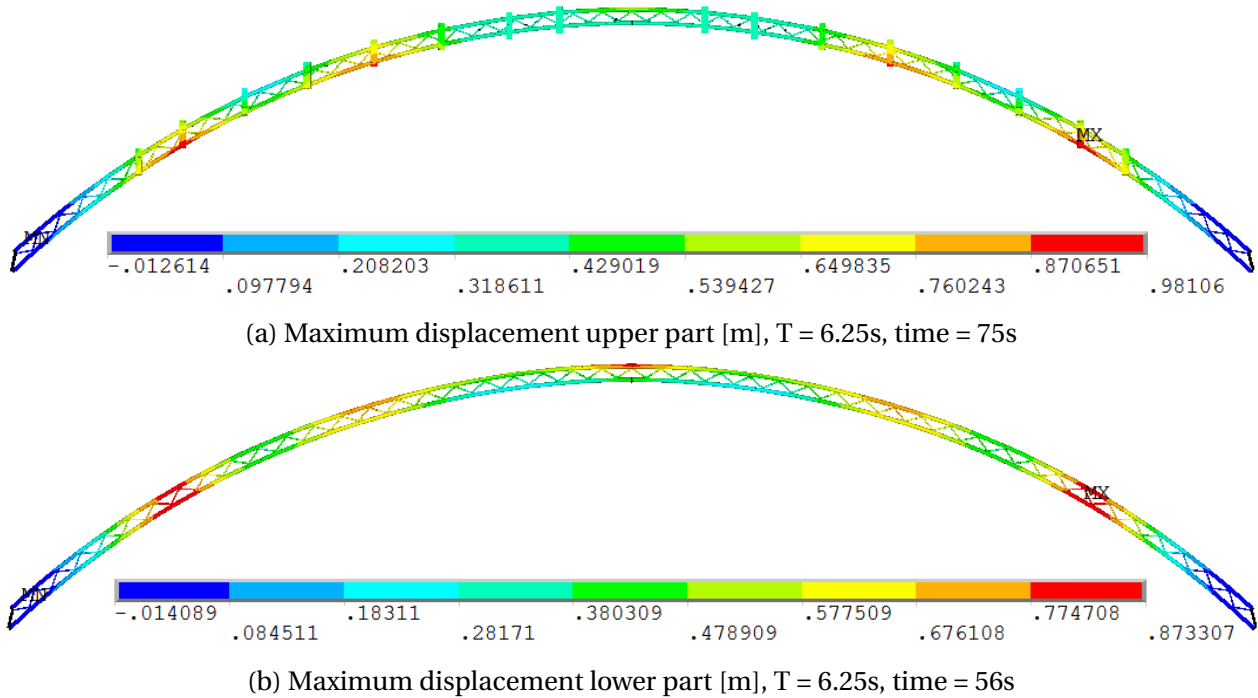


Figure 7.37: Maximum displacement [m], T = 6.25s

The three longest wave periods are the ones with the largest response. In order to describe the shapes of the maximum responses, the displacement shapes of the largest wave periods are included. Figure 7.37 shows the displacement for a wave period of 6.25 seconds. The two plots are from different time steps, but has the same shape. The maximum displacements occurs on the inner main tunnel at the second pontoons from the side.

Figure 7.38 shows the maximum displacement for the lower and upper parts of the structure for a wave period of 6.75 seconds. These maximum values are the points in the far upper right corner of Figure 7.36.

Depending on the rotation angle it is important to have in mind that the end of the pontoon will be displaced more than the main tunnel directly below it. This is shown in Figure 7.39, which is given at the end of this section. This is why the *max upper* displacement is higher than the *max lower* displacement in Figure 7.36. An example of this is also observable in Figure 7.38a where the maximum of the lower and upper part of the bridge is at the same place.

From the displacement considerations done in this section, it is clear that the three longest wave

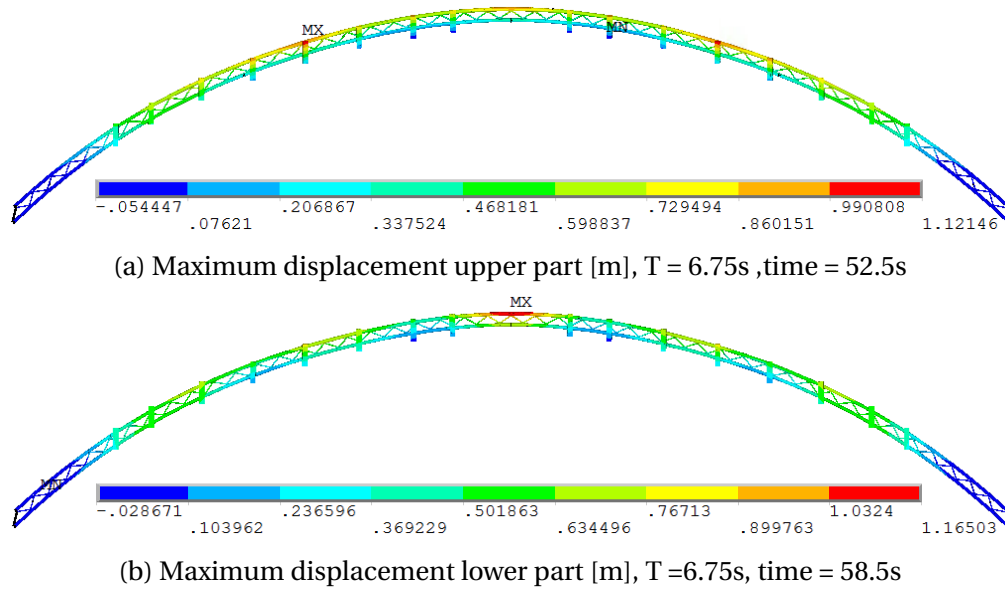


Figure 7.38: Maximum displacement [m], T = 6.75s

periods are the ones giving the highest response. It can be discussed whether the upper or the lower maximum displacement is of greatest importance. If the displacements are on the same spot, meaning on a pontoon end and directly below in the main tunnel, the observation basically means the same. The stresses and moments due to these displacement will be discovered if either of them are investigated. If the maximum displacement is in different places in the bridge, stresses and moments needs to be checked for both parts.

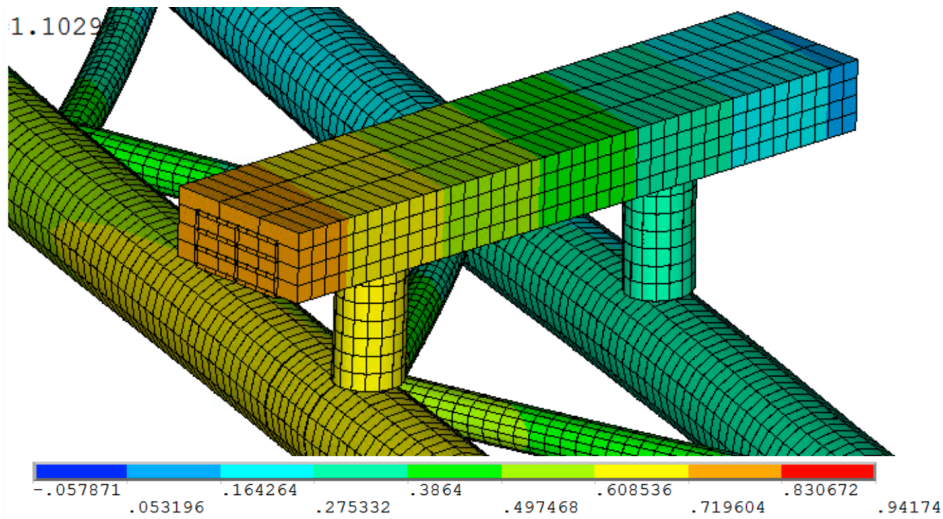


Figure 7.39: Difference in vertical displacement for pontoon ends and the main tunnels directly below [m]

7.5.1.3 Von Mises Stress due to Harmonic Wave Loading

The von Mises stress due to the harmonic loading with varying periods is shown in Figure 7.40. As for the displacement, the stress samples are divided into two categories. The first category is *lower*, being the stress for the main tunnels and the bracing. The other category concerns the connection shafts between the pontoons and the main tunnels. The pontoons are not taken into consideration, due to how they are modeled. As explained in Section 5.6 they are built up of many thin beam elements with very high Young's modulus. Due to this, they are not taken into account when checking maximum von Mises stress.

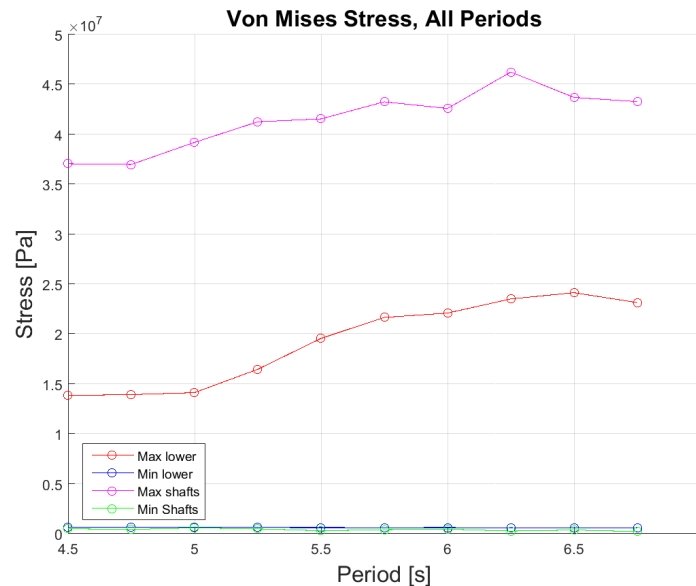


Figure 7.40: Maximum and minimum von Mises stress for wave periods

Figure 7.42 and 7.41 are element plots of the bridge center, but with and without the shafts. The max von Mises stress in the lower part of the bridge occurs in the center of the bridge span, while it for the upper part occurs in the shafts closest to the ship channel.

The von Mises stress is highest for the three longest wave periods. The higher stress in the shafts, compared to the main tunnels and bracing, is due to the wave force acting on the pontoons- This causes the bridge to rotate and the force moves through the pontoons, and down the connection shafts. All the energy causing most of the movement and stresses in the main tunnels has to go through the shafts, which causes the largest concentrations. This can be observed in Figure 7.41,

by looking closely at the shafts.

The max stress for the lower part of the structure happens in the connection between the main tunnels and the bracing elements. This is, as for the connection shafts, because the bracing elements are stresses when the model rotates about the X-axis due to the incoming waves. This can be observed in Figure 7.42.

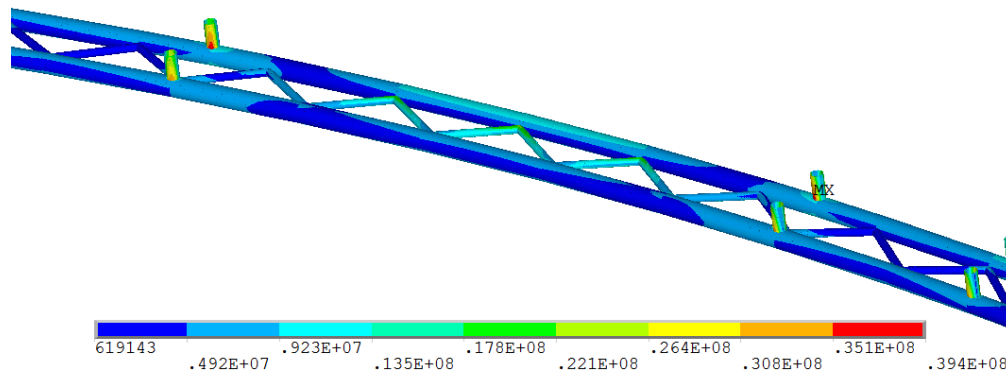


Figure 7.41: Maximum mid bridge stress with connection shafts [Pa], T = 6.75s

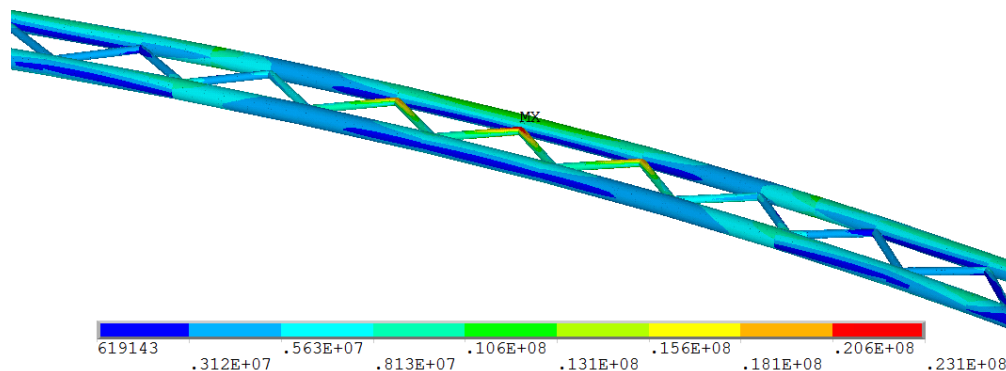


Figure 7.42: Maximum mid bridge stress without connection shafts [Pa], T = 6.75s

The maximum stresses for the lower part all appears in the middle of the bridge span for the three longest wave periods. For the upper part, it appears in the centered shafts for T = 6.25s and T = 6.75s. For a wave period of T = 6.50s, it appears in the outer most shafts. This can be seen inn Figure 7.43.

The values of the von Mises stresses (σ_{VM}) is given in Table 7.18. Based on this and the considerations above, the wave with a period of 6.25s is considered the worst due to the highest response in the shafts.

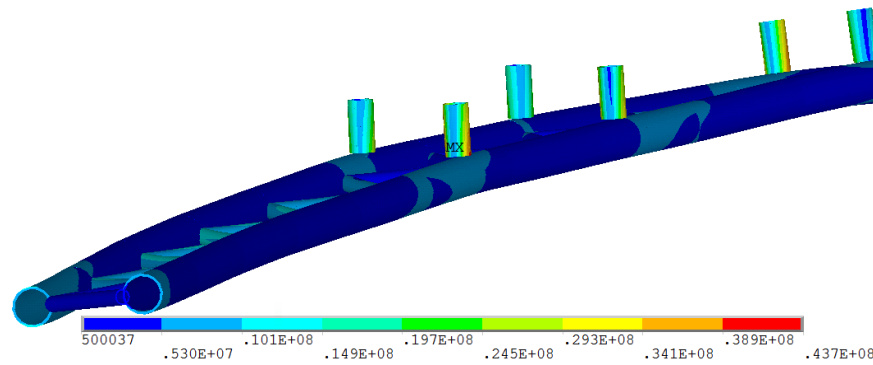
Figure 7.43: Maximum stress with connection shafts for [Pa], $T = 6.50s$

Table 7.18: Maximum von Mises stress

Wave period [s]	σ_{VM} , lower part [MPa]	Where [-]	σ_{VM} , shafts [MPa]	Where [-]
6.25	23.5	Center, bracing	46.2	Center, shafts
6.50	24.1	Center, bracing	43.7	Ends, shafts
6.75	23.1	Center, bracing	43.3	Center, shafts

7.5.2 Bending and Torsional Moments due to Harmonic Loading

The moments under consideration in this section are the bending moments about global Y- and Z-axis and rotational moment. The rotational moment is about the global X-axis. The moments are sampled for the main tunnels and the bracing, with both maximum and minimum values. Sampling maximum and minimum moments for these three different structural parts of the bridge, allows for a better understanding of the total response. It also opens for better comparison with the other responses mentioned in the previous sections in this chapter for the most critical wave period.

7.5.2.1 Bending Moment about Global Y-axis

The results for bending moment about the global Y-axis is given in Figure 7.44. The belonging moment magnitudes for the three longest wave periods are given in Table 7.19. These three periods are the ones which have the highest response for both the main tunnels and the bracing elements. The maximum and minimum moments for the bracing elements have small changes, compared to the bending for the outer and inner main tunnels.

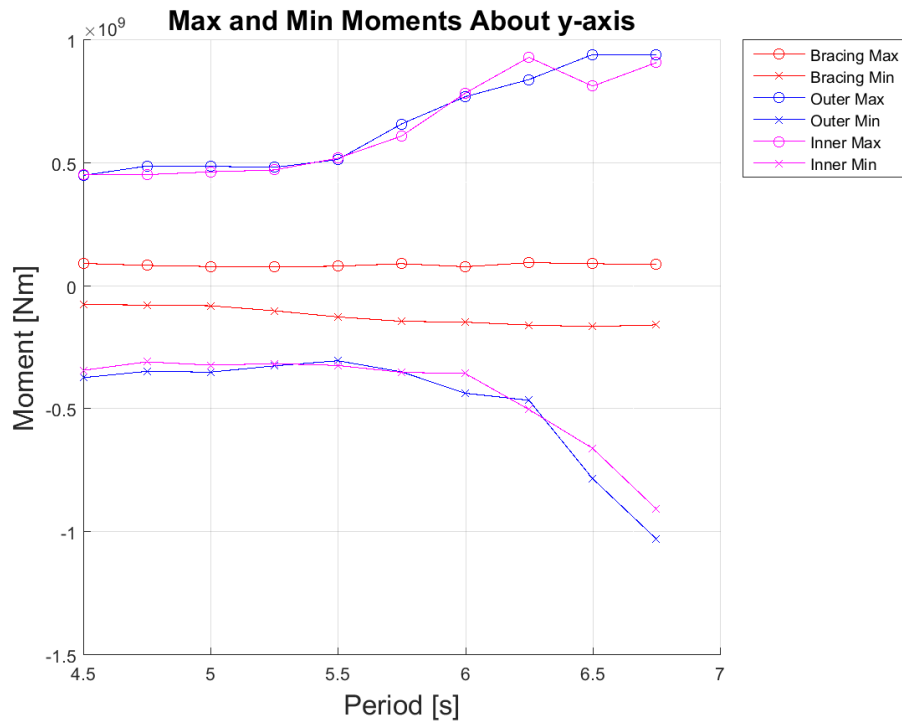


Figure 7.44: Maximum and minimum bending moment about Y-axis

For the bending moment about Y-axis, both maximum and minimum bending moment occurs in the outer main tunnel for the longest wave period of 6.75 seconds. This is shown by the blue lines in Figure 7.44. The minimum bending moment occurs in the middle of the main span, while the maximum bending moment occurs at the shafts closest to the ship channel. This can be observed in Figure 7.45.

Table 7.19: Bending moment about global Y-axis

Wave Period [s]	Bracing [MNm]		Outer tunnel [MNm]		Inner tunnel [MNm]	
	max	min	max	min	max	min
6.25	95.4	-158.5	839.7	-464.3	930.0	-501.6
6.50	91.3	-164.4	941.6	-782.6	812.9	-659.7
6.75	87.3	-157.7	939.0	-1027.7	908.6	-905.8

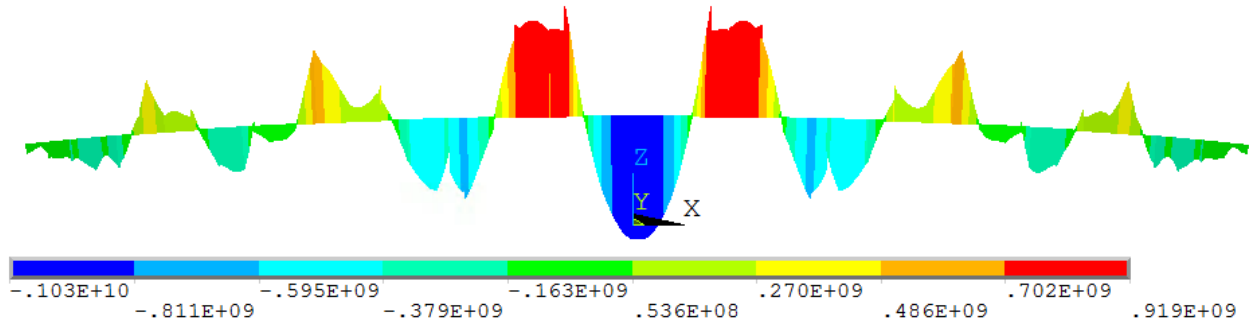


Figure 7.45: Maximum bending moment about Y-axis [Nm], T=6.75s

7.5.2.2 Bending Moment about Global Z-axis

The maximum and minimum bending moment about Z-axis for the bridge parts are shown in Figure 7.46, along with the magnitudes for the three highest periods in Table 7.20. The moments in the bracing elements are more or less constant for all wave periods. The critical bridge parts are the inner and outer main tunnels, where the moment increases with the period. Except for the outer minimum moment, all maximum bending moments about Z-axis occur in the longest wave period, T = 6.75.

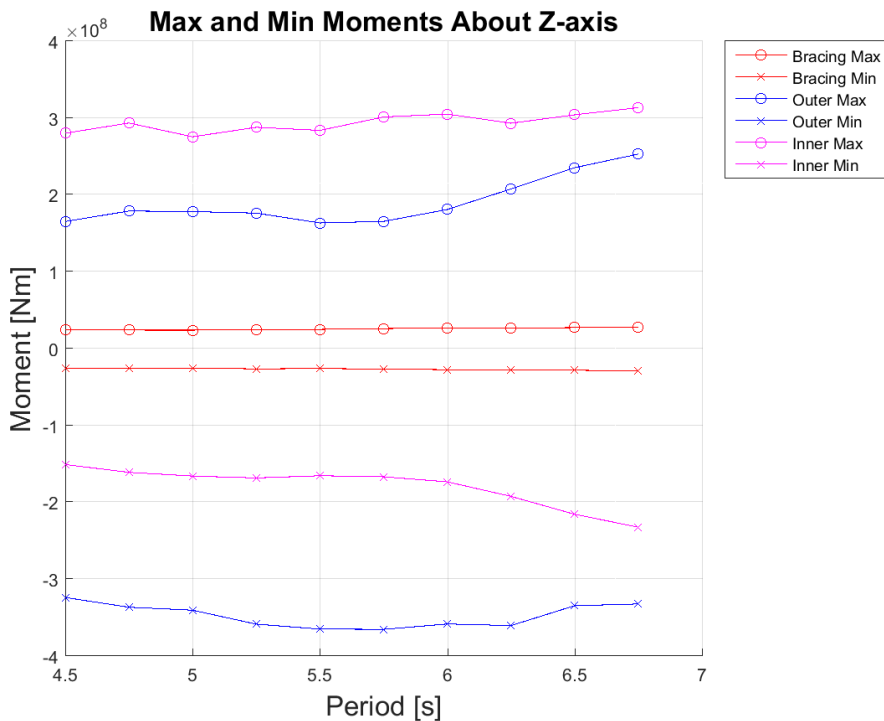


Figure 7.46: Maximum and minimum bending moment about Z-axis

Table 7.20: Bending moment about global Z-axis

Wave Period [s]	Bracing [MNm]		Outer tunnel [MNm]		Inner tunnel [MNm]	
	max	min	max	min	max	min
6.25	26.8	-27.9	207.7	-360.4	293.2	-192.2
6.50	27.3	-28.1	235.4	-334.5	304.1	-215.5
6.75	27.7	-29.1	253.0	-332.2	313.4	-232.4

The plots of the maximum and minimum bending moments about global Z-axis are shown in Figure 7.47 and 7.48, respectively. The maximum bending moment occurs in the inner main tunnel below the fifth pontoon from shore, in the connection shaft. The minimum moment occurs in the connection between shaft and outer tunnel at the pontoon closest to the ship channel. As seen before, the highest von Mises and bending moment about several axes occur in the bottom of the shafts closest to the channel. This is a very important point of the structure, where several kinds of responses are at their maximum.

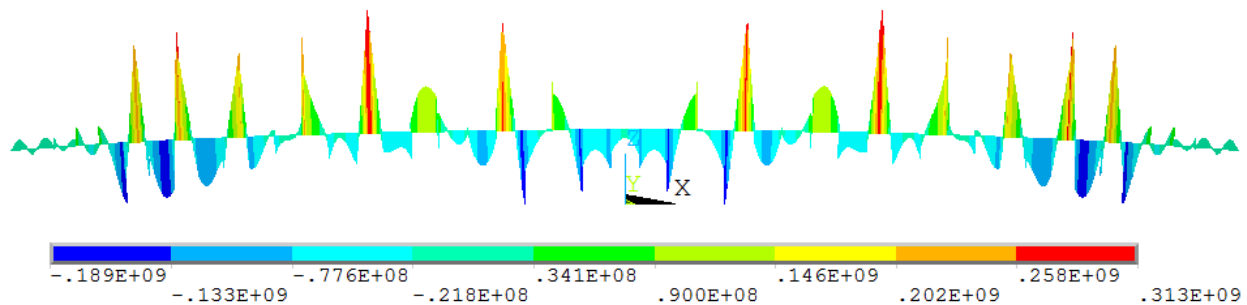


Figure 7.47: Maximum bending moment about global Z-axis in inner main tunnel [Nm], T=6.75s

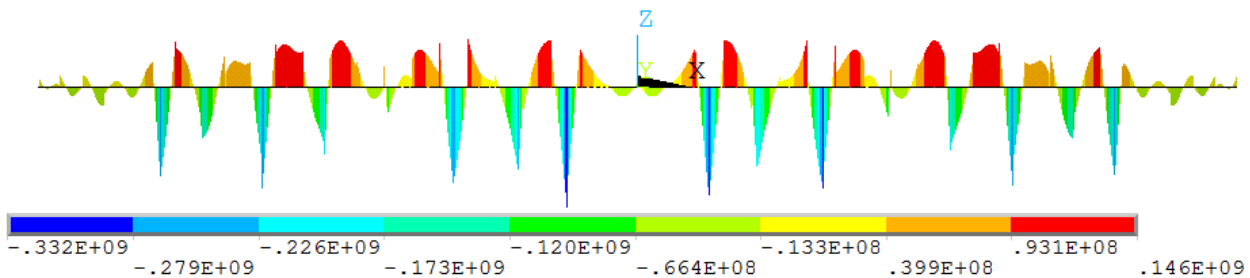


Figure 7.48: Minimum bending moment about global Z-axis in outer main tunnel [Nm], T=6.75s

7.5.2.3 Rotational Moment about Global X-Axis

The rotational moments for the submerged floating tunnel are of the same magnitude as the bending moment about Y-axis. As for the other moments, the maximum and minimum bracing moments are more or less constant for all wave periods. The maximum and minimum rotational moments for the outer and inner main tunnels vary less than the bending moments, but there is a small increase/decrease as the wave period increases. The maximum rotational moment occurs at $T=6.25$ seconds, but the difference is not big compared to the to higher periods.

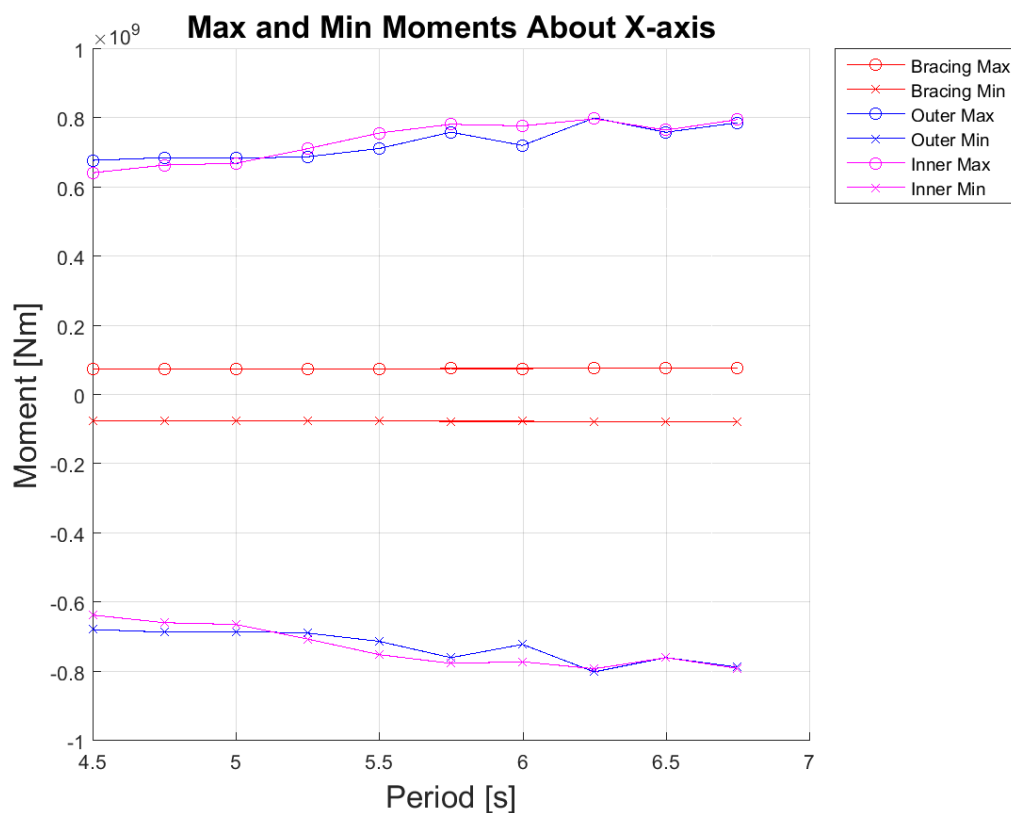


Figure 7.49: Maximum and minimum torsional moment about X-axis

While Figure 7.49 show the torsional moments for the different bridge parts, Table 7.21 shows the magnitude of the moments for the three highest wave periods. The moment is much smaller for the bracing elements than the tunnel pipes, as it is for the bending moments. Again, it is clear that the most critical geometrical part of the bridge are the main tunnels. This is off course when only considering the lower parts.

Table 7.21: Rotational moment about global X-axis

Wave Period[s]	Bracing [MNm]		Outer tunnel [MNm]		Inner tunnel [MNm]	
	max	min	max	min	max	min
6.25	77.0	-76.9	801.0	-801.0	798.5	-792.1
6.50	77.7	-77.7	759.5	-759.5	765.8	-759.9
6.75	77.0	-76.9	787.2	-787.2	796.3	-790.8

Figure 7.50 shows both the maximum and minimum torsional moments for the wave period equal to 6.25. This is also the highest torsional moments for all periods, and both minimum and maximum occur in the same time increment. The maximum and minimum values are equal, but with different sign. This is because the geometry of the bridge is built in the origin of the global X-axis, causing opposite magnitudes on opposite sides of the origo. The highest values occur at the biggest spans between pontoons, in the ship channel and at the spans on the sides.

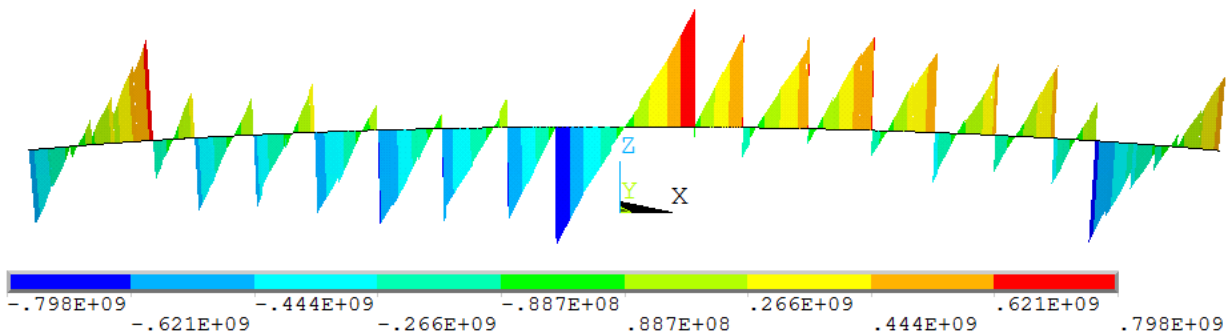


Figure 7.50: Maximum and minimum torsional moment about X-axis for inner main tunnel [Nm], $T = 6.25s$

Figure 7.51 is included to show the moment diagram for the bracing elements. The figure shows the maximum and minimum bending moment about the Y-axis for a wave period of $T=6.75$ seconds. Moment plots of the bracings have not been included previously due to the small moments occurring in this section.

Figure 7.51 shows both the vertical and horizontal view of the bending moments about global Y-axis in the bracing. For the vertical view, one can observe the moments from each bracing elements, crossing each other as they all are 45 degrees on the main tunnels. The maximum and minimum moment occurs at the largest spacings between pontoons, being at the ship channel and at the bridge ends. Here, the distance is approximately 400-500 meters between pontoons or pontoon and land.

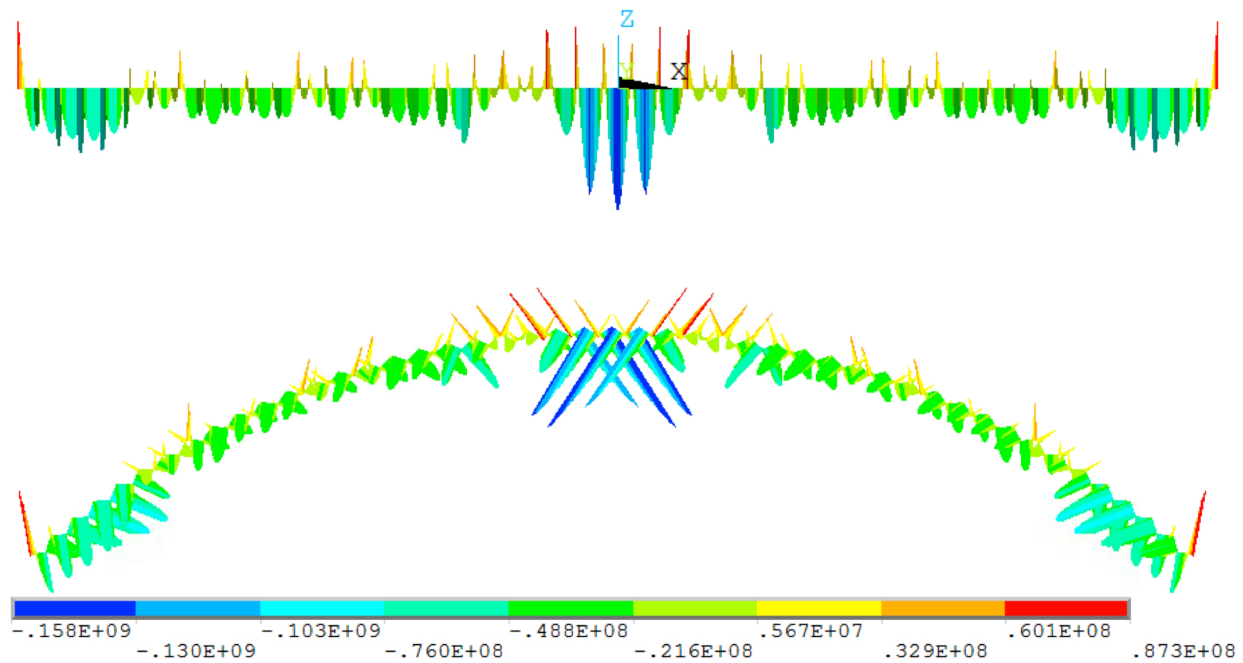


Figure 7.51: Maximum and minimum bending moment about the Y-axis for bracing [Nm], $T = 6.75s$

7.5.2.4 Worst Harmonic Wave Period

When defining the worst harmonic wave period, all of the responses described above need to be taken into account. When the structures displaces and rotates, stresses and moments occur as an effect of this. This means that displacements and rotations can give good indications of the worst harmonic wave period, but the stresses and moments are eventually what decides which period is deemed the most critical for the structure.

The biggest responses has clearly been for the three longest wave periods. In Table 7.22, a summarized list for the responses is given. The period with the highest magnitude for the chosen response is marked with an X. This maximum response includes both maximum and minimum responses. If two or more periods are crossed of as highest response, it means that the difference is insignificant.

The wave period causing the highest responses is $T = 6.75s$. Even though $T = 6.25s$ has a higher number of maximum/minimum responses, the maximum moments occur with the longest wave period. The wave period $T = 6.50s$ has no maximum or minimum values. The maximum

Table 7.22: Summarized grading of harmonic responses

Response	T = 6.25s	T = 6.50s	T = 6.75
Rotation about X-axis	X		
Rotation about Y-axis	X		
Rotation about Z-axis			X
Rotational sum	X		
Vertical Displacement	X		
Von Mises stress	X		X
Bending moment about Y-axis			X
Bending moment about Z-axis			X
Rotational moment about X-axis	X		X

responses for the wave period are given in Table 7.23. The displacement and rotation values are for the whole structure, the von mises stress for the whole structure except the pontoons and the moments are for the lower parts of the structure. Only maximum values are given for the von Mises stress and the rotations.

Table 7.23: Maximum responses for 50 year return period wave

Response	Magnitude	Unit
Displacement, max	1.11	[m]
Displacement, min	-0.26	[m]
Rotation about X-axis	0.015	[rad]
Rotation about Y-axis	0.006	[rad]
Rotation about Z-axis	0.001	[rad]
Rotational Sum	0.015	[rad]
Von Mises	43.8	[MPa]
Bending moment about Y-axis, max	939	[MNm]
Bending moment about Y-axis, min	-1028	[MNm]
Bending moment about Z-axis, max	313	[MNm]
Bending moment about Z-axis, min	-332	[MNm]
Torsional moment, max	796	[MNm]
Torsional moment, min	-791	[MNm]

The rest of the plots for the maximum wave periods is given in Appendix D.3.4. This includes displacement, rotation, stresses and moments. The plots only considers the maximum and minimum response for each time increment during the harmonic analysis of the structure.

7.6 Global Irregular Wave Analysis Results

This section contains the results from the irregular wave loading analysis in ANSYS. As explained in Section 6.7, the irregular wave loading is represented by a JONSWAP spectrum. The time span of the analysis is from 0 to 300 second, where the results from 40-300 seconds has been sampled for post processing. Due to the fact that the 50 year return period maximum wave is estimated based on three a hour sea state, the irregular analysis should be three hours long in order to compare results between the regular and irregular maximum responses. As a results of memory limitations when solving the analyses, as explained in Section 6.1, maximum analysis duration is 300s. When only analyzing 300 seconds, the maximum responses are likely to not occur. These responses can be estimated by using the variance and mean for the sampled data and a Gumbel maximum distribution.

As for the harmonic analysis, the included responses from the analysis results are:

- Rotation - Rotation about the global X-, Y- and Z-axis and rotational sum
- Displacement - Global maximum and minimum displacement
- Stress - Global maximum and minimum von Mises stress
- Moment - Elemental maximum and minimum bending and torsional moments

7.6.1 Maximum Global Response for a 300 Second Irregular Wave Loading Analysis

The first step to estimate the maximum 3-hour responses is to sample the maximum and minimum responses for each time step for the whole structure. By doing this, one can identify the node or element with the highest response. The responses for these nodes and elements are sampled for all time steps of the analysis. By sampling the results for all time steps, the variance and mean value can be calculated for the 300 second long analysis. This is then used to estimate the expected maximum response for a 3-hour sea state with a maximum Gumbel distribution.

Figure 7.52 shows the maximum and minimum rotation about the global axes for the SFT model in irregular wave loading. The biggest rotations are about the X-axis. This is because of the wave

direction, causing the two main tunnels to displace differently. This creates a rotation about the center between the tunnel pipes.

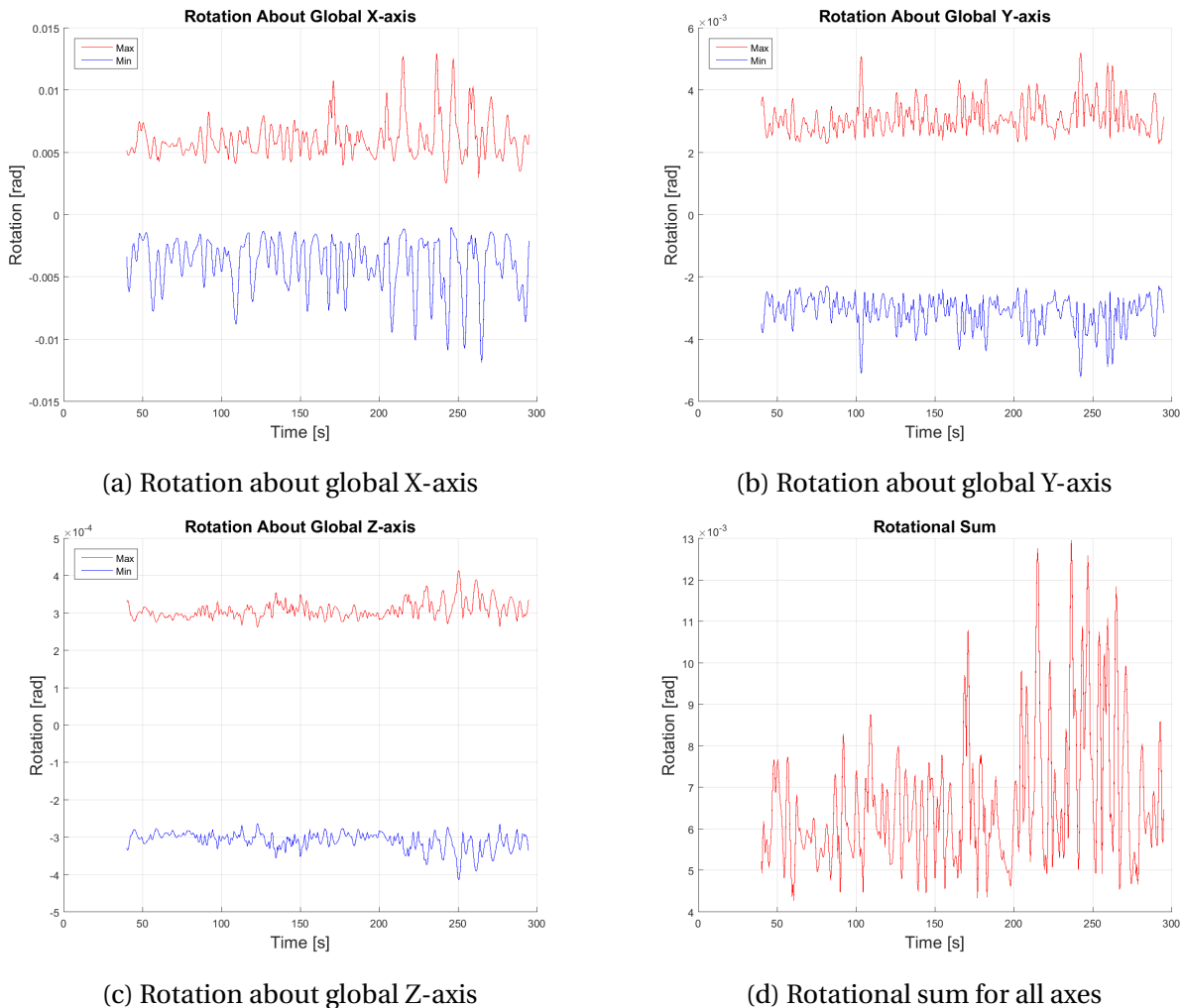


Figure 7.52: Maximum and minimum rotation about the global axes for irregular wave loading

The maximum and minimum bridge displacement is, as for the harmonic analysis, sampled for the lower and upper part of the bridge. The lower part consists of the main tunnels and the bracing in between. The upper part is the connection shafts and the pontoons. The displacements are shown in Figure 7.53 and as for the rotations, the highest responses occur towards the end of the analysis time. This is just due to the irregular wave loading. As for the harmonic wave loading, the highest displacement occurs in the ends off the pontoons when the main tunnels rotate about the global X-axis.

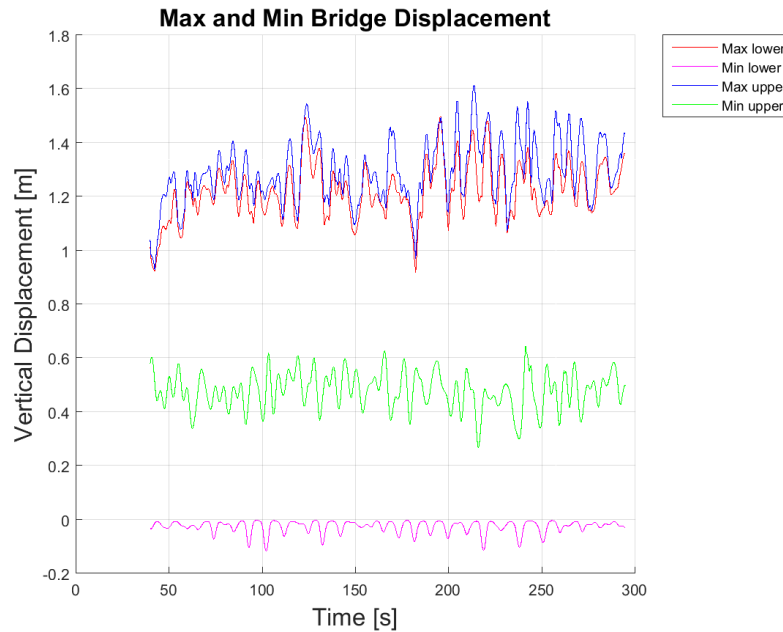


Figure 7.53: Maximum and minimum displacement for irregular wave loading

The plots for the maximum moments registered along the structure are shown in Figures 7.54, 7.55a and 7.55b. All given results concern the lower parts of the SFT. *Bracing* is naturally the bracing elements between the main tunnel, *outer* is the outer main tunnel and *inner* is the inner main tunnel. These figures show maximum and minimum sampled responses for the lower part of the structure, and not for any specific nodes or elements.

When all maximum and minimum response is sampled for the time series, the node and element numbers where these responses occur are found. The next task is to get the response for these items for throughout the time series.

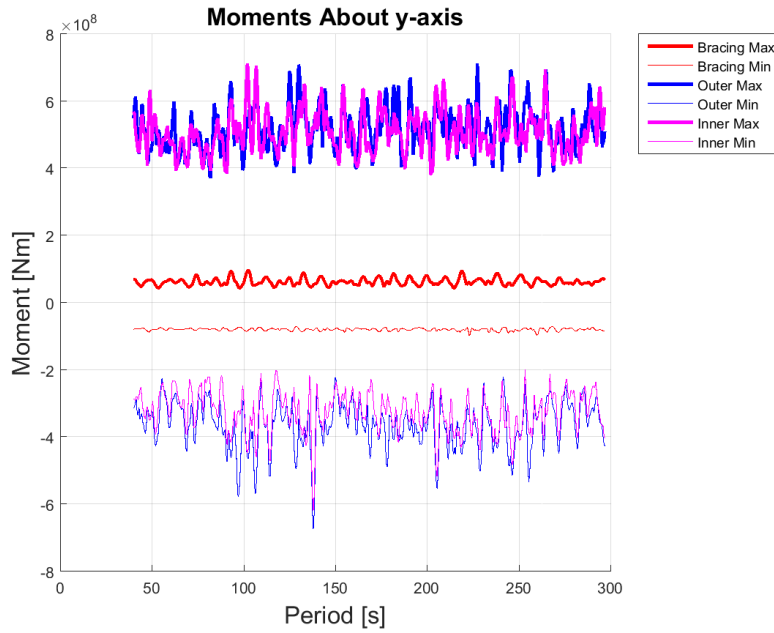
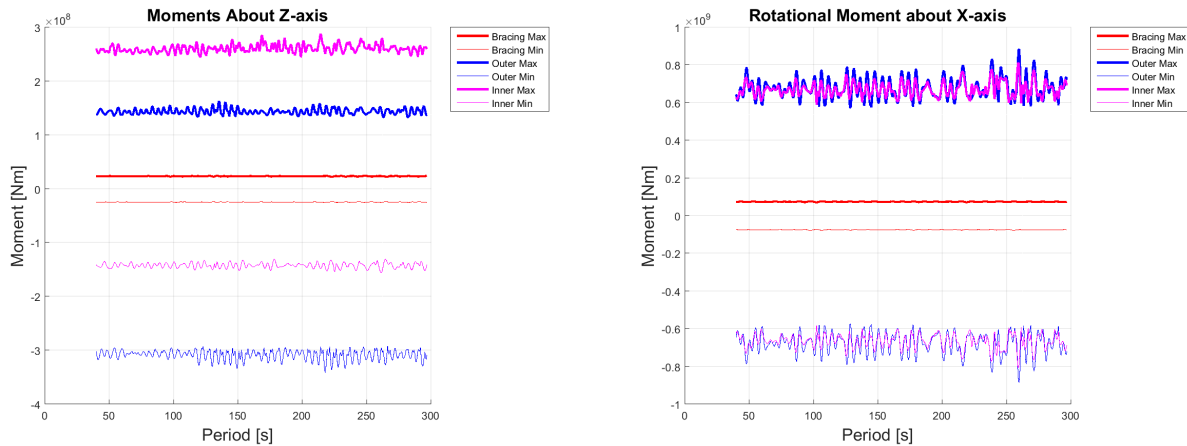


Figure 7.54: Maximum and minimum bending moment about Y-axis for irregular wave loading



(a) Bending moment about Z-axis

(b) Torsional moment about X-axis

Figure 7.55: Maximum and minimum moments for the lower part of the structure

7.6.2 Irregular 3-hour Sea State Results and Comparison

The response plots for the nodes and elements where maximum or minimum magnitudes occur, are all given in Appendix D.3.6. The appendix includes both nodal and elemental responses throughout the analysis time and the moment diagrams for the time instants with the highest moments. As an example, the bending moment about the global Z-axis is shown in Figure 7.56. What is important to understand, is that these plots is not the same as the ones in Section 7.6.1. This plot shows the bending moment for specific elements, while for the figures in Section 7.6.1 show the maximum and minimum responses for each time step throughout the whole structure.

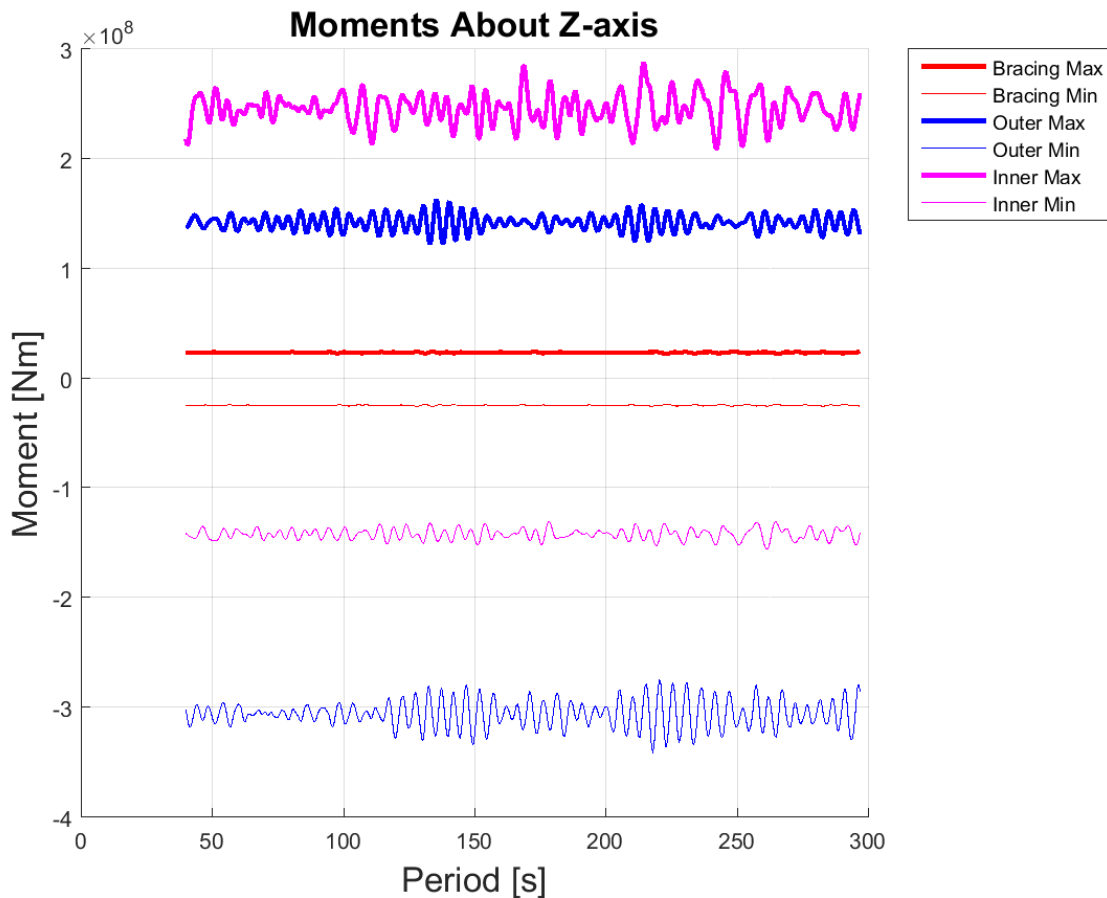


Figure 7.56: Bending moment about global Z-axis for the elements where maximum and minimum moment occurs

It is from Figure 7.56 and the other figures in Appendix D.3.6 that the variance and mean for the responses can be estimated. As explained in Section 4.5 about the Gumbel distribution, the

variance and mean for the responses from the 300 second irregular analysis is used to estimate the maximum 3 hour sea state responses. Both the most probable and the expected maximum values can be estimated from these values. The estimated extremes are shown in Table 7.24. The column "*3h most prob.*" shows the most probable extremes while "*3h max*" shows the expected maximum extremes for the 3-hour irregular sea state. "*300s*" is the maximum and minimum responses for the 300 second long ANSYS irregular wave analysis, while "*Harmonic*" shows the maximum and minimum responses for the 50 year return period harmonic wave.

Table 7.24: Comparison of dynamic responses for different wave loading

Response	Harmonic	300s	3h most. prob	3h max	Unit
Displacement, max	1.11	1.63	1.82	1.85	[m]
Von Mises	43.8	42.8	162.2	164.1	[MPa]
My, max	939	712.3	835.6	854.2	[MNm]
My, min	-1027.7	-673.8	-710.5	-727.6	[MNm]
Mz, max	313.4	288.5	299.3	301.4	[MNm]
Mz, min	-333.2	-341.3	-353.9	-355.7	[MNm]
Mx rot, max	796.3	883.6	921.6	931.4	[MNm]
Mx rot, min	-790.8	-883.6	-921.6	-931.4	[MNm]

From the Reinertsen Olav Olsen study (Group, 2013, p. 48), the maximum end moments for a static bridge with maximum weight is 1172 MNm. It doesn't say whether this is for the complete cross sections or for the outer or inner main tunnels. Considering that this also is a static moment, the value is only used as a comparison for the magnitude. When comparing with moments in Table 7.24 the results are considered go. This is due to the fact that the moments are in the same range as the maximum static moment from the Reinertsen Olav Olsen study.

When comparing the displacements for the different analysis and estimated results, it is clear that the harmonic analysis has the smallest displacement. The maximum displacement for the 3-hour sea state is a total of 0.74 meters higher. When comparing the moments, it is important to remember that the maximum displacements for each analysis not necessarily occur at the same time as the maximum or minimum moments. When this is said, the maximum moment about the global Y-axis actually occurs at the same time at the minimum vertical displacement. This is to be expected, because the difference in vertical displacement causes moments about the global Y-axis.

The highest moments about Y-axis happens for the harmonic analysis, in the middle of the main span. This is because of the difference in displacement between the middle of the bridge and the pontoons closest to the bridge center, is higher than for the irregular wave analysis. This goes for both the minimum and maximum moment about the Y-axis. This moment occurs for the same displacement shape, with small differences in maximum and minimum. This causes the min value to be registered for one time increment, while the maximum value is registered for another. The figures showing the maximum and minimum moments with belonging displacement shape i given in Appendix D.3.5.

For the bending moment about Z-axis and rotational moment about X-axis, the results are opposite. When comparing with the most probable maximum response for the 3-hour sea state the moments have higher magnitude, except for maximum bending moment about global Z-axis. This moment is higher for the harmonic analysis.

The main reason for the different responses, is simply because the ANSYS model reacts differently to the harmonic and irregular wave loading. This is only natural, considering the fundamental differences for the two loadings. The maximum and minimum moments and displacement shapes are still similar. This is, when considering that the harmonic maximum wave is estimated based on the JONSWAP spectrum defining the irregular wave loading, the reason for the similar response magnitudes.

Chapter 8

Discussion

As the results for the pontoon and global STF are described, a final discussion can be made. It concerns all the results presented in Chapter 7 and lays the foundation for a final conclusion in Chapter 9.

The final global mesh size for the SFT analyses is 2.0 meters per element. This mesh size is the mesh size for all the pipe and beam elements of the structure. It is based on both the decreasing mesh size analysis and the memory limitations connected to the ANSYS license and remote computers used. The mesh size could have been even smaller, but the amount of computational memory needed for the dynamic wave analyses would become too high, and impossible to perform with the given license. The analyses actually crashed numerous times due to the fact that they were too big to be solved by the allocated memory.

The results of the optimized mesh process served as a tool for controlling that different analyses in ANSYS completed as they should. The optimized mesh allowed for faster solving and results that were accurate enough for this stage of the analyses. It was used to save time in the early stages of the thesis, in order to prepare the harmonic and irregular wave analyses. The criteria for the optimized mesh size was based on the static results. It was therefore not used for the final time dependent analyses.

The pontoon analysis, carried out in both HydroD and ANSYS, gave good results. The characteristics for the final pontoon was established, a pontoon comparison between the two different

geometries was carried out and a verification of the ANSYS ocean input was completed. The simplified and final pontoon geometry proved to have almost identical restoring in heave. This was as expected, due to the water plane area being very similar for both configurations. The roll restoring was higher and the pitch restoring was lower. This is also in coherence with the geometrical differences of the pontoons, where the final geometry was wider, but less full in the front and aft.

A model of the final pontoon geometry was made in ANSYS with the pontoon characteristics from HydroD. In order to simulate pure heave, roll and pitch motions, the ANSYS model was created with the possibility of multiple boundary conditions, springs and dampers. The results from a beam and head harmonic wave loading were used to create RAOs for the model. These models were compared with the RAOs from HydroD for the same geometry. The comparison gave answers confirming the pontoon modeling in ANSYS. The main outlines, such as RAO shapes, were good for the head sea heave and pitch RAOs. Peaks and maximum responses occurred in the expected frequency ranges. The amplitude was still deviating from the assumed correct results in HydroD. This is most probably due to the added mass representation and the boundary conditions of the model. The added mass is frequency dependent for the surface piercing pontoon, and should have been modeled this way. This was not done due to difficulties with added mass representation and was therefore discarded. The overall pontoon results were still considered good for further analyses.

The characteristics for the final pontoon were then implemented in the global model. This included the restoring coefficients and frequency dependent damping for heave, pitch and roll. At this point the static analyses could be carried out with different kinds of mean water levels. In this stage of the thesis a lot of work was done in order to assign correct ballast for the structure. Different measurements were carried out and the final solution was to add extra ballast in the main tunnels beneath the pontoons. The smaller distance between pontoons, the more ballast. The ballast distribution was coarse in order to assimilate how it could be done in the real model. This resulted in some vertical displacement for the static analysis. This is of course affecting the displacements for the wave analyses, and needs to be taken into account when discussing the vertical displacement for the dynamic results.

A static analysis was also performed for a maximum and minimum tide. The displacement was almost equal to the change in tide, which means that the bridge follows the ocean levels, relieving the ends from moments due to resisting against the buoyancy force. However, this causes moment due to the bending of the pipes. The displacement is considered high, and has to be discussed in comparison to the harmonic and irregular wave results. The fact that the bridge follows the ocean tide, is assumed to be a good result. The static analysis for the mean sea level shows small displacement differences between the main tunnels along the x-axis, which implies small rotations. This means that the two tunnels are well ballasted compared to each other.

The modal analysis includes both an eigenfrequency and a mass participation analysis. Knowing the eigenfrequencies is a good way of understanding responses of the bridge in relation to the frequency of the loading. The results of the eigenfrequency analysis was good compared to the results obtained from the Reinertsen Olav Olsen study. With a mean deviation of 6.4 %, the modeling of the structure is considered accurate enough. The 10 first mode shapes are also very similar, indicating the same thing. The modal mass participation analysis was carried out after the eigenfrequency analysis. This is was done in order to improve the model towards the dynamic analyses, by calculating the Rayleigh damping coefficients. The coefficients were used to model Rayleigh damping in the dynamic analysis. The model still has no viscous damping, which would be necessary to obtain a true representation of the structure. This is outside the thesis objectives, and was therefore not included.

As input for the harmonic wave loading, an estimated 50 year return period wave was used. This wave was estimated with a Rayleigh distribution, based on the 50 year return period significant wave height, given by a JONSWAP spectrum. The maximum harmonic wave height of 4.85 meters seems reasonable in comparison to a 2.14 meter significant wave height. It is still very hard to decide which percentile to use when estimating such parameters, meaning that there is an uncertainty to the magnitude. In order to find the highest responses for the bridge, a range of periods around the spectral peak period of 4.8 seconds were tested in combination with the wave height.

Some of the responses for the periods were as expected. The highest bending moments about global Y-axis occurred in the middle main span and at the span between shore and the outer-

most pontoon. This was the case for the main tunnels and the bracing elements. The torsional maximum moments about X-axis, both negative and positive, occurred at the same spans or at the supports of these spans. Both moments have their maximum magnitudes in these regions due to the long distance between supports, either being pontoon to pontoon or pontoon to shore. The moment magnitudes about the X- and Y-axes are higher than for the bending moment about Z-axis. The maximum bending about Z-axis occurs in the vertical shafts between the pontoons and the main tunnels. It is natural that the maximum moment occur at this point, due to the fact that this part of the structure is the only part where the force moves vertically through the pipe elements. The smallest moments are in the bracings and highest close to the pontoons. It is realistic to assume that this is because of the wave-pontoon interaction. The forces are distributed from the pontoons, through the shafts to the main tunnels and then from the main tunnels to the bracing.

The maximum stresses for the lower part of the bridge occurs in the connection between the braces and main tunnels in the center of the bridge and in between the shore and the first pontoon. This is most likely due to rotation between the main pipes, causing moment and stresses in the connection between the main tunnels.

The magnitude of the stresses and moments seem reasonable when compared to the Reinertsen Olav Olsen Group (Group, 2013) maximum end bending moments for a fully loaded static analysis. This only works as a comparison for response magnitude, due to the fact that the moments in this thesis are results of dynamic analyses, not static.

While the moments and stress responses seem logical, the displacement and rotations responses might seem a bit off at first. The responses did often stabilize around a positive or negative displacement, and not the mean of the static analysis. For some periods, the bridge had a rotation about X-axis with a negative or positive mean. This implies that the model had a positive or negative rotation throughout the whole dynamic analysis. There can be many answers to why this happens. One on them is that for example the model rotation stabilizes around a certain angle for a certain wave period. As the displacement or angle is within tolerable magnitudes, it is not deemed a big problem.

The worst harmonic 50 year return period wave, was the wave with a period of 6.75 seconds

and height 4.85 meters. The responses for this wave could now be compared to an irregular wave response. The length of the irregular wave response had to be 3 hours long. This was because the maximum harmonic wave was estimated based on a 3-hour sea state. This was not feasible due to computational limitations. An irregular analysis lasting 300 seconds became the maximum duration for a feasible analysis. The variance and mean for the maximum responses for the analysis was computed and used to estimate the three hour maximum responses. This means that the variance and mean of the 3 hour sea state is assumed to be the same as for the 300 second analysis. This is of course a simplification which introduces uncertainties to the results of the maximum response. It was still the only way to estimate a maximum 50 year return period response for the JONSWAP spectrum, when a full analysis for the 3-hour sea state was unfeasible.

The responses for the harmonic maximum analysis and 300 second irregular analysis are in the same magnitude order. The moment and stress diagrams also have the same outlines, which implies that the harmonic maximum loading and the irregular loading has similar responses. While the moments about global Y-axis are higher for the harmonic analysis, the moments about the Z-axis are pretty similar. The moments about the X-axis are highest for the irregular analysis. The magnitudes are also in coherence with the magnitudes from the Reinertsen Olav Olsen study (Group, 2013).

The moment diagrams for the irregular wave loading have the same outlines as for the harmonic loading. This means that the maximum moments about X- and Y-axis occur at the longest spans between supports, or at the supports. The moments in the bracing is smaller than for the main tunnels, as explained for the harmonic moment results. The von Mises stress also occurs at the same locations as for the maximum harmonic wave loading.

The natural causes for the differences between the responses origins from the fundamental difference of the irregular and regular wave loading. When this is said, it is important to have in mind that the harmonic wave loading amplitude and period is estimated from the irregular wave spectrum. This is most likely the reason for the equal magnitudes, moment diagram shapes and displacement shapes for the two different loads.

Chapter 9

Concluding Remarks

9.1 Conclusion

The modeling of a global submerged floating tunnel is considered a success. The joint properties of the whole hydro-elastic system have been accounted for with belonging static and dynamic response analyses. The hydrodynamic and structural properties have been modeled in the structural analysis software ANSYS Mechanical. Marine bridge loading has been described and methods for both static and dynamic response analysis are elaborated with relevant numerical algorithms.

The Wadam pontoon comparison of the restoring coefficients are shown in Table 9.1. They coincide with the geometrical outlines of the two pontoons.

Table 9.1: Restoring Coefficients

Coefficients	Heave [N/m]	Roll [N/rad]	Pitch [N/rad]
Simplified Geometry	$1.59 \cdot 10^7$	$5.31 \cdot 10^8$	$8.50 \cdot 10^9$
Final Geometry	$1.55 \cdot 10^7$	$6.05 \cdot 10^8$	$5.05 \cdot 10^9$

The pontoon RAO comparison for ANSYS and Wadam proves that the modeling in ANSYS has good features. The uncertainties are the added mass representation and the boundary conditions created to assimilate pure heave, roll and pitch motion. The challenges due to boundary

conditions are not present in the global model, which makes the pontoon representation feasible for the analysis of the complete bridge.

The results for the static and modal analysis are reasonable. The static analysis proves a close to neutrally buoyant model with small vertical displacements. The maximum displacement is 24 cm while the minimum is -17 cm. The modal analysis results, where both the eigenfrequencies, mode shapes and directional mass participation are accounted for, are good. The eigenfrequencies, compared to the Reinertsen Olav Olsen study, has a mean deviation of 6.4%. The first eigenfrequency has a 19.2% difference while number four and five has 1.3% difference. The eigenperiods range for the 25 first modes, from mode 25 to 1, is 5.1 - 45.1 seconds. The direction of the first 10 mode shapes coincide with the compared study.

Dynamic analysis results with both harmonic and irregular wave loading are good. The harmonic wave with the highest response has a height of 4.85 meters and a period 6.75 seconds. It is estimated from the irregular JONSWAP spectrum in the fjord. The most important results for the main tunnels and bracing pipes are presented in Table 9.2. The maximum bending and torsional moments occur at the largest spans of the bridge, meaning at the middle and the ends. While moments about global X- and Z-axis occurs in the main pipes at the pontoon supports or at shore, the bending moments about Y-axis occur in the main tunnels between the supports in the largest spans.

Table 9.2: Comparison of maximum dynamic responses

Response	Harmonic	300s	3h most. prob	3h max	Unit
Displacement, max	1.11	1.63	1.82	1.85	[m]
Von Mises	43.8	42.8	162.2	164.1	[MPa]
My, max	939	712.3	835.6	854.2	[MNm]
My, min	-1027.7	-673.8	-710.5	-727.6	[MNm]
Mz, max	313.4	288.5	299.3	301.4	[MNm]
Mz, min	-333.2	-341.3	-353.9	-355.7	[MNm]
Mx rot, max	796.3	883.6	921.6	931.4	[MNm]
Mx rot, min	-790.8	-883.6	-921.6	-931.4	[MNm]

The maximum irregular results are estimated based on a shorter irregular analysis. These results are good compared to both the harmonic maximum wave amplitude results, considering both magnitude and direction. The maximum responses are split between the harmonic analysis and

maximum estimated irregular analysis.

9.2 Recommendations for Further Work

There are several points for recommendations for further work, which mainly can be divided into two groups. The first group is further structural modeling to improve and make the model more realistic. The second group is continued analyses with different load conditions.

Further structural modeling:

- Vertical curvature: The bridge has not been modeled with vertical curvature. This is another step in the direction of having a final model even closer to the proposed final concept.
- Damping properties: For a more complete model, the damping properties of the bridge can be improved. Viscous damping is not included, which would improve the model.
- Concrete modeling: Due to limited knowledge about concrete properties, a verification of the concrete modeling should be carried out to improve the verification of the results.

Continued Analyses:

- Different load combinations: It would be beneficial to introduce different kinds of load combinations and running both static and dynamic analyses. The load combinations could be for example maximum traffic loading in combination with lowest tide and worst harmonic wave. This would push the bridge towards the maximum loading in terms of displacement from static position and therefore maximum moments and stresses. Other combinations would also be of interest.
- Current implementation: It would be interesting to implement current loading both in combination and by its own, to check the model response.
- Complete irregular wave analysis: Due to the challenges with memory limitations, a complete irregular analysis was never performed. It would be interesting to have a complete irregular JONSWAP wave analysis to compare with the estimated maximum Gumbel responses and the Rayleigh harmonic wave. The sampling frequency could also have been increased to include all possible peaks in the responses.

Bibliography

(2004). Eurocode 2: Design of concrete structures - part 1-1: General rules and rules for buildings.

(2014). Dnv-os-j101 design of offshore wind turbine structures.

(2016). *Ansys Documentation 16.2.*

Administration, N. P. R. (2009). *Håndbok 185 Bruprosjektering.*

broer.no. Bergsøysundbrua.

broer.no. Nordhordlandsbrua.

Chowdhury, I. and Dasgupta, S. P. (2003). Computation of rayleigh damping coefficients for large systems.

Ehlers, S. (2012). Particle swarm algorithm-based optimization for high strength steel structures. *Journal of Ship Production and Design.*

Faltinsen, O. M. (1990). *Sea Loads On Ships And Offshore Structures.* Cambridge University Press.

Group, R. O. (2013). Mulighetsstudie for kryssing av sognedfjorden - nedykket rørbru.

Haver, S. (2016). *Stochastic Description of Ocean Waves & Response Analysis and Prediction of Extremes.*

Holtberget, S. H. (2015). Brukonferansen 2015: Fergefri e39 - fjordkryssningsprosjektet, multispansuspension bridge on floating foundations.

- Kennedy, J. and Eberhart, R. (1995). *Particle swarm optimization, Proceedings.*, volume Volume 4, pages 1942-1948. IEEE Institute of Electrical and Electronics Engineers, International Conference on Neural Networks, Piscataway.
- Langen, I. and Sigbjörnsson, R. (1979). *Dynamisk analyse av konstruksjoner*. Fagbokforlaget.
- Moan, T. (2003). *Finite Element Modelling and Analysis Of Marine Structures*. Marinteknisk senter, Institutt for marin teknikk.
- Myrhaug, D. (2004). *Kompendium - Emne TMR4180 Marin Dynamikk*. Akademika forlag.
- Myrhaug, D. (2005). *Stochastic Theory of Sealoards - Statistics of Narrow Band Processes and Equivalent Linearization*. Akademika forlag.
- Norge, S. (2007). Norsok standard n-003, action and action effects.
- Offshore-Technology. <http://www.offshore-technology.com/projects/glider/glider1.html>.
- Pettersen, B. (2007). *Marin teknikk 3 : hydrodynamikk*. Marinteknisk senter, Institutt for marin teknikk, Trondheim.
- Rahman, A. (2014). Dynamic analysis of floating bridges with transverse pontoons. Master's thesis, Norwegian University of Science and Technology.
- Vegvesen, S. (1994). Høgsfjordprosjektet.
- Vegvesen, S. (March 2011). A feasibility study - how to cross the wide and deep sognefjord, summary.
- Vegvesen, S., Aas-Jakobsen, Holt, J., Cowi, and Skanska (2013). Sognefjord mulighetsstudie flytebru. Technical report.
- Veritas, D. N. (2007). Dnv-rp-c205: Environmental conditions and environmental loads.
- Veritas, D. N. (2011). Dnv-os-c101: Design of offshore steel structures.
- Wikipedia (2016). Homer m. hadley memorial bridge.
- Ålesund Havnevesen (2016). Vannstand i Ålesund havn.

Appendix A

Program Descriptions and Flowcharts

A.1 Main Program

A.1.1 Main Program - Complimentary Program Description

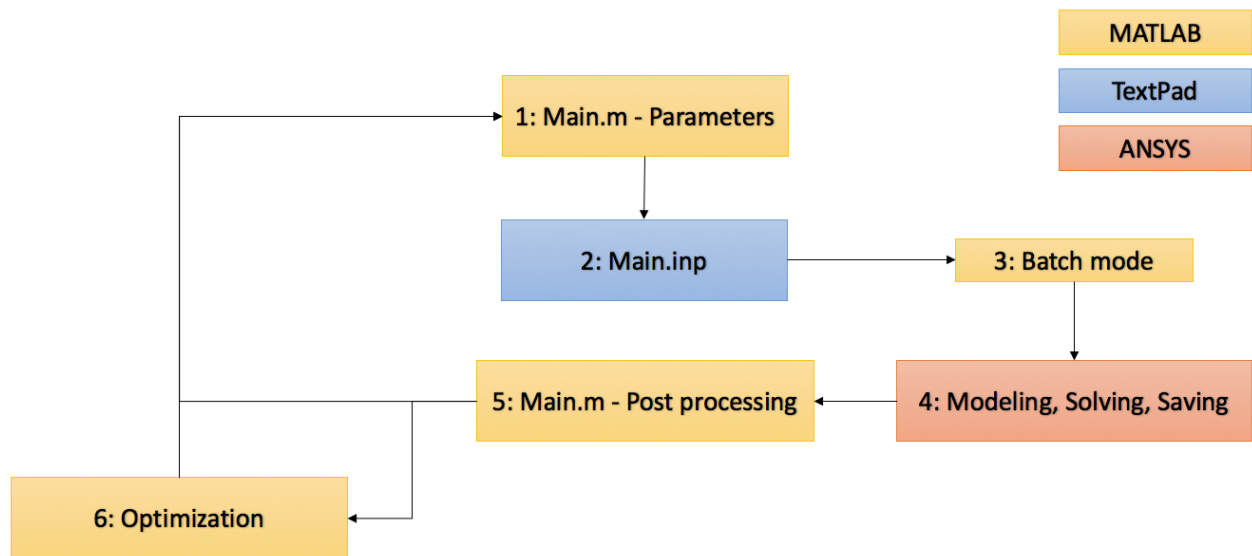


Figure A.1: Flowchart for the main program

The main program and its flowchart is described in Section 5.1.2. Figure A.1 shows the main flowchart. Figure A.2 shows all the input files which are a part of 2: *main.inp*. These are the files necessary to run and complete the ANSYS analysis in batch mode.

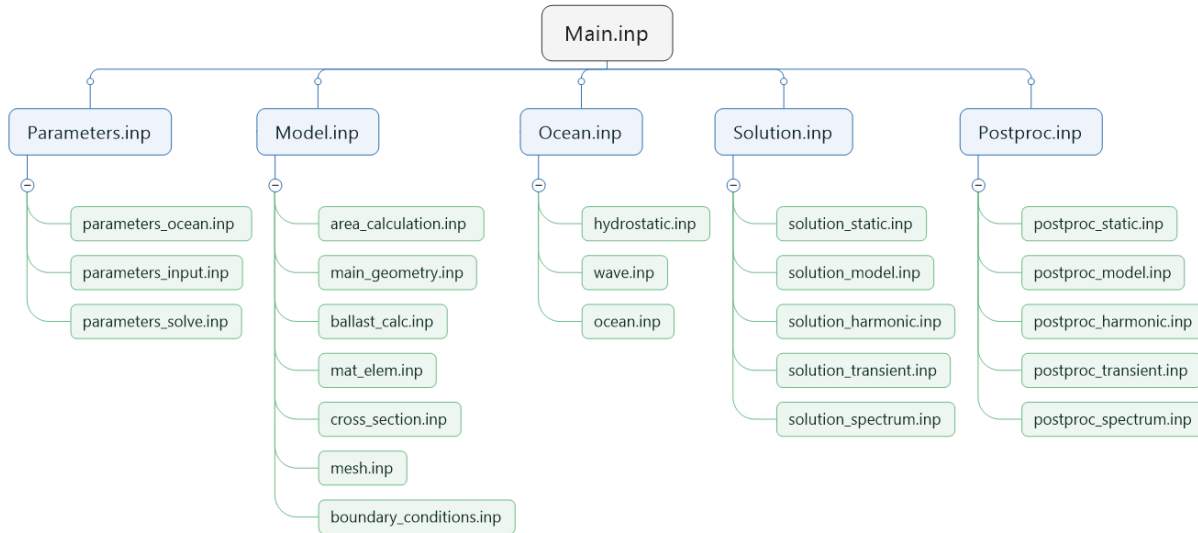


Figure A.2: Flowchart for APDL inputfiles

The hierarchy goes from left to right, top to bottom. For simplicity, we describe *Main.inp* as first level, the blue boxes as second level and the green boxes as third level. There are five bulks of input files, from left to right.

When *Main.inp* is called upon in ANSYS batch mode, *Parameters.inp* is the next file uploaded into ANSYS. After this, the third level boxes are uploaded from top to bottom. The first two bulks of third level boxes are all uploaded in each analysis from left to right, top to bottom. For the third bulk, parameters in *Parameters.inp*, controls which of the third level input files are used in *Ocean.inp*. This controls what kind of ocean loading we use in our analysis.

For the last two bulks, only one third level box can be chosen. This controls the type of analysis and post processing carried out.

A.1.2 How to Run the Program

The program is run from the *main.m* file. In order for the batch file to work, the location of Ansys on the computer must be updated in the batch file. When this is done, the required parameters for loading and solving should be set in the *main.m* file. When this is done, the program can be started. Depending on the different kind of solver chosen, the number of time steps, time

duration and sampled results, the analysis will use from 30 second to some hours to run.

Both a database which can be opened again in Ansys and post processed material saved in text files can be accessed when the analysis is complete.

A.2 Pontoon Program

A.2.1 Program Description

The pontoon program runs on the same principles as the main thesis program. Input parameters are set in the first block, `Main_pontoon_test.m`. These input parameters are uploaded in `main_pontoon_test.inp`, at 2.1: `matlab_variables.inp`. The other input files are APDL files. They are all uploaded when Matlab is running ANSYS in batch mode, respectively in the order from top to bottom. When the analysis is completed and results stored in files, post processing is carried out in Matlab.

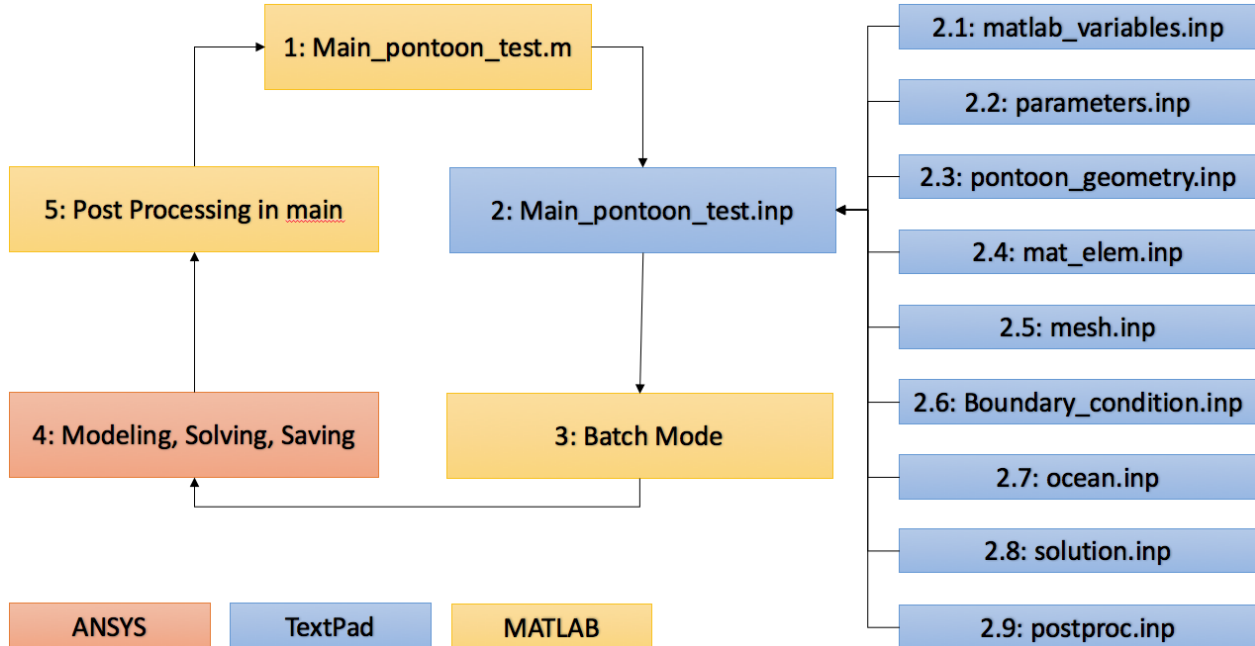


Figure A.3: Flowchart for pontoon testing program

The complete program is added in the electronic appendix, in a zipped file called ANSYS pontoon testing.

A.2.2 How to Run the Program

The program can be run in the exact same way as for the main SFT program. It is a bit smaller, and the analyses takes shorter time, but the principles are the same.

Appendix B

Scripts and Input Files

B.1 Matlab

```
1  % -----%
2  %%%%%%%%%%%%%%%%%%%%%%%%%%%%%%%%%%%%%%%%%%%%%%%%%%%%%%%%%%
3  %
4  % Master Thesis      : Title
5  %
6  % Program name      : Main function
7  %
8  % Author            : Hans Jakob Vik
9  %
10 % Creation date     : 28/04/2016
11 %
12 % Purpose           : Main program for creating parameters for input
13 %                   text files which create the model and run
14 %                   analyses in Ansys Mechanical
15 %
16 %%%%%%%%%%%%%%%%%%%%%%%%%%%%%%%%%%%%%%%%%%%%%%%%%%%%%%%%%%
17
18 %% Input parameters for creating the model in ANSYS
19
20 % Analysis counter
21 counter = 0;
22
23 %Dimensions of main pipe
24 R_main_i = 5.500;          % Inner radius of tunnel [m]
25 R_main_o = 6.300;          % Outer Radius of tunnel [m]
26
27 % Dimensions of the bracing pipe
28 D_bracing = 5.0;          % Diameter of truss pipe
29 t_bracing = 0.5;          % Wall thickness of truss pipe
30
31 % Dimensions of the shaft
32 D_shaft = 8;              % Diameter of truss pipe
33 t_shaft = 0.5;           % Wall thickness of truss pipe
34 shaft_height = 24;        % From top main pipe to top pontoon
35
36 % Global model geometry
```

```

37 span = 3700; % The span of the fjord where the bridge is ...
    crossing [m]
38 mean_c_d = 40;
39 secoffset = R_main_o; % The offset when modelling main pipes
40 c_d = mean_c_d-(2*secoffset); % Distance between the center of the tunnels [m]
41 R = 2682; % Horizontal mean radius of the system [m]
42 n_circles = 48; % Number of circles representing a arc
43 g = 9.81; % Gravitational accelertaion
44 ballast_factor = [0.7 0]; % Slurry, water filling of chamber
45
46 p_v = [500 150 205 205 205 205 150]; % Distance between pontoons, vector sum
47
48 % Densities
49 rho_main_inside = 0;
50 rho_slurry = 2400; % Density for ballast slurry
51 rho_concrete = 2400; % Density of concrete, no reinf.
52 rho_steel = 7800; % Density of steel
53 rho_w = 1025; % Density of fjord water
54 rho_pontoon_support = 1015; % No bouyancy from support elements
55
56 %% Mesh sizes
57
58 %for i = 1:length(main_mesh) % This is for decreasing mesh size test
59
60 % 1 = decreasing test, 2 = uniform global mesh
61 mesh_configuration = 2;
62
63 if mesh_configuration == 1
64     main_mesh = [30:-0.1:0.2,0.19:-0.01:0.1];
65 elseif mesh_configuration == 2
66     mesh_factor = 2.0;
67     mesh_size = mesh_factor*[1.0,1.0,1.0,1.0,1.0,1.0,1.0];
68 end
69
70 % Mesh sizes which are constant each round
71 radi_div = 5; % Radial divisions
72 circ_div = 16; % Circular division in the pipe
73 mesh_cross = 0.5; % Cross section mesh for beam
74
75 %% Pontoon dimensions
76 H_p = 8; % Pontoon height [m]
77 B_p = 20; % Pontoon beam [m]
78 L_p = 80; % Length of pontoon
79 n = 4; % Veritcal pontoon layers
80 m = 3; % Horizontal pontoon layers
81 t_p = 10*10^-3; % Pontoon wall thickness
82 A_p_ends = 2*B_p*H_p; % Area of ends
83 A_p_sides = 2*L_p*(B_p+H_p); % Area of top, bottom and sides
84 A_p = A_p_ends+A_p_sides; % Pontoon area
85 A_b = A_p_ends + (2*c_d*(B_p+H_p)); % Volume of model beam pontoon element
86 t_p_adjusted = 2*((A_p*t_p)/A_b); % Pontoon thickness in the model, added ...
    mass included
87 rho_pontoon = (A_p*t_p*rho_steel)/(L_p*H_p*B_p); %Density of the pontoon steel
88
89 %% Props of concrete, steel, water in pipe, air in pipe, pontoon steel
90 E = [40 210 30000 30000]*10^9; % Youngs modulus
91 v = [0.2 0.3 0.3 0.3]; % Poisson's number
92 rho = [rho_concrete,rho_steel,rho_pontoon,rho_pontoon_support]; % Density
93
94 %% Keeping track of cross sections, materials and elements
95 section_number = [3,1,2,4,5,6,7];
96 material_number= [1,1,1,2,2,3,4];
97 elem_type = [5 5 5 5 5 1 1]; % What element to assign, for all
98
99 %% Parameters for solving
100 % A parameter for solving, batch mode and data saving
101 solve_parameter = 4; % 0 = no solve, 1 = static, 2 = modal, 3 = harmonic, 4 = ...
    transient, 5 = spectrum
102 batch_solve = 1; % 1 = batch mode solve, 0 = no batch mode solve
103 batch_cs = 0; % 1 = cross section creation, 0 = no cross section
104 analysis = 1;
105

```

```

106 % Modal solving
107 n_modes = 30; % no. modes, !NB! n_modes/5 = integer !NB!
108 n_expand = 30; % Number of modes to expand
109
110 % Transient solving, parameters
111 n_runs = 1; % Number of time cycles
112 time_step = 0.5; % Time step for solving
113 T_wave = 8.0; % Harmonic wave period
114 H_wave = 4.85; % Harmonic wave height
115 end_time = T_wave*n_runs; % The time duration of the analysis
116
117 % Spectrum solving
118 time_step_spectrum = 0.5; % Time step size
119
120 % Spectrum and transient solving, time step saving
121 time_array = 1; % Using time array for solving time steps
122 Nth_save = 1; % Save Nth step, if time array = 0
123 end_time_spectrum = 2; % End time for analysis
124 %NB: If time_array equals 1, Nth_save and end_time_spectrum are not of
125 %importance
126
127 %Inputlist for the solve ocean parameters
128 parameters_solve(solve_parameter,n_modes,n_expand,time_step,end_time,...
129 time_step_spectrum,end_time_spectrum,Nth_save,time_array);
130
131 %% Setting parameters and creating input parameter list for Ocean inputs
132
133 %Basic ocean loading
134 matoc = 10; % Material number of the ocean
135 tc = 0; %+1.85 -1.58; % Tidal change
136 zmsl = 19.95; % Vertical offset from global origin to MWL
137 depth = 750 + zmsl; % Depth from MWL to sea floor
138 kflood = 0.0; % Wether the beams are flooded or not
139 cay = 1.0; % Added mass ratio, y
140 caz = 1.0; % Added mass ratio, z
141 cb = 1.0; % Ratio of buoyancy force used over buoyancy force
142
143 % Wave environment input
144 if solve_parameter == 4; % Harmonic Transient Analysis
145     Kwave = 0; % Incident wave type, Airy
146 elseif solve_parameter == 5; % Spectrum Transient Analysis
147     Kwave = 5; % Random (preparing Jonswap=
148 end
149 wave_angle = 90; % Angle of incoming waves, degrees
150 waveloc = 0; % Location of wave on elements
151 kcrc = 0; % Wave-current interaction key
152 Spectrum = 1; % 0 = Pierson Mos. 1 = Jonswap, 2 = user
153 Hs = 2.14; % Significant waveheight for Jonswap
154 Tp = 4.8; % Spectral peak period
155 Nwc = 50; % Number of wave components in spectrum
156 Gamma = 3.3; % Gamma for wave spectrum
157
158 % Checking the mesh size of the pontoons vs wave criteria
159 wave_length = (g*T_wave^2)/(2*pi);
160 wave_check = wave_length/20;
161
162 if mesh_size(1,6) > wave_check
163     mesh_size(1,6) = wave_check-0.01;
164 end
165
166 if mesh_size(1,7) > wave_check
167     mesh_size(1,7) = wave_check-0.01;
168 end
169
170 %Input list for the ocean parameters
171 parameters_ocean(tc,depth,kflood,rho_w,cay,caz,cb,matoc,zmsl,H_wave,T_wave,...
172 Kwave,wave_angle,waveloc,kcrc,Hs,Tp,Nwc,Gamma,Spectrum);
173
174
175 %% Main input parameter file
176 parameters(span,R_main_o,mean_c_d,R,n_circles,g,p_v,ballast_factor,...
177 rho_main_inside,rho_slurry,rho_concrete,rho_steel,rho_w,rho_pontoon_support,...

```

```

178     rho_pontoon, mesh_size, radi_div, circ_div, mesh_cross, R_main_i, D_bracing, ...
179     t_bracing, D_shaft, t_shaft, shaft_height, H_p, B_p, L_p, n, m, t_p, E, v, rho, ...
180     section_number, material_number, elem_type, ...
181     solve_parameter, batch_solve, batch_cs, analysis, n_modes, n_expand)
182
183 %% Running the main.inp file in batch mode. This file has to be altered in
184 %% textpad in order to change type of analysis
185
186 if batch_solve == 1
187     tic
188     !modeling_main.bat
189     time = toc;
190
191     if solve_parameter == 1
192         fid = fopen('analysis_time.txt', 'a+');
193         fprintf(fid, '%f %f\n', time(i,1), mesh_size(1));
194         fclose(fid);
195
196         fid = fopen('displacement_model.txt', 'r');
197         line = fgetl(fid);
198         vector(1,1:37)=str2num(line);
199         fclose(fid);
200
201         fid = fopen('displacement_model_append.txt', 'at');
202         for j = 1:length(vector);
203             fprintf(fid, '%f ', vector(1, j));
204         end
205         fprintf(fid, '\n');
206         fclose(fid);
207
208         fprintf('\n%d/%d analysis are done\n', i, length(main_mesh));
209         fprintf('Last analysis took %f minutes\n', time(i,1)/60);
210         fprintf('Current mesh size = %d\n', main_mesh(1,i));
211
212     elseif solve_parameter == 2
213         lol = 1;
214     elseif solve_parameter == 3
215
216         fid = fopen('displacement_wave.txt', 'r');
217         line = fgetl(fid);
218         vector(1,1:35)=str2num(line);
219         fclose(fid);
220
221         filename = sprintf('displacement_wave_TimeHist_H%d.txt', H_wave);
222         fid = fopen(filename, 'at');
223         for k = 1:length(vector);
224             fprintf(fid, '%f ', vector(1,k));
225         end
226         fprintf(fid, '\n');
227         fclose(fid);
228
229         fid = fopen('analysis_time.txt', 'a+');
230         fprintf(fid, '%f %f %f\n', time, H_wave, T_wave);
231         fclose(fid);
232
233     % Writing out some information to the command window
234     n_analysis = length(i_parameter)*length(j_parameter);
235     an_left = n_analysis - counter;
236     ETC = an_left*time/3600;
237     hours = floor(ETC);
238     fract_min = (ETC - hours)*60;
239     min = floor(fract_min);
240     fract_sec = (fract_min - min)*60;
241     sec = floor(fract_sec);
242
243     fprintf('\nWave height is: %d || Period is: %f\n', i, j);
244     fprintf('%d/%d analysis completed\n', counter, n_analysis);
245     fprintf('Last analysis took %f minutes\n', time/60);
246     if numel(num2str(min)) == 2 && numel(num2str(sec)) == 2
247         fprintf('The estimated time to completion is: %d:%d:%d\n', hours, min, sec);
248     elseif numel(num2str(min)) == 1
249         fprintf('The estimated time to completion is: %d:0%d:%d\n', hours, min, sec);

```

```

250     elseif numel(num2str(sec)) == 1
251         fprintf('The estimated time to completion is: %d:%d:0%d\n',hours,min,sec);
252     elseif numel(num2str(min)) == 1 && numel(num2str(sec)) == 1
253         fprintf('The estimated time to completion is: %d:0%d:0%d\n',hours,min,sec);
254     end
255 end
256 end
257 end
258
259 %end

```

B.2 TextPad Ansys Input File

```

1  %-----%
2  %
3  % Project Thesis      : Title
4  %
5  % Program name       : main_geometry.m
6  %
7  % Author             : Hans Jakob Vik
8  %
9  % Creation date      : 28/04/2016
10 %
11 % Purpose            : Program making the main geometry of the bridge
12 %                   : for assigning the right materials and sections
13 %                   : when meshing
14 %
15 %-----%
16
17
18 %-----%
19 %Creating the keykopint and lines for bracing elements in between the tunnel pipes.
20 %-----%
21
22 count_step = 10000           % Step for counting the KP and areas
23 KP_numbering = count_step   % Start number for key points
24 LINE_numbering = count_step % Start points for areas
25
26 *DO,i,1,2,1
27     NUMSTR,KP,KP_numbering   % Setting the LINE numbering
28     theta = asin((span/2)/R) % Half the span angle of the bridge
29     angle_step = (2*theta)/(n_circles-1) % Angle step between each circle
30
31     % Creating points on the arc
32     *DO,j,-theta,theta,angle_step
33         *IF,i,eq,1,then
34             x = R_horizontal(1,i)*sin(j+(angle_step/2)) % x-pos of new KP for R = 2702
35             y = R_horizontal(1,i)*cos(j+(angle_step/2)) % y-pos of new KP for R = 2702
36         *ELSE
37             x = R_horizontal(1,i)*sin(j) % x-pos of new KP for R = 2662
38             y = R_horizontal(1,i)*cos(j) % y-pos of new KP for R = 2662
39         *ENDIF
40         K,,x,y,0
41     *ENDDO
42     KP_numbering = KP_numbering + count_step % Updating KP numbering
43 *ENDDO
44
45 KP_count = KP_numbering-2*count_step
46 NUMSTR,LINE,LINE_numbering
47
48 *DO,i,1,n_circles-1,1
49     L,(count_step + KP_count)+(i-1),KP_count+(i-1)
50     L,(KP_count)+(i-1),(count_step+KP_count)+(i)
51 *ENDDO
52

```

```

53 end_BC = LINE_numbering % Line number for the end of the bridge
54 LINE_numbering = LINE_numbering + count_step % Updating line numbering
55
56 %-----%
57 % Storing the pontoon element keypoints and matrix with coordinates
58 %-----%
59
60 *GET,p_2,'PARM',p_v,DIM,Y % Half the number of pontoon vectors
61 n_pontoons = p_2*2 % Number of pontoons
62 *DIM,coordinates,ARRAY,4,p_2*2 % pontoon coordinates
63
64 % Creating the pontoon KP coordinates
65 *DO,k,1,2,1
66     counter = 0
67     theta = asin((span/2)/R)
68     *DO,j,1,p_2,1
69         counter = counter + 1
70         angle_1 = acos((2*R**2-(p_v(1,j)**2))/(2*(R**2)))
71         theta = theta-angle_1
72
73         x = R*sin(theta) % Using mean radius to calc. x-coord
74         y = sqrt(R_horizontal(1,k)**2-x**2) % Using local R to calc. y-coord
75         coordinates(k,counter) = x
76         coordinates(k+2,counter) = y
77     *ENDDO
78 *ENDDO
79
80 % Copy and flip the coordinates so both sides of the arc is represented
81 *DO,i,1,4,1
82     counter = 0
83     *DO,j,p_2+1,p_2*2
84         counter = counter + 1
85         coordinates(i,j) = coordinates(i,p_2+1-counter)
86     *ENDDO
87 *ENDDO
88
89 % Creating negative x-coordinates on the negative coordinate system side
90
91 *DO,i,1,2,1
92     *DO,j,1,p_2,1
93         coordinates(i,j) = coordinates(i,j)*(-1)
94     *ENDDO
95 *ENDDO
96
97 %-----%
98 % Creating the arc of the submerged floating tunnels, together with the
99 % pontoon KPs. Creating new keypoints for keypoint numbering to have the
100 % right order.
101 %-----%
102
103 *DIM,pontoon_numbering,ARRAY,2,n_pontoons
104
105 *DO,i,1,2,1
106     KP_pontoon = KP_numbering % A counter for KP number for pontoons
107     pontoon_counter = 1 % A counter for the pontoon key points
108     NUMSTR,KP,KP_numbering % Setting the KP numbering
109     NUMSTR,LINE,LINE_numbering % Setting the LINE numbering
110     theta = asin((span/2)/R) % Half the span angle of the bridge
111     angle_step = (2*theta)/(n_circles-1) % Angle step between each circle in tunnel
112
113     % Creating points on the arc
114     *DO,j,-theta,theta,angle_step
115
116         % x- and y-coordinates for the different radii
117         *IF,i,EQ,1,THEN
118             x = R_horizontal(1,i)*sin(j+(angle_step/2)) % x-pos of new KP for R = 2702
119             y = R_horizontal(1,i)*cos(j+(angle_step/2)) % y-pos of new KP for R = 2702
120         *ELSE
121             x = R_horizontal(1,i)*sin(j) % x-pos of new KP for R = 2662
122             y = R_horizontal(1,i)*cos(j) % y-pos of new KP for R = 2662
123         *ENDIF
124

```

```

125     % Creating the pontoon KP in between the arc KPs to make lines
126     % afterwards
127     *IF, pontoon_counter, LE, n_pontoons, THEN           % number of pontoons
128         *IF, x, GT, coordinates(i, pontoon_counter), THEN
129             Xx = coordinates(i, pontoon_counter)
130             Yy = coordinates(i+2, pontoon_counter)
131             K, , Xx, Yy, 0
132             pontoon_counter = pontoon_counter + 1
133             pontoon_numbering(i, pontoon_counter-1) = KP_pontoon
134             KP_pontoon = KP_pontoon + 1
135         *ENDIF
136     *ENDIF
137     K, , x, y, 0
138     KP_pontoon = KP_pontoon + 1
139 *ENDDO
140
141 % Create the lines between the KPs, different for R = 2702 and R = 2662
142 *IF, i, EQ, 1, THEN
143     for_end = n_circles+n_pontoons-2
144 *ELSEIF, i, EQ, 2, THEN
145     for_end = n_circles+n_pontoons-1
146 *ENDIF
147
148 % Creating the lines with key points
149 *DO, j, 1, for_end, 1
150     KP1 = (KP_numbering)+(j-1)           % First KP of the line
151     KP2 = (KP_numbering)+j             % Second KP of the line
152     L, KP1, KP2           % Creating the line
153 *ENDDO
154
155     KP_numbering = KP_numbering + count_step           % Updating KP numbering
156     LINE_numbering = LINE_numbering + count_step       % Updating line numbering
157 *ENDDO
158
159 %-----%
160 % Creating shaft and pontoon keypoints and lines for beam elements.
161 % Connecting lines between pontoon and submerged tunnels for steel shaft
162 %-----%
163 *DIM, L_px, ARRAY, 1, n_pontoons
164 *DO, i, 1, n_pontoons, 1
165     L_px(1, i) = (L_p - (coordinates(3, i)-coordinates(4, i)))/2
166 *ENDDO
167
168 vert_step = H_p/n           % Vertical pontoon layer step
169 hor_step = B_p/m           % Horizontal step
170 n_kp = n*m*2               % Number of keypoints per half pontoon
171
172 *DO, i, 1, 2, 1           % outer and inner main keypoints/lines
173     NUMSTR, KP, KP_numbering
174     NUMSTR, LINE, LINE_numbering
175
176     *DO, j, 1, n_pontoons, 1
177         *DO, k, 1, n, 1           % Variable for number of vertical layers
178             *DO, p, -((m-1)/2), (m-1)/2, 1           % Variable for horizontal layers
179                 x = coordinates(i, j)+hor_step*p
180                 y = coordinates(i+2, j)
181                 z = 16+(k-1)*vert_step
182                 % Creating the pontoon keypoints directly above shaft
183                 K, , x, y, z
184                 % Adding key points at the pontoon ends
185                 *IF, i, EQ, 1, THEN
186                     K, , x, L_px(1, j)+y, z
187                 *ELSEIF, i, EQ, 2, THEN
188                     K, , x, -L_px(1, j)+y, z
189                 *ENDIF
190             *ENDDO
191         *ENDDO
192         % Creating the shaft lines between main pipes and pontoons
193         L, pontoon_numbering(i, j), KP_numbering+(m-1)+(n_kp*(j-1))
194     *ENDDO
195
196     KP_numbering = KP_numbering + count_step

```

```

197     LINE_numbering = LINE_numbering + count_step
198 *ENDDO
199
200
201     % Creating the pontoon beam lines, all layers
202 NUMSTR,LINE,LINE_numbering
203 *DO,i,1,n_pontoons,1
204     *DO,j,1,n,1
205         *DO,k,1,m,1
206             KP1 = KP_numbering - (count_step*2)+(n_kp*(i-1)) + (k*2) + (j-1)*(m*2)-2
207             KP2 = KP_numbering - count_step + (n_kp*(i-1)) + (k*2) + (j-1)*(m*2)-2
208             % Creating horizontal pontonn lines
209             L,KP1+1,KP1 % Outer
210             L,KP1,KP2 % Midle
211             L,KP2,KP2+1 % Inner
212         *ENDDO
213     *ENDDO
214 *ENDDO
215
216 LINE_numbering = LINE_numbering + count_step
217 NUMSTR,LINE,LINE_numbering
218 % Creating the vertical pontoon end lines
219 *DO,i,1,n_pontoons,1
220     *DO,j,1,m,1
221         KP1 = KP_numbering - (count_step*2)+(n_kp*(i-1)) + (j*2) - 2
222         KP2 = KP_numbering - count_step + (n_kp*(i-1)) + (j*2) - 2
223         *DO,k,1,n-1,1
224             L,KP1+1+((k-1)*m*2),KP1+1+(k*m*2)
225             L,KP2+1+((k-1)*m*2),KP2+1+(k*m*2)
226             *IF,j,EQ,1,OR,j,EQ,m,THEN %Creating the middle hor lines
227                 L,KP1+((k-1)*m*2),KP1+(k*m*2)
228                 L,KP2+((k-1)*m*2),KP2+(k*m*2)
229             *ENDIF
230         *ENDDO
231     *ENDDO
232 *ENDDO
233
234 % Creating the middle and end horizontal lines
235 *DO,i,1,n_pontoons,1
236     *DO,j,1,n,1
237         *DO,k,1,m-1,1
238             KP1 = KP_numbering - (count_step*2)+(n_kp*(i-1)) + (j-1)*m*2 + (k-1)*2
239             KP2 = KP_numbering - count_step + (n_kp*(i-1)) + (j-1)*m*2 + (k-1)*2
240             L,KP1+1,KP1+3
241             L,KP2+1,KP2+3
242             *IF,j,EQ,1,OR,j,EQ,n,THEN %Creating the middle hor lines
243                 L,KP1,KP1+2
244                 L,KP2,KP2+2
245             *ENDIF
246         *ENDDO
247     *ENDDO
248 *ENDDO
249
250 LINE_numbering = LINE_numbering + count_step
251
252 LSEL,S,LINE,,LINE_numbering-count_step,LINE_numbering+count_step-1
253 LGLUE,all
254 LSEL,all
255
256 %-----%
257 % Sorting the line groups into named groups
258 %-----%
259
260 *DO,j,1,7,1
261     lsel,s,line,,(j*count_step),(j*count_step)+(count_step-1)
262     CM,beam_line_groups(1,j),LINE_numbering
263 *ENDDO
264
265 %-----%
266 % Creating the keypoints and lines for springs
267 %-----%
268

```



```

269 n_cs = 10
270 *DO,i,1,2,1
271   *IF,i,EQ,1,THEN % Setting the direction of the pitch spring
272     pitch = 1
273   *ELSE
274     pitch = -1
275   *ENDIF
276   NUMSTR,KP,KP_numbering
277   *DO,j,1,n_pontoons,1
278     n_cs = n_cs + 1
279     x = coordinates(i,j)
280     y = coordinates(i+2,j)
281     z = 24 - vert_step
282
283     LOCAL,n_cs,0,x,y,z,,,,1,1      ,x,y,z           % Creating a new CS
284     CSYS,n_cs                       % New CS
285     K,,0,0,50                       % Heave spring
286     K,,0,pitch*50,0                 % Pitch spring
287     K,,50,0,0                       % Surge spring
288     heave_KP = KP_numbering-count_step*2+n_kp*(j-1) + 2*m*(n-1) + m-1
289     surge_KP = heave_KP + 1
290     pitch_KP = KP_numbering-count_step*2+n_kp*(j-1) + 2*m*n - 2
291     NUMSTR,LINE,LINE_numbering
292     L,heave_KP,KP_numbering+((j-1)*3)           % Heave
293     NUMSTR,LINE,LINE_numbering+count_step       % Counter
294     L,surge_KP,KP_numbering+((j-1)*3)+1         % Surge
295     NUMSTR,LINE,LINE_numbering+count_step*2     % Counter
296     L,pitch_KP,KP_numbering+((j-1)*3)+2         % Pitch
297   *ENDDO
298   KP_numbering = KP_numbering + count_step
299 *ENDDO
300
301 ksel,s,KP,,KP_numbering-2*count_step,KP_numbering-1
302 cm,bc,KP
303 ksel,all
304
305 % Sorting the lines for the springs into groups
306 *DO,i,1,3,1
307   LSEL,S,LINE,,LINE_numbering+count_step*(i-1),LINE_numbering+count_step*i-1
308   CM,spring_line_groups(1,i),LINE_numbering
309 *ENDDO
310
311 CSYS,0 % Choosing the default first coordinate system

```


Appendix C

Wadam Results

C.1 Pontoon Analysis

C.1.1 Potential Damping - Curve Fitting Results

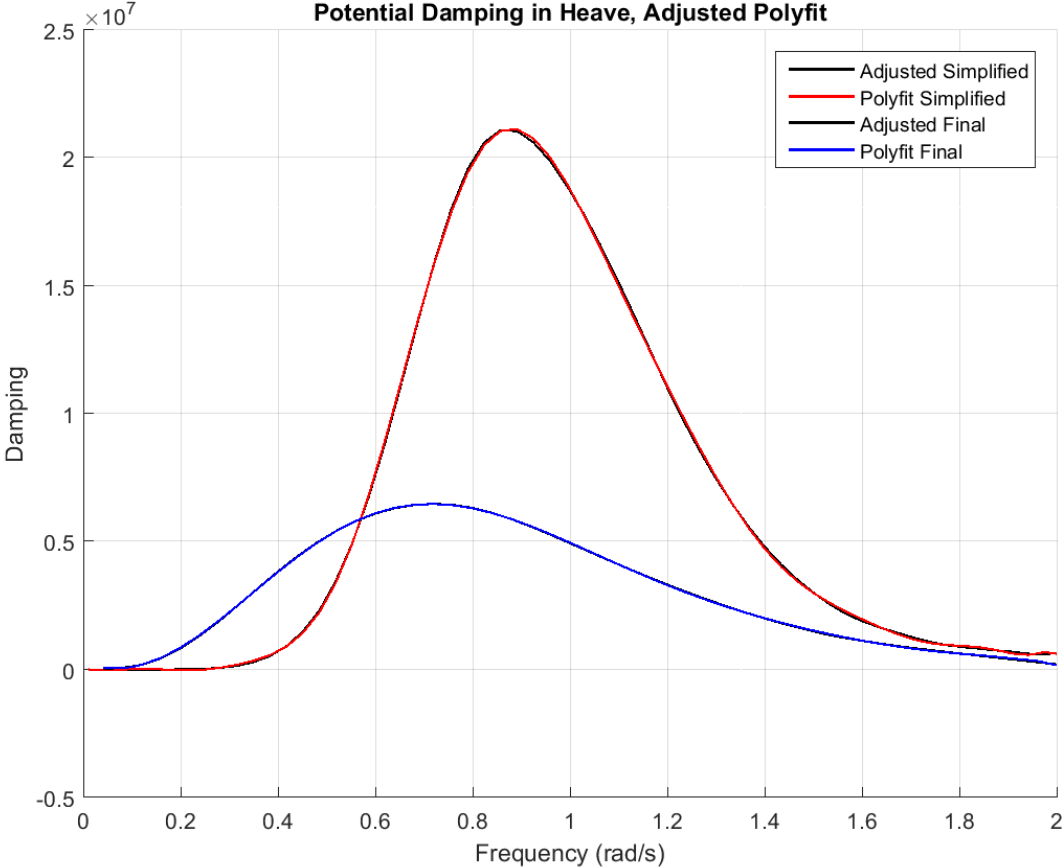


Figure C.1: Polyfitting of pontoon potential damping in heave

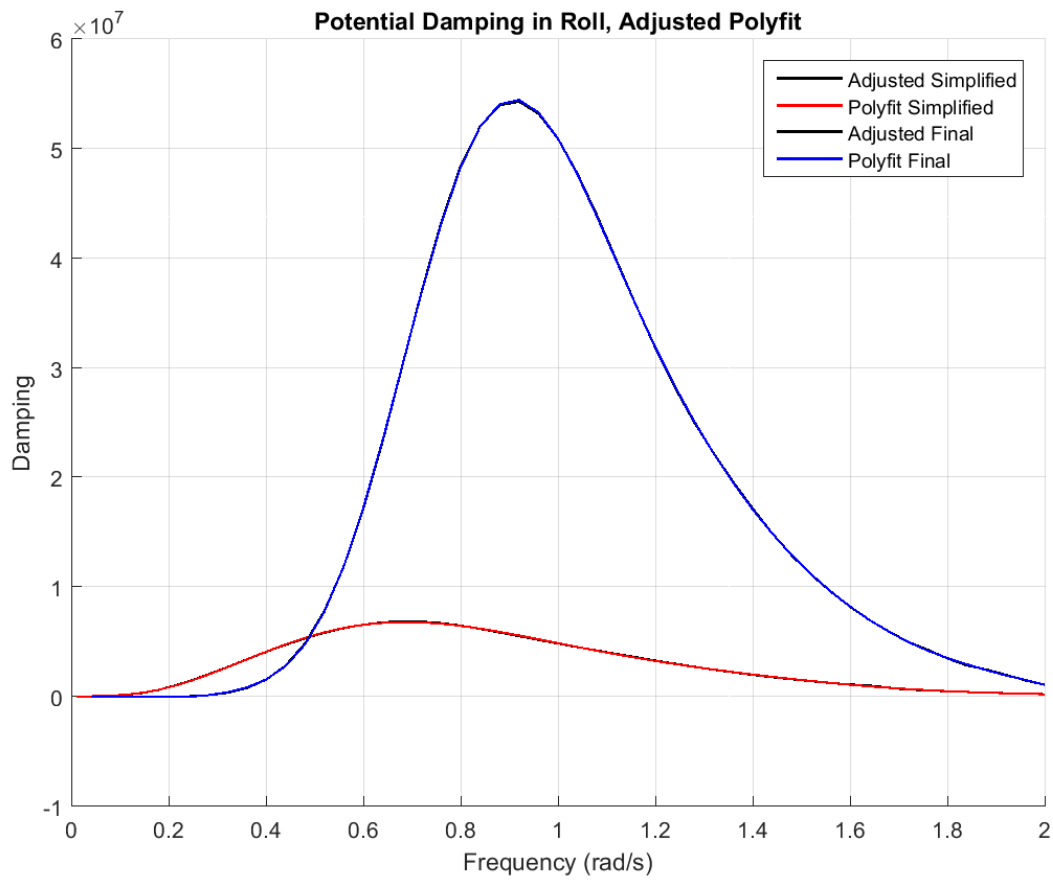


Figure C.2: Polyfitting of pontoon potential damping in roll

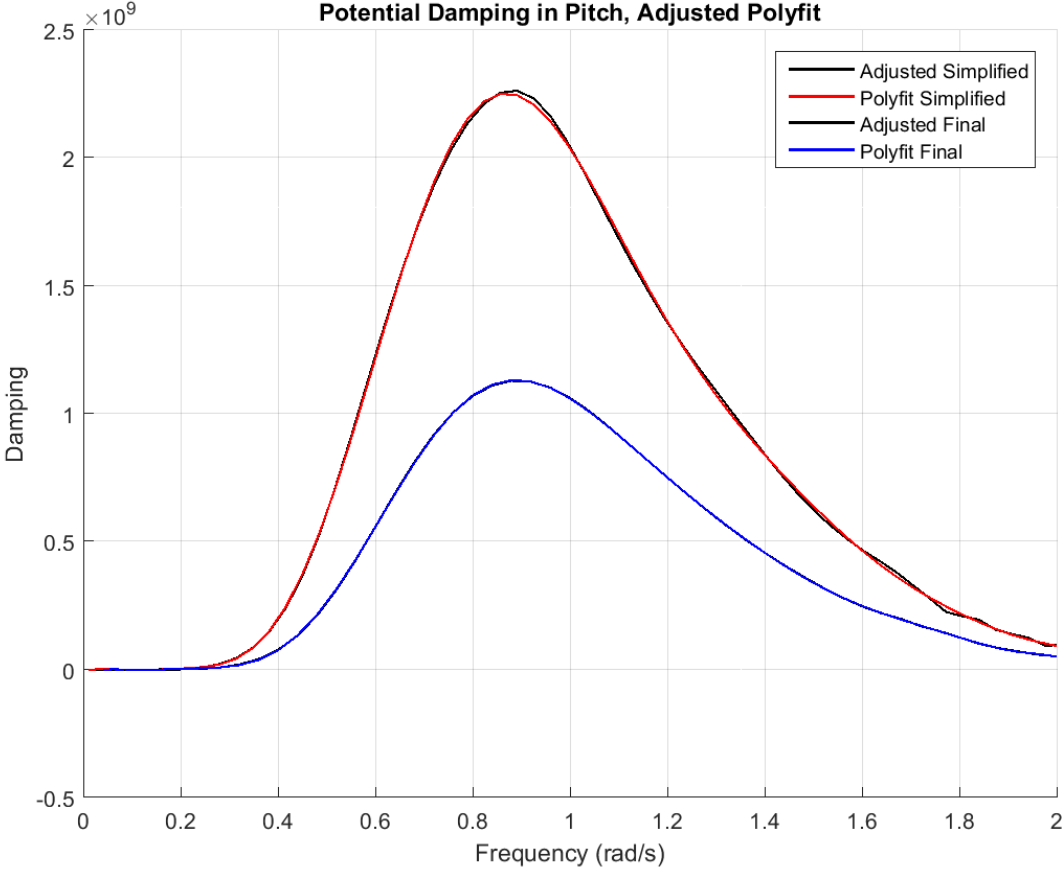


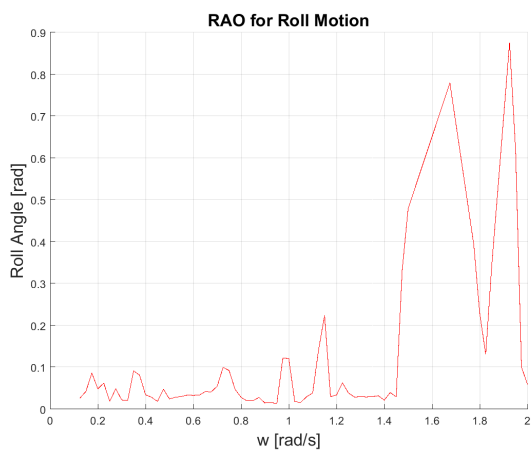
Figure C.3: Polyfitting of pontoon potential damping in pitch

Appendix D

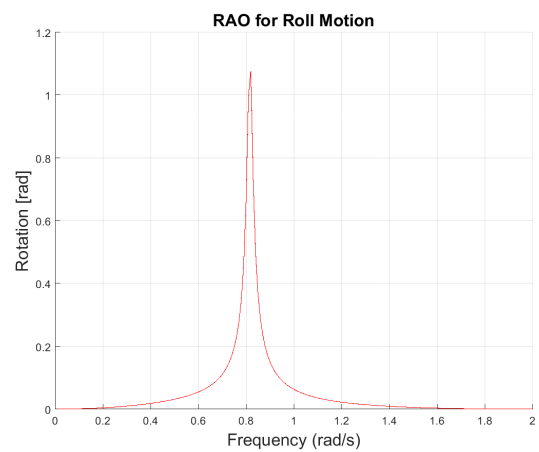
ANSYS Results

D.1 Pontoon Analysis

D.1.1 Roll RAO



(a) Ansys roll RAO



(b) Wadam roll RAO

Figure D.1: Roll RAO comparison for Ansys and Wadam

D.2 Static Analysis Results

This section contains the plots, figures and other information from the static analyses in Ansys. It is divided into the same order as in Chapter 6 and 7 about analyses and results, but some sections or parts might be missing. The sections or parts missing are the once which have not been referred to in the chapters about analysis and/or results.

D.2.1 Displacement

The displacement plots in this section are supplementary plots in order to, if necessary, get a better understanding of how the static displacements are for the different mean sea water levels.

D.2.1.1 Mean Sea Level

Figure D.2 shows the bridge displacement for the bridge when the required ballast is evenly distributed for the whole bridge. It has, compared to the distribution where the more heavily pontoon supported parts of the bridge has more ballast, higher global maximum and minimum displacement.

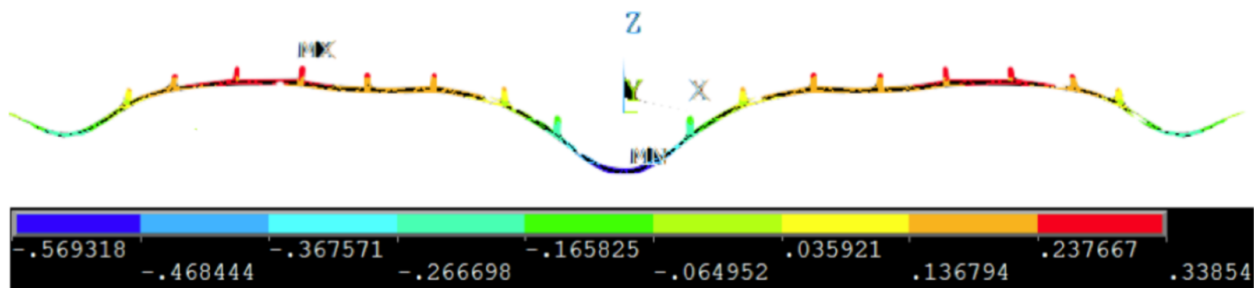


Figure D.2: Z-component of displacement with evenly distributed ballast

Figure D.3 and D.4 show the x- and y-component of the displacement for the SFT. The small differences is due to a small torsion or angle between the outer and inner main tunnels, due to the gravitational and buoyancy force. The displacement is also symmetrical.

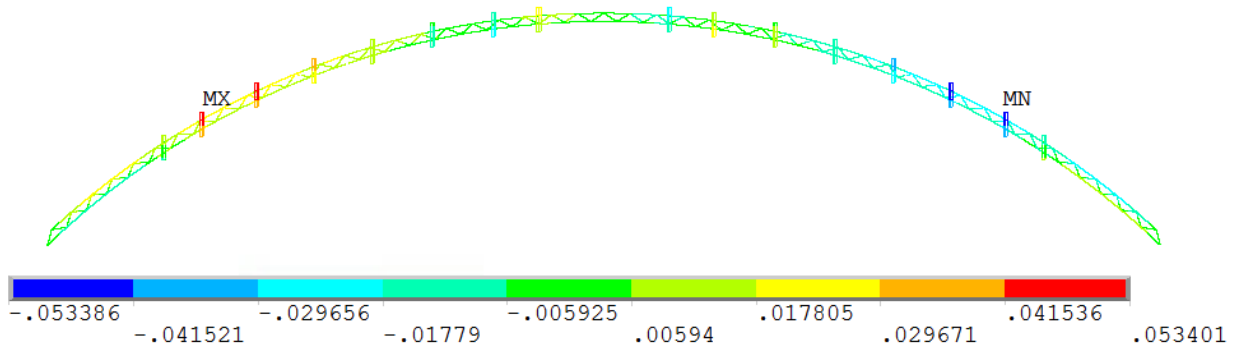


Figure D.3: X-component of global displacement, mean water level

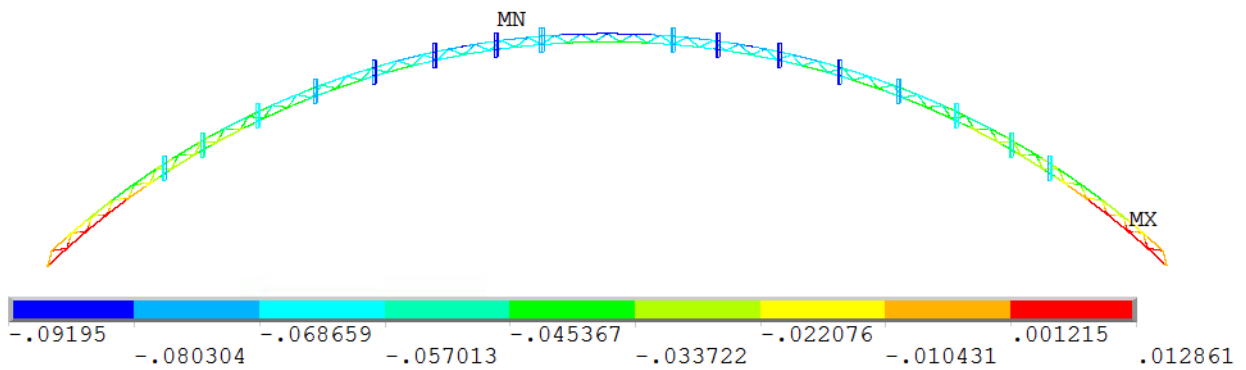


Figure D.4: Y-component of global displacement, mean water level

D.2.1.2 High Tide: +1.85m

Figure D.5 and D.6 show the x- and y-component displacement for the SFT model with a tidal change of 1.85 meters. This is maximum water level,

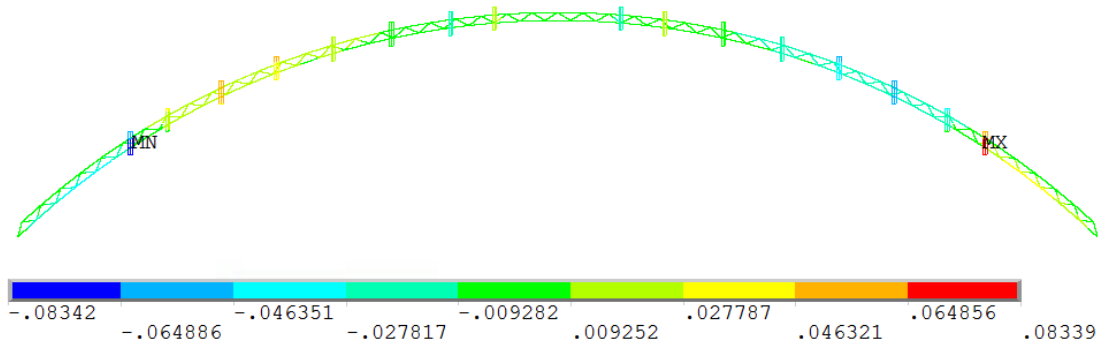


Figure D.5: X-component of global displacement, tidal change of 1.85 m

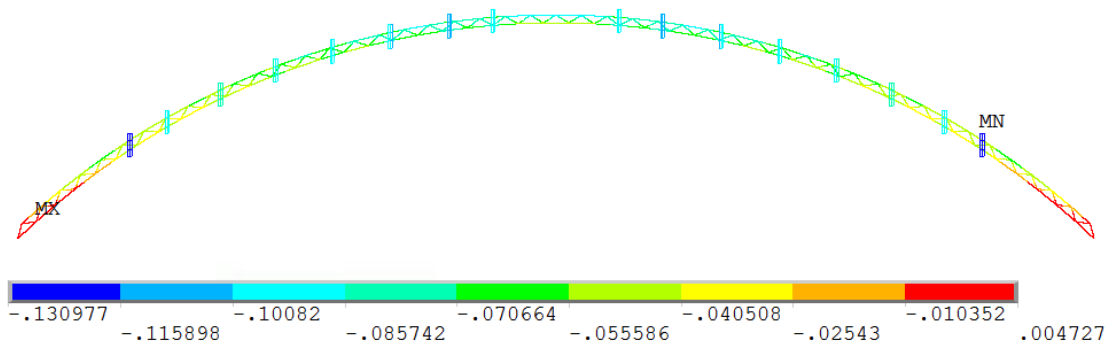


Figure D.6: Y-component of global displacement. tidal change of 1.85 m

D.2.1.3 Min Tide: -1.58m

Figure D.7 and D.8 show the x- and y-component of displacement for the SFT with a tidal change of -1.58 meters. This is the lowest water level.

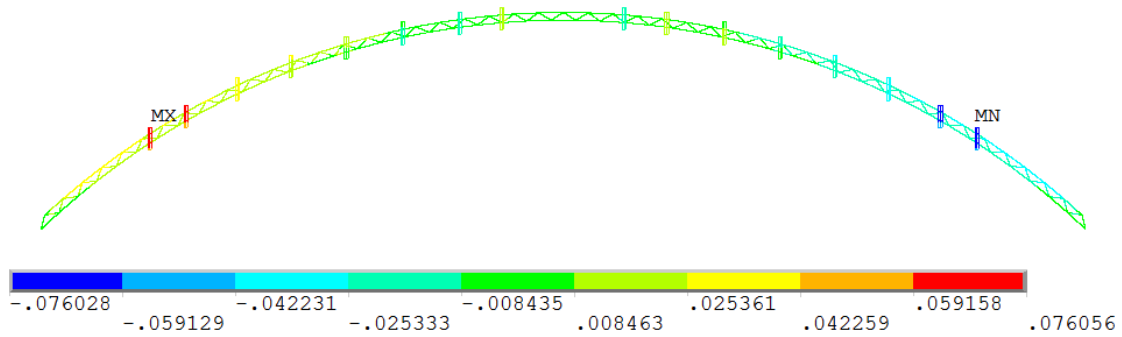


Figure D.7: X-component of global displacement, tidal change of -1.58 m

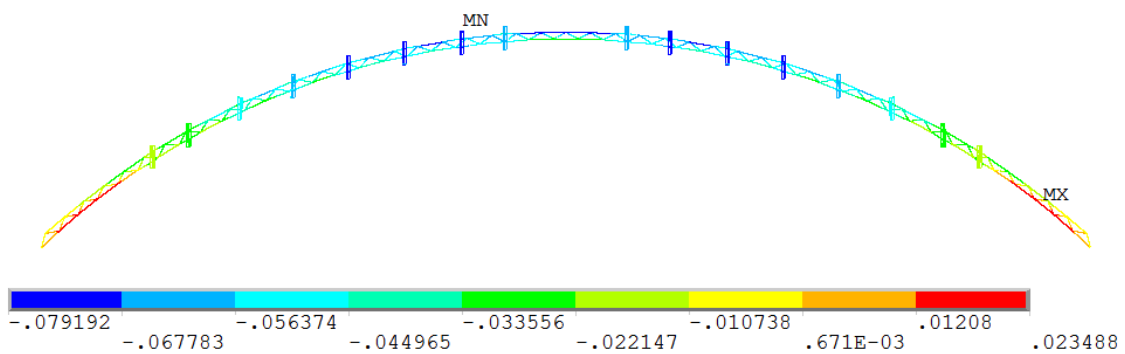


Figure D.8: Y-component of global displacement, tidal change of 1.58 m

D.3 Modal Analysis Results

D.3.1 Participating Masses

Figure D.9 shows the mass summation of the participating masses for the 200 first modes of the bridge. From the figure, it is clear that the necessary number of significant modes in order to obtain a mass participation of approximately 95% for all directions, is close to 160 modes. In the Rayleigh damping coefficient procedure, the number of modes used is 40 modes.

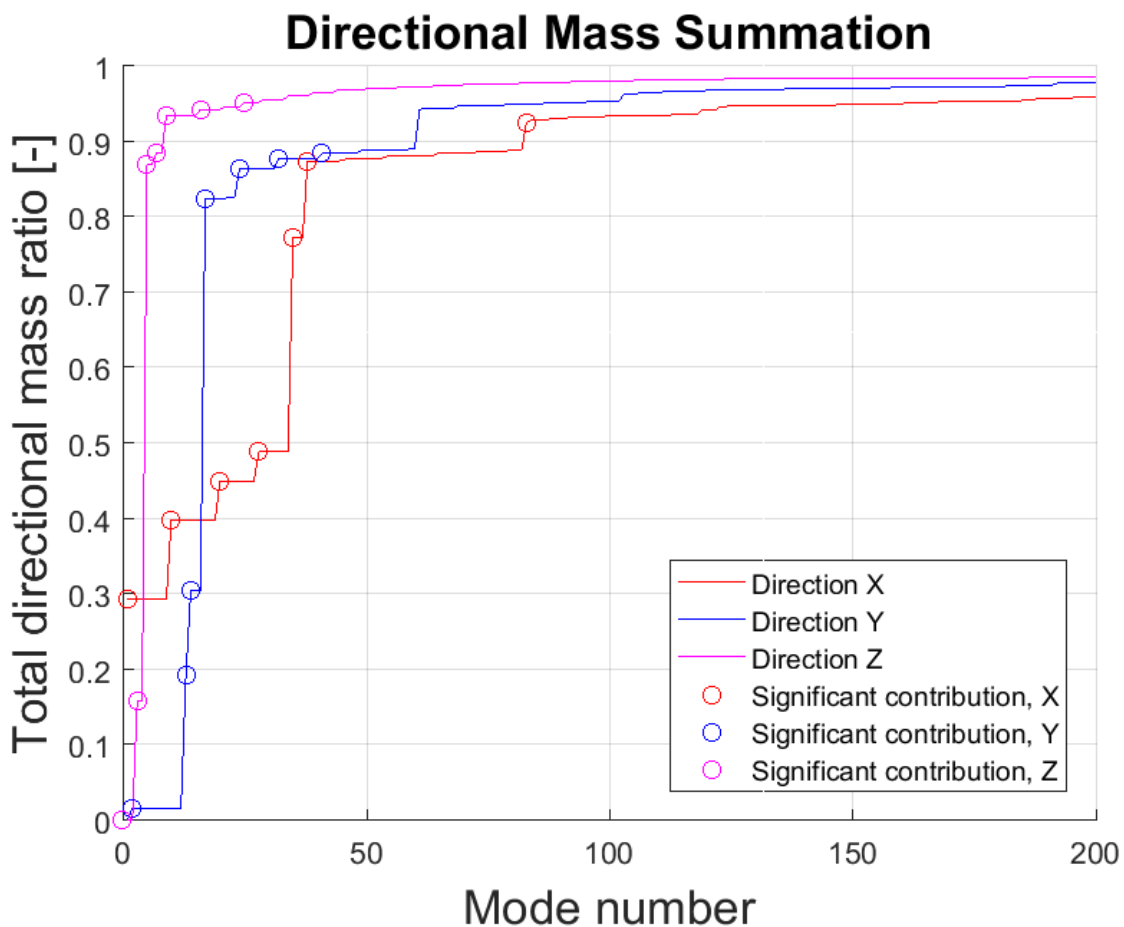


Figure D.9: Directonal mass summation for 200 modes

D.3.2 Rayleigh Damping Ratio Calculation

The Rayleigh damping ratio data for plot 7.28 in Section 7.4.3

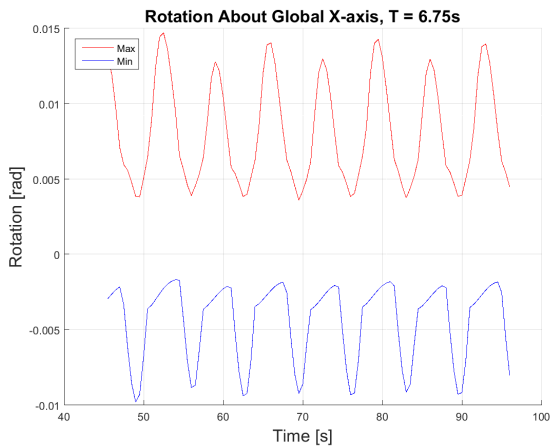
Table D.1: The data for the Rayleigh damping ratio plot in Section 7.4.3

Mode	ω [1/s]	Linear	m^{th}	Full	Average
1	0.02	0.050	0.050	0.050	0.050
2	0.04	0.053	0.035	0.032	0.034
3	0.05	0.053	0.033	0.031	0.032
4	0.06	0.055	0.032	0.028	0.030
5	0.06	0.055	0.032	0.028	0.030
6	0.06	0.055	0.032	0.028	0.030
7	0.06	0.055	0.032	0.028	0.030
8	0.06	0.056	0.032	0.027	0.030
9	0.07	0.056	0.032	0.027	0.030
10	0.07	0.057	0.032	0.027	0.030
11	0.08	0.058	0.033	0.027	0.030
12	0.09	0.059	0.034	0.027	0.031
13	0.09	0.060	0.034	0.028	0.031
14	0.10	0.061	0.035	0.028	0.032
15	0.10	0.061	0.036	0.028	0.032
16	0.12	0.063	0.039	0.030	0.034
17	0.12	0.064	0.040	0.030	0.035
18	0.13	0.065	0.041	0.031	0.036
19	0.13	0.066	0.042	0.032	0.037
20	0.15	0.067	0.044	0.033	0.039
21	0.15	0.069	0.046	0.034	0.040
22	0.17	0.071	0.050	0.036	0.043
23	0.17	0.072	0.051	0.037	0.044
24	0.19	0.074	0.055	0.040	0.047
25	0.20	0.075	0.056	0.041	0.048
26	0.21	0.077	0.060	0.043	0.051
27	0.22	0.078	0.062	0.044	0.053
28	0.24	0.080	0.065	0.047	0.056
29	0.25	0.082	0.068	0.048	0.058
30	0.26	0.083	0.070	0.050	0.060
31	0.27	0.085	0.074	0.053	0.063
32	0.29	0.088	0.078	0.056	0.067
33	0.30	0.089	0.081	0.057	0.069
34	0.30	0.090	0.082	0.058	0.070
35	0.33	0.094	0.089	0.063	0.076
36	0.34	0.095	0.091	0.064	0.077
37	0.34	0.095	0.091	0.064	0.077
38	0.35	0.096	0.093	0.065	0.079
39	0.36	0.098	0.097	0.068	0.083
40	0.38	0.100	0.100	0.070	0.085

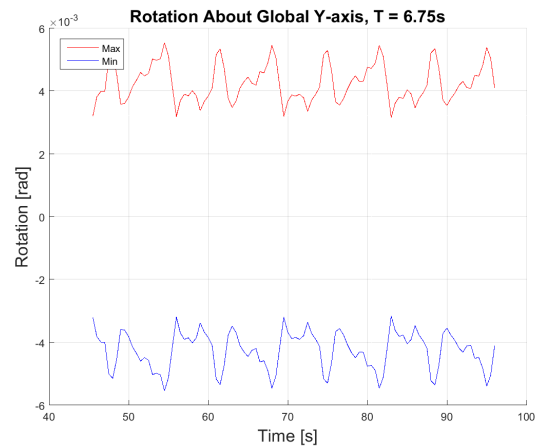
D.3.3 Harmonic Wave Results

D.3.4 Worst Harmonic Wave Period, $T = 6.75s$

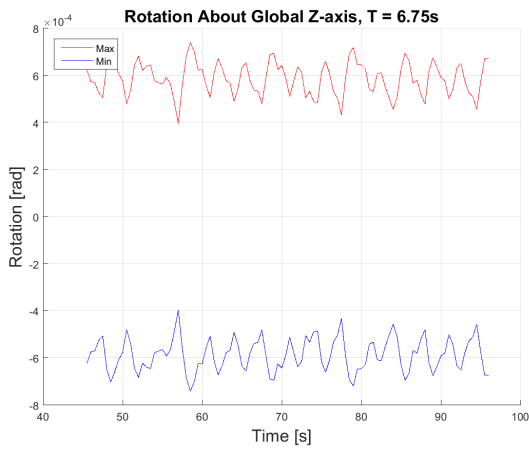
Rotations, Displacement, Stresses and Moments



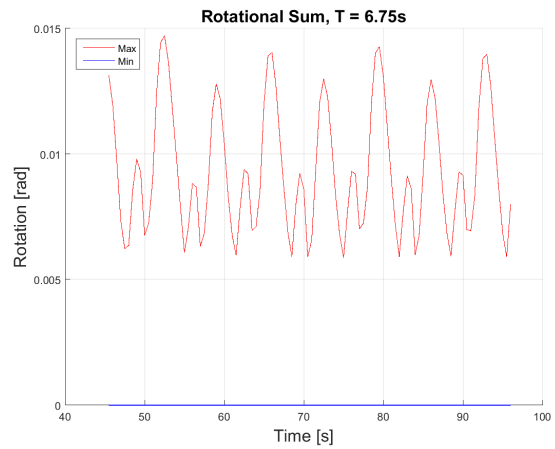
(a) Rotation in X-direction, Period = 6.75s



(b) Rotation in Y-direction, Period = 6.75s



(c) Rotation in Z-direction, Period = 6.75s



(d) Rotational sum of all global directions

Figure D.10: Rotations for wave period of 6.75s

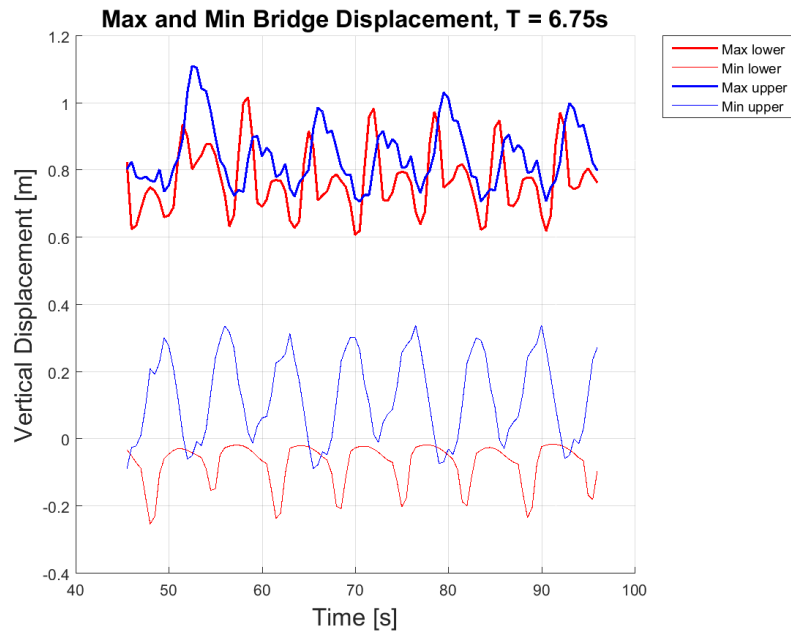


Figure D.11: The global maximum and minimum vertical displacement, T=6.75s

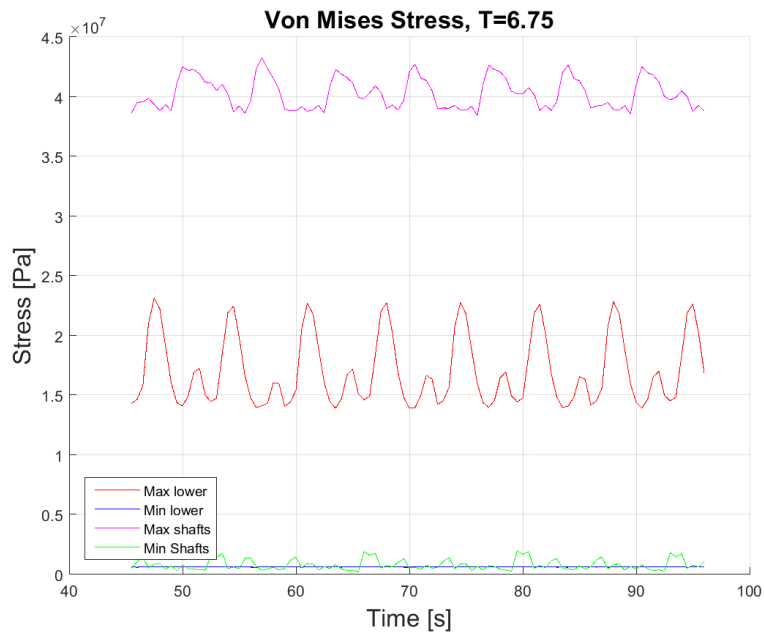


Figure D.12: Maximum and minimum von Mises stress, T=6.75s

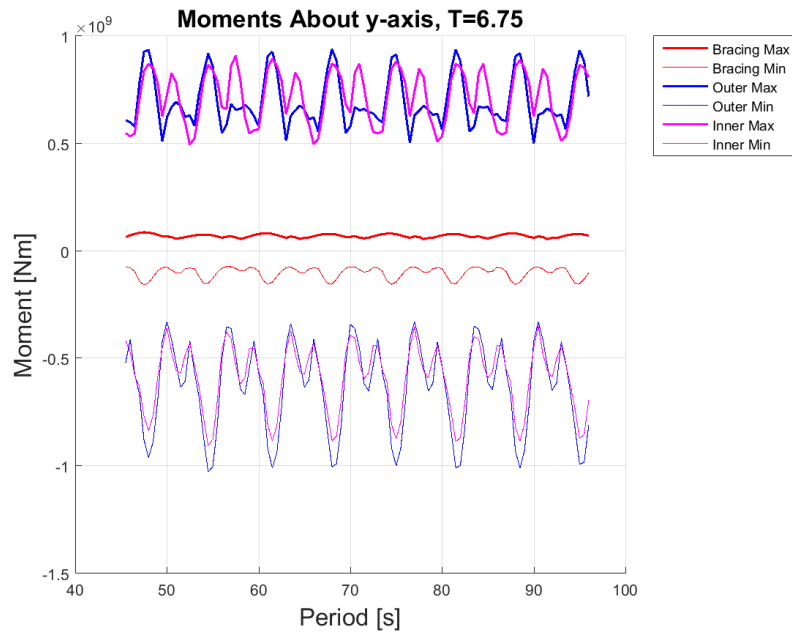


Figure D.13: Maximum and minimum bending moment about Y-axis, T=6.75s

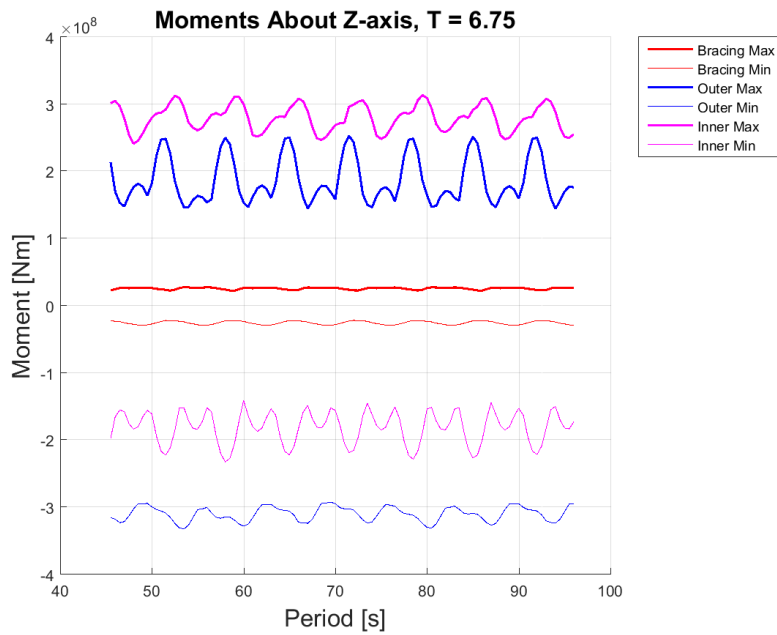


Figure D.14: Maximum and minimum bending moment about Z-axis, T=6.75s

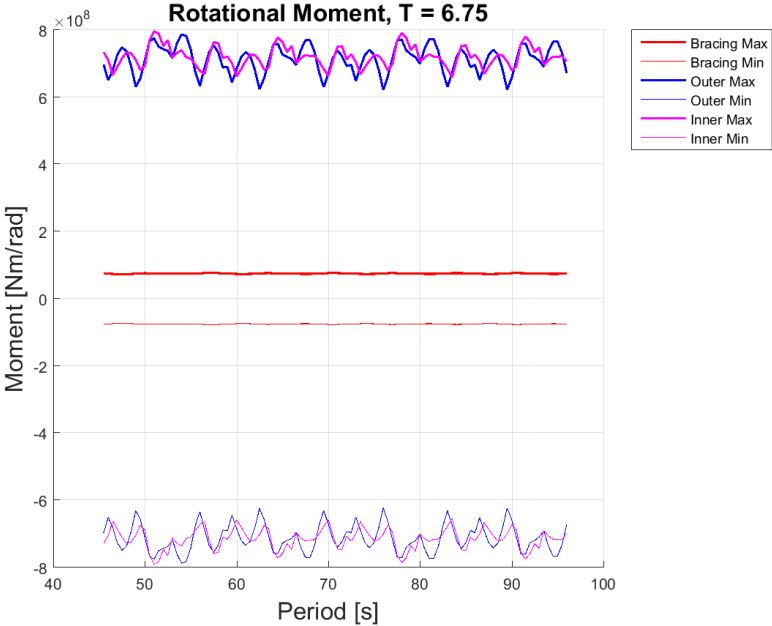


Figure D.15: Rotational maximum and minimum moment, T=6.75s

D.3.5 Harmonic Wave Results

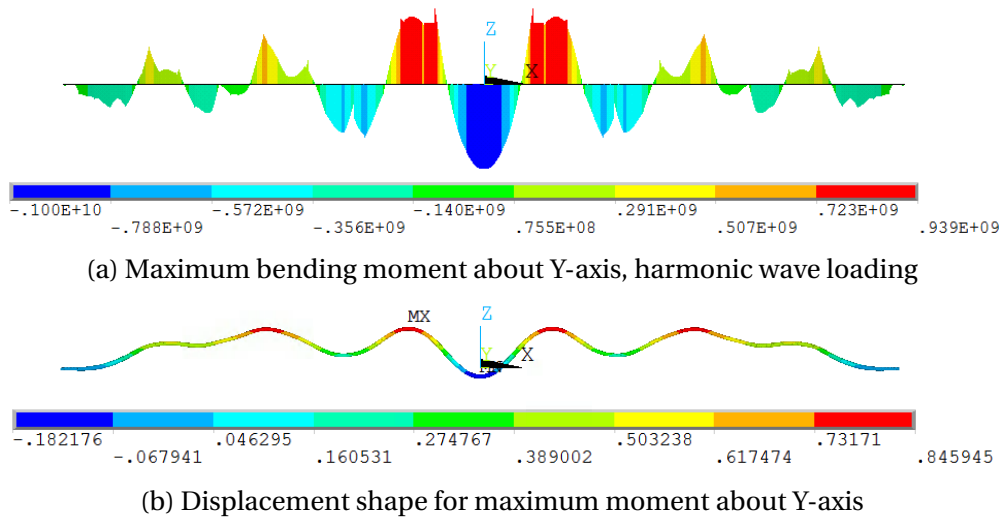


Figure D.16: Maximum bending moment about Y-axis for harmonic wave loading

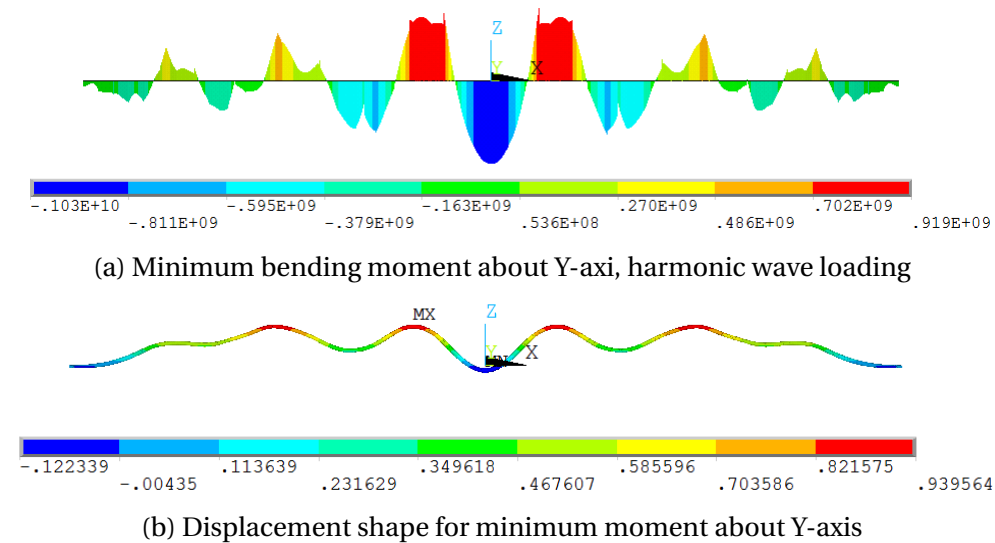


Figure D.17: Minimum bending moment about Y-axis for harmonic wave loading

D.3.6 Irregular Wave Results

D.3.6.1 Maximum and Minimum Nodal and Elemental Responses

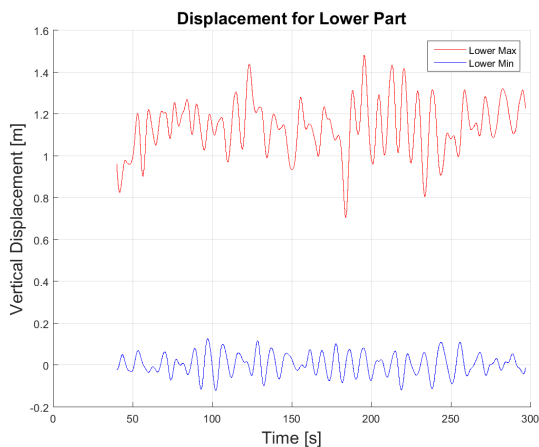
This appendix includes the response for specific nodes and elements. Each line in the figures represent one node or element, where the maximum response for the whole structure occurs.

The response for this certain node or element is collected through out the analysis.

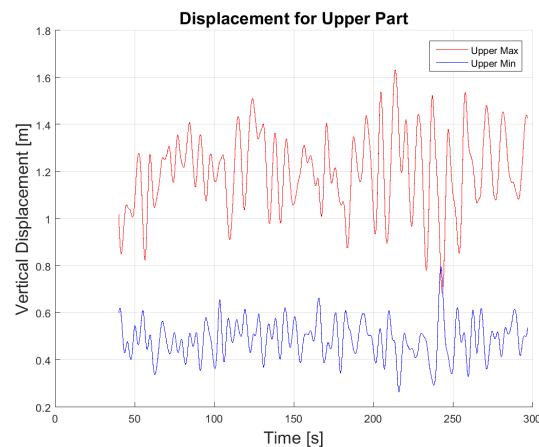
The analysis time series stretches from approximately 40 second to 300 seconds. The responses are used to estimate a variance for the maximum response for 300 seconds, and thereby estimate the maximum response for a three hour sea state (10800 seconds).

Some of the figures described either the *lower* or *upper part* of the structure. The lower part includes the main tunnels and the bracing elements, while the upper part includes the connection shafts and the pontoons. Other plots describe the *bracing*, outer and inner parts of the SFT. The bracing is naturally the bracing elements between the main tunnels. The *outer* part is the outer main tunnel (the one with the biggest radius). The *inner* part is the inner main tunnel.

Vertical Displacement



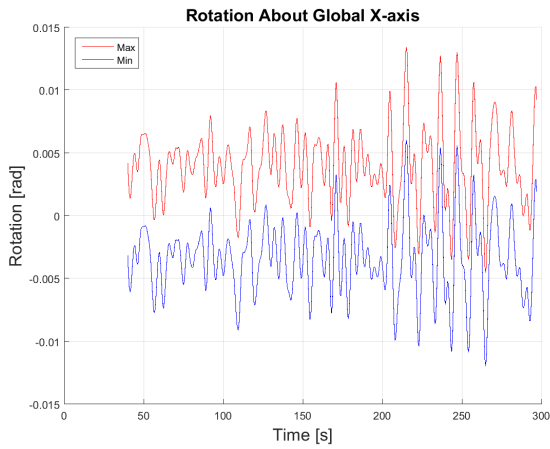
(a) Vertical displacement for the nodes with maximum and minimum response in the lower part of the structure



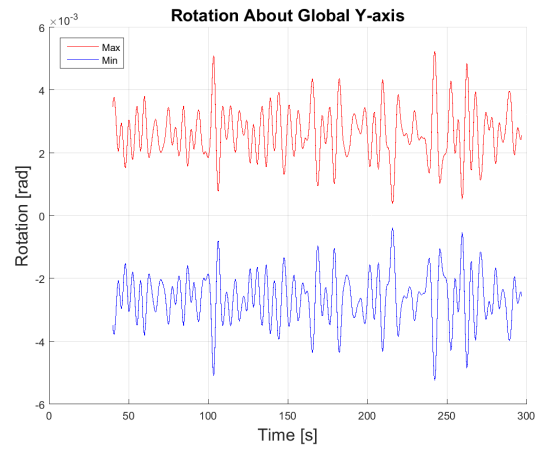
(b) Vertical displacement for the nodes with maximum and minimum response in the upper part of the structure

Figure D.18: Vertical displacement for the nodes with maximum and minimum response for the whole structure, irregular wave loading

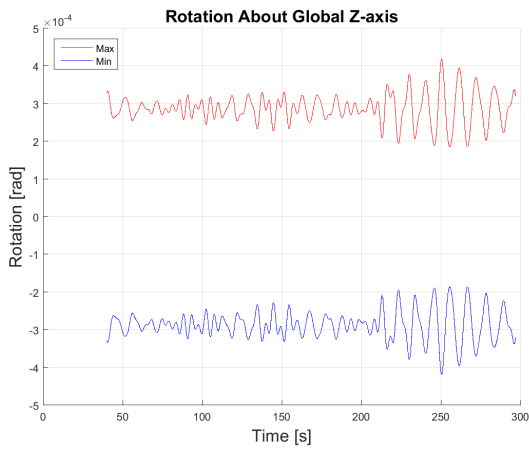
Rotations



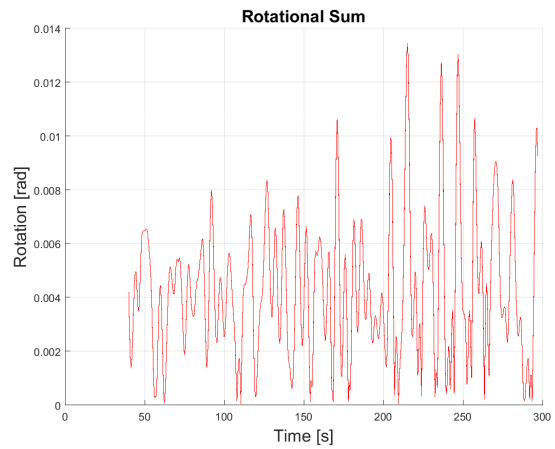
(a) Rotation about global X-axis for irregular wave loading



(b) Rotation about global Y-axis for irregular wave loading



(c) Rotation about global Z-axis for irregular wave loading

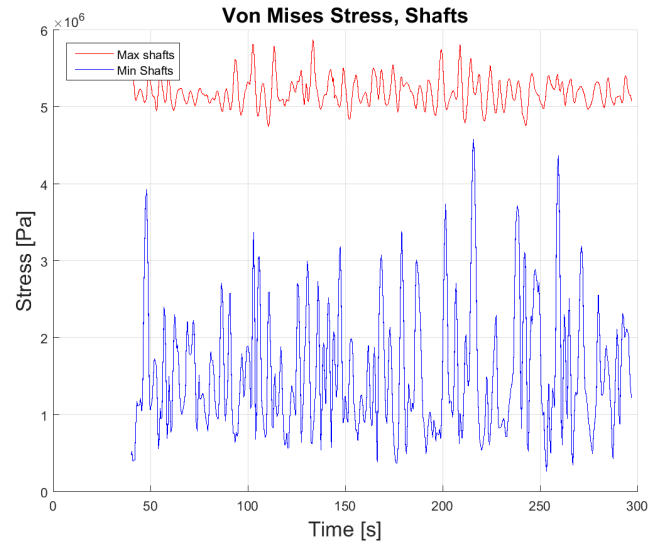


(d) Rotational sum for all axes for irregular wave loading

Figure D.19: Rotation for the nodes with maximum and minimum response about all global axes, irregular wave loading

Von Mises Stress

(a) Von Mises stress for the lower part of the structure



(b) Von Mises stress for the shafts of the structure

Figure D.20: Von Mises stress for the nodes where maximum and minimum stress occurs, irregular wave loading

Bending Moment About Global Y-axis

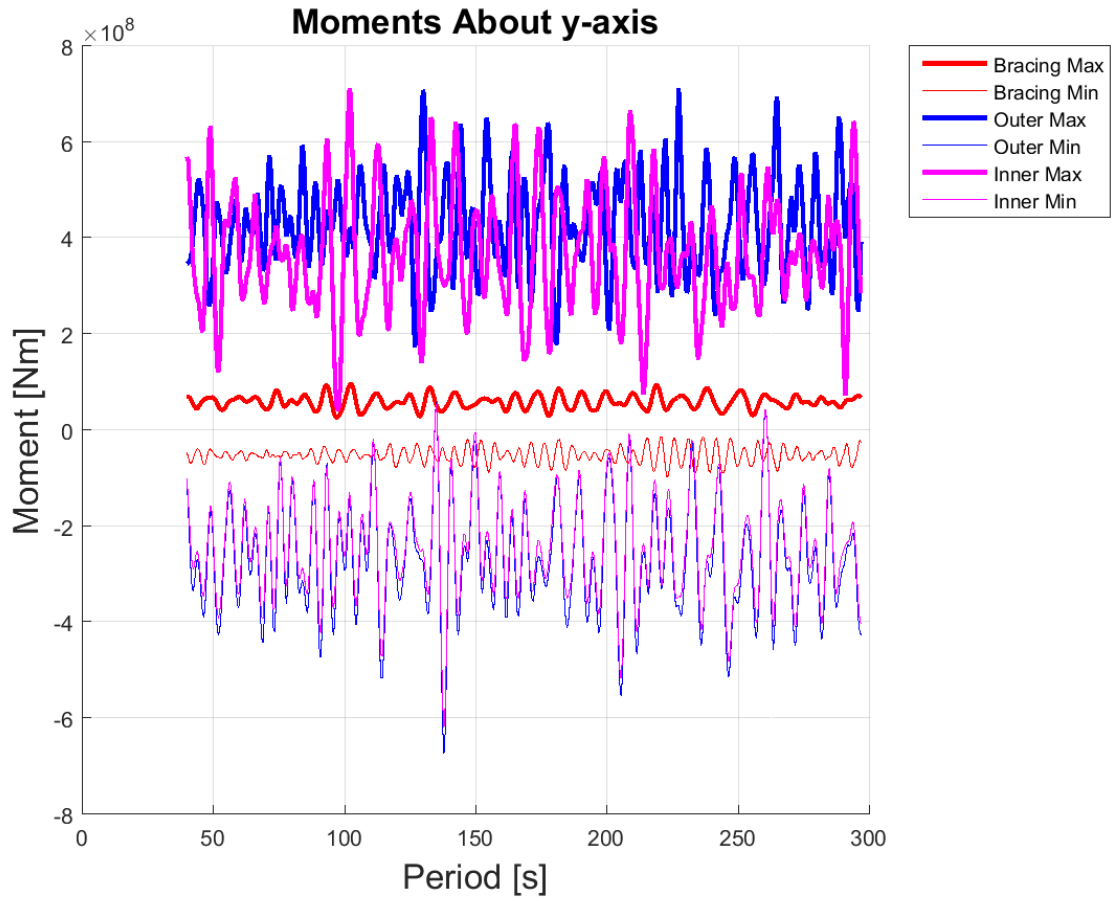
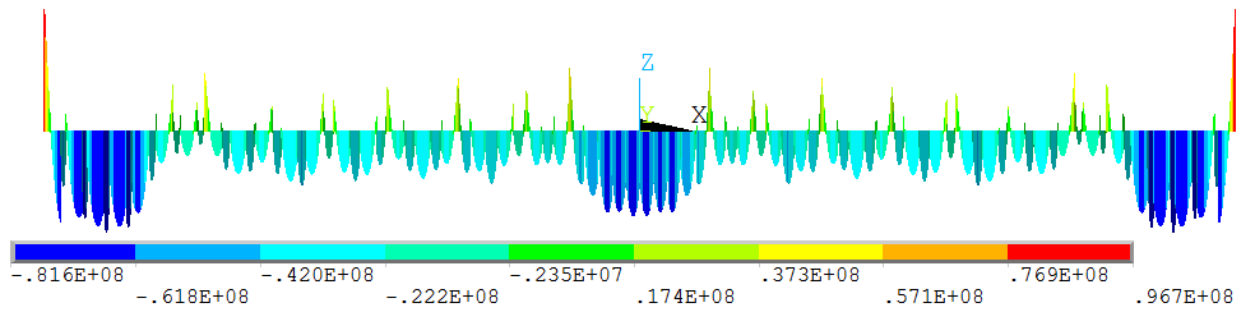
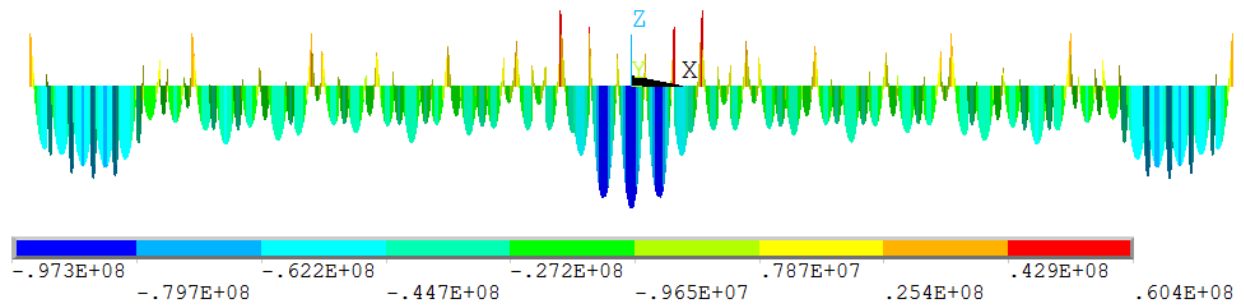


Figure D.21: Bending moment about global Y-axis for the elements where maximum and minimum moment occurs

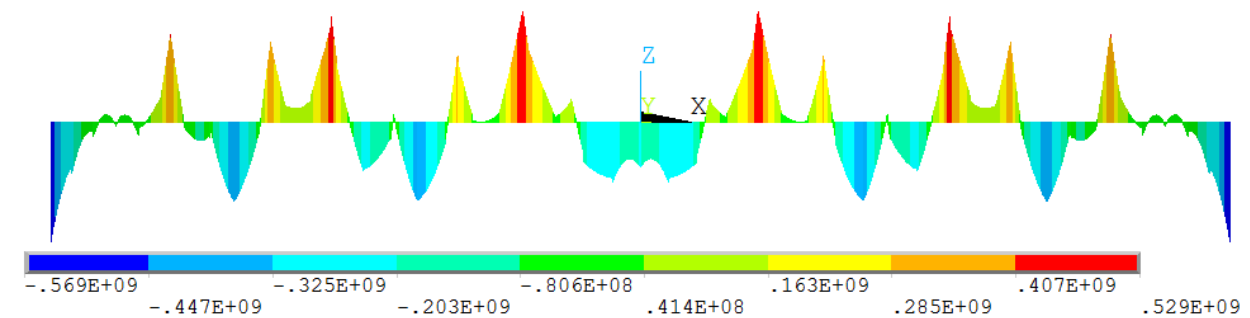


(a) Maximum bending moment about global Y-axis in bracing elements

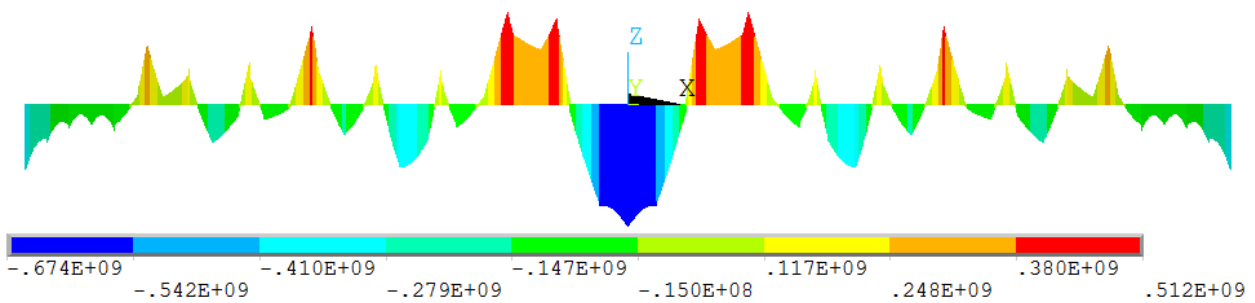


(b) Minimum bending moment about global Y-axis in bracing

Figure D.22: Bending moment about global Y-axis in the bracing

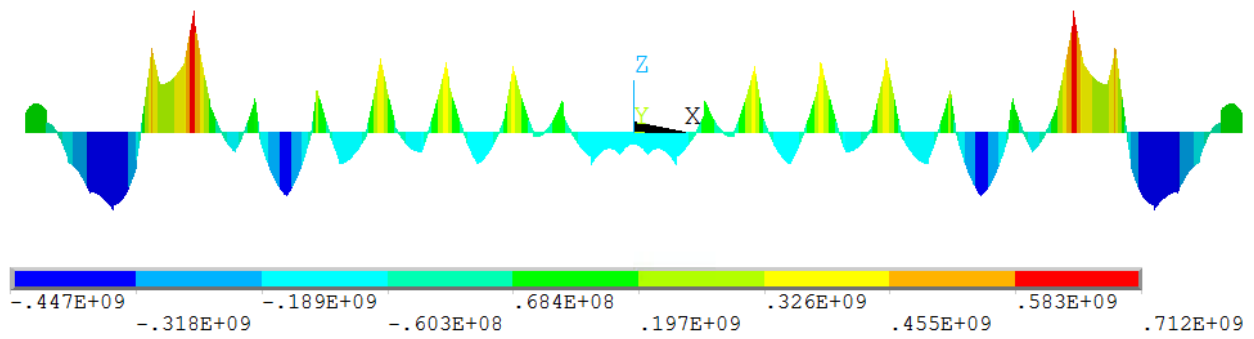


(a) Maximum bending moment about global Y-axis in outer main tunnel

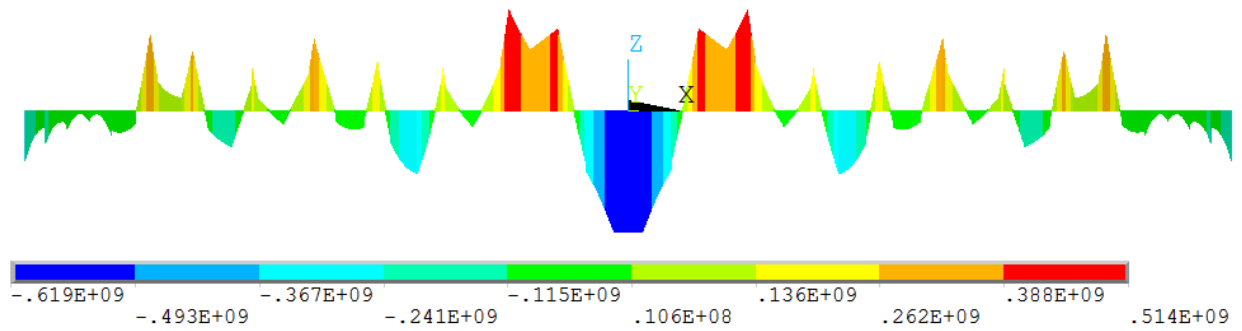


(b) Minimum bending moment about global Y-axis in outer main tunnel

Figure D.23: Bending moment about global Y-axis in the outer main tunnel



(a) Maximum bending moment about global Y-axis in inner main tunnel



(b) Minimum bending moment about global Y-axis in inner main tunnel

Figure D.24: Bending moment about global Y-axis in the inner main tunnel

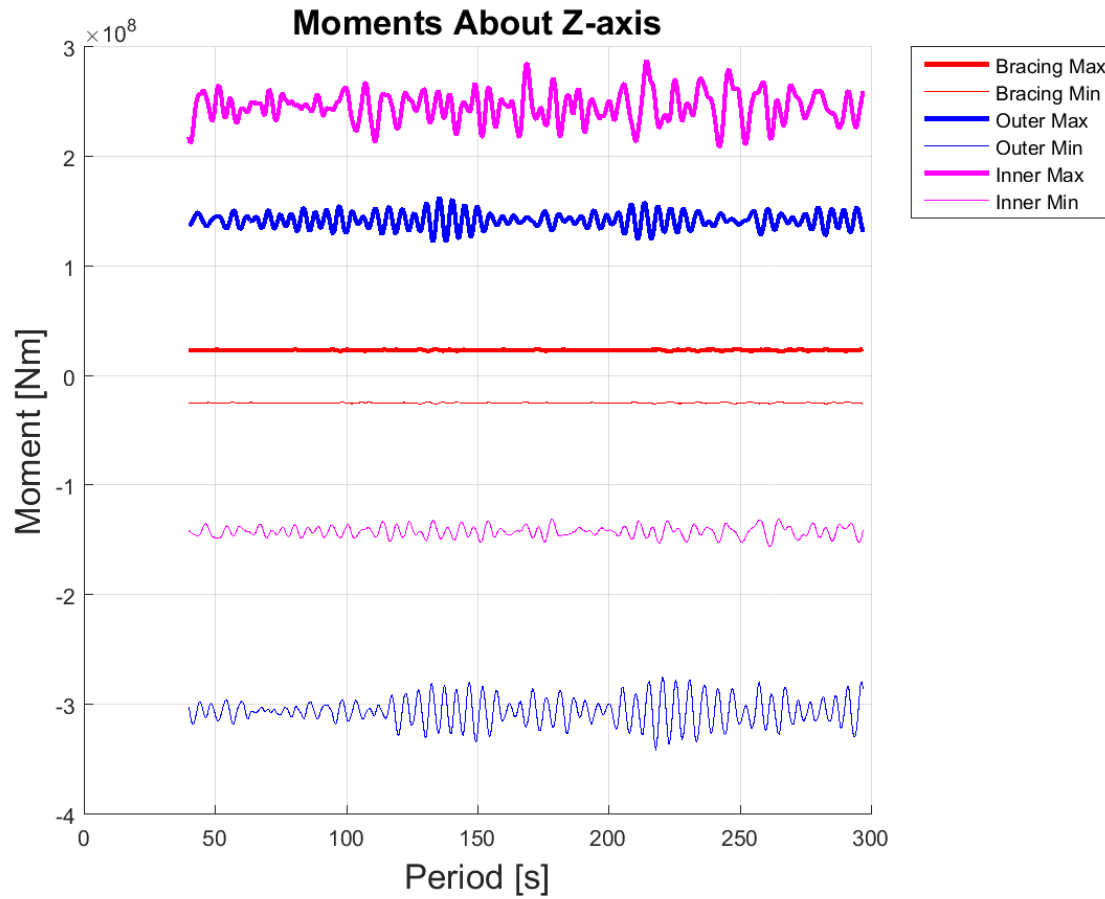
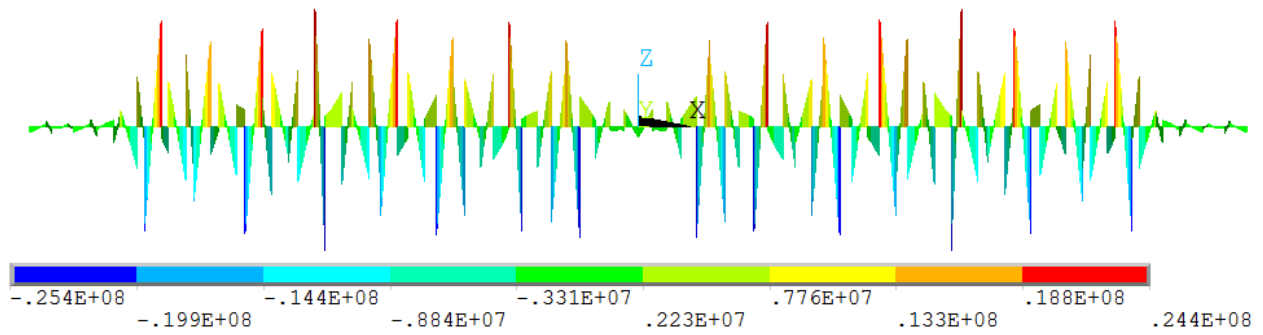
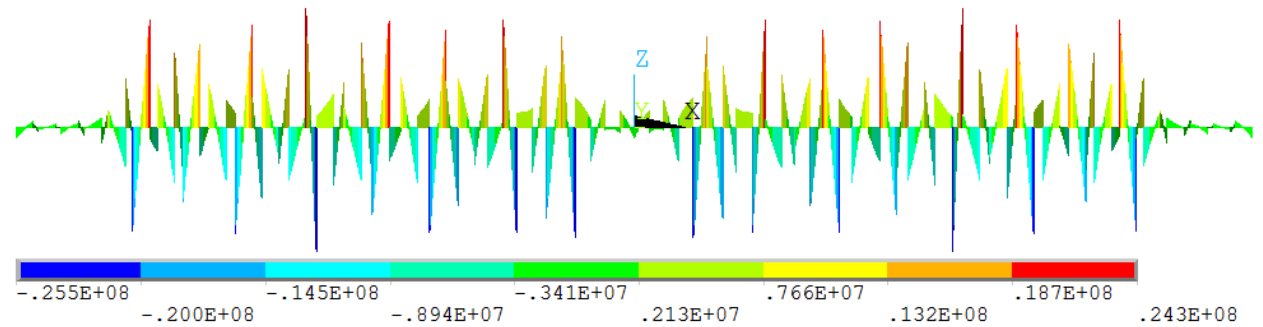
Bending Moment About Global Z-axis

Figure D.25: Bending moment about global Z-axis for the elements where maximum and minimum moment occurs

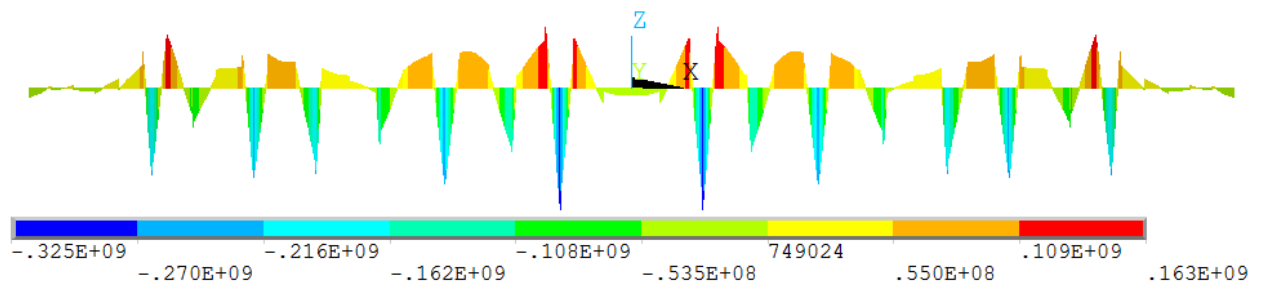


(a) Maximum bending moment about global Z-axis in bracing

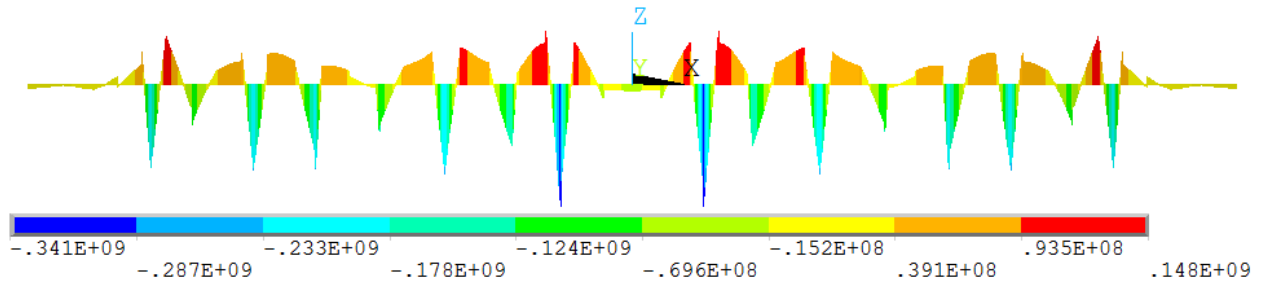


(b) Minimum bending moment about global Z-axis in bracing

Figure D.26: Bending moment about global Z-axis in bracing

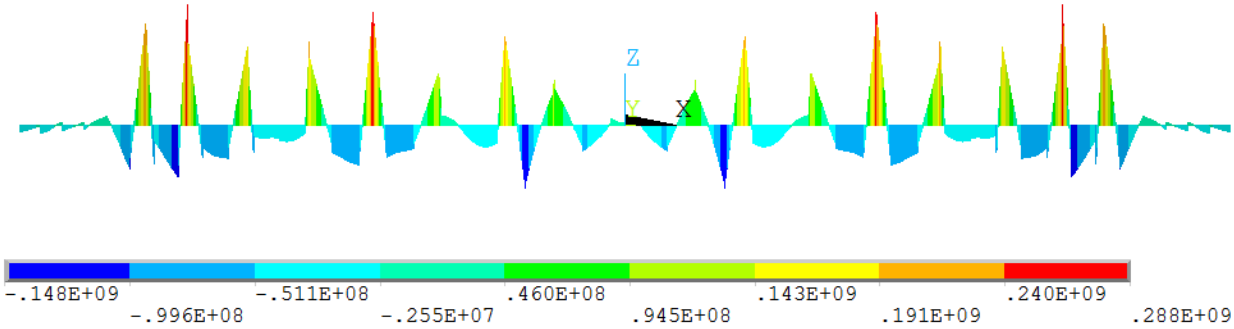


(a) Maximum bending moment about global Z-axis in outer main tunnel

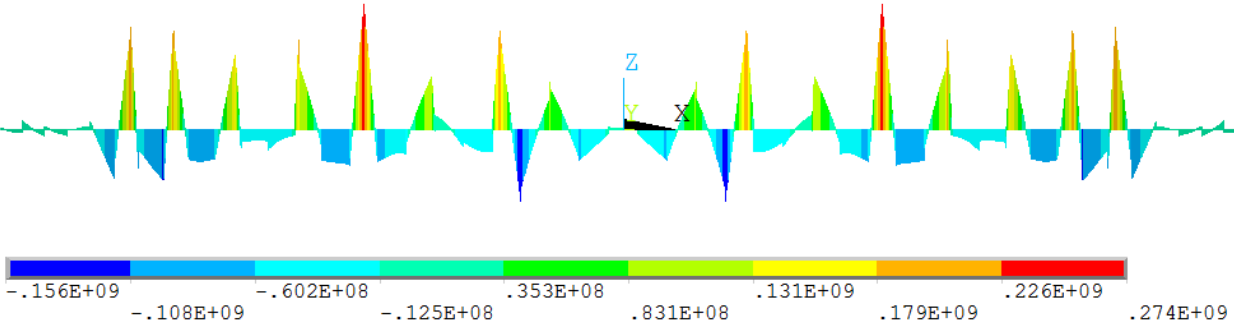


(b) Minimum bending moment about global Z-axis in outer main tunnel

Figure D.27: Bending moment about global Z-axis in the outer main tunnel



(a) Maximum bending moment about global Z-axis in inner main tunnel



(b) Minimum bending moment about global Z-axis in inner main tunnel

Figure D.28: Bending moment about global Z-axis in the inner main tunnel

Torsional Moment About Global X-axis

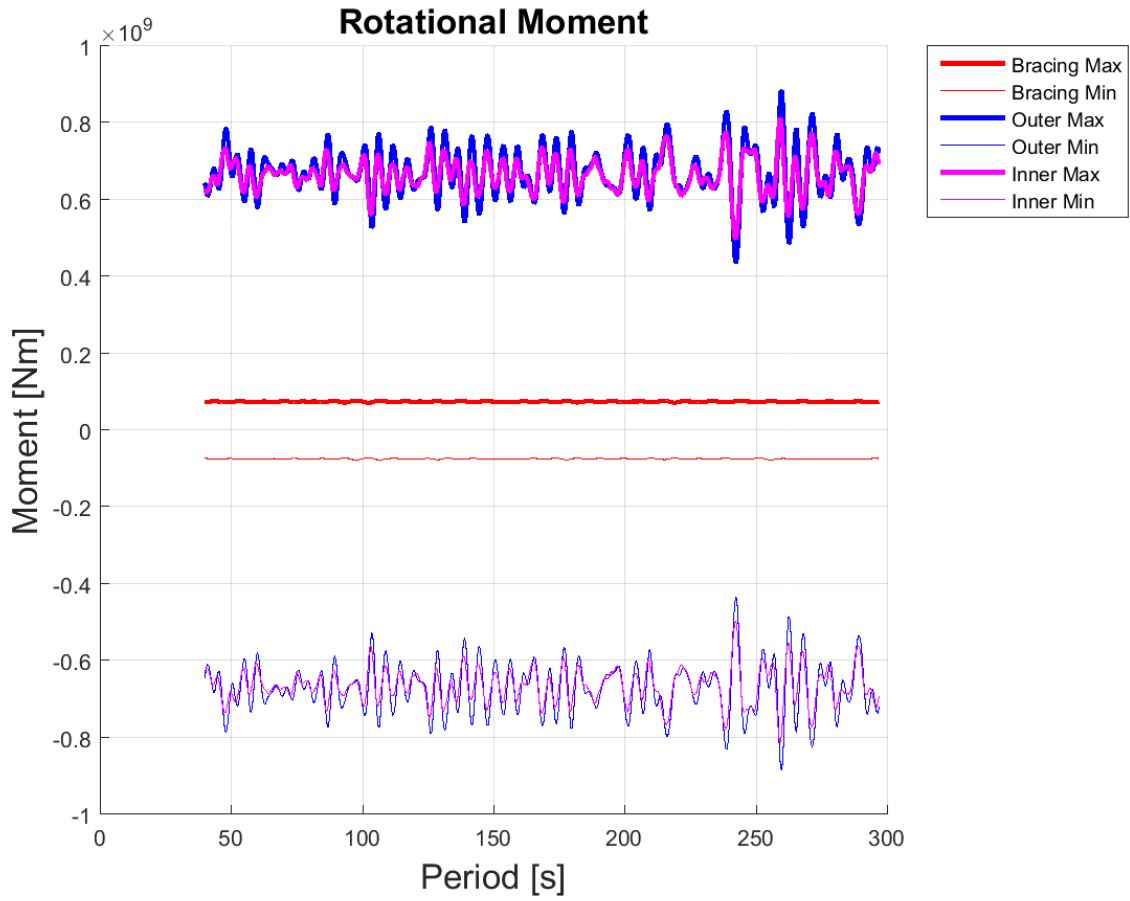
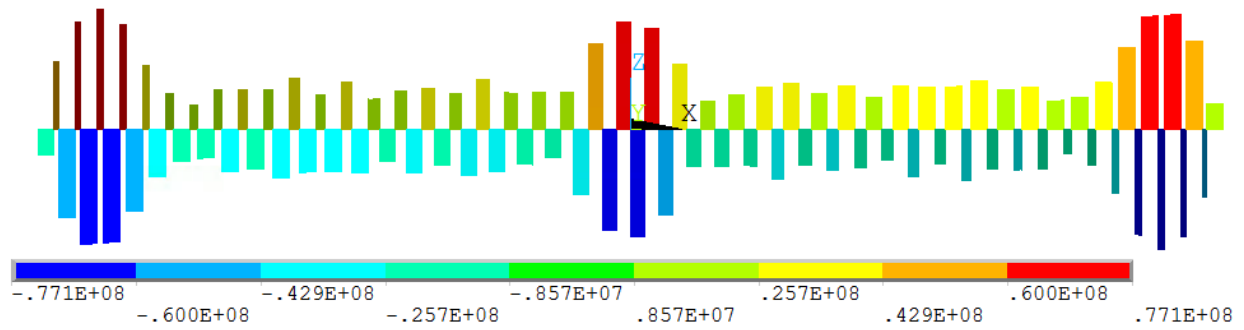
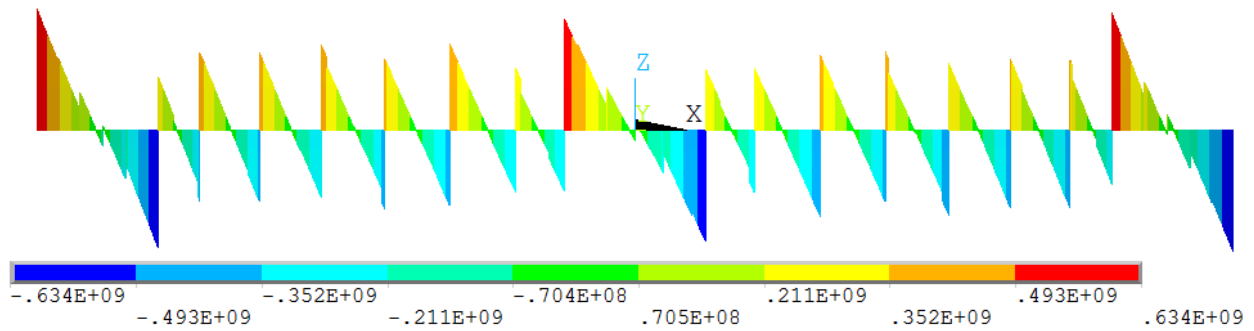


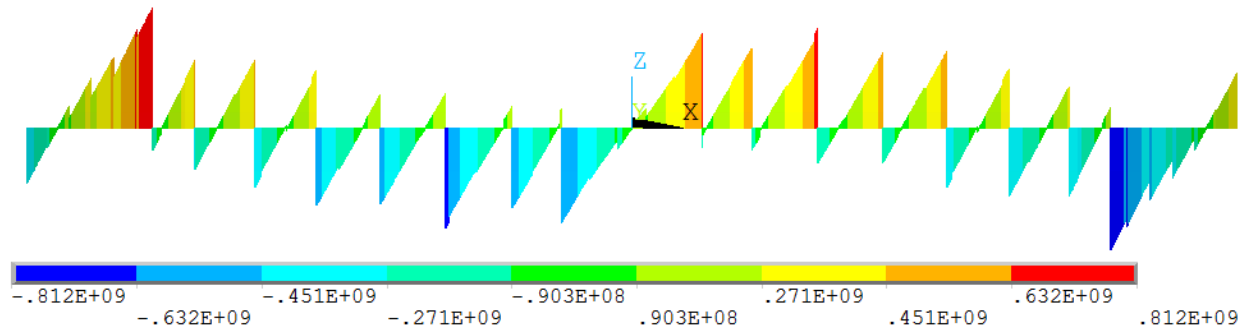
Figure D.29: Torsional moment about global Z-axis for the elements where maximum and minimum moment occurs



(a) Maximum and minimum torsional moment in bracing



(b) Maximum and minimum torsional moment in outer main tunnel



(c) Maximum and minimum torsional moment in inner main tunnel

Figure D.30: Torsional moment in the whole lower structure

Appendix E

Digital Appendix

The digital appendix the list below: It shows all the folder in the digital appendix and how what each folder contain.

Digital Appendix:

- Ansys Analyses - The files for running the Ansys analyses
 - Bridge - Harmonic wave: Program for running the harmonic wave analysis with the complete bridge model
 - Bridge - JONSWAP: Program for running the irregular wave analysis with the complete bridge model
 - Bridge - Decreasing Mesh Size: Program running a mesh convergency test with decreasing mesh size
 - Bridge - PSO: Program running a particle swarm optimization for the mesh convergency
 - Pontoon - RAO and wave input testing: Files for running harmonic wave analysis on the pontoon modeled in Ansys.
 - Archive:
- Wadam Analyses - The files and analyses done for the pontoon in Sesam

- Final Geometry: Contains the Genie input files and the finished Wadam analyses for the final pontoon geometry
- Simplified Geometry: Contains the Genie input files and the finished Wadam analyses for the simplified pontoon geometry
- Results - The post processed results from both Ansys and Wadam
 - Ansys Results
 - * Dynamic harmonic results - Pontoon model: Post processed results with finished RAO plots for the pontoon
 - * Dynamic harmonic results - Global model: Post processed results with all the responses saved in plots. Also contains the result files
 - * Dynamic irregular results - Global model: Post processed results with all the responses saved in plots. Also contains the result files
 - * Mesh convergence: The results for the mesh convergence test. Contains both plots and result files
 - * Modal analysis: The information from the modal analysis. Contains both plots and resultfiles for eigenfrequencies and directional mass participation. Also contains program for calculating the Rayleigh damping
 - Wadam Results - The results from Wadam
 - * Natural frequency iteration: A matlab file finding the natural frequencies for the motions based on a Wadam output file
 - * Potential Damping: The result files for pontoon potential damping. Also contains plots, curve fitting and mathematical expressions for the damping
 - * Results RAO: Plots and result files for the pontoon RAOs.
- Pictures from the Masters Thesis: All the pictures which can be found in the pdf version of the final Master Thesis

Fin